Modulation Spectroscopy of Ultracold Atoms in Optical Lattices

Dissertation
zur
Erlangung des Doktorgrades (Dr. rer. nat.)
der
Mathematisch-Naturwissenschaftlichen Fakultät
der
Rheinischen Friedrich-Wilhelms-Universität Bonn

von
Karla Henriette Loida
aus
Hamburg

Bonn, 2017

Dieser Forschungsbericht wurde als Dissertation von der Mathematisch-Naturwissenschaftlichen Fakultät der Universität Bonn angenommen und ist auf dem Hochschulschriftenserver der ULB Bonn `http://hss.ulb.uni-bonn.de/diss_online` elektronisch publiziert.

1. Gutachterin:	Prof. Dr. Corinna Susann Kollath
2. Gutachter:	Prof. Dr. Johann Kroha
Tag der Promotion:	26.02.2018
Erscheinungsjahr:	2018

Abstract

In the past fifteen years ultracold atoms confined to optical lattices, which are artificial crystals of light, have proven to be powerful tools in the study of strongly correlated many-body systems widely known from a condensed matter context. The detailed knowledge, high tunability and control of microscopic parameters has enabled the creation and control of highly non-trivial quantum systems for which a direct comparison of model calculations to experimental measurements is now possible. In order to gain precise information on the properties of ultracold gases in optical lattices, many powerful methods have been developed. In particular spectroscopic methods have enabled to probe different characteristic excitations. However, many fascinating properties of strongly interacting quantum many-body systems are not yet fully characterized. Therefore, this thesis explores further possibilities of lattice modulation spectroscopy which is a time-periodic modulation of the optical lattice amplitude. We theoretically investigate the response of different (mostly one-dimensional) cold atom systems to a lattice modulation by means of the time-dependent density matrix renormalization group method and different analytical approximations. In addition to the normal lattice modulation, we consider a *superlattice* modulation scheme where the lattice amplitude is modulated in a dimerized fashion, coupling to a certain class of excitations in the system. The lattice modulation spectroscopy is a versatile probe which we use to study different situations relevant for experimental applications. We show that a detection of signatures of the exotic *bond order wave* phase is feasible in a system of interacting fermions on a one-dimensional optical lattice with staggered energy offset. Moreover, we demonstrate that a temperature measurement of fermions confined to an optical lattice is possible as well as a determination of the interaction strength of bosonic atoms confined to a one-dimensional optical lattice. In addition, various excitations in all these systems are investigated in detail.

Zusammenfassung

In den letzten fünfzehn Jahren haben sich ultrakalte Gase in optischen Gittern, künstlichen Gittern aus Licht, als wirksame Plattform zur Untersuchung stark korrelierter Vielteilchensysteme, oftmals aus der Festkörperphysik bekannt, erwiesen. Die genaue Kenntnis, Einstellbarkeit und Kontrolle der mikroskopischen Parameter hat es ermöglicht nicht-triviale Quantensysteme zu erschaffen und zu kontrollieren wodurch ein direkter Vergleich von Modellrechnungen und experimentellen Messungen möglich ist. Um Informationen über die Eigenschaften ultrakalter Gase in optischen Gittern zu erhalten, wurden eine Vielzahl passender Messmethoden entwickelt. Insbesondere spektroskopische Methoden geben Aufschluss über unterschiedliche charakteristische Anregungen im System. Jedoch sind noch immer viele spannende Eigenschaften stark wechselwirkender Quantenvielteilchensysteme nicht vollständig charakterisiert. Daher werden in dieser Arbeit neue Anwendungsmöglichkeiten der Amplitudenmodulationsspektroskopie, einer periodischen Modulation der Lichtgitteramplitude, entwickelt. Wir untersuchen die Wirkung der Amplitudenmodulation auf unterschiedliche (meist eindimensionale) kalte Atom Systeme mit Hilfe der zeitabhängigen Dichtematrix-Renormierungsgruppe und unterschiedlicher analytischer Methoden. Insbesondere untersuchen wir eine *Supergitter*-Modulation, bei der die Gitteramplitude auf dimerisierte Art und Weise moduliert wird und somit an eine bestimmte Klasse von Anregungen im System koppelt. Die Modulationsspektroskopie ist eine vielfältig anwendbare Methode und wir untersuchen verschiedene Situationen, die auch relevant für experimentelle Anwendungen sind. Zum einen zeigen wir, dass man Charakteristika der exotischen *Bond-Order Welle* in einem System wechselwirkender Fermionen im eindimensionalen Gitter mit alternierendem Potential nachweisen kann. Zum anderen zeigen wir, wie die Temperatur von Fermionen im optischen Gitter bestimmt werden kann, sowie die Wechselwirkungsstärke von bosonischen Teilchen im eindimensionalen Gitterpotential. Außerdem werden diverse Anregungen in allen diesen Systemen im Detail untersucht.

List of publications related to this thesis

- K. Loida, A. Sheikhan and C. Kollath, Thermometry of ultracold fermions by (super)lattice modulation spectroscopy, *Physical Review A* **92**, 043624 (2015)

- K. Loida, J.-S. Bernier, R. Citro, E. Orignac and C. Kollath, Probing the bond order wave phase transitions of the ionic Hubbard model by superlattice modulation spectroscopy, *Physical Review Letters* **119**, 230403 (2017)

- K. Loida, J.-S. Bernier, R. Citro, E. Orignac and C. Kollath, Excitation spectrum of the one-dimensional ionic Hubbard model by superlattice modulation spectroscopy, *in preparation*

- K. Loida, J.-S. Bernier, R. Citro, E. Orignac and C. Kollath, Accessing finite momentum excitations of the one-dimensional Bose-Hubbard model using superlattice modulation spectroscopy, *arXiv:1803.01951*

Contents

CHAPTER 1

Introduction

Understanding interacting quantum many-body systems is one outstanding challenge of modern quantum physics. In principle, these can be any systems composed of three to a very large number of interacting particles. Particularly interesting physics happens when the individual particles' behavior triggers emergent collective phenomena. Inspiring examples are the intriguing properties of strongly correlated condensed matter systems such as high-temperature superconductivity whose microscopic origin is an unresolved question up to today. Due to their complexity, many of these systems push the limits of high-performance computers and sophisticated experimental tools. Exact numerical simulations of systems consisting of numerous particles are very limited, even on today's most powerful supercomputers. Advances in experimental and theoretical tools are required to further approach the intricate properties of many-body systems and to provide us with new insights on long-standing challenges which may also reveal surprising results.

During the past few decades, remarkable progress in the control and manipulation of atomic gases has profoundly influenced our understanding of quantum many-body physics. As a start, the increased control of atomic motion became possible by the application of laser light to cool and trap atoms which was awarded with the Nobel prize in physics in 1997 [1–3]. A major breakthrough towards creating and controlling quantum mechanical systems was the experimental realization of Bose-Einstein condensation [4–6] with ultracold atomic gases. This is one of the most intriguing phenomena predicted by quantum statistical mechanics where a macroscopic number of bosonic atoms collectively occupies the lowest energy state. Its realization in an atomic vapor, which was awarded with the Nobel prize in physics in 2001 [7, 8], presents a macroscopic piece of quantum matter that is well-defined and flexibly controllable. In the early days, research mainly focused on the properties of these condensates such as for example matter wave coherence [9, 10]. Nowadays, bosonic and fermionic species are routinely cooled into the so-called quantum degenerate regime where the physical characteristics are determined by quantum mechanical laws. In the case of fermions [11], this means that (almost) each single-particle state is occupied with one fermionic particle up to the so-called Fermi sea.

In recent years, a strong interest has developed in the study of ultracold atoms trapped in optical lattices which is more in line with situations encountered in condensed matter physics. A crystal of light is imposed on top of the atomic cloud in order to trap the atoms in periodic potentials. The light field acts as a conservative trapping potential for the atoms and almost arbitrary potential landscapes can be created that are highly controllable by varying external field parameters, even in a time-dependent way.

Ultracold atoms in periodic potentials constitute a powerful platform to realize strongly correlated states as the suppression of tunneling between neighboring potential wells effectively enhances interactions. The created systems are clean, simple and extremely versatile due to extensive control over, for instance, geometry, dimension, interactions and disorder. As a consequence one can engineer tunable quantum systems to study specific physical phenomena at interest. This is a major advantage compared to real crystals where one has to naturally deal with the interplay of different physical aspects due to, for example, defects or lattice vibrations. In a pioneering experiment, the authors of Ref. [12] loaded bosonic particles into an optical cubic lattice, implementing a strongly correlated many-body system described by the Bose-Hubbard model [13]. The authors succeeded in observing signatures of the underlying phase transition from a localized interaction-driven Mott insulating state to a delocalized superfluid state. In the case of fermionic particles, a degenerate gas in an optical lattice described by the Fermi-Hubbard model was realized soon after [14] and the Fermi surface was imaged, followed by the realization of a Mott insulating state [15, 16]. More recently, the investigation of magnetically ordered phases has come within reach as relevant spin correlations were observed [17–19]. Ultracold atoms in optical lattices provide a whole toolbox for engineering various Hubbard-type models in its cleanest form, for which the effective parameters can be derived from microscopic principles. There are numerous theoretical proposals to mimic various condensed matter systems and the number of experiments in the strongly correlated regime has been growing significantly. Notably, the quantum gas approach to many-body physics takes a many-body model as its starting point that can be realized experimentally. This is fundamentally different to condensed matter physics where experimentally observed phenomena trigger the search for a theoretical description. This corresponds to the concept of quantum simulation which can be seen as an implementation of Feynman's pioneering ideas for using one well-controlled quantum system to simulate another [20].

A field of special interest is the study of one-dimensional systems where the role of quantum fluctuations and quantum correlations is particularly important and dominates the system's behavior leading to physical properties that are drastically different from the 'normal' physics in three dimensions. Interactions play a very special role as hard-core particles in one dimension cannot pass each other, picture for example beads on a string, which leads to a collective behavior of the excitations. One-dimensional models were for a long time regarded as mathematical curiosities with little use for the real three-dimensional world. In the context of cold atomic gases quasi one-dimensional systems can be created by confining the motion of particles to one direction in space [21]. In the case of a degenerate gas which is usually produced in a three-dimensional geometry, one can realize quasi one-dimensional systems by making the trap very anisotropic. In an optical lattice, the tunnel barrier can be increased to suppress tunneling along certain directions and thus create one-dimensional geometries. In the past fifteen years there has been a variety of experimental studies of one-dimensional systems in the cold atom context which are in many cases well described by mathematical 'toy-models'. In return, this stimulated more theoretical investigations, leading to a fascinating interplay of theory and experiment. For example the transition from a superfluid state to a Mott insulating state in one dimension was investigated [22–25] and also the crossover regime to three dimensions. From the theory side, exact solutions in one dimension can be obtained using the Bethe-ansatz method [26]. However, this method is difficult to use to extract observables and it is limited to a few models such that alternative techniques are required. There are powerful approximate methods such as bosonization [27] which describes low-energy properties of one-dimensional systems. A major breakthrough has come with the development of effective numerical techniques, in particular the time-dependent density matrix renormalization group method [28, 29] which describes finite size and non-equilibrium situations well and enables a direct comparison to experiments in many cases.

Different experimental techniques have been developed to explore the characteristics of ultracold atoms in optical lattices. Among the available probes are most prevalent spectroscopic methods which quite generally rely on the interaction between light and matter. In the context of cold atoms powerful spectroscopic methods are radio frequency, Raman, Bragg or lattice modulation spectroscopy [30, 31]. For instance, these probes give access to single-particle, density or kinetic energy spectral functions encoding information on the underlying many-body state. In lattice modulation spectroscopy the amplitude of the light potential periodically oscillates in time such that excitations in the system are created whenever the modulation frequency corresponds to the energy of an available excitation. Monitoring the energy absorbed by the system, typically by a measurement of the induced heating [22] or the double occupancy [15] in the case of bosons and fermions respectively, yields information on the initial many-body state.

Taking this as a starting point, we can formulate the main objective of this thesis: to explore further the possibilities of lattice modulation spectroscopy in order to gain information on both, fermionic and bosonic systems confined to optical lattices. We focus mainly on the study of one-dimensional systems using the time-dependent density matrix renormalization group method to simulate the response of the system to a modulation of the lattice amplitude. We compare the obtained results to different analytical approximations and make close connection to available experimental setups. Notably, we introduce a 'novel' lattice modulation scheme which we call *superlattice* modulation spectroscopy and which is of dimerized geometry in the sense that while the lattice amplitude on one lattice site is increased by the modulation it is decreased on the neighboring lattice site. This modulation scheme transfers a finite momentum to the system and thus couples to a certain class of excitations. Our approach it twofold. On the one hand, our theoretical simulations can be used to determine unknown parameters from the experiment, for example temperature or interaction strength. On the other hand, we can identify suitable observables in order to investigate unexplored physical phenomena such as the exotic bond order wave phase. This opens up an avenue for future experimental investigations.

In the following we shortly motivate the different situations studied in this thesis.

Detection of bond order In chapter 4 we study the excitation spectrum of the one-dimensional ionic Fermi-Hubbard model as a response to superlattice modulation spectroscopy. The ionic Fermi-Hubbard model describes repulsively interacting fermionic particles on a lattice with alternating energy offset on neighboring sites. There are two competing energy scales, interactions and staggered energy offset, which both induce insulating behavior when taken separately. At dominating interactions, the system is Mott insulating where strong interactions prevent particles to pass each other. At dominating energy offset, the system is band insulating characterized by filled single-particle energy bands. If interactions and staggered energy offset are of comparable strength, these two energy scales compete and the additional kinetic energy term gains in influence. The ionic Hubbard model was originally introduced to describe the physics near the arising insulator-insulator transition in organic charge-transfer solids [32–34]. In fact, the competition gives rise to increased charge fluctuations, leading to the emergence of an intermediate exotic phase in one dimension: the so-called *bond order wave* phase [35] characterized by a spontaneous dimerization of the hopping and separated by two quantum phase transitions from the Mott and band insulating phases. Despite strong theoretical evidence, detecting the bond order wave phase and experimentally characterizing its neighboring phase transitions remains to be done. Ultracold fermionic gases provide an appealing novel possibility to detect this state as the ionic Hubbard model was

recently realized with fermionic atoms confined to an optical superlattice potential [36]. We investigate the possibilities of superlattice amplitude modulation spectroscopy to probe the phase diagram of the ionic Hubbard model. We find that it reveals features of both phase transitions, signaling the presence of the bond order wave phase, and that it provides valuable insights into the excitation spectra of the band and Mott insulating phases.

Thermometry A major challenge in fermionic lattice experiments is further cooling in order to probe interesting regimes such as antiferromagnetic order or unconventional superfluidity [37]. In the first case relevant correlations have recently been detected [17–19]. In addition, cooling is accompanied by the need of an accurate thermometer as the temperature is one of the important macroscopic control parameters, in particular for mapping out the Fermi-Hubbard phase diagram as a function of temperature. However, in cold gases temperature is intrinsically difficult to control as the system is not coupled to a reservoir. In particular the temperature determination in the lattice at low temperatures remains a delicate issue. Various schemes to measure the temperature of fermionic particles inside the optical lattice have been proposed and partly been experimentally tested [38] but all methods have their limitations and most cannot be extended into the low-temperature regime of interest. Motivated by the lack of suitable thermometry schemes we investigate the possibilities of thermometry by means of lattice modulation spectroscopy in chapter 5. We study the temperature-dependent atom excitation rate to higher Bloch bands and demonstrate that it shows clear signatures of the temperature-dependent Fermi distribution in the lowest band of the equilibrium system. Establishing a close relation to typical experiments we verify the measurability of temperature in one and two dimensions by a simple detection scheme.

Lattice calibration In chapter 6 we investigate the excitation spectrum of the one-dimensional Bose-Hubbard model as a response to superlattice modulation spectroscopy. At constant integer filling per site, the Bose-Hubbard model exhibits a quantum phase transition at a critical interaction strength from a strongly interacting Mott insulator, where particles localize on individual lattice sites, to a weakly interacting superfluid, where particles are delocalized over the entire lattice. At non-integer filling the system remains superfluid at arbitrary interaction strength. Particular of one dimension is that the single-particle correlations in the superfluid decay algebraically in contrast to higher dimensions where the single-particle correlations are finite and constant at arbitrary distances. This is known as long range order. On the one hand, we gain insights into the broad excitation spectrum of the superfluid phase by the superlattice modulation spectroscopy. On the other hand, in the Mott insulating region particle-hole excitation pairs are created on top of the commensurately filled background. We find that these excitations are confined to a narrow region in energy in contrast to the normal lattice modulation where the bandwidth of excitations is much larger [22, 39]. We demonstrate that the spectral response may serve as a precise calibration of the interaction strength in experimental setups.

This thesis is outlined as follows. In chapter 2, the physics of cold atomic gases confined to optical lattices, its theoretical description in terms of Hubbard models, and the lattice modulation spectroscopy are introduced. In chapter 3 we introduce the theoretical methods used throughout this thesis to describe the superlattice modulation spectroscopy, that are the time-dependent matrix renormalization group method, linear response theory and bosonization. Chapters 4, 5, and 6 give a detailed account of the study of the three situations shortly outlined above. Finally, a summary of the main results and an outlook are given in chapter 7.

CHAPTER 2

Ultracold atoms in optical lattices

In this chapter the basic principles of ultracold bosonic and fermionic gases confined to optical lattices are introduced and the underlying physics of the systems relevant for this work is discussed. Starting from a short historical perspective (Sec. 2.1), we explain the realization of optical (super)lattices (Sec. 2.2) and their theoretical description in terms of Hubbard models (Sec. 2.3). The quantum phase transition from a superfluid to a Mott insulating state in the one-dimensional Bose-Hubbard model is discussed (Sec. 2.4). Then, the main features of the Fermi-Hubbard phase diagram and the one-dimensional ionic Fermi-Hubbard model are examined (Sec. 2.5). Finally, we introduce lattice modulation spectroscopy (Sec. 2.6) which has proven to be a powerful tool for the investigation of ultracold atoms in optical lattices and which we apply to different equilibrium systems throughout this work. We consider two different configurations, the commonly used *normal* lattice modulation spectroscopy and a dimerized configuration which we call *superlattice* modulation spectroscopy.

2.1 From weakly interacting gases to strongly correlated systems

In 1925 A. Einstein predicted [40] that below a critical temperature a macroscopic number of bosons would occupy the lowest-lying single-particle state. His prediction was based on the statistics introduced by S. N. Bose for the ideal gas [41]. An experimental realization was made possible by achievements in the field of laser cooling [42] and evaporative cooling [43] which enables one to cool a dilute cloud of atoms to ultralow temperatures in the nano Kelvin regime. The first experimental realizations of Bose-Einstein condensation in ultracold weakly-interacting gases were accomplished in 1995 [4–6] for different atomic species. The collective occupation of the lowest energy state allows for the study of quantum phenomena on a macroscopic scale. The investigation of the effect of particle statistics and interactions becomes accessible in a controlled way. Prominent examples are the interference of two overlapping condensates after the release from a double well potential [9] or the observation of long range phase coherence [10]. In a dilute gas, the kinetic energy of the atoms is typically much larger than the interaction energy between particles. However, strongly correlated many body systems have also become accessible with the realization of strong and tunable interactions. The effective interparticle scattering length can be directly tuned by means of a Feshbach resonance [44, 45]. However, with increasing interactions inelastic losses increase due to three-body collisions which limits the life-time of the cloud. Another possibility is to load atoms into an optical lattice where the suppression of tunneling leads to an effective enhancement of interactions [12, 46]. It was proposed [13] and experimentally realized [12] to observe the quantum phase transition from a superfluid to a Mott insulator by loading a

Bose-Einstein condensate into an optical lattice and by increasing the lattice depth across a critical value. Other interesting experiments include the realization of a (Tonks-Girardeau) hard-core Bose gas in one dimension [47, 48] or the observation of Bloch oscillations in an optical lattice [49]. A broad selection of interesting phenomena occurring in strongly correlated bosonic systems can be found in Ref. [21] and the dynamics are discussed in Ref. [50].
In the case of fermions the Pauli exclusion principle prevents two fermionic particles to occupy the same single-particle state. At ultralow temperatures a gradual crossover from the non-degenerate gas (with decreasing temperatures) to the degenerate gas characterized by an (almost) filled Fermi sea occurs where (almost) all single-particle states up to the Fermi surface are occupied. The first degenerate Fermi gas [11] was realized in 1999 and the strongly-interacting regime is accessible by means of Feshbach resonances [51, 52]. This allows, for example, to investigate the crossover from a molecular Bose-Einstein condensate to a superfluid gas of weakly bound Cooper pairs when tuning the scattering length from repulsive to attractive [53]. The first Fermi gas in a three-dimensional optical lattice was characterized in 2005 [14]. The existence of a Fermi surface and the appearance of a band insulator were observed. Soon after, experimentalists succeeded in observing the fermionic Mott insulator [15, 16]. Other interesting examples include the measurement of the equation of state of fermionic particles in an optical lattice [54], or the creation of tunable Dirac points [55] where two energy bands intersect linearly and particles behave as quasi relativistic Dirac fermions. Several experiments with ultracold fermions in optical lattices are discussed in Ref. [56]. One of the remaining challenges is a further reduction in temperature to probe regimes where interesting physics, such as unconventional superfluidity [37] or antiferromagnetic order, occur. In the latter case, relevant correlations were recently observed in experiment [17–19].

2.2 Trapping of neutral atoms in optical lattices

In this section we outline how periodic trapping potentials for neutral atoms can be created. First, in Sec. 2.2.1, we introduce the optical dipole interaction between atoms and a light field which is the basic physical mechanism to create a periodic lattice potential for neutral atoms. We then discuss the creation of periodic structures and comment on the emerging band structure in Sec. 2.2.2.

2.2.1 Optical dipole force

The interaction of the light-induced dipole moment of neutral atoms with the laser light field has two effects [57, 58]. On the one hand, the interaction shifts the atomic energy levels (ac-Stark shift) which constitutes a conservative trapping potential for the neutral atoms proportional to the laser light intensity. On the other hand, photon scattering in cycles of absorption and subsequent spontaneous re-emission creates a dissipative contribution due to the momentum transfer of the photons. This dissipative contribution can be used for laser cooling [42]. If the detuning of the light field from the atomic resonance is large, the number of optical excitations is low, such that the dissipative force is negligible compared to the conservative optical dipole force and a conservative trapping potential can be created.

Dressed atom picture Here, we review the derivation of the optical dipole potential by a quantum mechanical treatment [58]. However, the same results can be found from a classical oscillator model [57]. The unperturbed system is given by the Hamiltonian of the quantized light field $H_L = \hbar\omega_L(a^\dagger a + 1/2)$ ($a^{(\dagger)}$ is the annihilation (creation) operator of the laser photons) and of the two-level atom $H_A = \hbar\omega_0|e\rangle\langle e|$ with $|e\rangle$ the excited state with energy $E_e = \hbar\omega_0$ and $|g\rangle$ the ground state with energy $E_g = 0$. Here, we only discuss the two-level atom. In reality, in the case of multi-level atoms all excited states should be

taken into account. However, in most experiments (performed with alkali atoms) the fine structure is not resolved for large enough detuning and one can use the two-level result [57].

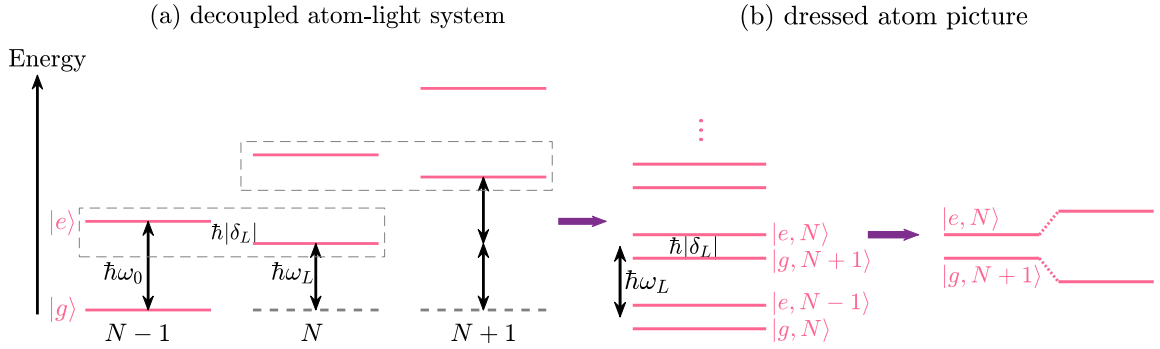

Figure 2.1: (a) The decoupled energy levels of a two-level atom with energy splitting $\hbar\omega_0$ between ground $|g\rangle$ and excited state $|e\rangle$ in a quantized light field with frequency ω_L where N denotes the number of photons in the light field. The detuning is given by $\delta_L = \omega_L - \omega_0$ and in this figure we show the case $\delta_L < 0$. (b) For small detuning, states such as $|g, N+1\rangle$ and $|e, N\rangle$ are near in energy, separated by $\hbar|\delta_L|$ (left sketch in (b)). Two such states get coupled by the atom-light interaction and the upper and lower level shift up and down in energy, respectively (right sketch in (b)).

The eigenstates of the unperturbed systems have to be labeled by the atomic quantum number g or e and by the number of photons N in the light field which shifts the bare atomic energy by $N\hbar\omega_L$, see Fig. 2.1(a). If the detuning $|\delta_L| \ll \omega_0$, $\delta_L = \omega_L - \omega_0$, only two levels such as for example $|g, N+1\rangle$ and $|e, N\rangle$ are close in energy, indicated by a dashed box in Fig. 2.1(a) in the decoupled picture. In Fig. 2.1(b) those states are grouped into 'copies' of two uncoupled states, each with energy difference $\hbar|\delta_L|$ between these two states which is much smaller than the gap $\hbar\omega_L$ to the next 'copy'. For $\delta_L > 0$, $|g, N+1\rangle$ is above $|e, N\rangle$ in energy, and vice versa for $\delta_L < 0$. Only such two levels are coupled by the atom-light interaction which is given by $H_{\text{int}} = -\vec{d}\vec{E}$ where $\vec{d} = e\vec{r}$ is the atomic dipole moment and $\vec{E}$ is the laser field operator. The resulting shift in the energy levels (see Fig. 2.1(b)) can be determined within second order non-degenerate perturbation theory,

$$\begin{aligned} \Delta E_{(g,N+1),(e,N)} &= \pm \frac{|\langle e, N|\vec{d}|g, N+1\rangle|^2}{\hbar\delta_L}|E|^2 \\ &= \pm \frac{3\pi c^2}{2\omega_0^3}\frac{\Gamma}{\delta_L} I, \end{aligned} \tag{2.1}$$

where + and − correspond to the states $|g, N+1\rangle$ and $|e, N\rangle$ respectively. It was used that the laser intensity is given by $I = 2\epsilon_0 c|E|^2$ and the on-resonant damping rate $\Gamma = (\omega_0^3/3\pi\epsilon_0\hbar c^3)|\langle e, N|\vec{d}|g, N+1\rangle|^2$ [57]. The atom is mostly in the ground state such that the light shift of the ground state results in an effective dipole potential $V_{\text{dipole}} = \Delta E_{(g,N)}$. Atoms are attracted to the nodes or anti-nodes of the laser intensity profile for blue detuned ($\omega_L > \omega_0$) or red-detuned ($\omega_L < \omega_0$) laser light respectively. Consequently, spatially modulated light fields lead to space-dependent trapping potentials for neutral atoms.

2.2.2 Periodic potentials

Optical lattices A periodic optical lattice potential can be created by superimposing counterpropagating laser beams and the standing wave interference pattern yields a periodic potential. By superimposing laser beams in one-, two- or three spatial directions one obtains stacks of two-dimensional pancakes,

arrays of one-dimensional tubes or point-like confinement of the atoms respectively. For example, a simple cubic lattice potential can be created by orthogonally superimposing three retro-reflected laser beams with polarizations between the three standing waves that are mutually orthogonal [21]. In the center of the trap, for distances much smaller than the beam waist, the potential can be approximated by the sum of a homogeneous lattice,

$$V_0(\vec{x}) = V_{0,x}\sin^2(k_L x) + V_{0,y}\sin^2(k_L y) + V_{0,z}\sin^2(k_L z), \tag{2.2}$$

and an additional external harmonic confinement created by the Gaussian intensity profile of the beam pairs,

$$V_{\text{trap}}(\vec{x}) = \frac{m}{2}\left(\omega_x^2 x^2 + \omega_y^2 y^2 + \omega_z^2 z^2\right). \tag{2.3}$$

The potential depth $V_{0,i}$, $i = x,\ y,\ z$, of the optical lattice ($V_{0,i} = V_0$ in the isotropic case, i.e. cubic lattice) can be experimentally adjusted by tuning the laser intensity. The mass of the atoms is given by m and ω_i are the effective trapping frequencies of the external confinement. The lattice spacing is given by $a = \lambda/2 = \pi/k_L$ where λ is the laser wave length and $k_L = 2\pi/\lambda$ the wave number. In this work we mainly consider one-dimensional lattice systems described by the above potential along one direction. Such systems can be approximately realized by suppressing tunneling in two directions, i.e. strongly increasing the lattice depth $V_{0,i}$ along two directions, which results in quasi one-dimensional arrays of lattices. Note, that this is intrinsically different from a one-dimensional laser setup, i.e. superimposing two counterpropagating laser beams, where atoms can move freely within the two-dimensional pancake-shaped potentials that are created orthogonal to the laser beams. The strength of the lattice potential is typically measured in units of the recoil energy $E_r = (\hbar k_L)^2/2m$. The recoil energy is the kinetic energy of an atom with mass m and momentum $\hbar k_L$ of a single lattice photon. Deep lattices $V_0 >> E_r$ can be approximated by decoupled harmonic wells $V_0(\vec{x} - \vec{x}_j) \approx (m/2)\omega_0^2(\vec{x} - \vec{x}_j)^2$ at each lattice site $\vec{x}_j$ with level spacing

$$\hbar\omega_0 = 2E_r\sqrt{V_0/E_r}. \tag{2.4}$$

Each well supports a number of vibrational levels. In principle, many different lattice geometries can be created by different intersection angles and/or controlling the relative phases between the beams [59].

Optical superlattices Throughout this work we also consider another lattice geometry in one dimension called a superlattice which is an array of double well potentials. It can be created by superimposing two standing waves created by laser beams of different wavelength λ_L and λ_L' that differ by a factor of two. In principle, one can create all kind of periodicities [60] by changing the ratio λ_L/λ_L' but here we only treat the double well case as for example realized in Refs. [61–63]. Generally, the one-dimensional optical superlattice potential can be written as

$$V_0(x) = V_1\sin^2(k_L x + \phi) + V_2\sin^2(2k_L x + 2\phi + \theta), \tag{2.5}$$

where $k_L = 2\pi/\lambda_L$ is the wave number of one of the laser beams and V_1, V_2 are the potential strengths. The lattice has the period $a = \lambda_L/2$ which is the size of one double well potential. The phase ϕ is an arbitrary shift of the whole potential whereas θ can be tuned, together with the ratio V_2/V_1, to modify the shape of the potential. The condition for having exactly two minima within one double well is $V_2 > 0.5V_1$ [64]. In the following we illustrate the creation of different kinds of double well potentials by discussing three distinct cases for the choice of θ which are displayed in Fig. 2.2. For $\theta = n\pi$ ($n \in \mathbb{Z}$) the

lattice is site-inversion symmetric, the wells alternate in potential depth but the bond height is constant throughout the system, see Fig. 2.2(a). For $\theta = \pi/2 + n\pi$ the lattice is bond-inversion symmetric, all wells have the same potential depth but alternate in bond height, see Fig. 2.2(b). Finally, for $\theta = \pi/4$ the lattice has no inversion symmetry centers. Both, potential depth and bond height alternate, see Fig. 2.2(c). By site- and bond-inversion we mean that the (infinite) system is identical when mirrored at a site or a bond respectively.
In Ch. 4 of this work we study the site-inversion symmetric kind of superlattice to realize the ionic Hubbard model with fermionic particles. The ionic Hubbard model will be discussed below in Sec. 2.5.

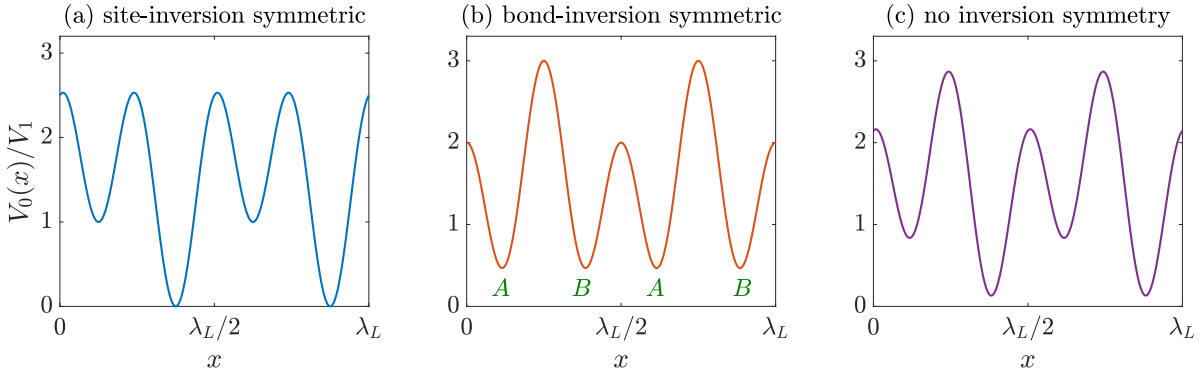

Figure 2.2: The one-dimensional optical superlattice given by Eq. (2.5) for $V_2 = 2V_1$ and three different values of the phase difference θ. (a) For $\theta = 0$ ($\phi = \pi/4$) the potential depth alternates and the lattice has site-inversion symmetry. (b) For $\theta = \pi/2$ ($\phi = 0$) the bond height alternates and the lattice has bond-inversion symmetry. The inequivalent sites within one unit cell are labeled A and B. (c) For $\theta = \pi/4$ ($\phi = \pi/8$), both, potential depth and bond height alternate and there is no inversion symmetry center.

Band structure The presence of a periodic potential leads to the emergence of an energy band structure which can be determined using Bloch's theorem for a single particle in a periodic potential. It states [65] that the solution of the (single-particle) Schrödinger equation for any periodic potential can be written as a product of a plane wave $\exp(ikx)$ and a lattice-periodic Bloch factor $u_{nk}(x)$. The Bloch function is given by $\Psi_{nk}(x) = \exp(ikx)u_{nk}(x)$ where the lattice-periodic Bloch factor $u_{nk}(x)$ has periodicity a (size of the unit cell) of the underlying lattice with L sites. The energy bands are denoted n and $k = 2\pi m/(La)$, $m = -L/2, -L/2+1, ..., L/2-1$, is the quasimomentum within the first Brillouin zone $[-\pi/a, \pi/a[$ which defines the periodicity of the reciprocal lattice. The single-particle Schrödinger equation $\left(\hat{p}^2/2m + V_0(x)\right)\Psi_{nk}(x) = E_n(k)\Psi_{nk}(x)$ becomes

$$\left(\frac{\hbar^2}{2m}(k^2 - 2ik\partial_x + \partial_x^2) + V_0(x)\right)u_{nk}(x) = E_n(k)u_{nk}(x), \tag{2.6}$$

where the potential $V_0(x)$ and $u_{nk}(x)$ both have periodicity a. The energy bands are obtained by solving one equation for each k in the first Brillouin zone of the reciprocal lattice. One can also express a in terms of the laser wave length λ, $a = \lambda/2$, such that the first Brillouin zone becomes $[-k_L, k_L[$. The obtained spectrum is shown in Fig. 2.3 comparing zero lattice depth to a finite value.
For $V_0(x) = 0$ one recovers the parabolic dispersion of the free particle. For finite $V_0(x)$ gapped energy bands develop which are k-dependent with the periodicity of the reciprocal lattice $2\pi/a = 2k_L$. With increasing lattice depth the bandwidth decreases while the band gap increases. For sufficiently deep lattices, the first band gap corresponds to the level spacing of the harmonic oscillator approximation (2.4). For a simple cubic lattice like the one given by Eq. (2.2) which is separable, the three-dimensional Bloch

function factorizes $\Psi_{n\vec{k}}(\vec{x}) = \Psi_{n_x k_x}(x)\Psi_{n_y k_y}(y)\Psi_{n_z k_z}(z)$ neglecting the coupling to other Bloch bands and the overlap of different sites, with quasimomentum $\vec{k} = (k_x, k_y, k_z)$, position vector $\vec{x} = (x, y, z)$ and band index $n = (n_x, n_y, n_z)$. It is thus sufficient to solve the one-dimensional case. In three dimensions, the energy bands are then given by $E_n(\vec{k}) = E_{n_x}(k_x) + E_{n_y}(k_y) + E_{n_z}(k_z)$.

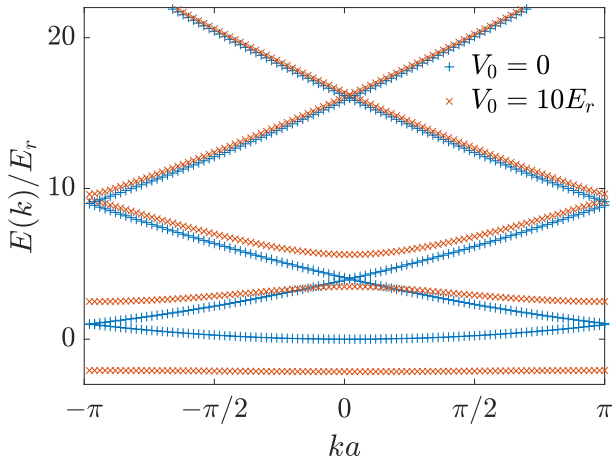

Figure 2.3: The band structure $E_n(k)$ within the first Brillouin zone for a particle in a one-dimensional homogeneous lattice $V_0(x) = V_0 \sin^2(x)$ obtained by solving Eq. (2.6) for a system of $L = 100$ sites. For a lattice depth $V_0 = 0$ (blue symbols +) one recovers the parabolic dispersion of a free particle whereas for $V_0 = 10E_r$ (orange symbols x) the spectrum is gapped.

2.3 Theoretical description: Hubbard models

From the theory side ultracold fermionic or bosonic atoms in optical lattices can be described by various types of Hubbard like models [13, 21] which are originally known from condensed matter physics. In cold atomic setups, Hubbard models may be realized in its cleanest form in a wide range of parameters with extensive control over system parameters, dimension and geometry by external fields. The intriguing interplay of quantum kinetic processes and local interactions can be investigated and theoretical predictions may be tested in a controlled way. Some examples have been given in Sec. 2.1 and can be found in Ref. [21] and references therein.

In this section, we first derive the Bose- and Fermi-Hubbard models from the Hamiltonian operator of bosonic and fermionic atoms in an optical lattice potential. We discuss the different terms describing the kinetic, potential and interaction energy and finally we consider the case of an optical superlattice potential.

We illustrate the derivation considering fermionic particles with two different internal states. The derivation for 'spinless' bosonic particles is analogous, merely dropping the spin index and using bosonic instead of fermionic single-particle operators, i.e. taking care of the proper commutation relations. The Hamiltonian for interacting fermionic atoms with two different spin states in an optical lattice with external confinement is given by

$$\begin{aligned} H &= \sum_\sigma \int \mathrm{d}^3x\, \Psi_\sigma^\dagger(\vec{x}) \left\{ \frac{-\hbar^2}{2m}\nabla^2 + V_0(\vec{x}) + V_{\text{trap}}(\vec{x}) \right\} \Psi_\sigma(\vec{x}) \\ &+ \frac{1}{2}\sum_\sigma \int \mathrm{d}^3x \mathrm{d}x'^3\, \Psi_\sigma^\dagger(\vec{x}) \Psi_{\bar{\sigma}}^\dagger(\vec{x}')\, V(\vec{x}-\vec{x}') \Psi_{\bar{\sigma}}(\vec{x}') \Psi_\sigma(\vec{x}), \end{aligned} \tag{2.7}$$

where $\Psi_\sigma^{(\dagger)}(\vec{x})$ denotes a fermionic annihilation (creation) operator for particles of mass m with two different internal states $\sigma = \uparrow$ or $\sigma = \downarrow$; $\bar{\sigma}$ denotes the opposite spin configuration with respect to σ. The first term describes the kinetic energy contribution and the influence of the lattice potential $V_0(\vec{x})$ and an additional confinement potential $V_{\text{trap}}(\vec{x})$ given by Eqs. (2.2) and (2.3), respectively. The second term describes the interaction between particles. The full interatomic scattering potential is complicated. However, it is typically short-ranged [21] and at low temperatures, the thermal de Broglie wave length (the wave length associated with a massive particle) is much larger than the effective extension of the interaction potential. Consequently, the details of the interaction potential are not resolved and play a minor role. The only relevant process is the low energy (or long wavelength) s-wave scattering. This corresponds to the lowest angular momentum scattering state in the relative motion. This scattering state is symmetric such that s-wave scattering is prohibited for identical fermions as they require a total antisymmetric wave function. However, different spin species can scatter if the spin wave function is antisymmetric. In the case of bosons, identical particles can scatter as they require a total symmetric wave function. The interaction potential is well approximated by an isotropic short-ranged pseudopotential $V(\vec{x} - \vec{x}') = g\delta(\vec{x} - \vec{x}')$, $g = 4\pi a_S \hbar/m$ which is governed by the s-wave scattering length a_S [66]. This approximation is valid in a wide range of situations in dilute atomic gases provided that longer range interactions do not contribute, such as for example the dipole-dipole interaction in dipolar gases [21]. The interaction is repulsive for $a_s > 0$ and attractive for $a_s < 0$ and the scattering length can be tuned by means of a Feshbach resonance [21].
If the energies involved in the system dynamics, i.e. recoil energy E_r, on-site interaction strength g and temperature T are small compared to the band gap, the motion of the atoms is confined to the lowest energy band. This is typically the case for sufficiently deep lattices at low temperature where the band gap is approximately given by the harmonic oscillator levels (2.4). The associated single-particle eigenstates are the Bloch waves $\Psi_{n\vec{k}\sigma}(\vec{x})$ (cf. Sec. 2.2.2) which are completely delocalized and carry an additional spin index in the case of fermions. It is more convenient to work in the orthonormal basis of Wannier functions [67, 68],

$$w_{n\sigma}(\vec{x} - \vec{x}_j) = \frac{1}{\sqrt{N}} \cdot \sum_{\vec{k}} \mathrm{e}^{-i\vec{k}\vec{x}_j} \Psi_{n\vec{k}\sigma}(\vec{x}), \tag{2.8}$$

$$\int \mathrm{d}^3x \; w^*_{n\sigma}(\vec{x} - \vec{x}_j) w_{n'\sigma'}(\vec{x} - \vec{x}_{j'}) = N\delta_{n,n'}\delta_{\sigma,\sigma'}\delta_{j,j'}, \tag{2.9}$$

where N is the normalization constant, $\vec{x}_j$ denotes the lattice site j and the sum runs over all quasimomenta $\vec{k}$ in the first Brillouin zone. We can neglect the band index n if the atoms remain in the lowest vibrational level as explained above and we will drop the band index from now on. For increasing lattice depth, the Wannier functions become more strongly localized such that the overlap between neighboring lattice sites decreases which supports localization of particles. The field operators can be expanded in the basis of Wannier functions,

$$\Psi_\sigma(\vec{x}) = \sum_j c_{j,\sigma} w_\sigma(\vec{x} - \vec{x}_j), \tag{2.10}$$

where $c_{j,\sigma}$ is the fermionic annihilation operator at site j satisfying fermionic commutation relations and we dropped the band index n. In the case of bosonic atoms the fermionic operator $c_{j,\sigma}$ has to be replaced by the bosonic annihilation operator b_j without spin index and satisfying bosonic commutation relations.

Inserting this expansion (2.10) into Eq. (2.7) yields,

$$H = \sum_{\sigma} \left\{ \sum_{j,\vec{d}} J_{j,\vec{d}} c^{\dagger}_{j+\vec{d},\sigma} c_{j,\sigma} + \sum_{j} \epsilon_j c^{\dagger}_{j,\sigma} c_{j,\sigma} + \frac{1}{2} \sum_{j,j',j'',j'''} U_{j,j',j'',j'''} c^{\dagger}_{j,\sigma} c^{\dagger}_{j',\bar{\sigma}} c_{j'',\bar{\sigma}} c_{j''',\sigma} \right\} \tag{2.11}$$

where $\vec{d}$ denotes the distance in x, y and z direction from a site j at position $\vec{x}_j$ to a site j' at position $\vec{x}_{j'} = \vec{x}_j + \vec{d}$. The tunneling amplitude $J_{j,\vec{d}}$, the on-site potential ϵ_j and the interaction strength $U_{j,j',j'',j'''}$ are given by

$$J_{j,\vec{d}} = \int \mathrm{d}^3x \, w^*_{\sigma}(\vec{x} - \vec{x}_j) \left(\frac{-\hbar^2}{2m} \nabla^2 + V_0(\vec{x}) + V_{\mathrm{trap}}(\vec{x}) \right) w_{\sigma}(x - (\vec{x}_j + \vec{d})), \ \vec{d} \neq (0,0,0) \tag{2.12}$$

$$\epsilon_j = \int \mathrm{d}^3x \, w^*_{\sigma}(\vec{x} - \vec{x}_j) \left(\frac{-\hbar^2}{2m} \nabla^2 + V_0(\vec{x}) + V_{\mathrm{trap}}(\vec{x}) \right) w_{\sigma}(\vec{x} - \vec{x}_j), \tag{2.13}$$

$$U_{j,j',j'',j'''} = g \int \mathrm{d}^3x \, w^*_{\sigma}(\vec{x} - \vec{x}_j) w^*_{\bar{\sigma}}(\vec{x} - \vec{x}_{j'}) w_{\bar{\sigma}}(\vec{x} - \vec{x}_{j''}) w_{\sigma}(\vec{x} - \vec{x}_{j'''}), \tag{2.14}$$

if $V_{\mathrm{trap}}(\vec{x})$ varies slowly with respect to the lattice potential $V_0(\vec{x})$. The nearest-neighbor interaction strength (compared to the on-site interaction strength) and the next-nearest-neighbor tunneling amplitude (compared to the nearest-neighbor tunneling amplitude) are typically two orders of magnitude smaller and can be neglected [13]. Consequently, the main contribution to the on-site interaction (2.14) is given by $j = j' = j'' = j'''$ and the main contribution to the tunneling amplitude (2.12) is given by $|d| = 1$. This is often called the tight-binding approximation. In the following we discuss in more detail the different terms of Eq. (2.11) and possible simplifications.

The trapping potential In typical experimental setups the trapping potential varies slowly with respect to the periodicity of the lattice potential such that its contribution to the Hamiltonian can be approximated by an on-site contribution

$$\int \mathrm{d}^3x \, w^*_{\sigma}(\vec{x} - \vec{x}_j) V_{\mathrm{trap}}(\vec{x}) w_{\sigma}(\vec{x} - (\vec{x}_j + \vec{d})) \approx V_{\mathrm{trap}}(\vec{x}_j) \delta_{\vec{d},0} := \epsilon_{\mathrm{trap},j} \tag{2.15}$$

where we used the orthonormality relation (2.9) of the Wannier functions. For the cubic lattice, where $V_0(\vec{x})$ is the same at each lattice site, the contributions from the remaining terms in Eq. (2.13) give a constant offset,

$$\epsilon_0 = \int \mathrm{d}^3x \, w^*_{\sigma}(\vec{x} - \vec{x}_j) \left(\frac{-\hbar^2}{2m} \nabla^2 + V_0(\vec{x}) \right) w_{\sigma}(\vec{x} - \vec{x}_j). \tag{2.16}$$

Consequently, ϵ_j (2.13) simplifies to $\epsilon_j \approx \epsilon_0 + \epsilon_{\mathrm{trap},j}$. The constant energy offset ϵ_0 can be neglected if the particle number is conserved. For working in the grand canonical ensemble one needs to subtract the chemical potential μ, $\epsilon_j \to \epsilon_j - \mu$, which acts as a Lagrangian multiplier in the Hamiltonian and controls the number of particles in the ground state of the system. Recently also homogeneous trapping potentials were realized [69–71] where the on-site contribution does no longer contribute.

The nearest-neighbor tunneling rate The tunneling amplitude can be expressed in terms of the eigenenergies of the system by transferring the tunneling matrix element (2.12) back into the Bloch basis

representation. Inserting Eq. (2.8) into Eq. (2.12) one obtains

$$\begin{aligned} J_{j,\vec{d}} &= \int \mathrm{d}^3x\, w_\sigma^*(\vec{x}-\vec{x}_j)\left(\frac{-\hbar^2}{2m}\nabla^2 + V_0(\vec{x})\right) w_\sigma(\vec{x}-(\vec{x}_j+\vec{d})) \\ &= \frac{1}{N}\int \mathrm{d}^3x \sum_{\vec{k},\vec{p}} e^{i\vec{x}_j(\vec{k}-\vec{p})} e^{-i\vec{p}\vec{d}} \Psi^*_{\vec{k},\sigma}(\vec{x})\left(\frac{-\hbar^2}{2m}\nabla^2 + V_0(\vec{x})\right)\Psi_{\vec{p},\sigma}(\vec{x}) \\ &= \sum_{\vec{k},\vec{p}} e^{i\vec{x}_j(\vec{k}-\vec{p})} e^{-i\vec{p}\vec{d}} \delta_{\vec{k},\vec{p}} E(\vec{k}) \qquad (2.17) \\ &= \sum_{\vec{k}} E(\vec{k}) e^{-i\vec{k}\vec{d}}. \qquad (2.18) \end{aligned}$$

The tunneling matrix element can thus be determined from a numerical band structure calculation (cf. Sec. 2.2.2). The main contribution for $|d| = 1$ in the cubic lattice is denoted $J_{j,|d|=1} = -J < 0$ and can be explicitly calculated for $V_0 \gg E_r$ [72],

$$J(V_0) = \frac{4}{\sqrt{\pi}} E_r \left(\frac{V_0}{E_r}\right)^{3/4} e^{-2\sqrt{V_0/E_r}}, \qquad (2.19)$$

which decays exponentially when the lattice depth V_0 is increased. In the homogeneous non-interacting case $E(\vec{k}) = -2J\left(\cos(k_x x) + \cos\left(k_y y\right) + \cos(k_z z)\right)$ in three dimensions such that J is simply related to the bandwidth by $E_{\max} - E_{\min} = 12J$. Generally, in arbitrary dimensions $E_{\max} - E_{\min} = 2zJ$ where z is the number of nearest neighbors.

The on-site interaction strength The main contribution (on-site contribution) to the interaction strength (2.14) becomes

$$U_{j,j',j'',j''',\sigma} \approx U_j = g\int \mathrm{d}^3x\, |w_\sigma^*(\vec{x}-\vec{x}_j)|^4. \qquad (2.20)$$

This integral can be evaluated numerically and for cubic lattices $U_j \equiv U$. For fermionic atoms the interaction term becomes

$$\frac{U}{2}\sum_\sigma \sum_j c^\dagger_{j,\sigma} c^\dagger_{j,\bar{\sigma}} c_{j,\bar{\sigma}} c_{j,\sigma} = \frac{U}{2}\sum_\sigma \sum_j n_{j,\sigma} n_{j,\bar{\sigma}} = U\sum_j n_{j,\uparrow} n_{j,\downarrow}, \qquad (2.21)$$

where again $\bar{\sigma}$ denotes the spin opposite with respect to σ and the fermionic anticommutation relation $\{c_{j,\sigma}, c^\dagger_{j',\sigma'}\} = \delta_{j,j'}\delta_{\sigma,\sigma'}$ was used. In contrast, for bosons one obtains

$$\frac{U}{2}\sum_j b_j^\dagger b_j^\dagger b_j b_j = \frac{U}{2}\sum_j n_j(n_j - 1), \qquad (2.22)$$

where the bosonic commutation relation was used $[b_j, b^\dagger_{j'}] = \delta_{j,j'}$. An analytical approximation can be obtained for $V_0 \gg E_r$ [72] by approximating the Wannier functions by the Gaussian ground state in the

local oscillator approximation which yields,

$$U(V_0) = \sqrt{\frac{8}{\pi}} k a_s E_r \left(\frac{V_0}{E_r}\right)^{3/4}. \tag{2.23}$$

This expression is an increasing function in V_0/E_r in contrast to the hopping amplitude which decays exponentially. The ratio U/J increases exponentially and can thus be continuously tuned over a wide range of parameters in experiments by changing the lattice potential strength.

Finally, one obtains the Fermi- and Bose-Hubbard Hamiltonians in the tight-binding approximation,

$$H_{\mathrm{FH}} = -J \sum_{\langle j,j'\rangle,\sigma} c^\dagger_{j,\sigma} c_{j',\sigma} + U \sum_j n_{j,\uparrow} n_{j,\downarrow} + \sum_{j,\sigma} (\epsilon_j - \mu) n_{j,\sigma}, \tag{2.24}$$

$$H_{\mathrm{BH}} = -J \sum_{\langle j,j'\rangle} b^\dagger_j b_{j'} + \frac{U}{2} \sum_j n_j (n_j - 1) + \sum_j (\epsilon_j - \mu) n_j, \tag{2.25}$$

respectively, where $\langle j, j'\rangle$ denotes the sum over nearest neighbors. In one dimension we will use the notation $c^\dagger_{j,\sigma} c_{j',\sigma} \to \left(c^\dagger_{j,\sigma} c_{j+1,\sigma} + \mathrm{H.c.}\right)$ and replace the sum over nearest neighbors ($\sum_{\langle j,j'\rangle}$) by the sum over j ($\sum_j$), and similar for the bosonic operators.

Tight-binding for optical superlattices Analogous to the above derivation, one can find a tight-binding description of the optical superlattice potential (2.5) by expanding the field operators in a basis of functions that are localized on each minimum of the periodic potential. However, this basis is not generally given by the Wannier functions defined in Eq. (2.8) as they can extend over both minima of a double well. Instead, one can construct a set of generalized Wannier functions that are maximally localized on each minimum from a linear combination of Bloch eigenstates in different bands [64, 73, 74]. The generalized Wannier functions also satisfy the orthonormality relation (2.9). Only considering nearest-neighbor tunneling processes, the tight-binding Hamiltonian for fermionic particles in one dimension becomes

$$\begin{aligned} H &= -\textstyle\sum_{j,\sigma} \left(J_1 c^\dagger_{j,A,\sigma} c_{j,B,\sigma} + J_2 c^\dagger_{j+1,A,\sigma} c_{j,B,\sigma} + \mathrm{H.c.}\right) \\ &\quad + \textstyle\sum_\nu \left(U_\nu \sum_j n_{j,\nu,\uparrow} n_{j,\nu,\downarrow}\right) + \sum_\nu \sum_j \left(\epsilon_{j,\nu} - \mu\right) n_{j,\nu,\sigma}, \end{aligned} \tag{2.26}$$

where $\nu = A, B$ denotes the inequivalent sites in the unit cell (cf. Fig. 2.2(b)), J_1 is the nearest-neighbor tunneling matrix element for a bond with an A-site to the left and a B-site to the right and J_2 is the nearest-neighbor tunneling matrix element for a bond with a B-site to the left and an A-site to the right. In the case $\theta = n\pi$, $J_1 \equiv J_2$ [64], which is shown in Fig. 2.2(a), and in the case $\theta = \pi/2 + n\pi$, $U_A \equiv U_B$ [64], which is shown in Fig 2.2(b). For $V_2 \gg V_1$ one can approximately assume $U_A = U_B$ [60].

2.4 Bosonic atoms in optical lattices

In this section we discuss the phase diagram of the Bose-Hubbard model (2.25). Its characteristic features are qualitatively similar in all spatial dimensions although strong quantum fluctuations in low dimensions lead to considerable quantitative differences [75]. In this section, we focus on general aspects and comment on the one-dimensional case in particular. The phase diagram of the three-dimensional Bose-Hubbard model is shown in Fig. 2.4(b). In the (μ, J)-plane there are Mott insulating regions at fixed

commensurate (integer) filling $\bar{n} = N/L$ where N is the number of particles and L is the number of lattice sites. These so-called Mott lobes are surrounded by the superfluid phase. The Mott lobes only exist at integer filling and are characterized by zero compressibility $\kappa = \partial n/\partial\mu = 0$ (where n is the density) and gapped excitations. In the superfluid, the system is compressible and has a gapless excitation spectrum. At incommensurate filling, the system is always superfluid and the incommensurate-commensurate phase transition (at the side of the lobes) is driven by density fluctuations and accompanied by a change in particle number. The phase transition at fixed commensurate filling (at the tip of the lobe) is driven by quantum fluctuations. Even in one dimension, the model is not exactly solvable but the phase diagram is well understood [76–78]. In one dimension, the Mott insulating regions become pointy at the tip of the lobe and the tips bend down.

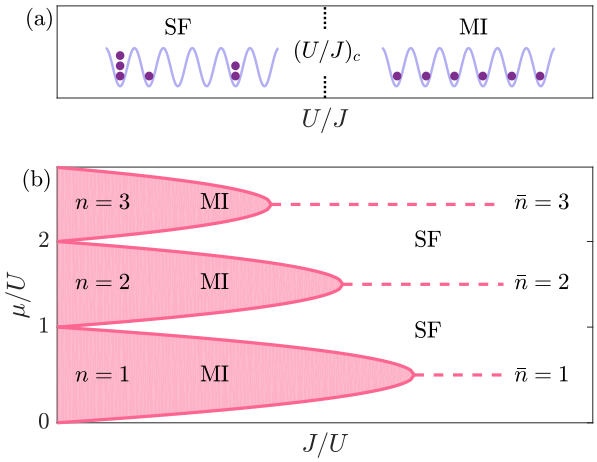

Figure 2.4: (a) Schematic drawing of the phase diagram of the Bose-Hubbard model and the corresponding ground state configurations at integer filling, here $\bar{n} = 1$, as a function of U. A quantum phase transition from a superfluid (SF) where the particles are delocalized over the entire lattice to a Mott insulator (MI) where particles are localized on each lattice site occurs at the critical value $(U/J)_c$. (b) Schematic drawing of the Bose-Hubbard phase diagram in three dimensions in the (μ, J)-plane. The shaded pink regions mark the Mott lobes at different fillings. The white region corresponds to the superfluid phase. The dashed lines indicated fixed integer filling $\bar{n}$ which enter the Mott lobes at the tip of the lobe.

The phase diagram at commensurate filling is shown in Fig 2.4(a) as a function of the interaction strength, together with a sketch of the corresponding ground state configurations. The quantum phase transition from a Mott insulator to a superfluid occurs at a critical value $(U/J)_c$. This phase transition is driven by the competition of the kinetic energy which tends to delocalize particles over the entire lattice and the repulsive interaction which disfavors having more than one particle per site. In one dimension, this phase transition occurs at a critical value of $(U/J)_c \sim 3.4$ [75] (for a filling $\bar{n} = 1$) and is of Kosterlitz-Thouless type. This means that it is accompanied by an exponentially slow closing of the Mott insulating gap which makes it difficult to determine the critical point. The two phases can be distinguished by the behavior of the single-particle correlations $\langle b_j^\dagger b_{j+d}\rangle$. In the Mott insulating region the single-particle correlations decay exponentially whereas they decay algebraically in the superfluid region in one-dimension. This is in contrast to higher dimensions where true long range order occurs in the superfluid, i.e. $\langle b_j^\dagger b_{j+d}\rangle$ finite and constant for $d \to \infty$. In order to understand the nature of the superfluid and the Mott insulating phases, it is instructive to consider the two limiting cases $U = 0$ or $J = 0$, respectively.

In the limit $U = 0$ the many-body ground state is simply given by an ideal Bose-Einstein condens-

ate where all N atoms occupy the lowest momentum ($k = 0$) Bloch state of the lowest band,

$$|GS\rangle_{U=0} = \frac{1}{\sqrt{N!}}\left(b_{k=0}^{\dagger}\right)^{N}|0\rangle = \frac{1}{\sqrt{N!}}\left(\frac{1}{\sqrt{L}}\sum_{j} b_{j}^{\dagger}\right)^{N}|0\rangle, \tag{2.27}$$

where $|0\rangle$ denotes the vacuum and $b_k^{\dagger} = \left(1/\sqrt{L}\right)\sum_j \exp(ikaj)b_j^{\dagger}$ creates a particle in momentum state k. This state is delocalized over the entire lattice of size L. The ground state energy is given by $E_0 = -2NJ$. There is large local particle number fluctuations obeying the Poissonian distribution $\langle n_j\rangle = N/L = \langle n_j^2\rangle - \langle n_j\rangle^2$. The momentum distribution is given by a zero momentum peak of weight N, $\langle n_k\rangle = N\delta_{k,0}$. The low energy excitation spectrum is continuous for $L \to \infty$. This state is well described by a macroscopic wave function with long-range phase coherence throughout the lattice. For finite but small interactions U the momentum distribution peak stays macroscopically occupied but the weight decreases $< N$ and the local number fluctuations remain large. The single-particle dispersion is linear at low energies and becomes particle-like at higher energies.

In the *atomic* limit $J = 0$ the ground state wave function at commensurate filling consists of localized wave functions where each lattice site is occupied by $\langle n_j\rangle = \bar{n}$ particles,

$$|GS\rangle_{J=0} = \prod_{j=1}^{L}\frac{1}{\sqrt{\bar{n}}}\left(b_j^{\dagger}\right)^{\bar{n}}|0\rangle. \tag{2.28}$$

The ground state energy is given by $E_0 = 0$. Local density fluctuations become energetically costly and are suppressed, $\langle n_j^2\rangle - \langle n_j\rangle^2 = 0$. The momentum distribution is constant for all momenta $\langle n_k\rangle = \bar{n}$. The lowest excited states are localized defects consisting of one doubly occupied and one empty site on top of a commensurately filled background. The energy needed to create such an excitation is the on-site interaction U which is called the Mott gap. This state cannot be described by a macroscopic wave function and phase coherence is lost. For finite but small J the many-body ground state is no longer given by the simple product state (2.28) but the particles remain localized as long as the gain J in kinetic energy due to the hopping is smaller than U.

Signatures of the superfluid to Mott insulator transition in optical lattices were first observed in a three-dimensional optical lattice [12]. The phase coherence of the wave function was probed by observing the interference pattern in a time-of-flight absorption image which reflects the momentum distribution of the particles trapped in the lattice [21]. In the superfluid regime, particles occupying the lowest Bloch state will expand according to its momentum distribution $k = 0, 2k_L, ...$ (multiples of the reciprocal lattice vector). This results in a series of interference maxima at multiples of the reciprocal lattice vector after time-of-flight. For increasing lattice depth, the strength of the higher order interference peaks increases due to the tighter localization of the wave function. Upon further increasing the lattice depth, at a critical value, the interference peaks vanish which the authors of Ref. [12] attribute to the onset of the Mott insulating phase where all quasimomenta k contribute and phase coherence is lost. The authors verify that phase coherence can be restored by reversing the process. Additionally, they probe the excitation spectrum of the two phases by applying a potential gradient and thus 'tilting' the lattice. At strong interactions, the authors observe two distinct excitation peaks at energies $\sim U$ and $\sim 2U$ as expected in the Mott insulator and in general for strong interactions, whereas the superfluid phase displays a broad continuous excitation spectrum. Soon after, the superfluid to Mott insulator transition was also investigated in a quasi one-dimensional system by lattice modulation spectroscopy [22]. The

periodic modulation of the lattice height transfers energy to the system which can be estimated by the increased broadening of the central momentum peak in a time-of-flight measurement. The authors of Ref. [22] probed the excitation spectrum for different U/J. The superfluid is characterized by a broad spectrum, whereas at strong interactions two peaks at $\hbar\omega = U$ and $2U$ appear in the one-dimensional system.

2.5 Fermionic atoms in optical lattices

Ultracold fermions in optical lattices are of particular interest due to their close analogy to electrons in solids for which the Fermi-Hubbard (2.24) model was originally introduced [79]. In many metals, the Coulomb interaction between the electrons is screened on the order of the lattice spacing [65] which justifies the replacement of the long-range Coulomb interaction by a local interaction U. However, in metals the screening length may vary and a derivation of an exact model Hamiltonian from first principles is often difficult due to the complex and imperfect structure of materials. In contrast, cold fermionic gases in optical lattices provide a clean realization of the Fermi-Hubbard model in a wide range of parameters [37]. The underlying physics is diverse and intriguing quantum phenomena occur due to the intricate interplay of interactions, delocalization, fermionic statistics and the spin degree of freedom, reaching from liquids to Mott insulators, from long-range antiferromagnetic order to paired superfluids. In this section, we give a short introduction to the repulsive Hubbard model for a three-dimensional optical lattice at half-filling (spin-balanced) and shortly comment on the one-dimensional case. For a more complete treatment of the various possible phases and different experimental examples see Refs. [30, 56] and references therein. Finally, we explain in detail the properties of the ionic Fermi-Hubbard model in one dimension.

2.5.1 Repulsive Fermi-Hubbard model

The phase diagram of the three-dimensional cubic lattice at half-filling (homogeneous system) is shown in Fig. 2.5. At moderate temperatures with increasing interaction (U/J) the system crosses over from a metallic Fermi liquid where atoms delocalize to minimize their kinetic energy to an incompressible Mott insulator where atoms localize due to the dominating on-site interaction, i.e. the lowest excitations are localized defects of excitation energy $\sim U$. At lower temperatures (below the Néel temperature $k_B T_N$) antiferromagnetic long-range order occurs. At weak repulsion, where density fluctuations are large in the liquid phase, spin ordering and the opening of a charge gap are connected and occur simultaneously at the transition to the antiferromagnet. At strong interactions in the Mott insulator for temperatures below the Mott gap, density fluctuations are frozen and only spin degrees of freedom are active. Spin-ordering occurs as a low-energy instability at temperatures below the antiferromagnetic superexchange coupling $\sim 4J^2/U$.
In the one-dimensional system antiferromagnetic long-range order is prohibited by the Mermin-Wagner theorem [80]. At zero temperature and half-filling, the system is a critical Mott insulator for any repulsive interaction [81] with algebraically decaying antiferromagnetic correlations. Away from half-filling, the low energy properties of the homogeneous system can be described by a Luttinger liquid [27] which predicts the phenomenon of spin-charge separation. A consequence of this is a complete separation of the dynamics of spin and density waves into two sound-like branches of different velocities. This phenomenon was observed using t-DMRG [82].
Fermi Hubbard systems are of relevance for Ch. 5 where we discuss the possibilities of thermometry by means of lattice modulation spectroscopy.

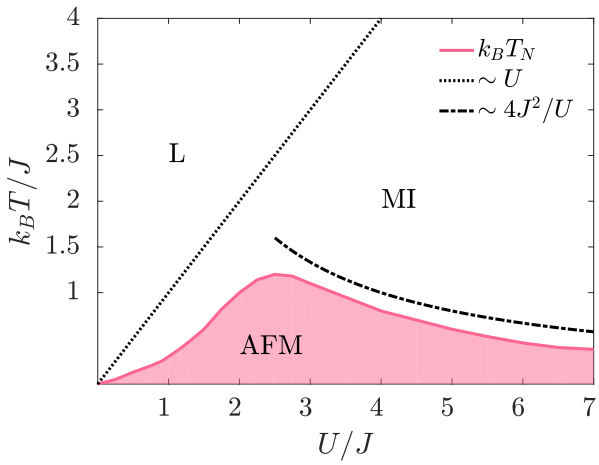

Figure 2.5: Schematic drawing of the repulsive Fermi-Hubbard phase diagram for the three-dimensional cubic lattice at half-filling. At moderate temperature a crossover from a Fermi liquid phase (L) to a Mott insulating phase (MI) takes place. The dotted line indicates the gap $\sim U$ when entering the incompressible Mott insulator. Long-range antiferromagnetic order (pink shaded region) occurs below the the Néel temperature k_BT_N (dark pink line). At strong interactions below the Mott gap, where charge fluctuations are frozen, the transition to the antiferromagnet occurs as a low-energy instability at temperatures below the antiferromagnetic superexchange coupling $\sim 4J^2/U$ (dash-dotted line).

2.5.2 Ionic Fermi-Hubbard model in one dimension

The one-dimensional ionic Fermi-Hubbard model is given by the Fermi-Hubbard model (2.24) with an alternating energy offset $\epsilon_j = (-1)^j(\Delta/2)$. Denoting inequivalent sites of energy $\pm\Delta/2$ by A and B, respectively, it becomes

$$H = H_K + H_V, \tag{2.29}$$

$$H_K = -J \sum_{l=1,\sigma}^{L/2} \left(c^\dagger_{lB\sigma}\, c_{lA\sigma} + c^\dagger_{lB\sigma}\, c_{l+1A\sigma} + \text{H.c.} \right), \tag{2.30}$$

$$V = U \sum_{l=1}^{L/2} (n_{lA\uparrow} n_{lA\downarrow} + n_{lB\uparrow} n_{lB\downarrow}) + \frac{\Delta}{2} \sum_{l=1,\sigma}^{L/2} (n_{lA\sigma} - n_{lB\sigma}), \tag{2.31}$$

where $c^{(\dagger)}_{lA\sigma}$ and $c^{(\dagger)}_{lB\sigma}$ are the fermionic annihilation (creation) operator acting on sites of type A and B and $l \in [1, L/2]$ is the double well index, L is the number of lattice sites and $\sigma \in \{\uparrow, \downarrow\}$ is the spin index. The schematic phase diagram at half-filling is shown in Fig. 2.6(a), together with a sketch of the ground state configurations (b) and the corresponding elementary excitations (c). For $\Delta \gg U$ the system is a band insulator where each low energy site is doubly occupied with equal spin and charge gaps that correspond to transferring one particle to a high energy site at an energy cost $\sim (\Delta - U)$. For $\Delta \ll U$ the system is a critical Mott insulator where each site is singly-occupied with gapless spin excitations but finite charge gap (creation of one doubly occupied site costing $\sim (U \pm \Delta)$).
It is instructive to consider some limiting cases before discussing the full phase diagram at half-filling. In the atomic limit $J = 0$, for $\Delta > U$ doubly occupied B-sites and empty A-sites minimize the ground state energy $E_0 = (L/2)(U - \Delta)$. For $\Delta < U$ it is most favorable to singly occupy each site, $E_0 = 0$. At $\Delta = U$ both configurations become degenerate and a first order transition occurs.
For finite J the situation is more complex. For $\Delta = 0$ the Hamiltonian corresponds to the standard Hubbard

model in one dimension discussed above which is known to be Mott insulating for all $U > 0$ [81]. For $U = 0$ the ionic model becomes diagonal in quasimomentum space. The ground state is a genuine band insulator with equal charge and spin gaps determined by Δ. At finite and strong interactions $(U - \Delta) \gg J$ the ionic Hubbard model maps to an isotropic Heisenberg chain with exchange interaction $J_{XY} = J_Z = (4J^2/U)1/[1 - (\Delta/U)^2]$ [83] and gapless spin excitations but clearly this description breaks down near $\Delta \sim U$.

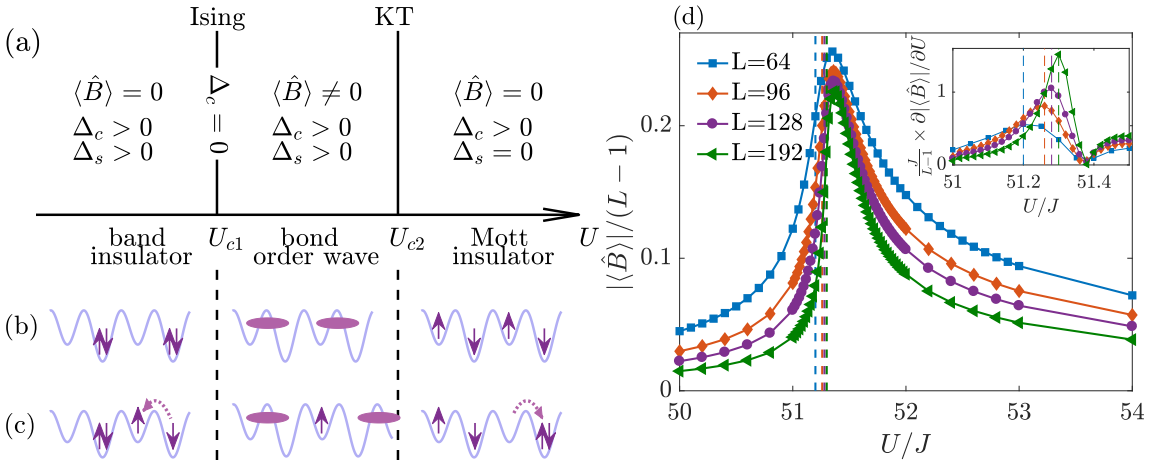

Figure 2.6: (a) Phase diagram of the one-dimensional ionic Hubbard model at half-filling at fixed Δ and J as a function of U. The charge and spin gaps are denoted Δ_c and Δ_s respectively and the order parameter $\langle\hat{B}\rangle$ is only finite in the intermediate bond order wave phase. (b) Schematic drawing of the ground states of the band insulator phase, bond order wave phase and Mott insulator phase from left to right. In the band insulator phase (left) all B-sites are doubly occupied while all A-sites are empty. In the bond order wave (middle) there is two degenerate ground states (at infinite system size) with dimers forming on either even or odd bonds, here one of these configurations is sketched. In the Mott insulator (right) each site is singly occupied. (c) Schematic drawing of the first gapped excited state. In the naive picture, in the band insulator (left) one doublon on a B-site is broken while one particle hops to a neighboring A site. This charge excitation requires an energy $\sim (\Delta - U)$. Within the bond order wave (middle) soliton-antisoliton pairs are created at an energy $\sim \Delta_s$ which can be interpreted as domain walls between the two different degenerate ground states. In the naive picture, the lowest charge excitation in the Mott insulator (right) corresponds to the hopping of one particle from an A-site to a B-site which means that a doublon is created on a B-site while an A-site is left empty. This requires an energy $\sim (U - \Delta)$. Note that the opposite process (hopping from a B-site to an an A-site) creates excitations at $\sim (U + \Delta)$ and that there are also gapless spin excitations. (d) The bond order parameter normalized by the number of bonds $|\langle\hat{B}\rangle|/(L-1)$ at fixed $\Delta = 50J$ for different system sizes calculated from DMRG keeping up to 400 states. The dashed vertical lines mark the position of the maximum of the derivative located at $U_{c1} \sim 51.2J,\ 51.26J,\ 51.28J,\ 51.3J$ for system sizes $L = 64,\ 96,\ 128,\ 192$, respectively. Figure adapted from Ref. [84]. Inset: Derivative of the bond order parameter with respect to U. The first maximum approximately corresponds to the Ising critical point which is marked by the dashed vertical lines.

In fact, the band insulator and Mott insulator are separated by a narrow exotic phase, the so-called bond order wave phase which occurs when Hubbard on-site interaction U and ionic energy offset Δ are comparable (cf.Fig. 2.6(a)). The occurrence of the bond order wave phase was first predicted in Ref. [35] based on field-theoretical arguments in the weak coupling regime. It is characterized by a spontaneous dimerization of the kinetic energy. The the associated bond order wave order parameter $|\langle\hat{B}\rangle|$, with

$$\hat{B} = \sum_{l=1,\sigma}^{L/2} \left(c^\dagger_{lA\sigma} c_{lB\sigma} - c^\dagger_{lB\sigma} c_{l+1A\sigma} + \text{H.c.} \right), \tag{2.32}$$

acquires a finite value. The phase transition from the band insulator to the bond order wave is of Ising type, accompanied by the closing of the charge gap at the critical point. The ground state in the bond order wave is two-fold degenerate in the infinite system with dimers forming on either even or odd bonds which breaks the discrete site-inversion symmetry of the Hamiltonian. Both, charge and spin gap are finite. The spin gap closes at the phase transition from the bond order wave to the Mott insulator which is of Kosterlitz-Thouless type. The bond order wave order parameter is shown in Fig. 2.6(d) at $\Delta = 50J$ as a function of U for finite systems obtained from static DMRG calculations keeping up to 400 states. It displays a steep increase at a certain value of U which indicates the Ising phase transition. The transition point in the finite system can be approximated as the first maximum of the derivative of the order parameter with respect to U, shown in the inset of Fig. 2.6(d). At the Kosterlitz-Thouless phase transition from the bond order wave to the Mott insulator the spin gap closes exponentially slow which makes it hard to locate this phase transition in a finite system which is reflected in the slow decay of the bond order parameter across a wide range of U-values.
Using static DMRG calculations keeping up to 160 states we study the density profile throughout the phase diagram. We confirm that the local density imbalance $\langle n_B - n_A \rangle$ crosses over from a value 2 deep in the band insulator to a very small but finite value in the Mott insulator, see Fig. 2.7(b). Bond order is expected to occur in the crossover region. Additionally, we study the unit cell density $\langle n_B + n_A \rangle_l$ in the band insulator and Mott insulator as well as within the bond order wave phase and at Ising criticality, see Fig. 2.7(a). In the first three cases, it is approximately 2 throughout the bulk as expected with slightly enhanced boundary effects in the bond order wave phase compared to the two other cases. At Ising criticality a strong asymmetry occurs due to boundary effects likely caused by the correlations length exceeding the system size at Ising criticality.

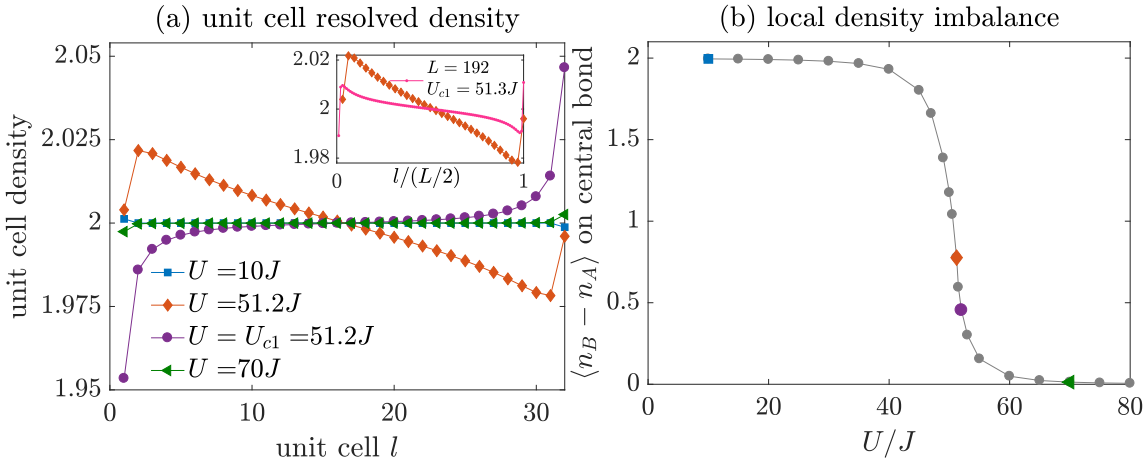

Figure 2.7: (a) The unit cell density $\langle n_B + n_A \rangle_l$ at fixed $\Delta = 50J$ for a system size $L = 64$. It is approximately 2 throughout the bulk of the lattice. Enhanced boundary effects occur at Ising criticality $U = 51.2J$. In this case, the system length matters as the correlation length diverges. We confirm that the asymmetry is due to boundary effects by a comparison to $L = 192$, $U_{c1} = 51.3J$ in the inset, for which the strength of the asymmetry decreases. Note, that the asymmetry depends on the AB configuration at the boundary. We checked that the asymmetry is mirrored when A and B sites are exchanged. (b) The density imbalance $\langle n_B - n_A \rangle$ on the central bond as a function of U at fixed $\Delta = 50J$ for a system size $L = 64$. It evolves from a value ~ 2 in the band insulator $U \ll \Delta$ to a small but finite value in the Mott insulator $U \gg \Delta$. The colored markers in (b) correspond the the U-values considered in (a).

The ionic Hubbard model was originally introduced [32, 85, 86] for the description of charge transfer interactions in aromatic donor (D) -acceptor (A) crystals where donors and acceptors alternate along quasi one-dimensional stacks. The lowest electronic excitation is an electron transfer $DA \rightarrow D^+A^-$. These

materials are either nominally neutral ...*DADADA*... or nominally ionic ...$D^+A^-D^+A^-D^+A^-$... and a neutral-to-ionic phase transition was believed to be of first order. It was first observed it tetrathiafulvalene-chloranil driven by a change in pressure [33] or temperature [34, 87] and it was, against expectation, found to occur continuously across a large temperature range where both neutral and ionic molecules coexist. The ionic Hubbard model gained further interest as it was investigated to explain the origin of ferroelectricity in transition metal oxides [88, 89].
After the authors of Ref. [35] suggested the two-transition scenario explained above (consisting of an Ising and a Kosterlitz-Thouless transition, cf. Fig. 2.6), numerous numerical work was carried out, trying to confirm this scenario. Despite the initial controversy the complete picture strongly supports the two-transition scenario which was found to persist even at strong coupling (see below). Exact diagonalization calculations were used to determine the closing of spin and charge gaps. The authors of Ref. [90] fail to resolve two different transition points, whereas the authors of Ref. [91] show that the spin and charge transition separate and that the bond order wave phase survives at strong coupling. The phase boundaries were calculated in Ref. [92], confirming the two-transition scenario at weak and strong coupling. In a quantum Monte Carlo study [93], the authors confirm the first phase transition to be of Ising type. However, the authors fail to observe the second phase transition and conclude that the Mott insulator only exists at infinite interactions. The exact bond ordered ground state at strong coupling is determined in the extended ionic Hubbard model and shown to survive in the purely ionic model [94]. Its elementary excitations are solitons separating one ground state configuration from the other [95] (cf. Fig. 2.6(c)). Different studies on the behavior of charge and spin gaps, the bond order parameter and static susceptibilities were carried out using DMRG [96–100] identifying one [97, 99] or two transition points [96, 98, 100]. In Ref. [100], the authors thoroughly extract the thermodynamic critical exponents verifying that the first transition belongs to the Ising universality class and find typical infinite-order transition signatures at the second transition point.
Far less attention has so far been paid to the excitations across the phase diagram. The one- and two-particle low energy dispersions and the quasiparticle spectrum were studied [101–104] in the three phases. The gaps determined in the band insulator [101] are identified to be in accordance with DMRG results [100]. At a critical value of the interaction strength a macroscopic number of excitations in the band insulator is found to condense [102], identified with the formation of the bond order wave phase. Both, spin and charge excitations contribute to the low-energy spectrum at similar energies [103] showing that spin and charge degrees of freedom are closely intertwined.
Despite the elaborate theoretical picture which points to the existence of the bond order wave, a detailed experimental study of the excitation spectrum in the ionic Hubbard model is still missing and the bond order wave still evades detection.
New appealing perspectives arise in the context of ultracold atoms in optical lattices that provide a clean and highly tunable realization of the ionic Hubbard model by fermionic atoms confined to an optical superlattice (cf. Sec. 2.2.2). The ionic Hubbard model was recently realized with fermionic atoms trapped in a superlattice potential [36]. In Ch. 4 we study of the excitation spectrum of the ionic Hubbard model in all phases by means of superlattice modulation spectroscopy. In particular, we analyze the excitation spectrum in the vicinity of the phase transitions and find that the superlattice modulation reveals signatures of both phase transitions.

2.6 Lattice amplitude modulation spectroscopy

Many powerful tools were developed to gain precise information on the properties of ultracold gases in optical lattices in order to tackle the intricate physics of many-body systems. Spectroscopic methods

such as radio frequency, Raman, Bragg and lattice modulation spectroscopy serve to probe characteristic excitations of correlated systems and are able to measure, for instance, single-particle or density spectral functions [21, 105, 106]. In lattice modulation spectroscopy the amplitude of the light potential is periodically modulated in time such that excitations in the system are created whenever the modulation frequency corresponds to the energy of an available excitation. Details on possible lattice modulation setups and their theoretical description are given below. First, we give an overview on previous work using lattice modulation spectroscopy.

Lattice modulation spectroscopy was first introduced for bosonic systems [22] to study the excitation spectrum and therewith characterize the transition from the superfluid to Mott insulating state in the one-dimensional system and the one- to three-dimensional crossover. The energy deposited in the system after a modulation of the lattice depth was estimated from the broadening of the central momentum peak in a time-of-flight measurement. The superfluid phase is characterized by a broad spectrum. At strong interactions two excitation peaks occur at energies $\sim U$ and $\sim 2U$ and the second peak is negligible at integer filling in the Mott insulator [107]. A more detailed study of the superfluid spectrum in three dimensions [108] followed. The observed broad superfluid spectrum (particularly broad in one dimension) could not be explained within standard Bogoliubov theory [109]. Other theoretical schemes were then considered, applying a linear response treatment [39, 110–112] or beyond, considering weak interactions using the Gross-Pitaevski equation [113] and carrying out a time-dependent simulation using t-DMRG [107]. Later, lattice modulation spectroscopy was suggested to reveal the gapped (amplitude) Higg's mode in the superfluid phase of the two-dimensional system [114, 115] near the transition to the Mott insulator and in Ref. [116] the authors report on the observation of such a gapped mode where the excitation energy is extracted from an increase in temperature observed in a single-atom-resolved detection. Furthermore, lattice modulation spectroscopy was suggested to obtain momentum -and frequency resolved spectral information about the excitations from time-of-flight measurements [117] and it was for example applied to the study of disordered lattices [118, 119] or spinor bosonic system with spin-orbit coupling [120].
In the case of fermionic atoms, a precise study of the excitation spectrum by the broadening of the momentum distribution in time-of-flight is not possible because the momentum distribution only depends on temperature by a smearing of the Fermi surface such that a very high momentum resolution is necessary to reliably extract the deposited energy. However, the double occupancy as a response to lattice modulation was suggested to measure the pairing gap in the superfluid state or the spin ordering in the Mott insulating state [121], followed by further detailed theoretical studies on the induced double occupancy [122–129]. In experiment, the fermionic Mott insulator [15], nearest-neighbor correlations [130] and the decay of doublon excitations [131] were probed using lattice modulation spectroscopy. It also serves to map out higher Bloch bands in a quasimomentum-resolved fashion [132] and to study interband dynamics [133]. Recently, charge density wave order in the two-dimensional ionic Hubbard model on a honeycomb lattice was studied using lattice modulation spectroscopy along one direction [36].

In this work, we employ lattice amplitude modulation to study the excitation spectrum of different fermionic and bosonic setups. We consider three different kinds of modulation along one direction which are sketched in Fig. 2.8. On the one hand, we consider the typical setup (Fig. 2.8(a)) used in most experiments and corresponding to the examples discussed above. We call this *normal* or *standard* lattice amplitude modulation. Furthermore, we consider lattice amplitude modulations of dimerized geometry, i.e. while the height of one bond increases, the height of the neighboring bond decreases. We refer to this kind of modulations as *superlattice* modulation and apply it to both, a 'normal' optical lattice and an optical superlattice.

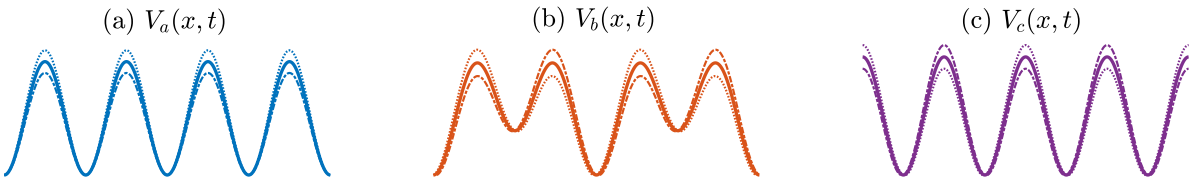

Figure 2.8: Sketch of the different lattice amplitude modulation setups discussed in the main text. The lattice amplitude is modulated between the two configurations indicated by dotted and dash-dotted lines around the equilibrium configuration (solid line). In (a) the standard lattice amplitude modulation is shown. In (b) and (c) we sketch superlattice amplitude modulation of an optical superlattice and a 'normal' lattice respectively.

Normal (standard) lattice amplitude modulation A periodic modulation of the lattice height $V_0 \to V_0 + \delta V(t)$ with $\delta V(t) \sim \sin(\omega t)$ leads to a time-dependent potential of the form

$$V_a(x,t) = V_0(x) + \delta V(t) \sin^2(k_L x), \tag{2.33}$$
$$V_0(x) = V_0 \sin^2(k_L x). \tag{2.34}$$

The modulation in time is sketched in Fig. 2.8(a). For a small modulation amplitude this leads to a modulation of the hopping amplitude and the on-site interaction strength in the tight-binding description [111]. However, as the tunneling (2.19) is exponentially dependent on the height of the optical lattice while the on-site interaction strength (2.23) has a much weaker dependence, the primary contribution of this perturbation is to modulate the hopping parameter $J(t) = J + A\sin(\omega t)$ with small amplitude A and frequency ω and the modulation of the on-site interaction strength can be neglected in the large U/J limit [123]. We refer to this kind of modulation as *normal* or *standard* lattice amplitude modulation. This modulation is applied to fermionic particles in an optical lattice in Ch. 5 in order to extract information of the initial filling of the lowest band and determine the temperature of the system.

Superlattice modulation of an optical superlattice In the case of an optical superlattice (cf. Sec. 2.2.2), a dimerized modulation can be achieved by time-dependently tuning the dephasing between the two laser waves constituting the optical superlattice. Consider an optical superlattice given by Eq. (2.5). For simplicity we can set $\phi = 0$ in Eq. (2.5) as this is a shift of the whole potential. Adding a small time-dependent phase difference $\delta\nu(t) \sim \sin(\omega t)$, the potential is given by $V_b(x,t) = V_1 \sin^2(k_L x + \delta\nu(t)) + V_2 \sin^2(2k_L x + \theta)$. For small $\delta\nu(t)$ the potential becomes (in lowest order in $\delta\nu(t)$)

$$V_b(x,t) = V_0(x) + \delta V(t) \sin(2k_L x), \tag{2.35}$$
$$V_0(x) = V_1 \sin^2(k_L x) + V_2 \sin^2(2k_L x + \theta), \tag{2.36}$$

where $\delta V(t) \sim \delta\nu(t)$. The time-dependence of the modulation is sketched in Fig. 2.8(b). The potential offset does not change in time whereas the lattice height is modulated in a dimerized fashion such that, in tight-binding, this approximately translates into a dimerized modulation of the hopping amplitude $J_j(t) \approx J + A(-1)^j \sin(\omega t)$ with small amplitude A and frequency ω where j denotes the lattice site. We employ this type of modulation in Ch. 4 in order to study the excitations in the one-dimensional ionic Fermi-Hubbard model.

Superlattice modulation of a 'normal' lattice One can also realize a dimerized modulation of a 'normal' lattice. By 'normal' lattice we mean an equilibrium potential of simple $\sin^2$- or $\cos^2$-configuration. A possible implementation is to create a 'normal' lattice from superimposing several laser standing waves of different wavelength. The phases and amplitudes have to be chosen such that the resulting superlattice reduces to a simple $\sin^2$- or $\cos^2$-configuration. For example, one could use the following configuration,

$$V_0(x) = -V_0\left(V_1 \sin^2(k_L x - \Omega) + V_2 \sin^2(k_L x) + V_1 \sin^2(k_L x + \Omega)\right) + V_0 \sin^2(2k_L x + \theta). \tag{2.37}$$

For $\theta = \pi/2$, $V_1 = \mathcal{J}_1(1.288)$, $V_2 = \mathcal{J}_0(1.288)$ where $\mathcal{J}_n(\beta)$ is the first kind Bessel function and $\Omega = 114\pi/300$ the resulting lattice has a configuration $\sim \cos^2(2k_L x)$ like a 'normal' lattice and is shown in Fig. 2.8(c) (solid line). A small time-dependent modulation $\Omega \to \Omega + \delta\Omega(t)$ yields (in lowest order in $\delta\Omega(t)$)

$$V_c(x,t) = V_0(x) + \delta V(t)\cos(2k_L x), \tag{2.38}$$

where $\delta V(t) \sim \delta\Omega(t)$ and $V_0(x)$ is given by Eq. (2.37). This corresponds to a modulation of dimerized geometry which is sketched in Fig. 2.8(c). Alternatively, if the equilibrium lattice has $\sin^2$-configuration, the perturbation is proportional to a sin-function. Again, the potential offset does not change in time such that in tight-binding this also approximately translates into a dimerized modulation of the hopping amplitude as introduced above, $J_j(t) \approx J + A(-1)^j \sin(\omega t)$. We employ this type of modulation in Ch. 6 in order to study the excitations in the one-dimensional Bose-Hubbard model.
To avoid confusion, note, that in this example the equilibrium configuration and the modulation have an argument $2k_L x$. This results from the chosen example (2.37). The essential point is that the equilibrium lattice (given by $\sin^2$- or $\cos^2$- configuration) and the modulation (given by a cos- or sin- configuration respectively) have the same argument such that the modulation doubles the period of the equilibrium setup. We can simply use $V_0(x) = \sin^2(k_L x)$ and $\delta V(x) \sim \sin(k_L x)$ for calculations and we do so for a determination of the transition matrix elements from the initial to an excited state by superlattice modulation for the non-interaction Fermi-Hubbard model in Bloch basis in Sec.5.5.

The lattice modulation spectroscopy can be theoretically described by adding, to the equilibrium Hamiltonian H_0, a time-dependent perturbation,

$$H_{\text{pert}}(t) = A \sin(\omega t)\hat{O}, \tag{2.39}$$

with small amplitude A and frequency ω where

$$\hat{O}_N = \sum_{j=1}^{L-1}\left(c^\dagger_{j,\sigma} c_{j+1,\sigma} + \text{H.c.}\right), \tag{2.40}$$

in the case of the normal lattice modulation, and

$$\hat{O}_S = \sum_{j=1}^{L-1}(-1)^j\left(c^\dagger_{j,\sigma} c_{j+1,\sigma} + \text{H.c.}\right) \tag{2.41}$$

in the case of the superlattice modulation. In Eqs. (2.40) and (2.41), $c^{(\dagger)}_{j,\sigma}$ denotes the fermionic annihilation (creation) operator which removes (creates) a particle at site j with spin σ. In the case of bosonic particles,

one just needs to replace $c_{j,\sigma}^{(\dagger)}$ by the bosonic operators $b_j^{(\dagger)}$.
Introducing the Fourier transform $c_{j,\sigma}^{\dagger} = (1/\sqrt{L}) \sum_k \exp(ia\,jk) c_{k,\sigma}$ Eqs. (2.40) and (2.41) become $\hat{O}_N = 2 \sum_k \cos(ak) c_{k,\sigma}^{\dagger} c_{k,\sigma}$ and $\hat{O}_S = 2i \sum_k \sin(ak) c_{k+\pi/a,\sigma}^{\dagger} c_{k,\sigma}$ respectively, where $k = 2\pi m/L$, $m = 1, \ldots, L$. Evidently the normal lattice modulation conserves quasimomentum while the superlattice modulation transfers momentum π to the lattice which is an important difference.

CHAPTER 3

Methods

In this chapter we introduce the theoretical methods used in this work to study the excitations created in bosonic and fermionic optical lattice systems by a periodic modulation of the lattice amplitude. Quite generally, highly sophisticated methods are required for the description of quantum many-body systems due to their complexity as, for example, the Hilbert space typically grows exponentially in the system size. Here, we focus on well-established methods suited for the study of one-dimensional systems which are mainly studied in this work.
First, we introduce the time-dependent density matrix renormalization group method in terms of matrix product states in Sec. 3.1. The density matrix renormalization group method is a powerful numerical technique for the simulation of static and dynamic properties of low-dimensional strongly-correlated quantum systems. The extension of this method to time-dependent phenomena enables us to compute the quasi-exact time evolution of the fermionic or bosonic systems in lattice shaking setups. The number of excitations created through the modulation is assessed by monitoring the absorbed energy which gives a good estimate of the energy absorbed in experimental setups. The time evolution of the energy can be related to the averaged energy absorption rate obtained within a linear response treatment which we introduce in Sec. 3.2. Linear response is a common method to probe the response of various physical properties to an external time-dependent perturbation, such as a modulation of the lattice amplitude, by an expansion of the perturbing Hamiltonian in lowest order. Within this approximation, observables only depend on correlation functions of the system in equilibrium. Here, we introduce the general concept of linear response and derive the formulas describing the energy absorption as a response to the perturbation. Finally, we introduce bosonization in Sec. 3.3 which is a low-energy field-theoretical description for one-dimensional systems where all operators are expressed in terms of collective excitations. It is well suited to describe the low-energy (long wavelength) physics of these systems exactly and enables one to obtain the response of the system to a modulation of the lattice amplitude within a linear response treatment. Bosonization calculations are not part of this thesis but a basic understanding of the main concept is of importance as we compare to calculations obtained in a collaboration.

3.1 Matrix product states

The density matrix renormalization group method (DMRG) is a highly reliable and versatile numerical method to determine the static and dynamic quantities of one-dimensional strongly correlated systems to a high precision. It was originally introduced by S. R. White [28, 134] for the study of static properties of one-dimensional systems. It is nowadays a well-established method and in this thesis we use its extension

to the study of time-dependent phenomena [135–137] known as time-dependent DMRG (t-DMRG). In quantum many-body systems the dimension of the full Hilbert space is typically too large to be treated exactly. The main idea of DMRG is to describe the quantum system, using a reduced effective Hilbert space. The algorithm iteratively and variationally reduces the degrees of freedom to the most important region of the Hilbert space at each iteration.
In this section an overview over the basic concepts is provided using a representation in terms of matrix product states (MPS) [29]. In Sec. 3.1.1, the definition and important characteristics of a quantum state in the MPS representation are given. Subsequently, the main points of the ground state calculation in DMRG are conveyed in Sec. 3.1.2 and finally the time evolution is introduced in Sec. 3.1.3. Here we stay within the framework of one-dimensional, zero temperature situations but the method can also been extended, for instance, to finite temperature or higher-dimensional systems and has been applied to various kinds of systems, for example spin chains or Hubbard type models [29, 138–140].

3.1.1 Basic ideas

Generally, any quantum state on a lattice with sites $j = 1, \ldots, L$ can be written as

$$|\Psi\rangle = \sum_{\sigma_1,\ldots,\sigma_L} c_{(\sigma_1,\ldots,\sigma_L)} |\sigma_1, \ldots, \sigma_L\rangle, \tag{3.1}$$

where $\{|\sigma_j\rangle\}$ is the local basis of dimension d at each site j and $|\sigma_1, \ldots, \sigma_L\rangle = |\sigma_1\rangle \otimes \ldots \otimes |\sigma_L\rangle \equiv |\vec{\sigma}\rangle$ is the tensor product of the local basis. The scalar (complex) coefficients $c_{(\sigma_1,\ldots,\sigma_L)}$ may be seen as entries of a vector $\vec{c}$ that has d^L components. In this section we will show how the coefficients can be decomposed into a product of local matrices M resulting in a so-called *matrix product state*. Before outlining the construction let us state the final form. An MPS is generally given by

$$|\Psi\rangle = \sum_{\sigma_1,\ldots,\sigma_L} M^{\sigma_1} M^{\sigma_2} \ldots M^{\sigma_L} |\sigma_1, \ldots, \sigma_L\rangle, \tag{3.2}$$

where M^{σ_1} is a collection of row vectors, M^{σ_L} is a collection of column vectors and all other M^{σ_j} are collections of matrices. The matrix product results in a scalar due to the vectorial nature of the first and the last matrix.
The basic tool needed to obtain the MPS representation is the so-called *singular value decomposition* (SVD) known from linear algebra which guarantees that an arbitrary rectangular matrix M of dimension $(m \times n)$ can be decomposed as

$$M = USV^\dagger, \tag{3.3}$$

where U and V are unitary matrices with U of dimension $(m \times \min(m, n))$ and $V^\dagger$ of dimension $(\min(m, n) \times n)$. The matrix S is a diagonal matrix and of dimension $(\min(m, n) \times \min(m, n))$ with non-negative entries $S_{aa} := \sqrt{\lambda_a} \geq 0$ which are called singular values. The number of non-zero singular values $\sqrt{\lambda_a} > 0$ of M is denoted the rank r of M.
Assuming the wave function (3.1) to be normalized, the typical procedure to construct a MPS is to reshape the d^L state vector components $c_{(\sigma_1,\ldots,\sigma_L)}$ into a matrix and to successively apply the SVD on the connecting bond index between two sites. We demonstrate this in the following, exemplary starting 'from the left'. In a first step, the components $c_{(\sigma_1,\ldots,\sigma_L)}$ are reshaped into a matrix $\Psi_{\sigma_1,(\sigma_2\ldots\sigma_L)}$ of dimension

$(d \times d^{L-1})$,

$$c_{(\sigma_1,\ldots,\sigma_L)} = \Psi_{\sigma_1,(\sigma_2\ldots\sigma_L)} = \sum_{a_1=1}^{r_1} U_{\sigma_1,a_1} S_{a_1,a_1} (V^\dagger)_{a_1,(\sigma_2\ldots\sigma_L)}, \tag{3.4}$$

which was decomposed by a SVD with bond dimension $r_1 = \min(d, d^{L-1})$. This can be rewritten as $U_{\sigma_1,a_1} S_{a_1,a_1} (V^\dagger)_{a_1,(\sigma_2\ldots\sigma_L)} = A^{\sigma_1}_{a_1} \Psi_{(a_1\sigma_2),(\sigma_3\ldots\sigma_L)}$. In order to do so one needs to reshape the product $S_{a_1,a_1}(V^\dagger)_{a_1,(\sigma_2\ldots\sigma_L)}$ into a vector component $c_{(a_1,\sigma_2,\ldots,\sigma_L)}$ and then again into a matrix $\Psi_{(a_1\sigma_2),(\sigma_3\ldots\sigma_L)}$ (of dimension $(r_1 d \times d^{L-1})$). At the same time the matrix U has to be reshaped into a collection of row vectors A^{σ_1} with entries $A^{\sigma_1}_{a_1} = U_{\sigma_1,a_1}$. The matrix $\Psi_{(a_1\sigma_2),(\sigma_3\ldots\sigma_L)}$ can again be decomposed by the SVD and reshaped as above. Successively repeating this procedure leads to,

$$\begin{aligned}
c_{(\sigma_1,\ldots,\sigma_L)} &= \sum_{a_1=1}^{r_1} A^{\sigma_1}_{a_1} \Psi_{(a_1\sigma_2),(\sigma_3\ldots\sigma_L)} \\
&= \sum_{a_1=1}^{r_1} \sum_{a_2=1}^{r_2} A^{\sigma_1}_{a_1} U_{(a_1\sigma_2),a_2} S_{a_2,a_2} (V^\dagger)_{a_2,(\sigma_3\ldots\sigma_L)} \\
&= \sum_{a_1=1}^{r_1} \sum_{a_2=1}^{r_2} A^{\sigma_1}_{a_1} A^{\sigma_2}_{a_1,a_2} \Psi_{(a_2\sigma_3),(\sigma_4\ldots\sigma_L)} \\
&\quad\vdots \\
&= \sum_{a_1\ldots a_{L-1}} A^{\sigma_1}_{a_1} A^{\sigma_2}_{a_1,a_2} A^{\sigma_3}_{a_2,a_3} \ldots A^{\sigma_{L-1}}_{a_{L-2},a_{L-1}} A^{\sigma_L}_{a_{L-1}} \\
&= A^{\sigma_1} A^{\sigma_2} \ldots A^{\sigma_L},
\end{aligned} \tag{3.5}$$

where A^{σ_1} is a collection of row vectors, A^{σ_L} is a collection of column vectors and all other A^{σ_j} are collections of matrices of dimension (r_{j-1}, r_j) and with entries $A^{\sigma_j}_{a_{j-1},a_j} = U_{(a_{j-1}\sigma_j),a_j}$. This gives the MPS form of the states,

$$|\Psi\rangle = \sum_{\vec{\sigma}} A^{\sigma_1} A^{\sigma_2} \ldots A^{\sigma_L} |\vec{\sigma}\rangle, \tag{3.6}$$

which is called *left-canonical* due to the normalization of the A matrices given by

$$\sum_{\sigma_j} A^{\sigma_j \dagger} A^{\sigma_j} = \mathbb{I}. \tag{3.7}$$

Each scalar coefficient is now the product of A matrices with maximal dimensions $(1 \times d), (d \times d^2), \ldots, (d^{L/2-1} \times d^{L/2}), (d^{L/2} \times d^{L/2-1}), \ldots, (d \times 1)$ from site 1 to site L for an even number of sites. Evidently, the matrix dimensions grow exponentially such that in calculations it is usually impossible to carry out the exact decomposition.

Analogously one can start decomposing the wave function (3.1) 'from the right',

$$\begin{aligned} c_{(\sigma_1,\ldots,\sigma_L)} = \Psi_{(\sigma_1\ldots\sigma_{L-1}),\sigma_L} &= \sum_{a_{L-1}} U_{(\sigma_1\ldots\sigma_{L-1}),a_{L-1}} S_{a_{L-1},a_{L-1}} (V^\dagger)_{a_{L-1},\sigma_L} \\ &= \sum_{a_{L-1}} \Psi_{(\sigma_1\ldots\sigma_{L-2}),(\sigma_{L-1}a_{L-1})} B^{\sigma_L}_{a_{L-1}} \\ &\vdots \\ &= \sum_{a_1,\ldots,a_{L-1}} B^{\sigma_1}_{a_1} B^{\sigma_2}_{a_1,a_2} \ldots B^{\sigma_{L-1}}_{a_{L-2},a_{L-1}} B^{\sigma_L}_{a_{L-1}}, \\ &= B^{\sigma_1} B^{\sigma_2} \ldots B^{\sigma_L}, \end{aligned} \tag{3.8}$$

where $B^{\sigma_L}_{a_{L-1}}$ is a collection of column vectors, $B^{\sigma_1}_{a_1}$ is a collection of row vectors and all other $B^{\sigma_j}_{a_{j-1},a_j}$ are collections of matrices of dimension (r_{j-1}, r_j). The B matrices are normalized as

$$\sum_{\sigma_j} B^{\sigma_j} B^{\sigma_j\dagger} = \mathbb{I} \tag{3.9}$$

and the resulting MPS is called *right-canonical*.
A so-called *mixed canonical* MPS can be obtained by decomposing from both sites,

$$c_{(\sigma_1,\ldots,\sigma_L)} = A^{\sigma_1} \ldots A^{\sigma_l} S B^{\sigma_{l+1}} \ldots B^{\sigma_L}. \tag{3.10}$$

All matrices A on sites $1 \ldots l$ are left-normalized and all matrices B on sites $l+1 \ldots L$ are right-normalized. The matrix S contains the singular values on the link $(l, l+1)$ given by the components $S_{a_l,a_l} = \sqrt{\lambda_{a_l}}$. Note, if one starts from an arbitrary wave function which is not normalized, one can analogously carry out the left- or right-normalization procedure. The obtained canonical form then contains an additional scalar factor which is the norm of the MPS.
Defining $|a_l\rangle_A = \sum_{\sigma_1\ldots\sigma_l} (A^{\sigma_1}\ldots A^{\sigma_l})_{(1,a_l)} |\sigma_1,\ldots,\sigma_l\rangle$ and $|a_l\rangle_B = \sum_{\sigma_{l+1}\ldots\sigma_L} (B^{\sigma_{l+1}}\ldots B^{\sigma_L})_{(a_l,1)} |\sigma_{l+1},\ldots,\sigma_L\rangle$, the mixed canonical MPS (3.10) can be rewritten as

$$|\Psi\rangle = \sum_{a_l=1}^{r} \sqrt{\lambda_{a_l}} |a_l\rangle_A \otimes |a_l\rangle_B, \tag{3.11}$$

which is equivalent to the so-called *Schmidt-decomposition* of a system of length L into subsystems A (sites $1 \ldots l$) and B (sites $l+1 \ldots L$). The states $|a_l\rangle_A$ form an orthonormal basis of A and the states $|a_l\rangle_B$ form an orthonormal basis of B. The rank of S, $r = \min(n, m)$, is the bond dimension at the bond $(l, l+1)$ where n and m are the dimension of A^{σ_l} and $B^{\sigma_{l+1}}$. The idea is now, to truncate S to dimension $D < r$ (at each bond), i.e., choose the state $|\tilde{\Psi}\rangle = \sum_{a_l=1}^{D} \sqrt{\lambda_{a_l}} |a\rangle_A \otimes |a\rangle_B$ with $\lambda_1 \geq \lambda_2 \geq \ldots$ and of fixed Schmidt rank $D < r$, which best approximates $|\Psi\rangle$. This is a good approximation if the ordered singular values decay fast (it becomes exact for $D \geq r$) and the quality of the truncation can be quantified by the norm

$$\left\| |\Psi\rangle - |\tilde{\Psi}\rangle \right\|^2 = \langle\Psi|\Psi\rangle + \langle\tilde{\Psi}|\tilde{\Psi}\rangle - \langle\Psi|\tilde{\Psi}\rangle - \langle\tilde{\Psi}|\Psi\rangle = 1 - \sum_{a_l=1}^{D} \lambda_{a_l}, \tag{3.12}$$

which gives the truncation error (sum of discarded singular values). The maximal bond dimension of a local matrix $M^{\sigma_j}_{a_{j-1},a_j}$ is now fixed to D and the system becomes numerically manageable in contrast to dealing with the full Hilbert space. This approximation typically works well for weakly entangled

systems which can be seen from the von Neumann entanglement entropy. It is given by the non-zero part of the eigenvalue spectrum of the reduced density matrices $\rho_A = \mathrm{Tr}_B\rho$ (or $\rho_B = \mathrm{Tr}_A\rho$) of the two subsystems,

$$S_{\mathrm{vN}} = -\mathrm{Tr}\rho_A \ln \rho_A = -\sum_\alpha \lambda_\alpha \ln \lambda_\alpha. \tag{3.13}$$

If the state $|\Psi\rangle$ can be decomposed into a product state between the two subsystems A and B, there is only one non-zero singular value $\lambda_1 = 1$ and thus $S_{\mathrm{vN}} = 0$. S_{vN} is maximal if all λ_α are equal and it is small if the eigenvalues λ_α decay quickly. The ground states of one-dimensional systems with short-ranged interactions and a finite excitation gap are weakly entangled as conjectured by the so-called *area laws* which predict that the entanglement entropy of such systems is proportional to the interface between two subsystems which is constant in one dimension [29]. This explains the success of DMRG in such systems. For non-gapped systems, there is logarithmic contributions in the system size such that the entanglement entropy grows with system size but such system can still be treated with more numerical effort.

Matrix product operators Analogously to matrix product states, one can construct matrix product operators,

$$\hat{O} = \sum_{\sigma_1\ldots\sigma_L\sigma_1'\ldots\sigma_L'} c_{(\sigma_1\ldots\sigma_L),(\sigma_1'\ldots\sigma_L')}|\vec{\sigma}\rangle\langle\vec{\sigma}'| = \sum_{\vec{\sigma},\vec{\sigma}'} W^{\sigma_1,\sigma_1'}\ldots W^{\sigma_L,\sigma_L'}|\vec{\sigma}\rangle\langle\vec{\sigma}'|, \tag{3.14}$$

where $W^{\sigma,\sigma'}$ are matrices that now have two physical indices for outgoing and ingoing states. The first and last matrix are indexed $W^{\sigma_1,\sigma_1'}_{b_1}$ and $W^{\sigma_L,\sigma_L'}_{b_L}$, and the intermediate matrices are indexed $W^{\sigma_j,\sigma_j'}_{b_{j-1},b_j}$ for $j \neq 1, L$. One can apply a matrix product operator to an MPS as,

$$\begin{aligned}
\hat{O}|\Psi\rangle &= \left(\sum_{\vec{\sigma},\vec{\sigma}'} W^{\sigma_1,\sigma_1'}\ldots W^{\sigma_L,\sigma_L'}|\vec{\sigma}\rangle\langle\vec{\sigma}'|\right)\left(\sum_{\vec{\sigma}''} M^{\sigma_1''}\ldots M^{\sigma_L''}|\vec{\sigma}''\rangle\right) \\
&= \sum_{\vec{\sigma},\vec{\sigma}'} W^{\sigma_1,\sigma_1'}\ldots W^{\sigma_L,\sigma_L'}M^{\sigma_1'}\ldots M^{\sigma_L'}|\vec{\sigma}\rangle \\
&= \sum_{\vec{\sigma}}\left(\sum_{\vec{\sigma}_1'} W^{\sigma_1,\sigma_1'}M^{\sigma_1'}\right)\left(\sum_{\vec{\sigma}_2'} W^{\sigma_2,\sigma_2'}M^{\sigma_2'}\right)\ldots|\vec{\sigma}\rangle \\
&= \sum_{\vec{\sigma}} N^{\sigma_1}N^{\sigma_2}\ldots N^{\sigma_L}|\vec{\sigma}\rangle,
\end{aligned} \tag{3.15}$$

where $N^{\sigma_j}_{(b_{j-1},a_{j-1}'),(b_j,a_j')} = \sum_{\sigma_j'} W^{\sigma_j,\sigma_j'}_{b_{j-1},b_j}M^{\sigma_j'}_{a_{j-1}',a_j'}$ is a matrix. The resulting state is also a matrix product state but of grown bond dimension.

3.1.2 Ground state calculation

In order to find the ground state of some Hamiltonian $\hat{H}$ one needs to find the quantum state $|\Psi\rangle$ of bond dimension D that minimizes the energy

$$E = \frac{\langle\Psi|\hat{H}|\Psi\rangle}{\langle\Psi|\Psi\rangle}. \tag{3.16}$$

This problem is difficult to solve for the full product of matrices but it can be done iteratively by keeping the matrices constant on all sites, but on one site l or on two sites $(l, l+1)$ and optimizing only these matrix entries, $M^{\sigma_l}_{a_{l-1}a_l}$ or $M^{\sigma_l\sigma_{l+1}}_{a_{l-1}a_{l+1}} = M^{\sigma_l}_{a_{l-1}a_l} M^{\sigma_{l+1}}_{a_l a_{l+1}}$, respectively. The algorithm consists of sweeping trough the lattice and successively optimizing locally until the ground state energy converges. In the case of the one-site optimization problem the bond dimensions stay fixed and the algorithm often gets stuck in local energy minima. Here, the two-site optimization is used, where an enlarged Ansatz space (growing bond dimension with subsequent truncation) renders the algorithm more robust against the danger of getting stuck in a local minimum. Essentially, for a mixed MPS with orthogonality center at site l or $l+1$, one needs to extremize (two-site optimization)

$$\frac{\partial}{\partial M^{\sigma_l\sigma_{l+1}*}_{a_{l-1}a_{l+1}}} \Big(\langle \Psi | \hat{H} | \Psi \rangle - \lambda \langle \Psi | \Psi \rangle \Big) = 0, \tag{3.17}$$

where $|\Psi\rangle$ will be the desired ground state and λ the ground state energy. This leads to an effective eigenvalue problem for the two-site matrix of interest $M^{\sigma_l\sigma_{l+1}}_{a_{l-1}a_{l+1}}$,

$$H_{\text{eff}} v - \lambda v = 0. \tag{3.18}$$

The eigenvector $v_{\sigma_l\sigma_{l+1}a_{l-1}a_{l+1}}$ to the lowest eigenvalue will be reshaped into the two-site matrix $\tilde{M}^{\sigma_l\sigma_{l+1}}_{a_{l-1}a_{l+1}}$ which replaces the previous $M^{\sigma_l\sigma_{l+1}}_{a_{l-1}a_{l+1}}$ and the lowest eigenvalue λ_0 gives the ground state energy estimate. In the subsequent SVD, the matrices on site l and $l+1$ need to be compressed to bond dimension D as they now have grown bond dimension dD. The updated state yields a variationally 'better' MPS. Starting from an initial guess for $|\Psi\rangle$ one sweeps through the lattice (repeatedly from site 1 to $L-1$ and back from site L to 2) while repeatedly solving the eigenvalue problem and updating the MPS as explained above until the ground state energy converges. Here, we use a combination of *infinite-system* DMRG and *finite-system* DMRG [134, 139] with open boundary conditions to find the ground state. It consists of first applying the build-up by the *infinite-system* algorithm: building up the system by increasing the system size while the bond dimension D of the MPS stays fixed until reaching the final system size L. The obtained state is taken as the initial guess for $|\Psi\rangle$. Then, the chosen basis is optimized by sweeping through the system as explained above (*finite-system* DMRG).

3.1.3 Time evolution

For the time evolution of a quantum state $|\Psi(t)\rangle$ one applies the time evolution operator $\exp\big(-i\hat{H}t\big)$ to the quantum state $|\Psi\rangle$. For a system with only nearest-neighbor interactions, the Hamiltonian $\hat{H}$ can be decomposed as

$$\hat{H} = \sum_j \hat{h}_j = \hat{H}_{\text{odd}} + \hat{H}_{\text{even}}, \tag{3.19}$$

where $\hat{h}_j$ acts on sites j and $j+1$ (it contains the interaction between these two sites). One can group odd bonds $\hat{H}_{\text{odd}} = \sum_{j\text{odd}} \hat{h}_j$ and even bonds $\hat{H}_{\text{even}} = \sum_{j\text{even}} \hat{h}_j$ separately. The bond Hamiltonians do not commute in general, $[\hat{h}_j, \hat{h}_{j+1}] \neq 0$, but even or odd bonds commute amongst each other, respectively. The second-order Suzuki-Trotter decomposition is given by

$$e^{-i\hat{H}\tau} = e^{-i\hat{H}_{\text{odd}}\frac{\tau}{2}} e^{-i\hat{H}_{\text{even}}\tau} e^{-i\hat{H}_{\text{odd}}\frac{\tau}{2}} + (\tau^3), \tag{3.20}$$

where $\tau = t/N$ is the discretized time step with N the number of time steps and t the total time. The exponentials factorize into $\exp\left(-i\hat{H}_{\text{odd}}\tau/2\right) = \prod_{j,\text{odd}} \exp\left(-i\hat{h}_j\tau/2\right)$ and $\exp\left(-i\hat{H}_{\text{even}}\tau\right) = \prod_{j,\text{even}} \exp\left(-i\hat{h}_j\tau\right)$ as even or odd bonds commute amongst each other. Each factor then acts onto a single bond and can be successively applied to adjacent sites of the MPS together with a truncation after each application (as the MPS has grown) which results in a sweep, for example 'right-left-right', for each time step. The error of the Trotter decomposition of nth order is given by τ^{n+1} which scales, after $N = t/\tau$ time steps, as $\tau^2 t$ (for the second order decomposition) which is linear in time. For decreasing τ this error decreases. At the same time, the reduction of τ increases the number of applications of the single-bond operators $\exp\left(-i\hat{h}_j\tau\right)$ such that the number of the subsequent truncations increases (if the total time stays fixed), thus increasing the truncation error. Consequently, both control parameters, matrix dimension D and Suzuki-Trotter time step τ need to be chosen carefully in order to avoid an increased error when decreasing the time step.

In the present thesis, we use t-DMRG to determine the time evolution of fermionic and bosonic particles confined to one-dimensional optical lattice geometries and subjected to a time-periodic lattice amplitude modulation, i.e. we time evolve the full time-dependent problem $\hat{H}_0 + \hat{H}_{\text{pert}}(t)$ where H_0 is the Hamiltonian of the equilibrium system and $H_{\text{pert}}(t)$ is the time-dependent perturbation introduced by a modulation of the lattice amplitude given by Eq. (2.39). We consider open boundary conditions and an even number of sites. We constrain our study to the quantum number sector with particle number $N = N_\uparrow + N_\downarrow = L$ and magnetization $S_z = N_\uparrow - N_\downarrow = 0$ for fermions. In the case of bosons, one has an additional control parameter which is the maximum allowed number of bosons per site which we denote by σ. For bosons we consider $N = L$ in most cases and $N < L$ in some cases. The t-DMRG codes used for the time evolution of bosonic and fermionic systems are based on codes developed by Corinna Kollath. In the present work they are adapted to simulate the lattice amplitude modulation by a modulation of the hopping parameter (cf. Sec. 2.6). We consider the global energy of the full time-dependent problem,

$$E(t) = \frac{\langle\Psi(t)|H(t)|\Psi(t)\rangle}{\langle\Psi(t)|\Psi(t)\rangle}, \tag{3.21}$$

as our observable. In lattice shaking setups, the system absorbs energy (in first order) whenever the modulation frequency $\hbar\omega$ corresponds to the energy of an available excitation in the system. Close to resonance, the time evolution of the energy typically shows an initial quadratic rise, then becomes linear in time at intermediate (and sufficiently large) times and eventually saturates at longer times. The slope of the linear region can be identified with the energy absorption rate which we will compare to analytical results obtained within a linear response treatment introduced in the following Sec. 3.2.
In Chapter 4 we determine the time evolution of the ionic Fermi-Hubbard model in a wide range of parameters subjected to a lattice amplitude modulation of superlattice geometry. In Chapter 6 we determine the time evolution of the Bose-Hubbard model in both, the Mott insulating and superfluid phases, subjected to a lattice amplitude modulation of superlattice geometry.
The chosen control parameters D, τ and σ (in the case of bosons) depend on the physical situation and are adjusted accordingly by monitoring the error on $E(t)$ at the final considered time upon variation of each of the control parameters separately. The chosen control parameter sets will be given throughout this thesis for each considered situation and the error analysis is explained in detail in appendix A.

3.2 Linear response theory

In the study of quantum many-body systems one is often confronted with the ambitious task of measuring and computing observables. A common method to probe such systems is to apply a small time-dependent perturbation and study the response of the system. For example, one can exert a small voltage or magnetic field and study the response of the conductance or magnetization, respectively. Instead of considering the full time-dependent system which is typically very difficult to solve, for sufficiently small perturbations, one can expand observables in the perturbing Hamiltonian. In lowest order, observables depend uniquely on ground state correlation functions, which can be computed more easily in many cases. This is known as linear response [141, 142]. On the one hand, it enables one to probe various physical properties of the equilibrium system by adding a slight perturbation. On the other hand, one can determine the response to arbitrary time- and space-dependent perturbations if one knows how to determine the equilibrium correlation functions.
Throughout this work linear response theory will be repeatedly used to study the energy absorption of optical lattice systems as a response to lattice amplitude modulation. It has been shown a reliable tool in the description of these kind of setups [107] where it applies to the intermediate linear region of the time evolution of the energy.
In this section we first present the main linear response formulas in Sec. 3.2.1. Then, in Sec. 3.2.2, we outline the description of energy absorption as a response to a perturbation $H_{\text{pert}}(t) = A\sin(\omega t)\hat{O}$ (2.39) which corresponds to the situation present in lattice shaking experiments (cf. Sec. 2.6).

3.2.1 General aspects

Consider an equilibrium system which is described by a generic Hamiltonian H_0 which does not contain an explicit time-dependence. The time-dependent perturbation can be written as

$$H_{\text{pert}}(t) = \int \mathrm{d}\vec{r}\, h(\vec{r},t)O(\vec{r}), \tag{3.22}$$

where $h(\vec{r},t)$ is the external field which acts locally and is coupled to a local operator $O(\vec{r})$. The full Hamiltonian is then given by $H(t) = H_0 + H_{\text{pert}}(t)$ and is usually very difficult to solve exactly. One chooses $\langle O(\vec{r})\rangle_0 = 0$ where $\langle\cdot\rangle_0$ denotes the expectation value with respect to H_0 in absence of the perturbation. The aim is to calculate the expectation value of some physical observable $A(\vec{r},t)$ at point $\vec{r}$ and time t with respect to the full time-dependent Hamiltonian $H(t)$. The idea is to relate it to the properties of H_0 by expanding the perturbation in powers of the small amplitude h. Also choosing $\langle A(\vec{r})\rangle_0 = 0$, in lowest order (linear response) one finds

$$\langle A(\vec{r})\rangle_t = \int d\vec{r}' \int_{-\infty}^{t} dt' h(\vec{r}',t')\chi(\vec{r},\vec{r}',t,t'), \tag{3.23}$$

with the complex susceptibility

$$\chi(\vec{r},\vec{r}',t,t') := -\frac{i}{\hbar}\theta(t-t')\langle[A(\vec{r},t),O(\vec{r}',t')]\rangle_0, \tag{3.24}$$

where the operators are given in the Heisenberg representation $A(\vec{r},t) = e^{iH_0t}A(\vec{r})e^{-iH_0t}$ and similar for $O(\vec{r}',t')$. The complex susceptibility measures the way the system responds to the perturbation and it only depends on the equilibrium system H_0. The θ-function ensures causality as a measure at time t can only depend on the perturbation at earlier times, i.e. the correlation function (3.24) is only non-zero for

$t > t'$. Translational invariance in space and the fact that χ is an equilibrium quantity which only depends on the time difference of operators, implies $\chi(\vec{r}, \vec{r}', t, t') = \chi(\vec{r} - \vec{r}', t - t')$. Thus, one can compute the double Fourier transform,

$$\begin{aligned}
\langle A(\vec{q}, \omega)\rangle &= \mathcal{FT}\left(\langle A(\vec{r})\rangle_t\right) \\
&= \mathcal{FT}\left(\int d\vec{r}' \int_{-\infty}^{t} dt' h(\vec{r}', t')\chi(\vec{r} - \vec{r}', t - t')\right) \\
&= \mathcal{FT}\left(\int d\vec{r}' \int_{-\infty}^{\infty} dt' h(\vec{r}', t')\chi(\vec{r} - \vec{r}', t - t')\right) \\
&= \mathcal{FT}\left((h * \chi)(r, t)\right) = \mathcal{FT}\left(h(\vec{r}, t)\right)\mathcal{FT}\left(\chi(\vec{r}, t)\right) = \chi(\vec{q}, \omega)h(\vec{q}, \omega), \\
\chi(\vec{q}, \omega) &= \int \mathrm{d}\vec{r} \int_{-\infty}^{+\infty} \mathrm{d}t e^{-i(\vec{q}\vec{r} - \omega t)}\chi(\vec{r}, t) = -\frac{i}{\hbar}\int \mathrm{d}\vec{r} \int_{0}^{+\infty} \mathrm{d}t e^{-i(\vec{q}\vec{r} - \omega t)} \langle [A(\vec{r}, t), O(0, 0)]\rangle_0 \,, \qquad (3.25)
\end{aligned}$$

where one extends the integral to $t \to +\infty$ as it is zero for all $t' > t$ and the convolution in one dimension is defined as $(f * g)(x) = \int_{-\infty}^{\infty} f(\tau)g(x - \tau)\mathrm{d}\tau$ $(f, g : \mathbb{R} \to \mathbb{C})$ with the property $\mathcal{FT}(f * g) = \mathcal{FT}(f)\mathcal{FT}(g)$. Convergence of the integral for $t \to \infty$ is ensured by replacing $\omega \to \omega + i\delta$. This corresponds to adding an infinitesimal positive imaginary part to the frequency where δ is an infinitesimal positive number.

3.2.2 Energy absorption

Under the influence of a time-dependent external potential, some energy is absorbed by the system, in contrast to the unperturbed system where energy is conserved. The observable of interest is the change in energy $dE(t)/dt = \langle dH(t)/dt\rangle = \langle dH_{\mathrm{pert}}(t)/dt\rangle$. Consider a sinusoidal perturbation as present in typical lattice shaking setups with $H_{\mathrm{pert}}(t) = A\sin(\omega t)\hat{O}$ given by Eq. (2.39) for which

$$\frac{dE(t)}{dt} = A\omega\cos(\omega t)\langle\hat{O}\rangle_t = \frac{A^2}{4i}\omega\left(e^{i\omega t} + e^{-i\omega t}\right)\int_{-\infty}^{t}\left(e^{i\omega t'} - e^{-i\omega t'}\right)\chi(t - t')\mathrm{d}t', \qquad (3.26)$$

with $\chi(t - t') = -(i/\hbar)\,\theta(t - t')\left\langle\left[\hat{O}(t - t')), \hat{O}(0)\right]\right\rangle_0$ as the perturbation is space-independent. Note that the upper bound of the integral t can be replaced by $+\infty$ as the integral is zero for any $t' > t$ and the lower bound $-\infty$ can be replaced by t_0, the time at which the perturbation is switched on, and one can set $t_0 = 0$. Averaging over one period $T = 2\pi/\omega$ of the sinusoidal perturbation and assuming positive frequencies, one obtains the averaged rate of dissipation

$$\overline{\frac{dE(t)}{dt}}(\omega) = \frac{1}{T}\int_0^T \mathrm{d}t\frac{dE}{dt} = -\frac{\omega}{2}A^2\mathrm{Im}\chi(\omega). \qquad (3.27)$$

The dissipation in the system brought by the perturbation is controlled by the imaginary part of the complex susceptibility which describes the response to this perturbation. This relation is known as the fluctuation-dissipation theorem. In many cases, it is more conveniently expressed in terms of the eigenstates $|n\rangle$ of H_0. In order to do so one first re-expresses χ as

$$\chi(t) = -\frac{i}{\hbar}\theta(t)\langle[\,\hat{O}(t), \hat{O}(0)]\rangle_0 = -\frac{i}{\hbar}\frac{1}{Z_0}\theta(t)\mathrm{Tr}\left(e^{-\beta H_0}\left[\hat{O}(t), \hat{O}(0)\right]\right), \qquad (3.28)$$

using $\langle A\rangle_t = \mathrm{Tr}\left[\rho_0 A\right]$ where $\mathrm{Tr}\left[\cdot\right]$ denotes the trace of an operator and ρ_0 is the density matrix of the time-independent system. The density matrix ρ_0 is given by a superposition state where each level $|n\rangle$ with energy E_n (corresponding to the eigenstates of H_0) is occupied with a probability given by the Boltzmann

factor $\rho = \sum_n (\exp(-\beta E_n)/Z_0)|n\rangle\langle n| = \exp(-\beta H_0)/Z_0$. Here, $\beta = 1/(k_B T)$ is the inverse temperature with k_B the Boltzmann constant and $Z_0 = \sum_n \exp(-\beta E_n) = \mathrm{Tr}\left[\exp(\beta H_0)\right]$ is the partition function of the equilibrium system which ensures normalization. Repeatedly inserting the identity $\mathbb{I} = \sum_n |n\rangle\langle n|$ and rewriting yields

$$\chi(t) = -\frac{i}{\hbar}\frac{1}{Z_0}\theta(t)\sum_{n,m} e^{i(E_n - E_m)t/\hbar}\left|\left\langle n\left|\hat{O}\right|m\right\rangle\right|^2\left(e^{-\beta E_n} - e^{-\beta E_m}\right). \tag{3.29}$$

Taking the Fourier transform and taking the imaginary part of Eq. (3.29) and inserting it into Eq. (3.27), one obtains

$$\begin{aligned}\overline{\frac{dE}{dt}}(\omega) &= \omega\frac{|A|^2}{2Z_0}\left(1 - e^{\beta\hbar\omega}\right)\sum_{n,m}\left|\left\langle n\left|\hat{O}\right|m\right\rangle\right|^2 e^{-\beta E_n}\frac{\eta}{\eta^2 + (\hbar\omega - (E_m - E_n))^2} \\ &= \omega\frac{\pi|A|^2}{2Z_0}\left(1 - e^{\beta\hbar\omega}\right)\sum_{n,m}\left|\left\langle n\left|\hat{O}\right|m\right\rangle\right|^2 e^{-\beta E_n}\delta\left(\hbar\omega - (E_m - E_n)\right),\end{aligned} \tag{3.30}$$

where we used the definition of Dirac's δ-function by a sequence Lorentz-functions, $\delta(x) = \lim_{\eta\to 0^+}\delta_\eta(x)$, $\delta_\eta(x) = (\eta/\pi)/(\eta^2 + x^2)$. This formula is known as the spectral representation and has an intuitive interpretation. A transition between an initial state $|n\rangle$ and an excited state $|m\rangle$ can occur when the energy difference $E_m - E_n$ between the two states is equal to the energy $\hbar\omega$ provided by the modulation with frequency ω. The energy conservation is ensured by the δ-function and the initial occupation is determined by the weight $\exp(-\beta E_n)$. The probability of the transition is proportional to the square of the transition matrix element coupling the two states by the perturbation $\sim \left|\left\langle n\left|\hat{O}\right|m\right\rangle\right|^2$. At zero temperature, the energy absorption rate becomes

$$\overline{\frac{dE}{dt}}(\omega) = \omega\frac{\pi|A|^2}{2}\sum_m\left|\left\langle 0\left|\hat{O}\right|m\right\rangle\right|^2\delta\left(\hbar\omega - (E_m - E_0)\right), \tag{3.31}$$

where $|0\rangle$ is the ground state of H_0 with ground state energy E_0. For a finite system one can again replace the δ-function by a sequence Lorentz-functions.
Alternatively, one can integrate the energy absorption rate (3.26), also expressing it in terms of the eigenstates, to obtain $E(t) - E_0 = \int_0^t \mathrm{d}t'(dE(t')/dt')$. The dominant contribution to the time evolution of the absorbed energy is then given by

$$E(t) - E_0 \approx \frac{\omega|A|^2}{4\hbar}\sum_m |\langle 0|\hat{O}|m\rangle|^2\frac{\sin^2\left((E_m - E_0 - \hbar\omega)t/(2\hbar)\right)}{\left((E_m - E_0 - \hbar\omega)/(2\hbar)\right)^2}, \tag{3.32}$$

where 'anti-resonant' and fast oscillating terms are neglected. For $t \to \infty$ [142], one can use the definition of Dirac's delta function by a sequence of sinc-functions, $\delta(x) = \lim_{\eta\to 0^+}\delta_\eta(x)$, $\delta_\eta(x) = (\eta/\pi)\sin^2(x/\eta)/x^2$, with $\eta := 1/t \to 0$ and $x = (E_m - E_0 - \hbar\omega)/(2\hbar)$ such that the oscillating term in Eq. (3.32) becomes

$$\begin{aligned}\frac{\sin^2\left((E_m - E_0 - \hbar\omega)t/(2\hbar)\right)}{\left((E_m - E_0 - \hbar\omega)/(2\hbar)\right)^2} &\to \pi t\delta\left((E_m - E_0 - \hbar\omega)/(2\hbar)\right) \\ &= 2\pi\hbar t\delta\left(E_m - E_0 - \hbar\omega\right)\end{aligned} \tag{3.33}$$

which linearly rises in time. Note that the same result can be obtained by integrating the averaged rate (3.31).

In all projects constituting this thesis we obtain analytical results for the energy absorption as a response to a modulation of the lattice amplitude by means of the linear response treatment given by Eqs. (3.27), (3.30) and (3.32). The remaining difficulty in this approach lies in determining the eigenstates and eigenenergies of the many-body problem which can be an ambitious task in general. However, in certain physical situations where the exact states are unknown, good approximations can be found by means of, for example, perturbation theory or effective Hamiltonians. In Ch. 4 we derive an effective model describing the charge fluctuations in the lowest band of charge excitations in the ionic Fermi-Hubbard model by superlattice modulation spectroscopy for which we can determine the eigenstates in the band and Mott-insulating limits. In the bond order wave phase and in the vicinity of the two bordering phase transitions as well as in the Mott insulator, the low energy excitations can be described by linear response within bosonization introduced in the following section. In Ch. 5 we study non-interacting fermions in an optical lattice for which the states are determined by the occupation of the single-particle Bloch states (which depends on the Fermi function). The Bloch functions and corresponding eigenenergies can be determined by a numerical band structure calculation. Finally, in Ch. 6 the linear response in the Mott insulator will be obtained by means of degenerate perturbation theory in the lowest lying excitations.

When conducting experiments or t-DMRG simulations, the modulation amplitude must be adequately chosen as it determines the duration of the time interval over which the linear regime takes place. The intermediate linear region is required to be large enough to obtain a reliable fit of the energy absorption rate. In other words, the amplitude needs to be chosen sufficiently large to obtain a measurable signal, but also small enough for the response to remain in the linear regime long enough and not saturate at short times. In the past, modulation spectroscopy experiments [15, 36] were used successfully, fulfilling these requirements. Throughout this thesis, in each case using t-DMRG we choose the modulation amplitude accordingly and a detailed discussion is given in App. B.

3.3 Bosonization

Bosonization is a field theoretical method in one dimension which is well suited to describe the low-energy properties of interacting systems and extract universal features. The basic idea is to re-express operators in terms of collective excitations which are dominant in interacting one-dimensional systems and thus constitute a good basis. The collective excitations have Bose-like statistics, since they are mainly density excitations, from which originates the term *bosonization* but it can be applied to both, bosonic and fermionic systems.
In this section, we outline the derivation of the main bosonization formulas in a phenomenological approach [27, 143] which gives an intuitive physical interpretation of most of the results. The derivation of precise formulas, which is essentially exact, is based on a linearization of the spectrum close to the Fermi surface and is not treated here, see Ref. [27] for details. We start by considering spinless bosons in Sec. 3.3.1 and extend the discussion to spinless fermions. Then, the effects of spin and an additional periodic lattice potential will be subsequently added. Finally, the ionic Hubbard model in bosonization and the nature of the occurring phase transitions are discussed in Sec. 3.3.2.
In Chapter 4, we study the low-energy excitations in the one-dimensional ionic Hubbard model as a response to superlattice modulation, comparing t-DMRG to bosonization. The bosonization calculations were obtained in collaboration with Roberta Citro (Università degli Studi di Salerno) and Edmond

Orignac (ENS de Lyon). This section serves to give a brief introduction in order to lay a foundation for the interpretation of the bosonization results in comparison to our numerical results.

3.3.1 Basic ideas

Bosonization for spinless particles One can start from the simple Hamiltonian

$$H = \frac{\hbar^2}{2m}\int \mathrm{d}x \left(\nabla\Psi^\dagger(x)\right)\left(\nabla\Psi(x)\right) + \frac{g}{2}\int \mathrm{d}x\mathrm{d}x'\delta(x-x')\rho(x)\rho(x') \tag{3.34}$$

where $\Psi^{(\dagger)}(x)$ denotes a bosonic annihilation (creation) operator for particles of mass m, $\rho(x)$ is the density operator and g is the interaction strength. The first step in order to express everything in terms of collective excitations is to introduce a continuous labeling field $\phi_l(x)$ which varies smoothly at the scale of the interparticle distance and which labels the particles in an unambiguous way, for example from left to right, with $\phi_l(x_j) = 2\pi j$ at the position of the j-th particle. The perfect crystalline solution with average density ρ_0 is clearly given by the linear field $2\pi\rho_0 x$. Defining a relative field which describes deviations from this perfect solution, $\phi_l(x) = 2\pi\rho_0 x - 2\phi(x)$, the density operator can be expressed as

$$\rho(x) = \sum_j \delta(x-\hat{x}_j) = |\nabla\phi_l(x)|\sum_j \delta\left(\phi_l(x) - 2\pi j\right) = \left(\rho_0 - \frac{1}{\pi}\nabla\phi(x)\right)\sum_p e^{ip2(\pi\rho_0 x - \phi(x))}. \tag{3.35}$$

The $p = 0$ component of the sum corresponds to a compression or dilatation of the lattice which means that $\phi(x)$ is the displacement of the particle from a perfect lattice. One can now write the bosonic single-particle operator in terms of collective variables,

$$\Psi_B^\dagger(x) = \sqrt{\rho(x)}e^{-i\theta(x)} = \sqrt{\rho_0 - \frac{1}{\pi}\nabla\phi(x)}\sum_p e^{i2p(\pi\rho_0 x - \phi(x))}e^{-i\theta(x)}, \tag{3.36}$$

where $\theta(x)$ can be interpreted as the superfluid phase of the system. The two phases $\phi(x)$ and $\theta(x)$ are canonically conjugate which reflects the quantum fluctuations of the system. They fulfill $[\phi(x), (1/\pi)\nabla\theta(x')] = i\delta(x-x')$ and thus $\Pi(x) = (1/\pi)\nabla\theta(x)$ is the momentum conjugate to $\phi(x)$.
One can now re-express the Hamiltonian in terms of collective variables. Assuming that the compression or dilatation of the lattice is much smaller than ρ_0, which ensures that the 'lattice' is not too soft and which is typically satisfied for repulsive bosons, and removing all oscillating terms from the density as they will vanish in the integration, the kinetic term (first term in Eq. (3.34)) becomes $\left(\nabla\Psi(x)^\dagger\right)\left(\nabla\Psi(x)\right) \approx \rho_0\left(\nabla\theta\right)^2 + \left(\nabla^2\phi\right)^2/(4\pi^2\rho_0)$. Again dropping oscillating terms, the interaction term (second term in Eq. (3.34)) becomes $(\rho(x))^2 \approx \rho_0^2 + (\nabla\phi)^2/\pi^2 - 2\rho_0\nabla\phi/\pi$ where the first term (constant energy offset) can be dropped and the last term can be absorbed in a chemical potential term $\sim \int \mathrm{d}x\mu\rho(x)$. Thus, the interaction term is quadratic and much easier to solve in contrast to the single-particle basis where this term is quartic in the operators. The Hamiltonian becomes $H = \int \mathrm{d}x\left\{(\hbar^2\rho_0/(2m))\left(\nabla\theta(x)\right)^2 + (g/2\pi^2)\left(\nabla\phi(x)\right)^2 + \hbar^2\left(\nabla^2\phi(x)\right)^2/(8\pi^2\rho_0 m)\right\}$. Decomposing $\phi(x)$ in Fourier modes $\sim e^{ikx}$, one gets $\left(\nabla\phi(x)\right)^2 \sim k^2\phi$ and $\left(\nabla^2\phi(x)\right)^2 \sim k^4\phi$. The second term is negligible in the low energy limit $k \to 0$ and one obtains the bosonized Hamiltonian

$$H = \frac{1}{2\pi}\int \mathrm{d}x\left\{(\hbar u K)\left(\nabla\theta(x)\right)^2 + \frac{\hbar u}{K}\left(\nabla\phi(x)\right)^2\right\} \tag{3.37}$$

which only depends on the two parameters u and K that depend on the microscopic parameters such as for example the interaction parameter g. The parameter u describes the velocity of sound excitations and K is dimensionless. This Hamiltonian for free and massless bosonic excitations describes the asymptotic (long distance, large time) properties of the complex interacting system provided that the exact u and K are used. This is known as the Luttinger liquid description [144]. An important result is that the parameter K controls the power law decay of the dominating correlation functions. These correlation functions reflect the one-dimensional character of the system under study. Real long range order cannot occur but quasi-long range order can be attributed to the slowest decaying correlation function. The single-particle and density correlation functions are given by [143] $\left\langle \Psi(x)\Psi^\dagger(0)\right\rangle = \rho_o A_1 \left(\alpha/x\right)^{1/(2K)}$ and $\langle(\rho(x)-\rho_0)\left(\rho(0)-\rho_0\right)\rangle = -K/(2\pi^2x^2) + \rho_0^2 A_2 \left(\alpha/x\right)^{2K} + \ldots$ respectively where A_1 and A_2 are non-universal amplitudes that depend on the precise microscopic model and α is a short-distance cutoff which is typically of the order of the lattice spacing below which the low-energy effective theory is not valid. Evidently, for large K the system is dominated by single-particle correlations and can essentially be seen as superfluid. In contrast, for small K the system is dominated by density correlations and can be seen as a crystal of bosons.
In the case of fermions, the density formula (3.35) is the same but the single-particle operators have to anticommute which is fulfilled by the following expression for the fermionic single-particle operators

$$\Psi_F^\dagger(x) = \Psi_B^\dagger(x) e^{i\phi_I(x)/2} = \sqrt{\rho_0 - \frac{1}{\pi}\nabla\phi(x)} \sum_p e^{i(2p+1)(\pi\rho_0 x - \phi(x))} e^{-i\theta(x)}. \tag{3.38}$$

The excitations of the collective field are still described by Eq.(3.37). More rigorously, one has to consider right (positive momenta) and left (negative momenta) moving particles near the Fermi surface and the different possible scattering processes amongst them which contribute to the interaction term. However, for spinless fermions the Hamiltonian remains quadratic and the only change is that the parameters u and K get modified. There is clearly a connection between bosons and fermions in one dimension, however, the single-particle correlations are very different. For example, the momentum distribution which is the Fourier transform of the equal-time single-particle correlation shows a power law divergence $n(k) \sim k^{1/2K-1}$ for bosons in contrast to fermions where the momentum distribution is very similar to the free-particle step function with a drop at k_F. The momentum distribution displays a singularity instead of a sharp drop at k_F, $n(k) \sim 1/2 + \mathrm{sign}(k_F - k)|k - k_F|^{(K+1/K)/2-1}$.

Particles with spin If now, the fermionic particles carry a spin, one can introduce boson representation for both spin species $(\phi_\uparrow, \theta_\uparrow)$ and $(\phi_\downarrow, \theta_\downarrow)$ from which one can construct new bosonic fields, the charge $\phi_c = (\phi_\uparrow + \phi_\downarrow)/\sqrt{2}$ and spin $\phi_s = (\phi_\uparrow - \phi_\downarrow)/\sqrt{2}$ fields and similar for the θ-fields. The resulting low-energy effective Hamiltonian is given by $H = H_c^0 + H_s$ where H_c^0 is given by the free Hamiltonian (3.37) such that the charge sector is described by a Luttinger liquid but with different parameters u_c and K_c. The spin sector is described by the *sine-Gordon*-Hamiltonian $H_s = H_s^0 + 2g_{1\perp}/(2\pi\alpha)^2 \int \mathrm{d}x \cos\left(\sqrt{8}\phi_s(x)\right)$ where H_s^0 is given by the free Hamiltonian (3.37) again with different parameters u_s, K_s. The additional perturbation of amplitude $g_{1\perp}$ in the spin term stems from the back scattering of particles with opposite spin $H_{1\perp} = \int \mathrm{d}x g_{1\perp} \sum_\sigma \Psi_{L,\sigma}^\dagger \Psi_{R,\bar\sigma}^\dagger \Psi_{L,\bar\sigma} \Psi_{R,\sigma}$ where the indices L and R denote left -or right moving particles respectively and $\Psi(x) = \Psi_L(x) + \Psi_R(x)$. All other scattering processes are absorbed in the quadratic terms. The charge and spin degrees of freedom are completely decoupled which is known as spin-charge separation and implies that single-particle excitations that would carry both, charge and spin, cannot persist [27, 82].

Influence of a periodic lattice In the presence of a lattice potential, additional interaction processes are possible as the momentum is only conserved modulo the reciprocal lattice vector. The particles can transfer momentum to the lattice. At half-filling so-called Umklapp processes occur which lead to an additional charge term of amplitude g_3 in the Hamiltonian, $H_c = H_c^0 + 2g_3/(2\pi\alpha)^2 \int \mathrm{d}x \cos\big(\sqrt{8}\phi_c(x)\big)$, with the spin part of the Hamiltonian unchanged.

3.3.2 Ionic Fermi-Hubbard model

In the presence of an ionic lattice, charge and spin degrees of freedom get coupled. Taking the continuum limit and using the bosonization representation discussed above, the low-energy effective description of the ionic Hubbard model given by Eq. (2.29) becomes [35],

$$\begin{aligned} H &= \int \frac{dx}{2\pi}\left[\hbar u_c K_c(\pi\Pi_c)^2 + \frac{\hbar u_c}{K_c}(\partial_x\phi_c)^2\right] + \frac{2g_3}{(2\pi\alpha)^2}\int dx \cos\left(\sqrt{8}\phi_c\right) \\ &+ \int \frac{dx}{2\pi}\left[\hbar u_s K_s\,(\pi\Pi_s)^2 + \frac{\hbar u_s}{K_s}(\partial_x\phi_s)^2\right] + \frac{2g_{1\perp}}{(2\pi\alpha)^2}\int dx \cos\left(\sqrt{8}\phi_s\right) \\ &+ \frac{\Delta}{2\pi\alpha}\int dx \cos\left(\sqrt{2}\phi_c\right)\cos\left(\sqrt{2}\phi_s\right), \end{aligned} \tag{3.39}$$

where the first and second lines are the charge and spin Hamiltonians introduced above, perturbed by Umklapp processes and back scattering, respectively. The last term couples the charge and spin sectors due to the ionicity of the lattice where Δ is the staggered energy offset between neighboring sites from Eq. (2.29).

The ground state phase diagram was discussed in Sec. 2.5 (cf. Fig. 2.6(a)). Here, we again discuss the different phases in the context of the bosonized Hamiltonian. Taking the continuum limit and using the bosonization representation discussed above, the bond order parameter (2.32) takes the form

$$\hat{B} = \frac{\mathcal{A}}{\alpha}\int_0^{aL} dx \left[\sin\left(\sqrt{2}\phi_c\right)\cos\left(\sqrt{2}\phi_s\right)\right], \tag{3.40}$$

where $\mathcal{A}$ is a non-universal dimensionless constant which depends on the parameters of the ionic Hubbard model.

The fluctuations in the fields (quadratic terms) in the Hamiltonian (3.39) compete with the cos-terms that would like to lock the field in one of their minima. In the band insulator, both charge sector and spin sector are gapped, and the classical ground state energy is minimized by locking the fields in the expectation values $\langle\phi_c\rangle = \pi/\sqrt{2}$ and $\langle\phi_s\rangle = 0$. At the transition to the bond order wave, the charge gap closes while the spin remains gapped ($\langle\phi_s\rangle = 0$). In the intermediate bond order wave phase the charge gap reopens and the charge field expectation value is now $\langle\phi_c\rangle = \pi/\sqrt{8}$. In this phase, the bond order wave parameter (3.40) acquires a non-zero expectation value. At the transition from the band insulator to the bond order wave, the effective Hamiltonian describing the physics at energies well below the spin gap is the two-frequency sine-Gordon model [145],

$$\begin{aligned} H_{\text{eff}} &= \int \frac{dx}{2\pi}\left[\hbar u_c K_c\,(\pi\Pi_c)^2 + \frac{\hbar u_c}{K_c}\,(\partial_x\phi_c)^2\right] + \frac{2g_3}{(2\pi\alpha)^2}\int dx \cos\left(\sqrt{8}\phi_c\right) \\ &+ \frac{\Delta\left\langle\cos\sqrt{2}\phi_s\right\rangle}{2\pi\alpha}\int dx \cos\left(\sqrt{2}\phi_c\right). \end{aligned} \tag{3.41}$$

which is known to exhibit a transition in the Ising universality class [35, 145–147].
To gain a more intuitive understanding of the existence of the Ising phase transition [148], one can inspect the profile of the potential part given by integrand of the second and third term in Eq. (3.41), $\mathcal{U}(\phi_c) = (8g_3)/(2\pi\alpha)^2 \left((1/4)\cos\left(\sqrt{8}\phi_c\right) + X\cos\left(\sqrt{2}\phi_c\right)\right)$ with $X = \left(\Delta\left\langle\cos\sqrt{2}\phi_s\right\rangle 2\pi\alpha\right)/(8g_3)$. It is shown in Fig. 3.1 for different X. For $X = 0$ the potential reduces to the periodic potential of the single-frequency sine-Gordon model. For $X \neq 0$ the periodicity is doubled. For $0 < X < 1$ the potential is split in a sequence of double well potentials with a local structure $\sim A\phi_c^2 + B\phi_c^4$ ($A < 0$, $B > 0$). At $X = 1$ each double well transforms to a potential $\sim \phi_c^4$ ($A = 0$) which, in the Ginzburg-Landau sense, is a signature of Ising criticality. At $X > 1$ it remains one potential well. Note, that this is only valid for $g_3 > 0$.

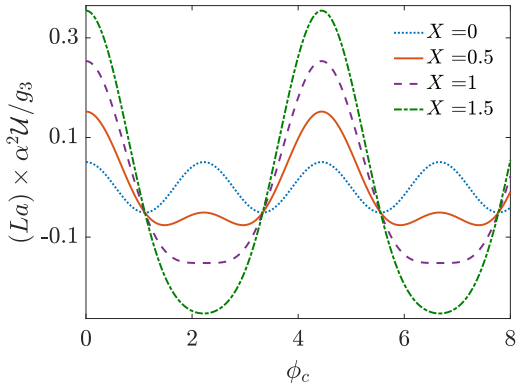

Figure 3.1: Sketch of the potential profile of the two-frequency sine-Gordon model (3.41) in the charge sector for different values of the parameter X (see main text). For $0 < X < 1$ the potential displays a sequence of double wells that transform to one potential well at $X = 1$ which indicates Ising criticality.

In the Mott insulator, only the charge sector is gapped with $\langle\phi_c\rangle = \pi/\sqrt{8}$ while the spin sector is gapless. The transition between the Mott insulator and the bond order wave takes place in the spin sector and belongs to the Kosterlitz-Thouless universality class [149–151].

In Ch. 4 we investigate the spectral response in the vicinity of the two phase transitions bordering the bond order wave phase which enables us to probe the onset of bond order at the Ising critical point and to find signatures of the low-energy spin excitations in the bond order wave phase. Moreover, the low-energy spectrum in the Mott insulator is probed. We compare the bosonization results to our t-DMRG calculations and find good agreement. Details of the bosonization calculations, obtained in collaboration [84], are given in appendix C.

CHAPTER 4

Superlattice modulation spectroscopy of ultracold fermions in optical superlattices: Study of the excitation spectrum of the one-dimensional ionic Fermi-Hubbard model

In this chapter we study the excitation spectrum of the one-dimensional ionic Fermi-Hubbard model as a response to a lattice amplitude modulation of superlattice geometry. The ionic Fermi-Hubbard model (2.29) was introduced in Sec. 2.5.2. It is given by the Fermi-Hubbard model with an additional staggered energy offset. At dominating energy offset, the system is band insulating with finite spin and charge gaps. At dominating on-site interaction strength, the system is Mott insulating with finite charge but zero spin gap. When energy offset and on-site interaction strength are of comparable strength, these two energy scales compete and the smaller kinetic energy term gains of importance. In this region of the phase diagram an intermediate bond order wave (BOW) phase occurs characterized by a spontaneous dimerization of the hopping [35]. A more detailed discussion of the ground state phase diagram at half-filling was given in Sec. 2.5.2 (cf. Fig. 2.6). In cold atom setups, the ionic Fermi-Hubbard model can be realized by fermionic particles confined to an optical superlattice [36].

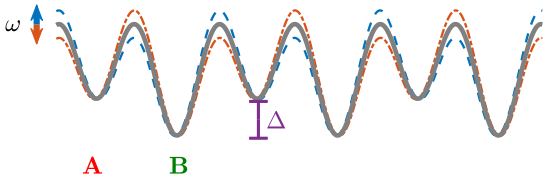

Figure 4.1: Schematic drawing of the superlattice modulation of an optical superlattice corresponding to the ionic Hubbard model. The unit cell of the equilibrium lattice (gray solid line) consists of two inequivalent sites, denoted A and B, separated in energy by an offset Δ (Δ corresponds to the staggered energy offset in the ionic Hubbard model given by Eq. (2.29)). The optical lattice is modulated in time with frequency ω in a dimerized fashion, that means between the two configurations indicated by dashed blue and dash-dotted orange lines around the ionic equilibrium lattice.

Detecting the bond order wave and its neighboring phase transitions remains to be done. An important challenge is to identify a suitable observable. Directly measuring the order parameter is difficult as this would require a measurement of the staggered kinetic energy. A promising approach to characterize the phase transitions is to study the response of the system to a perturbation. However, this requires

the development of a probe which directly couples to the order parameter in contrast to available techniques. We apply a superlattice amplitude modulation as sketched in Fig. 4.1 (cf. Sec. 2.6 where we discuss different lattice amplitude modulation setups). Notably, the perturbing operator $\hat{O}_S$ (2.41) which describes the superlattice modulation is equivalent to the bond order parameter $\hat{B}$ (2.32) which acquires a finite value in the BOW phase. Consequently, the superlattice modulation directly couples to the order parameter of the BOW phase which allows for the detection of signatures of the BOW phase. Moreover, valuable insights into the excitation spectra in the band- and Mott insulating limits are obtained.

Throughout this chapter we denote the perturbing operator associated with the superlattice modulation $\hat{O}_S$ in the band and Mott insulating phases and in the absence of interaction. When discussing the bond order wave and its neighboring phase transitions we denote the perturbing operator $\hat{B}(\equiv \hat{O}_S)$ in order to emphasize its close relation to the BOW order parameter.
This chapter is organized as follows. First, in in Sec. 4.1, we analytically study the non-interacting model which is exactly solvable. In all other sections we consider the presence of a finite interaction. In Sec. 4.2 we derive an effective model, using a Schrieffer-Wolff transformation for the excited states, which enables us to analytically describe the gapped excitation spectra in the band and Mott insulating limits. This section is quite technical. It focuses on the derivation of the effective model and the identification of a suitable basis in the band and Mott insulating limits in order to diagonalize the corresponding eigenproblem. No results for the energy absorption rate are given in this section and it may be skipped if one is only interested in the discussion of the results. In the remaining sections we study the energy absorption rate using t-DMRG[1] and we compare to different analytical approximations. In Sec. 4.3, we investigate the excitation spectrum in the band insulating phase. We start by presenting the results obtained for the energy absorption rate in t-DMRG comparing to the effective model in Sec. 4.3.1. We study the energy absorption rate deep in the band insulator at $\Delta \gg U$ where excitations are created near $\sim (\Delta - U)$, and we investigate how the structure and location of the observed absorption rate evolve for increasing interaction strength U (at fixed Δ). We analyze the time-dependence of the absorbed energy in Sec. 4.3.2 and we study the structure of the transition matrix elements in Sec. 4.3.3. Then, in Sec. 4.4 we investigate the BOW and its neighboring phase transitions in the region $\Delta \sim U$. We demonstrate, using t-DMRG and bosonization techniques, that superlattice amplitude modulation spectroscopy reveals features of both the Ising (Sec. 4.4.1) and Kosterlitz-Thouless (Sec. 4.4.2) transitions signaling the presence of the BOW phase in contrast to the normal lattice amplitude modulation which fails to couple to the order parameter. In Sec. 4.5 we study the excitation spectrum in the Mott insulator at $\Delta < U$. We investigate the spin excitation spectrum in Sec. 4.5.1 and the charge excitation spectrum where excitations are naively created near $\sim (U \pm \Delta)$ in Sec. 4.5.2. Finally, we make connection to realistic experimental systems in Sec. 4.6, considering suitable parameter ranges and discussing the influence of finite temperatures or the presence of an external harmonic trapping potential.
The main results of this chapter are published in Ref. [84] and a more detailed account of the results is in preparation [152].

4.1 Absence of interaction

At zero interaction $U = 0$ (but finite Δ) the ionic Hubbard model becomes diagonal in quasimomentum space and the ground state is given by a genuine band insulator with equal spin and charge gaps. Each low

[1] In all analytical calculations we consider a lattice of *A*-*B* configuration as sketched in Fig. 4.1 and given by Eq. (2.29). In t-DMRG we have implemented a lattice of *B*-*A* configuration which is a redefinition of the lattice but this has no effect on the time evolution of energy which is a global observable.

energy site is doubly occupied while all other sites are empty. The response to normal and superlattice amplitude modulation can be calculated exactly, giving an intuitive picture of the excitations created which is instructive as it gives a good flavor of the situation at weak but finite interactions $\Delta \gg U$. The non-interacting model is given by Eq. (2.29) with $U = 0$. One can pass to quasimomentum space by using the Fourier transform

$$c_{lA\sigma} = \sqrt{\frac{2}{L}} \sum_q e^{iql2a} c_{qA\sigma}, \tag{4.1}$$

and likewise for $c_{lB\sigma}$ where $2a$ is the size of the unit cell and $q = 2\pi m/aL$, $m = -L/4 + 1, ..., L/4$, is the quasimomentum in the first Brillouin zone (BZ) $]-\pi/2a, \pi/2a]$. Using $\sum_{l=1}^{L/2} e^{2ial(q-q')} = (L/2) \times \delta_{q,q'}$, one obtains

$$H = \sum_{q,\sigma} \begin{pmatrix} c^\dagger_{qA\sigma} & c^\dagger_{qB\sigma} \end{pmatrix} F_q \begin{pmatrix} c_{qA\sigma} \\ c_{qB\sigma} \end{pmatrix}, \tag{4.2}$$

where

$$F_q = \begin{pmatrix} \Delta/2 & -J\left(1 + e^{-2iqa}\right) \\ -J\left(1 + e^{2iqa}\right) & -\Delta/2 \end{pmatrix}. \tag{4.3}$$

The Hamiltonian can now be diagonalized,

$$H = \sum_{q,\sigma} \begin{pmatrix} \alpha^\dagger_{q,\sigma} & \beta^\dagger_{q,\sigma} \end{pmatrix} D_{F_q} \begin{pmatrix} \alpha_{q,\sigma} \\ \beta_{q,\sigma} \end{pmatrix} = \sum_{q,\sigma} E_q \left(\beta^\dagger_{q,\sigma}\beta_{q,\sigma} - \alpha^\dagger_{q,\sigma}\alpha_{q,\sigma}\right), \tag{4.4}$$

where

$$D_{F_q} = S^\dagger F_q S = \begin{pmatrix} -E_q & 0 \\ 0 & E_q \end{pmatrix}, \qquad \begin{pmatrix} \alpha_{q,\sigma} \\ \beta_{q,\sigma} \end{pmatrix} = S^\dagger \begin{pmatrix} c_{qA\sigma} \\ c_{qB\sigma} \end{pmatrix}. \tag{4.5}$$

The transformation S is given by

$$S = \begin{pmatrix} -\left(\Delta - 2E_q\right) \Big/ \left(N_1(J,q) 2J(1 + e^{2iaq})\right) & -\left(\Delta + 2E_q\right) \Big/ \left(N_2(J,q) 2J(1 + e^{2iaq})\right) \\ 1/N_1(J,q) & 1/N_2(J,q) \end{pmatrix}, \tag{4.6}$$

with

$$N_1(J,q)^2 = 1 + \frac{(\Delta - 2E_q)^2}{8J^2(1 + \cos(2qa))}, \text{ and } N_2(J,q)^2 = 1 + \frac{(\Delta + 2E_q)^2}{8J^2(1 + \cos(2qa))}. \tag{4.7}$$

There are two energy bands $\pm E_q$ given by

$$E_q = \frac{1}{2}\sqrt{\Delta^2 + 8J^2(1 + \cos(2qa))}, \tag{4.8}$$

which are separated by an energy difference $\delta E_q = 2E_q$ and shown in Fig. 4.2(a).
The new operators $\beta^{(\dagger)}_{q,\sigma}$ and $\alpha^{(\dagger)}_{q,\sigma}$ annihilate (create) a quasiparticle in the upper or lower band respectively with quasimomentum q and spin σ. The energy difference is minimum at the BZ border, i.e. the gap is given by $\delta E_{q=\pi/2a} = \Delta$, and it is maximum in the center of the BZ, $\delta E_{q=0} = \sqrt{\Delta^2 + 16J^2}$. In the ground

state at half-filling the lower band is completely filled whereas the upper band is completely empty such that the system is band insulating with equal charge and spin gaps given by Δ. The ground state is given by

$$|\mathrm{BI}\rangle_{U=0} = \prod_{q\in\mathrm{BZ},\sigma} \alpha^\dagger_{q,\sigma}|0\rangle, \tag{4.9}$$

where $|0\rangle$ denotes the vacuum of quasiparticles.

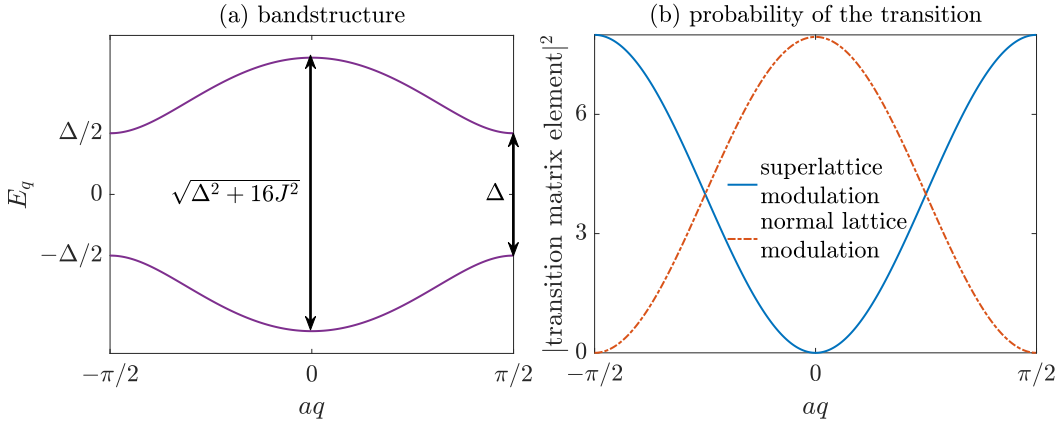

Figure 4.2: (a) Sketch of the band structure of the ionic Hubbard model at zero interaction. (b) The transition matrix element squared at $\Delta = 50J$ and zero interaction as a response to superlattice modulation (blue solid line) and to normal lattice amplitude modulation (dash-dotted orange line).

The perturbing operator $\hat{O}_S$ (2.41) corresponding to the superlattice modulation analogously transforms as

$$\hat{O}_S = \sum_{q,\sigma} \frac{2iE_q \tan(qa)}{JN_1(J,q)N_2(J,q)} \left(\alpha^\dagger_{q,\sigma}\beta_{q,\sigma} - \mathrm{H.c.}\right). \tag{4.10}$$

As the ground state $|\mathrm{BI}\rangle_{U=0}$ (4.9) is known, the complex susceptibility (3.24) within linear response can be straightforwardly calculated as

$$\chi(t) = -\frac{i}{\hbar}\theta(t)\left\langle\left[\hat{O}_S(t)), \hat{O}_S(0)\right]\right\rangle_0 = -\frac{i}{\hbar}\theta(t)\sum_q 8\sin^2(qa)\left(e^{-2iE_qt/\hbar} - e^{2iE_qt/\hbar}\right), \tag{4.11}$$

where we used the Heisenberg representation $\hat{O}_S(t) = \exp\left(i\hat{H}t/\hbar\right)\hat{O}_S \exp\left(-i\hat{H}t/\hbar\right)$ which can be expressed in terms of the time-dependence of the annihilation operators as

$$\alpha_{q,\sigma}(t) = e^{iE_qt/\hbar}\alpha_{q,\sigma}, \qquad \beta_{q,\sigma}(t) = e^{-iE_qt/\hbar}\beta_{q,\sigma}, \tag{4.12}$$

obtained from Heisenberg's equation of motion. We obtain the imaginary part of the complex susceptibility at positive frequencies

$$\mathrm{Im}\chi(\omega) = -8\sum_q \sin^2(qa)\frac{\eta}{\eta^2 + (\hbar\omega - 2E_q)^2} = -8\pi\sum_q \sin^2(qa)\delta(\hbar\omega - 2E_q), \tag{4.13}$$

which determines the averaged energy absorption rate $\overline{dE}/dt \sim -\omega\mathrm{Im}\chi(\omega)$ (3.27). Note that the spin index has transformed into a simple factor 2. The obtained energy absorption rate is shown in Fig. 4.3(a).

It shows enhanced absorption at the possible minimum excitation energy $\hbar\omega_{\min} = \Delta$ corresponding to the BZ edge $q = \pi/2a$. It decays across the resonant region and it is very small at the possible maximum excitation energy $\hbar\omega_{\max} = \sqrt{\Delta^2 + 16J^2}$ which corresponds to the BZ center $q = 0$. This behavior corresponds to the behavior of the transition matrix element squared $\sim \sin^2(qa)$ being zero in the BZ zone center and finite at the BZ zone border, see Fig. 4.2(b).

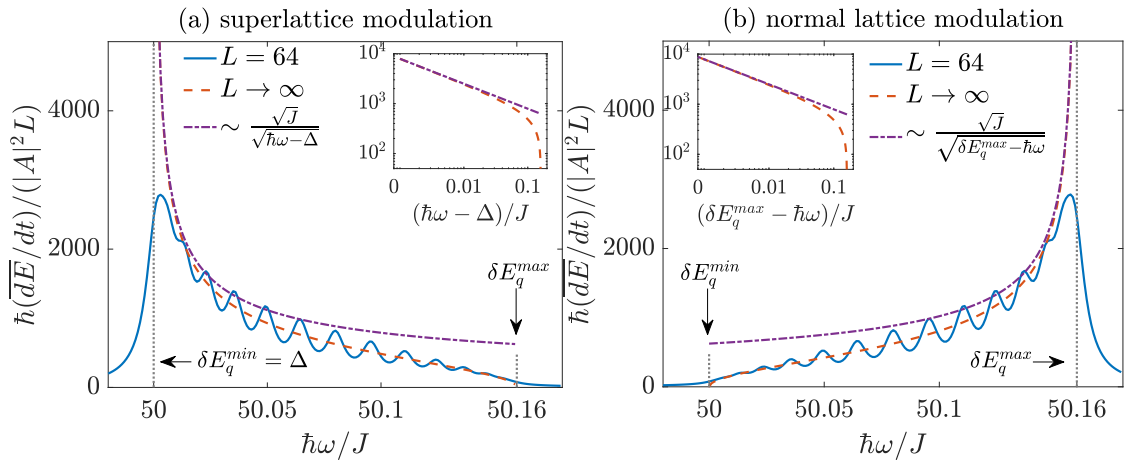

Figure 4.3: The energy absorption rate at $\Delta = 50J$ and zero interaction and for an amplitude of the modulation $A = 0.001J$ (a) as a response to superlattice amplitude modulation and (b) as a response to normal lattice amplitude modulation. The averaged rate (blue solid line) for a broadening $\eta = 0.005J$ is shown in comparison to the continuum limit result (orange dashed line) and the first order expansion (purple dashed line) at the location of the infinite system size divergence. Vertical dashed lines indicated the gap $\delta E_q^{\min} = \Delta = 50J$ and the maximum possible excitation energy $\delta E_q^{\max} = \sqrt{\Delta^2 + 16J^2} = 50.16J$. Inset: The first order expansion $\sim (J/(\hbar\omega - \Delta))^{1/2}$ or $\sim \left(J/(\delta E_q^{\max} - \hbar\omega)\right)^{1/2}$ respectively, behaves like the continuum limit result near the divergence. Farther away from the divergence it decays with an exponent $> 1/2$.

We take the continuum limit $L \to \infty$ by replacing $\sum_q \to (La)/(2\pi) \int_{-\pi/2a}^{\pi/2a} \mathrm{d}q$ and using $\int \mathrm{d}q f(q)\delta(g(q)) = \sum_i f(q_i)/|g'(q_i)|$ where the sums runs over all zeros q_i of $g(q)$ within the first Brillouin zone. This yields

$$\frac{1}{L}\frac{\overline{dE}}{dt} = \frac{\omega}{2}|A|^2 \frac{(\hbar\omega)(\Delta^2 + 16J^2 - (\hbar\omega)^2)}{16J^4 \sqrt{1 - \left(\frac{(\hbar\omega)^2 - \Delta^2 - 8J^2}{8J^2}\right)^2}}, \tag{4.14}$$

which is also shown in Fig. 4.3(a). An expansion around the divergence at $\hbar\omega_{\min} = \Delta$ yields

$$\frac{\hbar}{L|A|^2}\frac{\overline{dE}}{dt} = \tilde{A}\frac{1}{\sqrt{\hbar\omega - \Delta}} + \tilde{B}\sqrt{\hbar\omega - \Delta} + O(\hbar\omega - \Delta)^{3/2} \tag{4.15}$$

with $\tilde{A} = \Delta\sqrt{2\Delta}/J$, $\tilde{B} = -\sqrt{\Delta}(\Delta^2 - 28J^2)/(8\sqrt{2}J^3)$. The lowest order expansion is also shown in Fig. 4.3(a) and it coincides well with the full continuum limit result near the divergence. Away from the divergence, the full result decays faster, i.e. $\sim (\hbar\omega - \Delta)^{-\alpha}$ with $\alpha > 1/2$.
We now compare to the case of a normal lattice amplitude modulation. The perturbing operator $\hat{O}_N$ (2.40)

corresponding to the normal amplitude modulation analogously transforms to

$$\hat{O}_N = \sum_{q,\sigma} \frac{4J\cos^2(qa)}{E_q}\left(\alpha^\dagger_{q,\sigma}\alpha_{q,\sigma} - \beta^\dagger_{q,\sigma}\beta_{q,\sigma}\right) + \frac{\Delta\cos qa}{E_q}\left(\beta^\dagger_{q,\sigma}\alpha_{q,\sigma} + \text{H.c.}\right). \tag{4.16}$$

Similar to the superlattice case, we determine the imaginary part of the complex susceptibility at positive frequencies which we find to be

$$\text{Im}\chi(\omega) = -2\pi\sum_q \frac{\Delta^2\cos^2(qa)}{E_q^2}\delta(\hbar\omega - 2E_q) = -2\sum_q \frac{\Delta^2\cos^2(qa)}{E_q^2}\frac{\eta}{\eta^2 + (\hbar\omega - 2E_q)^2}. \tag{4.17}$$

The probability of transferring a particle from the lower band to the upper band by the normal lattice perturbation is proportional to $\Delta^2\cos^2(qa)/E_q^2$ which is approximately $\sim \cos^2(qa)$ for $\Delta >> J$. It is maximum in the BZ zone center (corresponding to maximum excitation energy) and zero at the BZ zone boundary (minimum energy), see Fig. 4.2(b). Accordingly, the response peaks at maximum excitation energy corresponding to the BZ center and is very small at the minimum energy corresponding to the BZ zone boundary, see Fig. 4.3(b). This behavior is opposite to the superlattice modulation case. Taking the continuum limit yields

$$\frac{1}{L}\frac{\overline{dE}}{dt} = \frac{\omega}{2}|A|^2\frac{\Delta^2}{2J^2\hbar\omega}\sqrt{\frac{(\hbar\omega)^2 - \Delta^2}{16J^2 - (\hbar\omega)^2 + \Delta^2}}, \tag{4.18}$$

which is also shown in Fig. 4.3(b). Again, expanding around the divergence which is now located at $\hbar\omega_{\text{min}} = \sqrt{\Delta^2 - 16J^2}$, yields

$$\frac{\hbar}{LA^2}\frac{\overline{dE}}{dt} \approx \tilde{A}\frac{1}{\sqrt{-\left(\hbar\omega - \sqrt{\Delta^2 - 16J^2}\right)}}, \tag{4.19}$$

in lowest order, with $\tilde{A} = \Delta^2/[\sqrt{2}J(\Delta^2 + 16J^2)^{1/4}]$. Again, this coincides well with the full continuum limit result near the divergence, see Fig. 4.3(b).

4.2 Derivation of an effective Hamiltonian for $J \ll |U - \Delta|, \Delta$

At finite interaction, the ionic Hubbard model can no longer be solved exactly. In this section we derive an effective model in the limit $J \ll |U - \Delta|, \Delta$ which enables us to analytically describe the gapped part of the energy absorption spectrum as a response to superlattice modulation. Starting with a short motivation, we then derive the Hamiltonian which is general in the considered limit. We then consider the band and Mott insulating limits in Secs. 4.2.1 and 4.2.2 respectively where the effective model applies to the gapped spectra. We define a suitable basis in order to diagonalize the corresponding Hamiltonian matrix. This section is rather technical. We derive the effective model and characterize its eigenspectrum but no results for the energy absorption rate are given. A discussion of the obtained energy absorption rate follows in the subsequent sections 4.3 and 4.5.2 in direct comparison to our t-DMRG calculations for the band and Mott insulators respectively.

First order hopping processes change the system's energy by $|\delta E| = \Delta, |\Delta - U|, (\Delta + U)$ depending on the initial occupation of a given state. For $J \ll |\Delta - U|, \Delta$ (this also implies $J \ll \Delta + U$) the

Hamiltonian naturally divides the Hilbert space into different sectors that are separated by the energies $|\delta E|$ and coupled by an energy $J \ll |\delta E|$. This is the case in the band insulating limit $\Delta \gg U$ and in the Mott insulating limit $\Delta \ll U$ at large $\Delta \gg J$. If we are interested in the low-energy dynamics in a sector at fixed δE, we can include the couplings to other sectors perturbatively. This will serve us to describe the fluctuations in the lowest band of charge excitations by superlattice modulation. The effective Hamiltonian can be obtained by employing a unitary transformation and the matrix elements of the effective Hamiltonian will be given by $\sim J^2/|\delta E|$. A prominent example is the Schrieffer-Wolff transformation which was originally introduced to derive the Kondo Hamiltonian from the Anderson Hamiltonian [153]. An application of relevance in the context of ultracold fermions in optical lattices is the derivation of the Heisenberg model from the Hubbard model [154].
Within the basis of the lowest band of excitations the effective Hamiltonian can be diagonalized numerically and the bandwidth of the eigensystem describes the width of the lowest charge excitation peak in the energy absorption rate within linear response. The transition matrix elements from the ground state to the lowest band of excitations by superlattice modulation determine the shape of the peak. In the band insulating limit, where the perfect ground state consists of doubly occupied B-sites and empty A-sites, the lowest band of excitations is located around energies $\sim (\Delta - U)$ and naively corresponds to breaking one doublon on a B-site and transferring one particle to a neighboring A-site (cf. Fig. 2.6(c)). In the Mott insulating limit, where the groundstate consists of one particle per site, the lowest band of charge excitations is located around energies $\sim (U - \Delta)$ and naively corresponds to the creation of one doublon on a B-site and one hole on an A-site (cf. Fig. 2.6(c)).

A suitable procedure to obtain the unitary transformation which we follow is presented in Ref. [155]. The main steps, applied to the ionic Hubbard model, are given in the following. We separate the kinetic part H_K (2.30) into terms that either change (by one) or conserve the number of doubly occupied sites on A-sites and/or B-sites,

$$H_K = (A_{00} + B_{00}) + (A_{+-} + B_{-+}) + (A_{+0} + B_{-0}) + (A_{0-} + B_{0+}), \tag{4.20}$$

where the notation $X_{m_A m_B}$ is such that a fermion hops onto a site $X = A$ or B with m_A and m_B the change in the number of doublons on A and B-sites by one and $(+ = 1)$, $(- = -1)$, with

$$A_{00} = B_{00}^\dagger = -J \sum_{l\sigma} (h_{lA\bar{\sigma}}\, c_{lA\sigma}^\dagger\, c_{lB\sigma}\, h_{lB\bar{\sigma}} + h_{l+1A\bar{\sigma}}\, c_{l+1A\sigma}^\dagger\, c_{lB\sigma}\, h_{lB\bar{\sigma}}), \tag{4.21}$$

$$A_{+0} = B_{-0}^\dagger = -J \sum_{l\sigma} (n_{lA\bar{\sigma}}\, c_{lA\sigma}^\dagger\, c_{lB\sigma}\, h_{lB\bar{\sigma}} + n_{l+1A\bar{\sigma}}\, c_{l+1A\sigma}^\dagger\, c_{lB\sigma}\, h_{lB\bar{\sigma}}), \tag{4.22}$$

$$A_{0-} = B_{0+}^\dagger = -J \sum_{l\sigma} (h_{lA\bar{\sigma}}\, c_{lA\sigma}^\dagger\, c_{lB\sigma}\, n_{lB\bar{\sigma}} + h_{l+1A\bar{\sigma}}\, c_{l+1A\sigma}^\dagger\, c_{lB\sigma}\, n_{lB\bar{\sigma}}), \tag{4.23}$$

$$A_{+-} = B_{-+}^\dagger = -J \sum_{l\sigma} (n_{lA\bar{\sigma}}\, c_{lA\sigma}^\dagger\, c_{lB\sigma}\, n_{lB\bar{\sigma}} + n_{l+1A\bar{\sigma}}\, c_{l+1A\sigma}^\dagger\, c_{lB\sigma}\, n_{lB\bar{\sigma}}), \tag{4.24}$$

where $h_{l,\sigma} = 1 - n_{l,\sigma}$ and with $A_{m_A m_B}^\dagger = B_{m_B m_A}$ and $\bar{\sigma}$ denotes the opposite spin configuration with respect to σ. We seek a unitary transformation that eliminates all processes which couple different sectors separated by the energies δE, i.e. we need to conserve the number of doubly occupied sites as well as the number of singly occupied sites on both, A- and B-sites. None of the $X_{m_A m_B}$ conserves both such that all terms of H_K have to be eliminated. Generally, the unitary transformation S is given by

$$H' = e^{iS} H e^{-iS} = H + \frac{[iS, H]}{1!} + \frac{[iS, [iS, H]]}{2!} + \ldots. \tag{4.25}$$

We construct S such that it fulfills $i[S,V] = -H_K$ where V (2.31) is the interaction and potential part of the ionic Hamiltonian and, using $[V, B_{m_A m_B}] = \Delta\,(U/\Delta\,(m_A+m_B)-1)\,B_{m_A m_B}$ and $[V, A_{m_A m_B}] = \Delta\,(U/\Delta\,(m_A+m_B)+1)\,A_{m_A m_B}$, we obtain

$$iS = \frac{1}{\Delta}\Big((A_{+-}-B_{-+}) + \frac{1}{U_-}(A_{0-}-B_{0+}) + \frac{1}{U_+}(A_{+0}-B_{-0}) + (A_{00}-B_{00})\Big), \tag{4.26}$$

with $U_- = 1 - U/\Delta$ and $U_+ = 1 + U/\Delta$. Consequently, to first order in the $J^2/|\delta E|$, the effective Hamiltonian becomes

$$H_{\text{eff}} = V + \frac{1}{\Delta}([A_{00},B_{00}] + [A_{+-},B_{-+}] + \frac{1}{U_-}[A_{0-},B_{0+}] + \frac{1}{U_+}[A_{+0},B_{-0}]). \tag{4.27}$$

It conserves separately the number of doublons on sites A and B as well as the number of singly occupied A- and B-sites. We consider H_{eff} in the basis of the lowest band of excitations in order to describe the low-energy charge physics in this sector.
In the band insulating limit it turns out to be a powerful tool as it succeeds in precisely describing the location, width and shape of the excitation spectrum which is discussed in Sec. 4.3. In the Mott insulating limit it correctly captures the main features such as location and approximate width which is discussed in Sec. 4.5.

4.2.1 Application to the band insulating limit

In this section, we consider the effect of H_{eff} (4.27) on the lowest band of excitations by superlattice modulation in the band insulator. We assume a genuine band insulator, i.e. the ground state is given by,

$$|BI\rangle = \left(\prod_{n=1}^{L/2} c^\dagger_{nB\uparrow}\, c^\dagger_{nB\downarrow}\right)|0\rangle, \tag{4.28}$$

where all B-sites are doubly occupied and all A-sites are empty, $|0\rangle$ denotes the vacuum. In first order, superlattice modulation of the lattice, i.e. the application of $\hat{O}_S$ (2.41) onto $|BI\rangle$, breaks doublons on B-sites by transferring one particle to a neighboring A-site at an energy difference $(\Delta - U)$ with respect to the ground state. The corresponding (first) band of excitations is composed of linear combinations of all states that consist of a background of $(L/2-1)$ doubly occupied (empty) $B(A)$-sites and two fermions of opposite spin on an arbitrary B-site and A-site. We choose open boundary conditions and define the $2(L/2)^2$-degenerate basis of this energy sector as

$$|l,A,\sigma;d,B,\bar{\sigma}\rangle = \left(\prod_{n=1}^{l-1} c^\dagger_{nB\uparrow}\, c^\dagger_{nB\downarrow}\right) c^\dagger_{lA\sigma} \left(\prod_{m=l}^{l+d-1} c^\dagger_{mB\uparrow}\, c^\dagger_{mB\downarrow}\right) c^\dagger_{l+dB\bar{\sigma}} \left(\prod_{r=l+d+1}^{L/2} c^\dagger_{rB\uparrow}\, c^\dagger_{rB\downarrow}\right)|0\rangle, \tag{4.29}$$

where the singly occupied A-site at position l occurs before the singly occupied B-site at position $l+d$, $l \in (1, L/2)$ and $d \in (0, L/2-l)$, and

$$|l,B,\sigma;d,A,\bar{\sigma}\rangle = \left(\prod_{n=1}^{l-1} c^\dagger_{nB\uparrow}\, c^\dagger_{nB\downarrow}\right) c^\dagger_{lB\sigma} \left(\prod_{m=l+1}^{l+d-1} c^\dagger_{mB\uparrow}\, c^\dagger_{mB\downarrow}\right) c^\dagger_{l+dA\bar{\sigma}} \left(\prod_{r=l+d}^{L/2} c^\dagger_{rB\uparrow}\, c^\dagger_{rB\downarrow}\right)|0\rangle, \tag{4.30}$$

where the singly occupied B-site at position l occurs before the singly occupied A-site at position $l+d$, $l \in (1, L/2-1)$ and $d \in (1, L/2-l)$. An application of H_{eff} (4.27) to the above continuum of states

virtually couples to other energy sectors separated by an energy $\delta E = \Delta, \pm(\Delta - U), (\Delta + U)$ from the first band of excitations. The action of each term of H_{eff} onto the continuum of states is described in detail in the following and the different sectors and processes are visualized in Fig. 4.4(a).

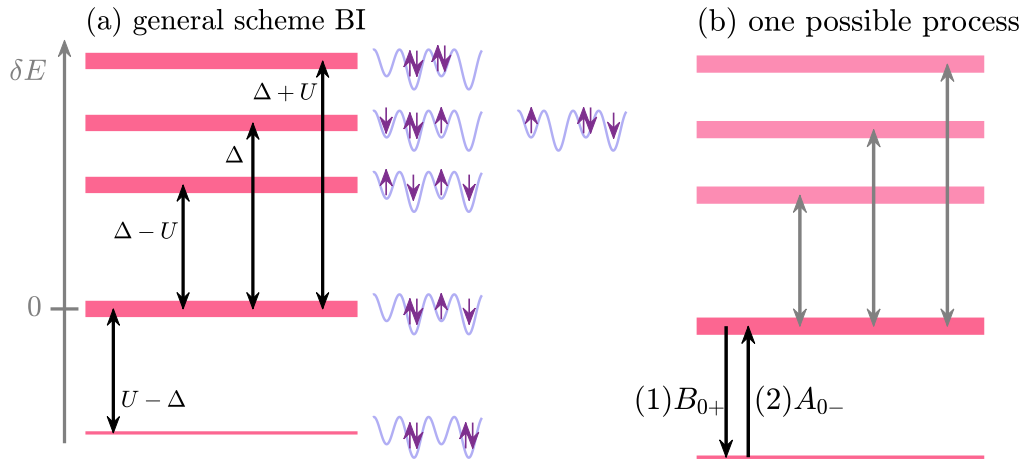

Figure 4.4: (a) Sketch of the general scheme of the effective model acting on the lowest band of excitation in the band insulator (BI). The different energy sectors (pink horizontal bars) contributing to the effective model are displayed together with the energy differences δE with respect to the lowest band of excitations (indicated by black vertical double arrows). The four-site lattices next to the bands show a possible basis state (on four sites) of each subspace. The double arrows indicate the different virtual processes contributing to the effective Hamiltonian. One possible process is sketched in more detail in (b). The sketch corresponds the term $(1/(\Delta U_-))A_{0-}B_{0+}$ in the effective Hamiltonian (4.27). First (1), the application of B_{0+} to the lowest band of excitations transfers the system to the band insulating ground state. The subsequent (2) application of A_{0-} transfers the system back from the ground state to the first band of excitations. The energy corresponding to this process is $\sim J^2/|\Delta U_-| = J^2/|\Delta - U|$.

- $\delta E =\sim -(\Delta - U)$: The term $(1/(\Delta U_-))A_{0-}B_{0+}$ virtually couples to the band insulating ground state. As an example this process is sketched in Fig.4.4(b).

- $\delta E =\sim (\Delta - U)$: The term $-(1/(\Delta U_-))B_{0+}A_{0-}$ virtually couples to the next (second) band of excitations which consists of a background of $(L/2 - 2)$ doubly occupied (empty) $B(A)$-sites and four fermions (two of each spin) on two arbitrary B-sites and two arbitrary A-sites.

- $\delta E =\sim \Delta$: The terms $-(1/\Delta)B_{00}A_{00}$ and $-(1/\Delta)B_{-+}A_{+-}$ virtually couple to the third band of excitations which consists of two classes of states.

  The term $-(1/\Delta)B_{00}A_{00}$ couples to states that consist of a background of $(L/2 - 1)$ doubly occupied B-sites and two fermions of opposite spin on arbitrary A-sites.

  The term $-(1/\Delta)B_{-+}A_{+-}$ couples to states that consist of a background of $(L/2 - 2)$ doubly occupied B-sites, two fermions of opposite spin on two arbitrary B-sites and one doubly occupied A-site.

- $\delta E =\sim (\Delta + U)$: The term $-(1/(\Delta U_+))B_{-0}A_{+0}$ virtually couples to the fourth band of excitations which consists of one doubly occupied A-site and a background of $(L/2 - 1)$ doubly occupied B-sites

- The terms $(1/\Delta)A_{00}B_{00}$, $(1/\Delta)A_{+-}B_{-+}$ and $(1/(\Delta U_+))A_{+0}B_{-0}$ give zero.

The renormalized ground state energy within the effective model becomes

$$E_{0,\text{eff}} = \langle BI|H_{\text{eff}}|BI\rangle = \frac{L}{2}(U-\Delta) - \frac{J^2}{\Delta - U}2(L-1), \tag{4.31}$$

where the first term corresponds to the ground state energy of H_0 (2.29). We numerically diagonalize H_{eff} (4.27) within the basis consisting of the closed subset of states given by Eqs. (4.29) and (4.30) and obtain $2(L/2)^2$ eigenstates $|\alpha\rangle$ with corresponding eigenvalues ϵ_α. The obtained band structure is displayed in Fig. 4.5(a). We find that the bandwidth is approximately constant with system size L for sufficiently large systems, see Fig. 4.5(b).

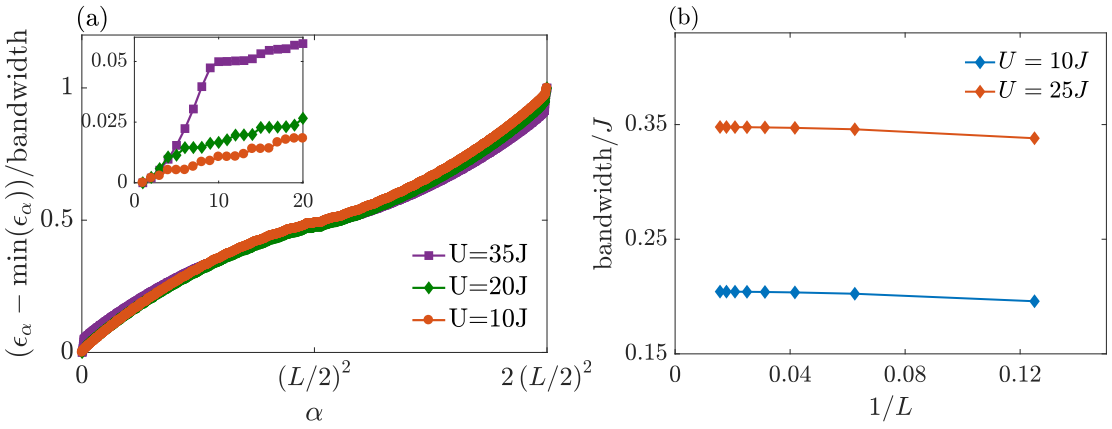

Figure 4.5: (a) Band structure of the effective model at $\Delta = 50J$ for a system size $L = 64$ and different U. Inset: Zoom into the band structure, showing the first few eigenvalues. The lowest (and highest) eigenvalues are very discrete in energy compared to the bulk. (b) The system size dependence of the bandwidth at $\Delta = 50J$, $U = 10J,\ 25J$. The bandwidth is approximately constant with system size for large L.

We find that the bandwidth scales approximately as $J^2/(\Delta - U)$ (see Fig. 4.6(a)) which matches our expectations as the term of amplitude $\sim J^2/(\Delta - U)$ is the dominating term in H_{eff} as $\Delta - U < \Delta < \Delta + U$ in the band insulator. Furthermore, we find that the lowest eigenvalue $\min(\epsilon_\alpha) - E_{0,\text{eff}} - (\Delta - U)$ scales approximately as $\left(J^2/(\Delta - U) - J^2/\Delta\right)$ (see Fig. 4.6(b)) and the largest eigenvalue $\max(\epsilon_\alpha) - E_{0,\text{eff}} - (\Delta - U)$ scales approximately as $\left(J^2/(\Delta - U) - J^2/(4\Delta)\right)$ (see Fig. 4.6(c)). We expect further corrections, possibly in $1/L$.

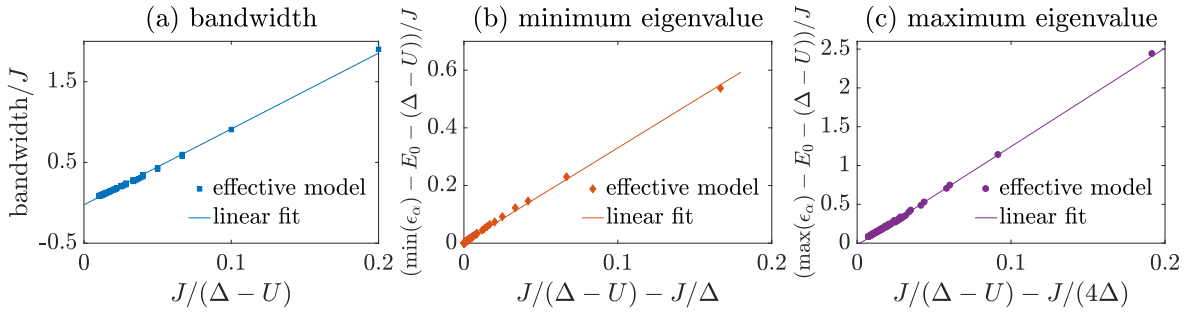

Figure 4.6: The bandwidth (a) as well as the minimum (b) and maximum (c) eigenvalue for a system size $L = 64$ for different $\Delta > U$, $U/J = 0,\ 1,\ 2,\ 3,\ 4,\ 5,\ 10,\ 15,\ 20,\ 25$, $\Delta/J = 30,\ 40,\ 50,\ 60,\ 70,\ 80,\ 90,\ 100$.

Within the obtained eigensystem we can calculate the transition matrix elements $|\langle BI|\hat{O}_S|\alpha\rangle|^2$ where $\hat{O}_S$ is the perturbing operator (2.41) and deduce analytical expressions of the absorbed energy and the energy

absorption rate within linear response theory using Eqs. (3.32) and (3.31) (cf. Sec. 3.2.2), respectively, where the ground state is given by the band insulating ground state $|BI\rangle$ (4.28) and the sum over the many-body state $|m\rangle$ runs over all eigenstates $|\alpha\rangle$ of the effective model and $E_m = \epsilon_\alpha$. We study energy absorption in comparison to our numerical t-DMRG results in Sec. 4.3.1 and we find excellent agreement. In particular, the effective model serves to explain finite size effects observed in the energy absorption and a thorough study of the transition matrix elements enables us to connect the different features in the response to the different processes between energy sectors.

4.2.2 Application to the Mott insulating limit

In this section, we consider the effect of H_{eff} (4.27) on the lowest band of charge excitations by superlattice modulation in the Mott insulator. The ground and excited states are intrinsically different to the band insulating case but the concept is the same and less details will be given here. In the Mott insulating ground state each site is occupied by one particle. Here, we assume a classical antiferromagnetic ground state,

$$|AFM\rangle \quad = \quad |\uparrow\downarrow\uparrow\downarrow \ldots \uparrow\downarrow\rangle = \left(\prod_{n=1}^{L/2} c^\dagger_{nA\uparrow}\, c^\dagger_{nB\downarrow}\right)|0\rangle. \tag{4.32}$$

In reality, this is clearly not the quantum mechanical ground state as quantum fluctuations lead to a reduction of the staggered magnetization and this effect is is particularly strong in one dimension. However, we use this state as a first approximation here since it turns out to yield reasonable results for the energy absorption rate as a response to superlattice modulation despite the crudeness of the approximation. In this case, superlattice modulation of the lattice in first order creates a doublon on a B-site (A-site) and a hole on a neighboring A-site (B-site) at an energy difference $U-\Delta$ ($U+\Delta$) with respect to the ground state. We comment on the validity of this approximations in Sec. 4.5.2 when we discuss the results of the effective model. We only study the subspace located at an energy difference $(U-\Delta)$ (one can consider the subspace at energy difference $(U+\Delta)$ analogously). The corresponding (first) band of charge excitations is composed of linear combinations of all states that consist of a doublon on a B-site and a hole on an A-site with an antiferromagnetic background (the spin configuration of the antiferromagnetic background is considered the same as in the ground state). We again choose open boundary conditions and define the $(L/2)^2$-degenerate basis of this energy sector as

$$|l,A,0;d,B,D\rangle = \left(\prod_{n=1}^{l-1} c^\dagger_{nA\uparrow} c^\dagger_{nB\downarrow}\right) c^\dagger_{lB\uparrow} \left(\prod_{m=l+1}^{l+d-1} c^\dagger_{mA\downarrow} c^\dagger_{mB\uparrow}\right) c^\dagger_{l+dA\downarrow} \left(c^\dagger_{l+dB\uparrow} c^\dagger_{l+dB\downarrow}\right) \left(\prod_{r=l+d+1}^{L/2} c^\dagger_{rA\uparrow} c^\dagger_{rB\downarrow}\right)|0\rangle, \tag{4.33}$$

where the hole comes first with $l \in (1, L/2)$ and $d \in (1, L/2-l)$, and for $d=0$,

$$|l,A,0;d=0,B,D\rangle \quad = \quad \left(\prod_{n=1}^{l-1} c^\dagger_{nA\uparrow}\, c^\dagger_{nB\downarrow}\right) \left(c^\dagger_{lB\uparrow} c^\dagger_{lB\downarrow}\right) \left(\prod_{r=l+1}^{L/2} c^\dagger_{rA\uparrow}\, c^\dagger_{rB\downarrow}\right)|0\rangle, \tag{4.34}$$

and,

$$|l,B,D;d,A,0\rangle = \left(\prod_{n=1}^{l-1} c^\dagger_{nA\uparrow} c^\dagger_{nB\downarrow}\right) c^\dagger_{lA\uparrow} \left(c^\dagger_{lB\uparrow} c^\dagger_{lB\downarrow}\right) \left(\prod_{m=l+1}^{l+d-1} c^\dagger_{mA\downarrow} c^\dagger_{mB\uparrow}\right) c^\dagger_{l+dB\downarrow} \left(\prod_{r=l+d+1}^{L/2} c^\dagger_{rA\uparrow} c^\dagger_{rB\downarrow}\right)|0\rangle, \tag{4.35}$$

if the doublon comes first with $l \in (1, L/2-1)$ and $d \in (1, L/2-l)$. Here, an application of H_{eff} (4.27) to the above continuum of states virtually couples to other energy sectors separated by an energy $\delta E = \Delta, \pm(U-\Delta), (\Delta+U)$ from the first band of excitations. Note, that the energy gaps are the same as in the band insulating case but the state vectors are different and therefore also the action of H_{eff} onto the continuum of states. The different processes are in detail described in the following and the different sectors and processes are visualized in Fig. 4.7(a).

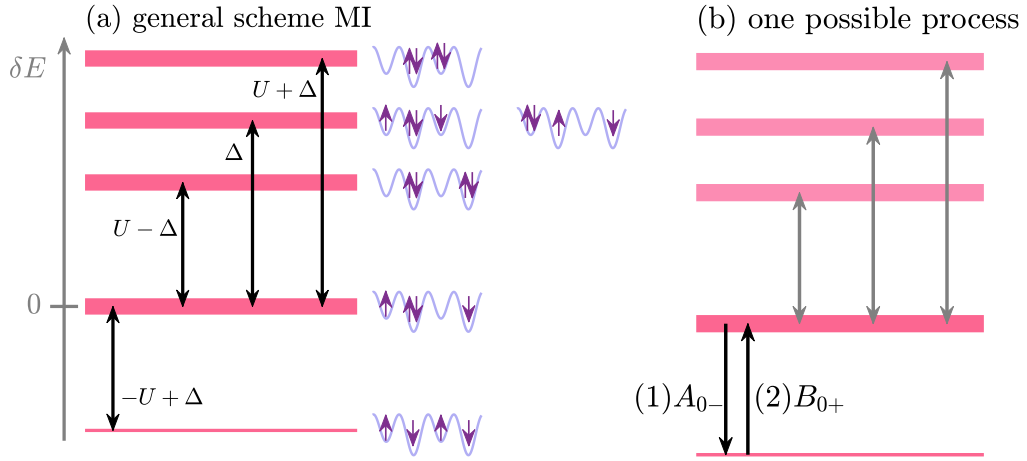

Figure 4.7: (a) Sketch of the general scheme of the effective model acting on the lowest band of excitation in the Mott insulator (MI). The different energy sectors (pink horizontal bars) contributing to the effective model are displayed together with the energy differences δE with respect to the lowest band of excitations (indicated by black vertical double arrows). The four-site lattices next to the bands show a possible basis state (on four sites) of each subspace. The double arrows indicate the different virtual processes contributing to the effective Hamiltonian. One possible process is sketched in more detail in (b). The sketch corresponds the term $(1/(\Delta U_-))B_{0+}A_{0-}$ in the effective Hamiltonian (4.27). First (1), the application of A_{0-} to the lowest band of excitations transfers the system to the antiferromagnetic ground state. The subsequent (2) application of B_{0+} transfers the system back from the ground state to the first band of excitations. The energy corresponding to this process is $\sim J^2/|\Delta U_-| = J^2/|\Delta - U|$.

- $\underline{\delta E =\sim -(U-\Delta)}$: The term $-(1/(\Delta U_-))B_{0+}A_{0-}$ virtually couples to the antiferromagnetic ground state. As an example this process is sketched in Fig.4.7(b).

- $\underline{\delta E =\sim (U-\Delta)}$: The term $(1/(\Delta U_-))A_{0-}B_{0+}$ virtually couples to the next (second) band of excitations which consists of two doublons on B-sites and two holes on A-sites with an antiferromagnetic background.

- $\underline{\delta E =\sim \Delta}$: The terms $-(1/\Delta)B_{00}A_{00}$ and $-(1/\Delta)B_{-+}A_{+-}$ virtually couple to the third band of excitations which consists of two classes of states.

  The term $-(1/\Delta)B_{00}A_{00}$ couples to states that consist of one doublon on a B-site and one hole on a B-site with an antiferromagnetic background.

  The term $-(1/\Delta)B_{-+}A_{+-}$ couples to states that consist of one doublon on an A-site and one hole on an A-site with an antiferromagnetic background.

- $\underline{\delta E =\sim (\Delta+U)}$: The term $-(1/(\Delta U_+))B_{-0}A_{+0}$ virtually couples to the fourth band of excitations which consists of one doublon on a B-site, one doublon on an A-site, one hole on a B-site and one hole on an A-site with an antiferromagnetic background.

- The terms $(1/\Delta)A_{00}B_{00}$, $(1/\Delta)A_{+-}B_{-+}$ and $(1/(\Delta U_+))A_{+0}B_{-0}$ give zero.

The renormalized ground state energy becomes

$$E_{0,\text{eff}} = \langle GS|H_{\text{eff}}|GS\rangle = -J^2\,(L-1)\left(\frac{1}{U-\Delta}+\frac{1}{U+\Delta}\right). \tag{4.36}$$

In this case, numerical diagonalization of H_{eff} (4.27) within the closed subset of states given by Eqs. (4.33), (4.34) and (4.35) yields $(L/2)^2$ eigenstates $|\alpha\rangle$ with corresponding eigenvalues ϵ_α. We again find that the bandwidth is approximately constant with system size L for sufficiently large systems but the scaling behavior differs from the band insulating case. We find that the bandwidth scales approximately as $J^2/(U-\Delta)+J^2/\Delta$ which matches our expectations as either the term of amplitude $\sim J^2/(U-\Delta)$ is the dominating term in H_{eff} if $U-\Delta<\Delta$ or the term of amplitude $\sim J^2/\Delta$ is the dominating term in H_{eff} if $U-\Delta>\Delta$. Both cases are possible in the Mott insulating limit. The lowest eigenvalue $\min(\epsilon_\alpha)-E_{0,\text{eff}}-(U-\Delta)$ scales approximately as $\left(-J^2/2(\Delta+U)+J^2/\Delta\right)$ and the largest eigenvalue $\max(\epsilon_\alpha)-E_{0,\text{eff}}-(U-\Delta)$ scales approximately as $\left(J^2/2(\Delta+U)+J^2/(U-\Delta)\right)$. As in the band insulating case, we can study the energy absorption (3.31) and the time evolution of energy (3.32) within linear response. In Sec. 4.5.2 we study energy absorption in comparison to our numerical t-DMRG results which enables us to describe the main features of the observed response in some parameter ranges and a study of the transition matrix elements gives insight into the role of the different contributing processes.

4.3 Band insulating limit

In this section we study the energy absorption as a response to superlattice amplitude modulation on the band insulating side of the phase diagram. At fixed $\Delta = 50J$ we numerically determine the energy absorption within t-DMRG and compare to analytical results obtained within the effective model (cf. Sec. 4.2). In Sec. 4.3.1 we analyze the energy absorption rate deep in the band insulator $\Delta \gg U$ and for increasing U approaching the phase transition to the BOW phase. We find excellent agreement between t-DMRG and the effective model for $\Delta \gg U$ which persists for increasing interactions until the effective model ceases to describe well the results obtained using t-DMRG near the phase transition to the BOW phase at $\Delta \sim U$. We confirm that the charge gap closes when approaching the quantum phase transition. In Sec. 4.3.2 we then investigate in more detail the time evolution of the energy which enables us to identify finite-size effects while in Sec. 4.3.2 we analyze the structure of the transition matrix elements allowing us to explain the different observed features in the energy absorption rate.

In t-DMRG we study systems of sizes up to $L = 64$. In order to obtain sufficient accuracy in the absorbed energy $E(t)$ we keep a matrix dimension of $D = 120$. We conduct an error analysis by increasing the matrix dimension to 160 states. In the Trotter-Suzuki time evolution we set $J\tau = 0.001\hbar$ and we use $J\tau = 0.0005\hbar$ to perform the error analysis. We determine the maximal uncertainties in the energy absorption rate due to the matrix dimension, the time step and the variation of the fit range (see App. A for details). The error bars are provided in the figures.

4.3.1 Energy absorption

On resonance, a linear rise in time of the absorbed energy $E(t)-E_0$ is observed which is superimposed by a low frequency oscillation ω_{obs}. We extract the slope m, which we identify with the energy absorption rate, and ω_{obs} from a fit of the absorbed energy. Details of the time evolution of the energy and on the fitting procedure are given below in Sec. 4.3.2. In the mean time, we discuss the results obtained for the

energy absorption rate and for ω_{obs}.

First we discuss the results obtained using t-DMRG. Fig. 4.8(a) shows the energy absorption rate as a response to the superlattice modulation as a function of the modulation frequency deep in the band insulator at $U = 10J$ for system sizes $L = 32$ and $L = 64$. Sizable energy absorption occurs near $\hbar\omega \approx (\Delta - U) = 40J$ which corresponds to the naive expectation of breaking a doublon on a low energy site and transferring one particle to the neighboring high energy site. The absorption peak is very sharp and has a small width $\sim 0.2J$. A strong rise occurs at its left boundary corresponding to the divergence at the lower excitation band edge seen in the non-interacting model (cf. Sec. 4.1). The absorption decreases across the resonant region to very small values at its right boundary. To the right of the peak, the absorption rate approximately behaves proportional to $\sim (J/(\hbar\omega - (\Delta - U)))^{\alpha}$ with an exponent $\alpha > 1/2$ (see inset of Fig. 4.8(a)). This is also in accordance with the behavior found in the non-interacting model where, away from the divergence, the rate similarly decays with an exponent $> 1/2$. The comparison of the two system sizes shows that finite size effects are negligible in most parts of the resonant region except at the left boundary where deviations occur. In the next Sec. 4.3.2 we analyze further these deviations in the time-dependence of the energy absorption and confirm that they originate from finite size effects.
The energy absorption as a response to the normal lattice modulation is also shown in Fig. 4.8(a). Comparing the energy absorption rate as a response to superlattice modulation and normal lattice modulation, we find that the width overlaps fully in the two cases. For the normal lattice modulation enhanced absorption occurs at the right boundary of the resonant region in contrast to the superlattice modulation. This enhancement corresponds to the divergence at the upper excitation band edge seen in the non-interacting model for the normal lattice modulation.

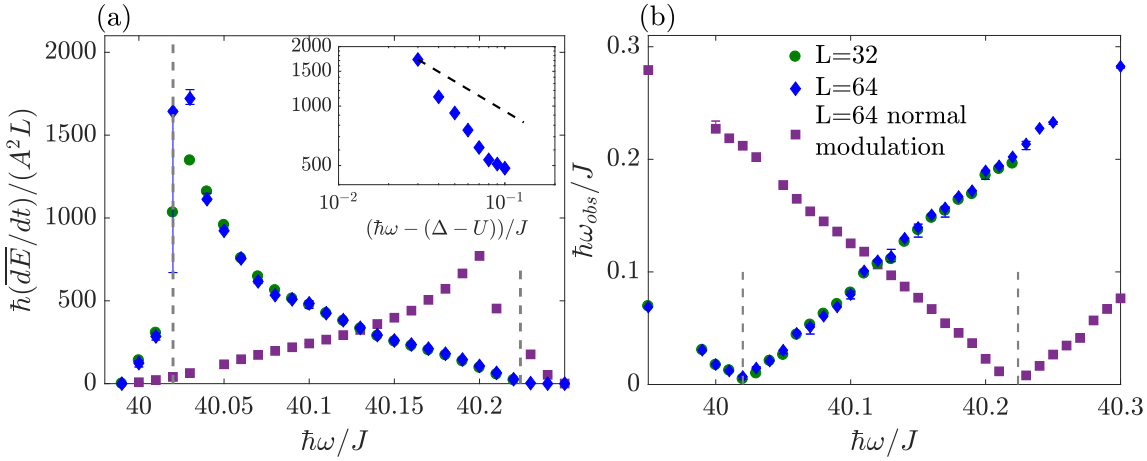

Figure 4.8: The energy absorption rate (a) and $\hbar\omega_{\text{obs}}$ (b) in t-DMRG at $\Delta = 50J$, $U = 10J$ and for an amplitude of the modulation $A = 0.001J$. The response to superlattice modulation for system sizes $L = 64$ (blue diamonds) and $L = 32$ (green circles) is shown in comparison to the response to normal lattice amplitude modulation for a system size $L = 64$ (violet squares). Vertical dashed lines indicate the bandwidth of the effective model. Inset: The energy absorption rate near the left edge of resonance decays with an exponent $> 1/2$ as may be seen from a comparison to $\sim (J/(\hbar\omega - (\Delta - U)))^{1/2}$ (black dashed line) which corresponds to the behavior of the divergence in the non-interacting case.

Let us now discuss the extracted frequency ω_{obs}. It is shown in Fig. 4.8(b) at $U = 10$ obtained from t-DMRG for different system sizes $L = 32$ and $L = 64$. For the superlattice modulation, the observed frequency becomes very small and minimum at the left boundary of the response where maximum

absorption occurs. The deviations between the different system sizes observed in the absorption rate (see above) do not occur in ω_{obs}. This is a consequence of the fitting procedure which fails to provide reliable values for the slope at strong absorption whereas the obtained values for the frequency ω_{obs} are much better. This is discussed in more detail in the following section 4.3.2. For the normal lattice modulation the minimum of ω_{obs} occurs at the right boundary at which maximum absorption occurs for the normal lattice modulation.

Now, we discuss the results obtained within the effective model (cf. Sec. 4.2). Within the effective model there is two routes to obtain the energy absorption rate. Similar to our t-DMRG study, we can extract the energy absorption rate and ω_{obs} from a fit of the time evolution of energy. Using the eigensystem of the effective model obtained in Sec. 4.2.1 the time evolution of energy is given by Eq. (3.32). Alternatively, we can determine the averaged rate given by Eq. (3.31) within linear response, also using the eigensystem of the effective model. We replace the δ-function by a Lorentz-function with finite broadening η (cf. Sec. 3.2). The obtained energy absorption rates in comparison to the t-DMRG result are shown in Fig. 4.9 for two different interaction strengths $U = 10J$ (a) and $U = 35J$ (b). We find excellent agreement across the resonant region except at the left boundary where deviations occur due to the finite size of the system. These deviations are discussed in more detail below in Sec. 4.3.2. The width of the resonance is given by the lowest band of excitations within the effective model which is approximately proportional to $J^2/(\Delta - U)$ (cf. Fig. 4.6(a)). The strong enhancement in the response at the left boundary corresponds to the behavior of the transition matrix elements squared $|\langle BI|\hat{O}_S|\alpha\rangle|^2$ within the effective model. The different features of the transition matrix element squared will be discussed in detail below in Sec. 4.3.3 (see also Fig. 4.15). A comparison of the extracted frequency within the effective model and t-DMRG at $U = 10J$ and $U = 35J$ is shown in the insets of Figs. 4.9(a) and (b) respectively and yields very good agreement. We conclude, that the location, width and shape of the peak deep in the band insulator are well described by the effective model.

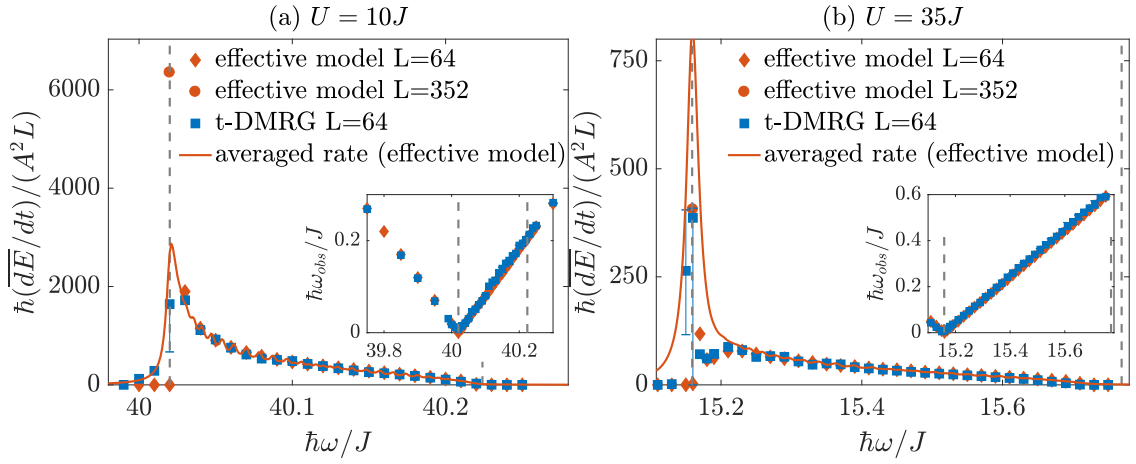

Figure 4.9: The energy absorption rate (main plots) and $\hbar\omega_{\text{obs}}$ (insets) within the effective model and t-DMRG at $\Delta = 50J$, $U = 10J$ (a) and $U = 35J$ (b) and for an amplitude of the modulation $A = 0.001J$ and $A = 0.0005J$, respectively. The response to superlattice modulation for a system size $L = 64$ within t-DMRG (blue squares) is shown in comparison to the effective model. We compare the absorption rate extracted from the time evolution of energy within the effective model (orange diamonds) and the averaged rate (orange solid line) for a broadening $\eta = 0.003J$ and $\eta = 0.01J$, respectively. At $\hbar\omega = 40.02J$ and $\hbar\omega = 15.16J$, respectively, the result for the effective model at $L = 352$ (orange circle) is displayed which illustrates the strong finite size effects present at the left edge of the resonant region. Vertical dashed lines indicate the bandwidth of the effective model.

Let us now discuss the observations for increasing U. For increasing U the location of the absorption peak shifts to smaller values of $\hbar\omega$ approaching zero energy when $\Delta \sim U$ while the resonant region broadens, see Fig. 4.10(a). Both effects are expected. The shift is related to the decreasing charge gap while the width increases due to the increase of the bandwidth of the lowest band of excitations within the effective model $\sim J^2/(\Delta - U)$ (cf. Fig. 4.6(a)).

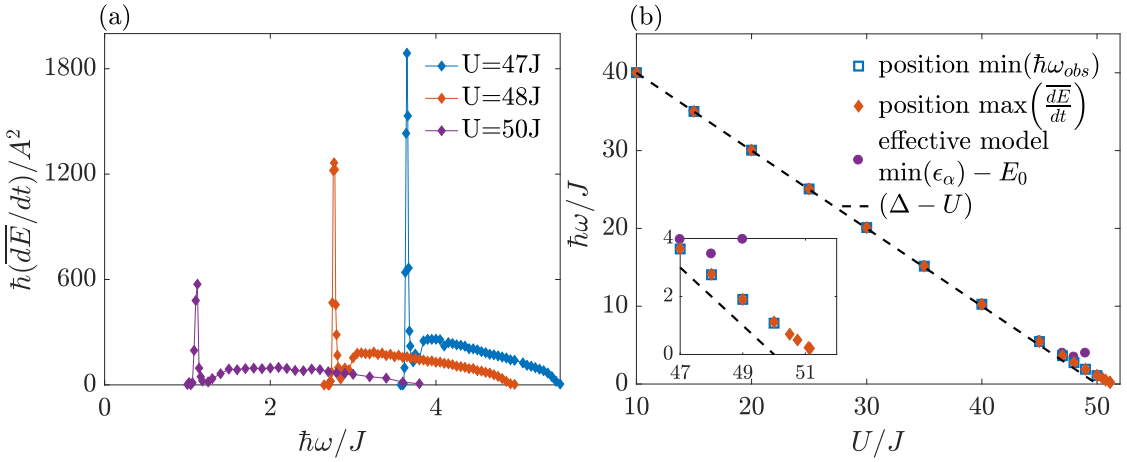

Figure 4.10: (a) The energy absorption rate at $\Delta = 50J$, for a system size $L = 64$ and an amplitude of the modulation $A = 0.005J$ for different interactions $U \lesssim \Delta$. For increasing U the position of the absorption peak shifts closer towards zero which indicates the closing of the charge gap. (b) The position of the maximum of the absorption rate peak (orange filled diamonds) and the position of the minimum of the observed oscillation frequency $\hbar\omega_{\text{obs}}$ (blue open squares) correspond approximately to the charge gap for $\Delta > U$, here $\Delta = 50J$, $L = 64$. The position of the lower band edge within the effective model (purple filled circles) is shown in comparison. Note that for $U \geq 50J$ we have no data points for the frequency ω_{obs} as the time evolution of the energy no longer shows this additional modulation with frequency ω_{obs}. Inset: Close to the transition $U \sim \Delta$ deviations in t-DMRG from the naive expectation $\Delta - U$ (dashed line) and from the effective model occur (which limits the validity of the effective model near the transition).

In Fig. 4.10(b) we show the locations of the maximum of the absorption peak (orange filled diamonds) and the minimum of ω_{obs} (blue open squares), which agree well, as a function of U. The location is approximately proportional to $(\Delta - U)$ for $\Delta >> U$. We identify this with the charge gap and confirm that it closes when approaching $\Delta \sim U$. In the range of validity of the effective model, this location corresponds to the lower band edge in the effective model which is also shown in the figure (purple filled circles). The effective model is valid for a wide range of $U < \Delta$ but fails when approaching the Ising critical point which is illustrated in the figure where a sizable deviation of the lower band edge of the effective model from the observed location of the absorption peak maximum or the minimum ω_{obs} occurs approximately for $U \gtrsim 45J$. Note that for $U \geq 50J$ we have no data points for the frequency ω_{obs} as the time evolution of the energy no longer shows this additional modulation with frequency ω_{obs}. The observed time evolution for $U \geq 50J$ shows a linear increase modulated by the modulation frequency ω similar to the time evolution at Ising criticality. The energy absorption rate near the phase transition to the BOW for $U \geq 50J$ but still below the Ising critical point is discussed in more detail in Sec. 4.4.1 where we analyze energy absorption at the Ising critical point and in its vicinity.
Additionally, for increasing U a 'dip' emerges to the right of the divergence for $U \gtrsim 25J$. As an example, we carry out a more detailed analysis of the response at increased U for $U = 35J$ (and at $A = 0.0005J$) which is shown in Fig. 4.9(b). At this interaction strength, the result obtained using t-DMRG is still well described by the result obtained from the effective model by a fit of the time evolution of energy (3.32). In contrast, the averaged rate fails (3.31) to capture the additional 'dip' which is possibly washed out due

to the finite broadening η of the Lorentz-function. The occurrence of the 'dip' can be explained within the effective model where the 'dip' similarly appears in the transition matrix elements squared. The origin of the 'dip' will be discussed in detail below in Sec. 4.3.3.

4.3.2 Time-dependence of the absorbed energy

In this subsection we discuss in detail the time-dependence of the energy absorption $E(t) - E_0$. We give details on the fitting procedure and discuss the observed finite size effects.
As an example, the time evolution of the energy at $U = 10J$ for different perturbing frequencies across the resonant region is shown in Fig. 4.11 in t-DMRG (orange dots) and within the effective model (purple line). A strong increase in energy occurs in a narrow region $\hbar\omega \gtrsim (\Delta - U)$ where the total energy of the system shows an overall linear dependence in time as in (a) and (b). An additional oscillation of amplitude $\tilde{A}$ and small frequency $\omega_{\text{obs}} \ll \omega$ occurs. Off-resonance (c), only small amounts of energy are absorbed on average. The modulation of the energy with the perturbation frequency ω in t-DMRG, see inset in (b), is negligible in the overall behavior. We observe that energy absorption becomes maximal near the left boundary of the resonant region $\hbar\omega = 40.02J$ (a) and ω_{obs} becomes minimal. For increasing $\hbar\omega$ (b,c) energy absorption decreases whereas ω_{obs} increases. Deviations between t-DMRG and the effective model occur at late times (see for example Fig. 4.11(b)).

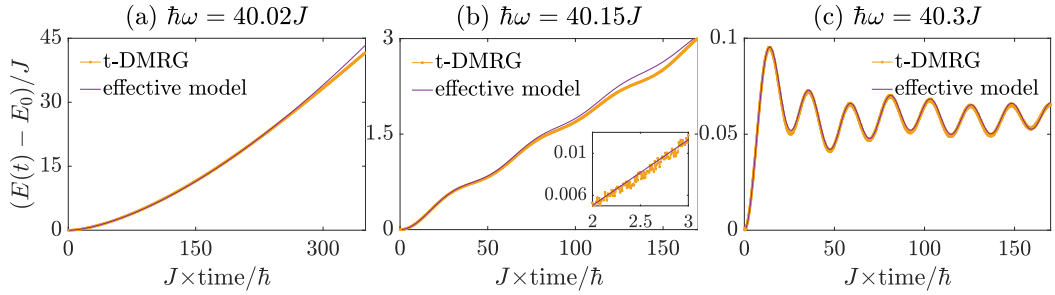

Figure 4.11: The time evolution of the energy as a function of time at $\Delta = 50J$, $U = 10J$ for a system size $L = 64$ and an amplitude of the modulation $A = 0.001J$ in t-DMRG (orange dots, connecting lines are a guides to the eye) compared to the effective model (purple solid line) for different frequencies $\hbar\omega$ of the perturbation across the resonant region. We show frequencies $\hbar\omega = 40.02J$ (a) at the left edge of the resonant region, $\hbar\omega = 40.15J$ (b) within the resonant region and $\hbar\omega = 40.3J$ (c) off resonance. The inset of (b) shows a zoom where an oscillation with perturbation frequency ω is visible in t-DMRG. The y-axis label is the same in (a)-(c) but the scale changes as absorption decreases considerably from (a) to (c).

We extract the slope m, which we identify with the energy absorption rate, from a fit of

$$E(t) - E_0 = mt + \text{offset} + \tilde{A}\cos(\omega_{\text{obs}}t + \varphi) \tag{4.37}$$

with fit parameters slope m, y-intercept offset, amplitude $\tilde{A}$, frequency ω_{obs} and phase φ of the superimposed oscillation. Fit ranges have to be chosen carefully to obtain reliable fits, taking into account the validity of linear response, and they may vary for each perturbing frequency. The fitting region has to be chosen within the intermediate linear region (after an initial quadratic rise and before saturation occurs) which is observed in typical lattice shaking setups. The extent of the linear region depends on the choice of the amplitude of the modulation A (cf. Sec. 3.2.2).

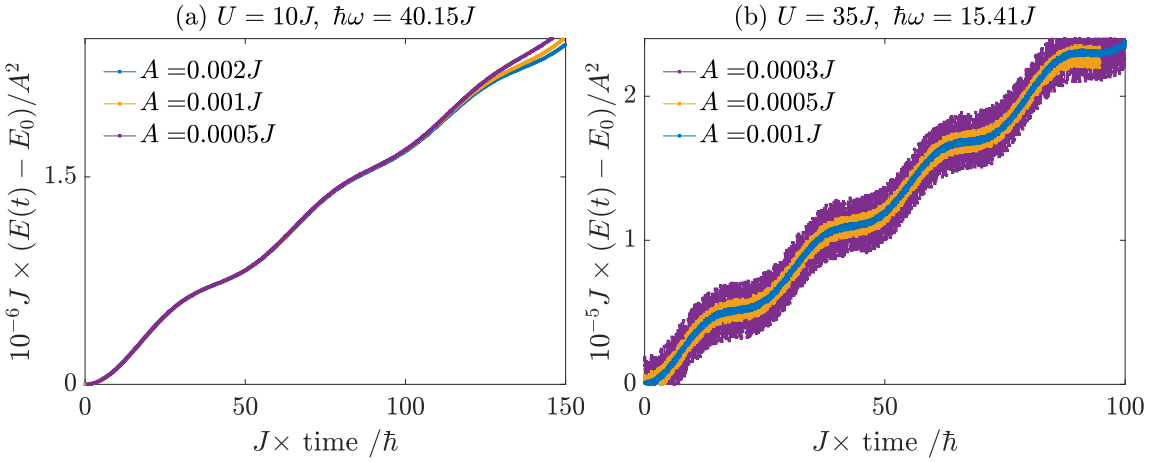

Figure 4.12: The absorbed energy as a function of time at $\Delta = 50J$, for a system size $L = 64$ in t-DMRG for different amplitudes of the modulation A. (a) The time evolution of the energy at $U = 10J$, $\hbar\omega = 40.15J$ and $A = 0.002J,\ 0.001J,\ 0.0005J$. (b) The time evolution of the energy at $U = 35J$, $\hbar\omega = 15.41J$ and $A = 0.001J,\ 0.0005J,\ 0.0003J$.

In summary, the amplitude A has to be chosen large enough to obtain a detectable signal but small enough to stay within the linear response regime for large enough times in order to obtain reliable fits, i.e. the absorbed energy should not saturate at short times. For $U = 10J$ we choose an amplitude $A = 0.001J$ and for $U > 10J$ we choose an amplitude $A = 0.0005J$. The choice is illustrated for one frequency within the resonant region at $U = 10J$ and $U = 35J$ in Figs. 4.12(a) and (b) respectively where we show $(E(t) - E_0)/A^2$ for different amplitudes of the modulation. We find that the time evolution of energy is not very sensitive to the choice of A and we are well within the linear response regime. In reality, we have verified the choice for many more frequencies. The chosen fit ranges vary for different perturbing frequencies ω as the time scales present change (for example the frequency ω_{obs}) and the fit ranges have to be adapted accordingly. For all frequencies, the typical linear time-dependence is observed for times $> 50\hbar/J$. It is sufficiently large and saturation does not occur within in the considered time interval. To reliably extract the absorption from a fit, we consider times up to $\sim 300\hbar/J$ near maximum absorption (see Fig. 4.13(a)). Further away from resonance as shown in Fig. 4.13(b), using shorter time intervals, for example up to $150\hbar/J$, is often adequate and can also be used off-resonance, see Fig. 4.13(c).

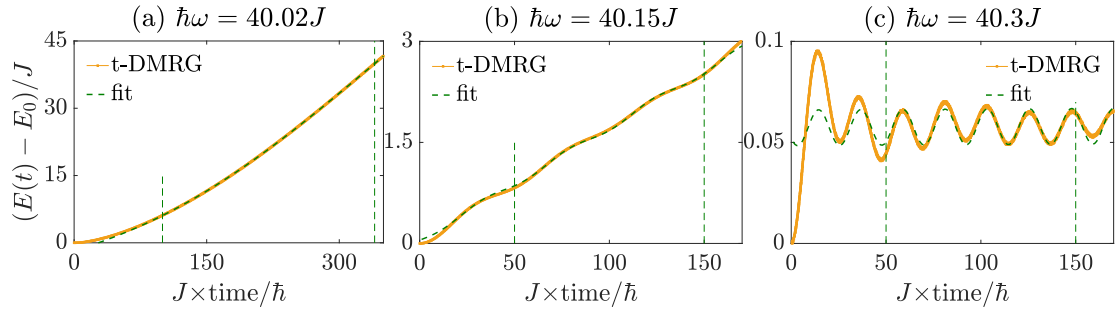

Figure 4.13: The absorbed energy as a function of time at $\Delta = 50J$, $U = 10J$ for a system size $L = 64$ and an amplitude of the modulation $A = 0.001J$ in t-DMRG (orange dots, connecting lines are a guides to the eye) compared to the obtained fit (dashed green line) for different frequencies $\hbar\omega$ of the perturbation across the resonant region. Vertical dashed lines indicated the chosen fit range. We show frequencies $\hbar\omega = 40.02J$ (a) at the left edge of the resonant region, $\hbar\omega = 40.15J$ (b) within the resonant region and $\hbar\omega = 40.3J$ (c) off resonance. The y-axis label is the same in (a)-(c) but the scale changes as absorption decreases considerably from (a) to (c).

We now discuss the finite size effects. A reliable fit of the t-DMRG data becomes difficult near maximum absorption where $\omega_{\text{obs}} \to 0$. In the considered time interval less that one period of this oscillation is observed, see Fig. 4.13(a). The frequency ω_{obs} can still be extracted well but a reliable determination of the slope is very difficult. This leads to very large error bars when conducting the error analysis, see for example the error bars on the energy absorption rate in Figs. 4.9(a) and (b). In contrast, within the effective model we can easily access much longer times which are beyond the reach of numerical accuracy. We consider longer times as an example, again for $U = 10J$ and $U = 35J$, at the the left boundary of the resonant region (maximum absorption) at $\hbar\omega \approx \min(\epsilon_\alpha) - E_0 \approx 40.02J,\ 15.16J$ respectively. The absorbed energy (within the effective model) for different system sizes $L = 64 - 352$ is shown in Fig. 4.14. We ascertain that for a system size $L = 64$ (blue dotted lines in the main plot and in the inset) no linear rise occurs but oscillations of very small frequency ω_{obs} (and very large period) exist. In t-DMRG we only observe part of the initial rise of this oscillation, see for example Fig. 4.13(a). Consequently, the finite slope which we obtain from a fit in t-DMRG is incorrect. At this frequency corresponding to the left boundary of the response, the physics is similar to that of a two-level system yielding Rabi oscillations in time. Within the effective model we find a strong enhancement in the transition matrix element squared at the left boundary which will be discussed in the following section 4.3.3 (see also Fig. 4.15). Furthermore, the eigensystem is very discrete near the left boundary for the smaller considered system sizes, e.g. $L = 64$ (see also following section and Fig. 4.16(b)). Due to the discreteness of the finite size system only few transitions are promoted. Consequently, only few states couple and linear response is not valid here. Note, that the two-level picture is in accordance with our observation that ω_{obs} becomes minimum at maximal absorption (where the transition matrix elements are strongest) as the Rabi frequency of a two-level system becomes minimum on resonance (zero detuning).

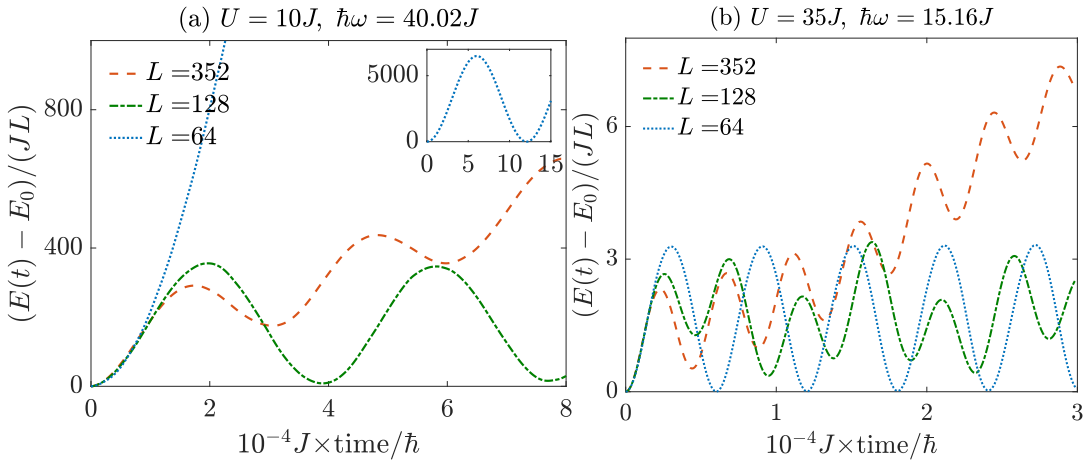

Figure 4.14: The absorbed energy as a function of time at $\Delta = 50J$ at the left edge of the resonant region in the effective model for different system sizes and long times beyond the reach of t-DMRG. (a) The time evolution of the energy at $U = 10J$, $\hbar\omega = 40.02J$, $A = 0.001J$. The inset shows even longer times for $L = 64$. (b) The time evolution of the energy at $U = 35J$, $\hbar\omega = 15.16J$, $A = 0.0005J$.

For increasing system sizes the density of states increases and eventually linear response is recovered for $L = 352$ (orange dashed line in Fig. 4.14) as expected in the continuum limit. We extract the absorption rate at maximum absorption from the $L = 352$ curve which gives a more reliable result for the energy absorption rate than the result extracted from the $L = 64$ curve. In Figs. 4.9(a) and (b) this additional point is indicated by an orange circular marker. We find very strong absorption which hints at the infinite system size behavior expected to reflect the divergence observed in the non-interacting case. One needs to keep in mind, in particular for experimental realizations, that a quantitative result for the absorption

rate will be difficult to obtain from any smaller system size. However, let us point out that if one is only interested in the qualitative result that strong absorption occurs here, the small system sizes are sufficient.

4.3.3 Transition matrix elements

In this subsection we study in more detail the square of the transition matrix elements $|\langle BI|\hat{O}_S|\alpha\rangle|^2$ from the band insulating ground state $|BI\rangle$ (4.28) to the eigenstates $|\alpha\rangle$ of the effective model within the lowest band of excitations given by Eqs. (4.29) and (4.30) which we determined in Sec. 4.2.1. This enables us to interpret the different features of the response in terms of the different processes contributing to the effective model.

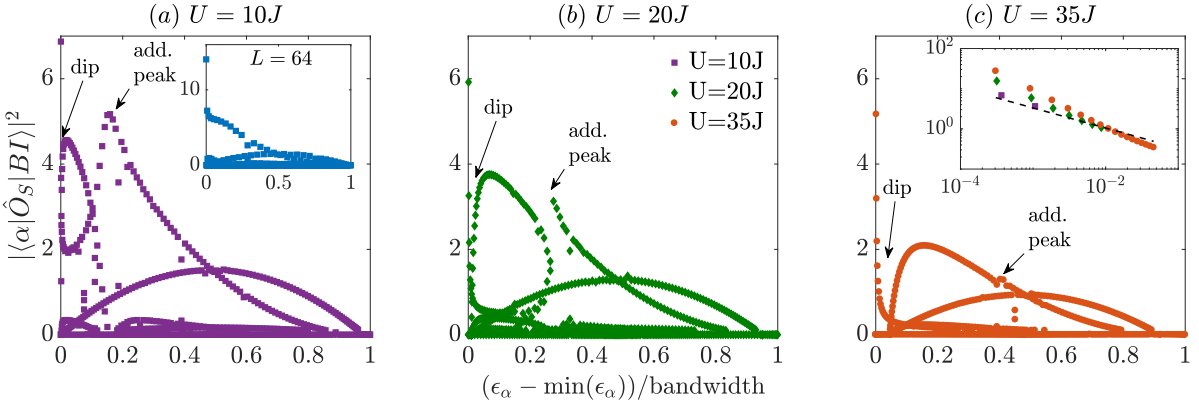

Figure 4.15: The transition matrix element squared $|\langle BI|\hat{O}_S|\alpha\rangle|^2$ by superlattice modulation at $\Delta = 50J$ for a system size $L = 256$ at different interactions (a) $U = 10J$, (b) $U = 20J$, (c) $U = 35J$. Note that the vertical axis is cropped as the matrix elements become very large when approaching $(\epsilon_\alpha - \min(\epsilon_\alpha))$/bandwidth=0 such that the substructure is not visible on the full range. The full vertical range near $(\epsilon_\alpha - \min(\epsilon_\alpha))$/bandwidth=0 is shown in the inset of (c) in comparison to $\sim 1/\left((\epsilon_\alpha - \min(\epsilon_\alpha))/\text{bandwidth}\right)^{1/2}$ (black dashed line). The inset in (a) shows a comparison to the system size $L = 64$ where not all of the substructures are resolved.

Let us first discuss the full transition matrix element. In Fig. 4.15 the transition matrix element squared for a system size $L = 256$ is shown as a function of the shifted eigenenergy $\epsilon_\alpha - \min(\epsilon_\alpha)$ normalized by the bandwidth for different $U = 10J,\ 20J,\ 35J$ (a-c). For all U the transition matrix element squared shows a strong rise at the left boundary, with the maximum transition matrix element squared corresponding to the lowest eigenvalue. The transition matrix element then quickly decays reflecting the behavior of the peak observed in the energy absorption rate (cf. Fig. 4.9). The transition matrix element squared near the left boundary decays with an exponent $> 1/2$, see inset of Fig. 4.15(c), in accordance with our findings for the absorption rate (cf. inset of Fig. 4.8(a)). To the right of the peak a broad substructure emerges which mainly consists of two superimposed 'lobes' and becomes very small at the right boundary, similar to the observed energy absorption rate. For small U an additional peak appears to the right of the maximum of the first 'lobe'. This additional peak is strong for $U = 10$ (a) and still visible for $U = 20$ (b) and has essentially disappeared for $U = 35$ (c). At $U = 10J$ for the smaller system size $L = 64J$ the additional peak is not resolved, see inset of Fig. 4.15(a), which explains why we do not observe an additional peak in the energy absorption rate studied for $L = 64$ (cf. Fig. 4.8(a)). In addition, to the right of the strong peak (at the left boundary of the resonant region) but to the left of the first 'lobe' of the substructure, a 'dip' appears in the square of the transition matrix element. For small U, deep in the band insulator, the maximum of the first 'lobe' is located near the strong peak at the boundary, such that the 'dip' essentially disappears in the strong enhancement at the left boundary. For increasing U the location of the 'lobe' maximum and the 'dip' shift to the right such that the 'dip' becomes distinctly visible (even at small

system sizes) which explains our observation of the 'dip' in the energy absorption rate for increasing U (cf. the absorption rate for $U = 35J$ in Fig. 4.9(a)).
Studying different system sizes, we find that the 'dip' becomes more pronounced for increasing system sizes, see Fig. 4.16(a), and the 'dip' corresponds to a 'kink' in the band structure, see Fig. 4.16(b).

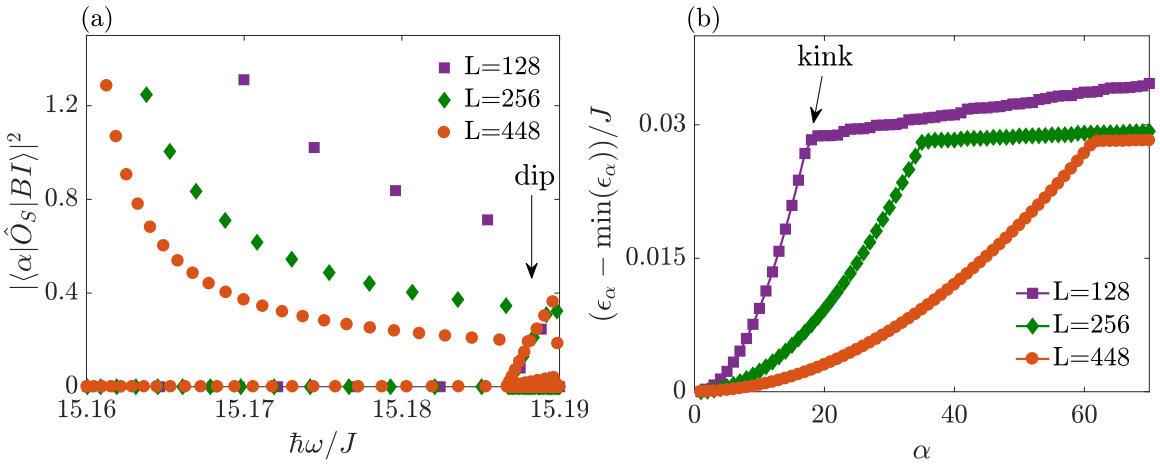

Figure 4.16: (a) Zoom into the transition matrix elements as a function of perturbation frequency at $\Delta = 50J$ and $U = 35J$ for different system sizes. The zoom contains the observed 'dip' which becomes more pronounced for increasing system sizes. (b) Zoom into the eigenspectrum at $\Delta = 50J$ and $U = 35J$ for different system sizes. The first 70 eigenvalues are shown. The 'kink' in the spectrum corresponds to the 'dip' in the transition matrix elements.

We can attribute the different features of the matrix elements to the different virtual processes contributing to the effective model. All these processes were explained in detail in Sec. 4.2.1 (cf. Fig. 4.4). The influence of the single contributions onto the structure of the transition matrix elements can be analyzed by diagonalizing the effective model considering only these contributions, i.e. all terms in the Hamiltonian that stem from the other processes are set to zero. The resulting eigensystem is then used to determine the transition matrix elements. Let us first analyze those processes that couple to the two bands closest in energy to the lowest band of excitations, that is the ground state and the second band of excitations separated by an energy $\mp(\Delta - U)$ from the lowest band of excitations respectively. The transition matrix element squared resulting from uniquely coupling to the ground state is shown in Fig. 4.17(a). This process clearly leads to the strong enhancement at the left boundary but no substructure occurs. The transition matrix element squared resulting from uniquely coupling to the second band of excitations is shown in Fig. 4.17(b). Here, no enhancement at the boundary occurs but a substructure which is somewhat similar to the two 'lobes' occurring in the full result. A hybridization of these processes, considering both types of processes in the diagonalization, is shown in Fig. 4.17(c) and contains the main features of the full result. It displays the strong increase at the left boundary as well as the substructure consisting of two 'lobes'. Consequently, the terms in the Hamiltonian (4.27) proportional to $1/|\Delta - U|$ dominate the response which is well justified as $\Delta - U < \Delta < \Delta + U$.

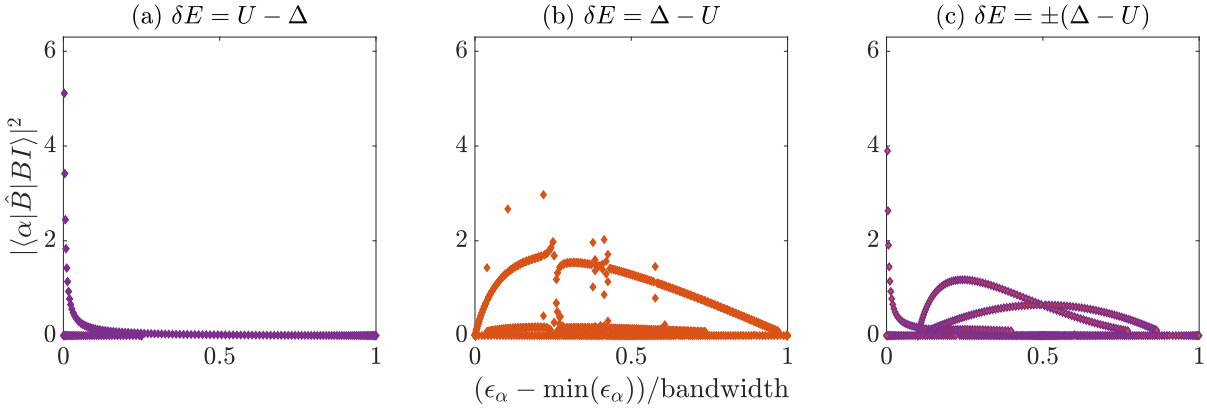

Figure 4.17: Single contributions of the effective Hamiltonian to the transition matrix element squared by superlattice modulation for a system size $L = 256$ and arbitrary Δ and U. (a) Uniquely coupling via the ground state separated by an energy $U - \Delta$ from the first band of excitations. (b) Uniquely coupling via the second band of excitations separated by an energy $\Delta - U$ from the first band of excitations. (c) Hybridization of processes in (a) and (b) which captures most of the features present in the full description (cf. Fig. 4.15). Note that the vertical axis is cropped for a better view of the substructures since the matrix elements become very large at the left boundary in (a) and (c)

However, this contribution is independent of the choice of U and Δ and further contributions are needed to obtain the U-dependence observed in the full result. Considering only those processes that couple to the third band of excitations at an energy Δ from the first band of excitations, we find a strong increase at the right boundary, see Fig. 4.18(a). This feature does not survive in the full result as the terms of amplitude $1/\Delta$ contribute much more weakly to the Hamiltonian. A hybridization of the processes of amplitude $1/\Delta$ with the two types of processes of amplitude $1/|\Delta - U|$ is shown in Figs. 4.18(b) and (c) for $U = 35J$ and $U = 10J$ respectively. The 'lobe' structure is now different for the two U but does not yet reflect the full result. For example, the additional peak at $U = 10J$ is still missing. All contributions are of relevance to reproduce the full response although those processes of amplitude $1/(\Delta + U)$ that couple to the fourth band of excitations are much weaker.

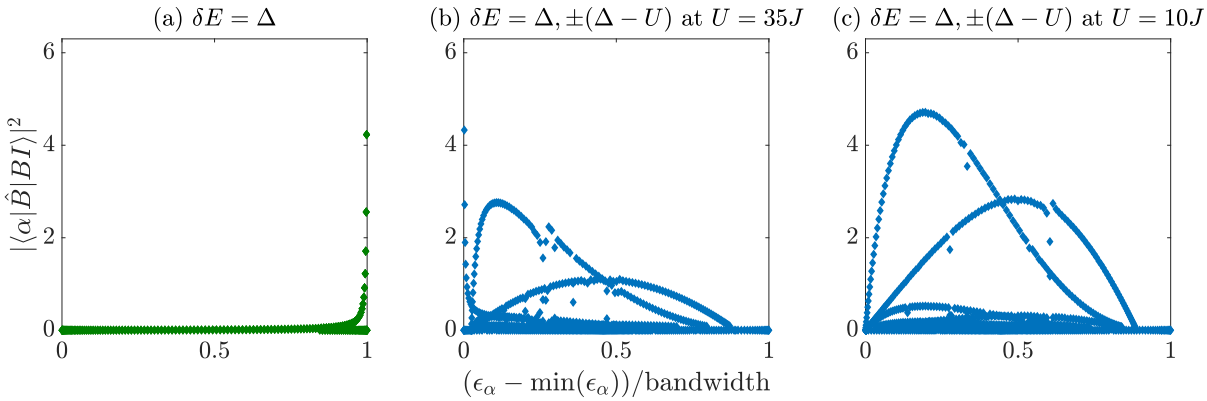

Figure 4.18: Single contributions of the effective Hamiltonian to the transition matrix element squared by superlattice modulation for a system size $L = 256$. (a) Uniquely coupling via the third band of excitations separated by an energy Δ from the first band of excitations, arbitrary Δ. (b-c) Hybridization with processes from Fig. 4.17(c) at $\Delta = 50J$, $U = 35J$ (b) and $U = 10J$ (c) which deforms the substructure from Fig. 4.17(c) and becomes more similar to the full description in Fig. 4.15. As processes with different energy spacing hybridize, the transition matrix element now depends on Δ and U. Note that the vertical axis is cropped for a better view of the substructures since the matrix elements become very large at the boundaries.

4.4 Signals of bond order

In this section we study the energy absorption rate as a response to superlattice modulation spectroscopy at $\Delta \sim U$ in the bond order wave phase and in the vicinity of the phase transitions separating it from the band and Mott insulating phases. We study the response of the system at Ising criticality in Sec. 4.4.1 and within the bond order wave phase in Sec. 4.4.2 using t-DMRG and bosonization and show that the superlattice modulation spectroscopy reveals features of both phase transitions. We discuss how a divergence in the response function at the Ising critical point signals the onset of bond order and how the presence of soliton-antisoliton excitations within the BOW phase can be probed.
In t-DMRG we study systems of sizes up to $L = 192$. In order to obtain sufficient accuracy in the absorbed energy $E(t)$ we keep a matrix dimension of $D = 120$ within the bond order wave at $L = 64$, $D = 160$ within the bond order wave at $L = 128$ and at Ising criticality for all L. We conduct an error analysis by increasing the matrix dimension from 120 to 160 states (160 to 240). In the Trotter-Suzuki time evolution we set $J\tau = 0.001\hbar$ and we use $J\tau = 0.0005\hbar$ to perform the error analysis. We determine the maximal uncertainties in the energy absorption rate due to the matrix dimension, the time step and the variation of the fit range (see App. A for details). The error bars are provided in the figures.
We compare to bosonization calculations obtained in a collaboration [84]. The derivations of the main formulas are sketched in appendix C.

4.4.1 Ising criticality

Using t-DMRG we time evolve systems of different sizes $L = 64,\ 96,\ 128,\ 192$ at the Ising critical point for a range of modulation frequencies and extract the energy absorption rate from a fit of the slope (see App. B.1.1 for details). To identify the interaction values U approximately corresponding to the Ising critical point $(U/J)_{c1}$, we find for each system size the location of the maximum of the derivative of the order parameter, $\partial|\langle\hat{B}\rangle|/\partial U$, shown in the inset of Fig. 2.6(d). The energy absorption rate for the different system sizes is shown in Fig. 4.19(a) for two different amplitudes of the modulation $A = 0.001J$ and $A = 0.0005J$. We find distinct absorption peaks located at very small perturbation frequencies which shift closer to the origin for increasing system sizes while the peak amplitude increases. The observed peaks for the two modulation amplitudes A do not agree in peak amplitude due to saturation effects. The time evolution of energy saturates at early times for the larger modulation amplitude $A = 0.001J$ such that we underestimate the absorbed energy when extracting the absorption rate from a fit of the time evolution of energy, see App. B.1.1 for details.
In bosonization, see App. C, the imaginary part of the complex susceptibility as a response to the superlattice modulation for a finite system is found to be

$$\mathrm{Im}\chi(\omega) \quad \sim \quad \left(\frac{aL}{\alpha}\right)^{7/4} \sum_{n=0}^{\infty} \left(\frac{\Gamma\left(n+\frac{1}{8}\right)}{\Gamma(n+1)}\right)^2 \times \delta\left(\hbar\omega - \hbar\Omega(n)\right), \tag{4.38}$$

where a is the lattice spacing, L is the number of lattice sites and α is the short distance cutoff, typically of the order of the lattice spacing. The response displays a series of peaks n occurring at

$$\hbar\Omega(n) = 4\pi\frac{\hbar u_c}{aL}\left(n + \frac{1}{16}\right) \tag{4.39}$$

where u_c is the sound velocity of the low-energy charge excitations. The spectral weight of Eq. (4.38) scales as $\omega^{-7/4}$. Consequently, the spectral weight of the absorption rate $\overline{dE}/dt \sim \omega\mathrm{Im}\chi(\omega)$ scales

as $\omega^{-3/4}$. This signals the divergence expected for the infinite system $\overline{dE}/dt \sim L\omega^{-3/4}$ which can be extracted by taking the limit $\omega \gg u_c/(aL)$. At frequencies lower than the spin gap, the charge fluctuations dominate causing the divergence as the system tends to order.

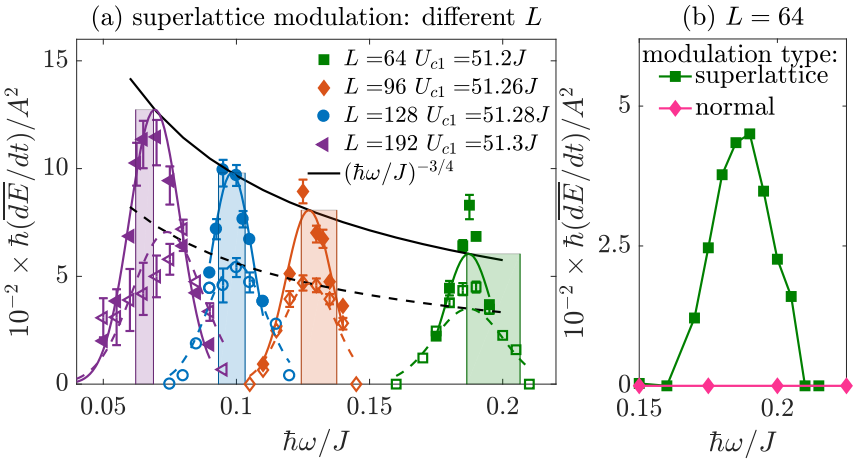

Figure 4.19: (a) The $n = 1$ peak of the energy absorption rate at Ising criticality U_{c1} for fixed $\Delta = 50J$ for system sizes $L = 64,\ 96,\ 128,\ 192$ and amplitudes $A = 0.001J$ (open symbols) and $A = 0.0005J$ (filled symbols). The Gaussian fits (dashed and solid lines) are guides to the eye. The Gaussian fits approximate the δ-function with finite broadening and the maxima are fixed to $\lambda(\hbar\omega/J)^{-3/4}$ with λ chosen to agree with the $L = 128$ peak. Vertical bars indicated the predicted peak position where the $L = 128$, $A = 0.0005J$ peak was chosen to determine the velocity of charge excitations. Figure adapted from Ref. [84]. (b) The energy absorption rate for $L = 64$ at Ising criticality $U_{c1} = 51.2J$ and amplitude $A = 0.001J$ as a response to superlattice modulation (green squares) and to normal lattice modulation (pink diamonds) where no excitations are created.

At low energies ($\hbar\omega/J < 0.15$) our t-DMRG results are in good agreement with the predictions from bosonization. The peaks' height follows well the predicted $(\hbar\omega/J)^{-3/4}$ divergence, see Fig. 4.19(a). We identify our t-DMRG absorption peaks with the $n = 1$ peak. In contrast, the $n = 0$ peaks are expected at energies $\hbar\omega \sim (\pi\hbar u_c)/(4aL)$ which are too low in frequency to be resolved by our numerics. In our t-DMRG study (and also in experiments), these peaks acquire a finite width due to, for example, the finite perturbation time which limits the frequency resolution. We estimate the peak position by fitting to the t-DMRG data for the amplitude $A = 0.0005J$ a Gaussian approximating the δ-function with a finite broadening. However, any distribution approximating the δ-function in the limit of small widths would equally work. The obtained peak positions $\hbar\omega_{\text{peak}}$ from a fit of the peaks for the different system sizes are given in table 4.1. From each position we extract the sound velocity of charge excitations u_c using Eq. (4.39) which are also listed in table 4.1. Note, that the $A = 0.0005J$ data is more suitable to extract the sound velocity than the $A = 0.001J$ data due to saturation effects, see App. B.1.1. The different extracted sound velocities have values typical for lattice systems.

Table 4.1: Estimated position $\hbar\omega_{\text{peak}}$ of the $n = 1$ peak at Ising criticality for an amplitude of the modulation $A = 0.0005J$ and the extracted sound velocity of charge excitations u_c.

L	$\hbar\omega_{\text{peak}}/J$	$\hbar u_c/(aJ)$
64	0.187 ± 0.005	0.89 ± 0.03
96	0.127 ± 0.005	0.91 ± 0.04
128	0.098 ± 0.005	0.94 ± 0.05
192	0.069 ± 0.005	1.0 ± 0.08

In principle, the largest L should give the best estimate but due to enhanced saturation effects occurring in the time-dependence of the absorbed energy for $L = 192$, see App. B.1.1, we choose the result for $L = 128$ as our best estimate. The extracted sound velocity is $\hbar u_c/(aJ) = 0.94 \pm 0.05$ and the values extracted for the other system sizes agree within the error bars. Even the extracted value for $L = 64$ is still reasonable even though the peak is already appearing at large frequencies where bosonization is expected to break down. We use the sound velocity extracted from the $L = 128$ peak to predict the expected (within bosonization) position of the peaks for the other L. The predicted peak positions are indicated in Fig. 4.19(a) by shaded regions and agree well with the peaks obtained using t-DMRG. We attribute the disagreement in the peak position and height for $L = 64$ to the breakdown of bosonization in the energy range where the corresponding $n = 1$ peak appears. The asymmetry of the $n = 1$ peak at $L = 192$ and $A = 0.001J$ is due to saturation effects in the numerics, see app. B.1.1.
We stress that the normal lattice modulation fails to detect the existence of the Ising phase transition. Within bosonization, the energy absorption rate does not present a divergence at the Ising transition as this modulation scheme does not couple to the bond order wave. We confirm using t-DMRG that no energy is absorbed. The vanishing absorption rate is shown in comparison to the superlattice modulation peak in Fig. 4.19(b).

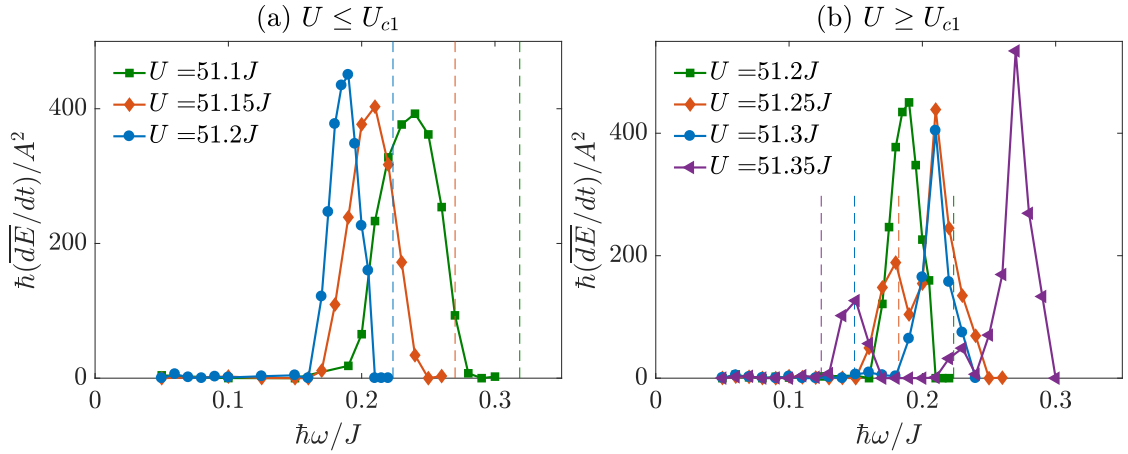

Figure 4.20: The energy absorption rate at $\Delta = 50J$ for a system size $L = 64$ and for an amplitude of the modulation $A = 0.001J$ at Ising criticality $U_{c1} = 51.2J$ and slightly below at $U = 51.1J$, $51.15J$ (a) and slightly above $U = 51.25J$, $51.3J$, $51.35J$ (b). Solid lines are guides to the eye and vertical dashed lines indicate the spin gap. The spin gap is obtained from static DMRG calculations keeping up to 240 states. More details on the calculation of the spin gap are given in the next section 4.4.2. Figures adapted from Ref. [84].

Slightly above and slightly below Ising criticality the charge gap reopens. In Fig. 4.20(a), we show the energy absorption rate at U_{c1} compared to the absorption rates for two interaction values slightly below criticality. For increasing U, the peaks shift to lower energies and their respective width decreases. This behavior indicates the closing of the charge gap as the absorption peaks are located at energies clearly below the spin gap (indicated by vertical dashed lines in the figure). Furthermore, the increasing spectral weight when approaching the Ising transition signals the expected divergence. In Fig. 4.20(b), we show the energy absorption rate at U_{c1} compared to the rates at three interactions slightly above criticality. For increasing interactions $U = 51.25$ and $51.3J$, the large peak slowly shifts to larger frequencies, i.e. the charge gap reopens. At $U = 51.35J$ which approximately corresponds to the maximum of the bond order parameter (cf. Fig.2.6(d)) the structure of the spectrum changes. The charge gap shifts to even larger frequencies while a peak arises near the spin gap. We attribute this additional peak to soliton-antisoliton excitations occurring at multiples of the spin gap near the Kosterlitz-Thouless transition and which will

be discussed in depth in the next section 4.4.2. Such excitations can already contribute to the spectrum in the bond order wave phase when the system is probed to the right of the maximum of the order parameter.

Another route to test the bosonization prediction is to consider multiple n peaks for the same system size. In Fig. 4.21 we show the energy absorption rate for a system size $L = 192$ extended to larger frequencies where the $n = 2$ and $n = 3$ peaks are expected. The expected positions are determined from the sound velocity u_c obtained from the $n = 1$ peak at $L = 192$ and are indicated by shaded regions in the figure. Absorption occurs in the expected locations but the absorption at the the expected location of the $n = 2$ peak is very weak compared to the other peaks and the $(\hbar\omega/J)^{-3/4}$ behavior cannot be recovered. Furthermore, an additional rather strong peak occurs between the expected $n = 2$ and $n = 3$ peak which may originate from a hybridization of the different charge modes (different n). We attribute these discrepancies to the breakdown of bosonization at these energies corresponding to higher n peaks. Consequently, several system sizes have to be considered for an unambiguous detection of the predicted scaling behavior.

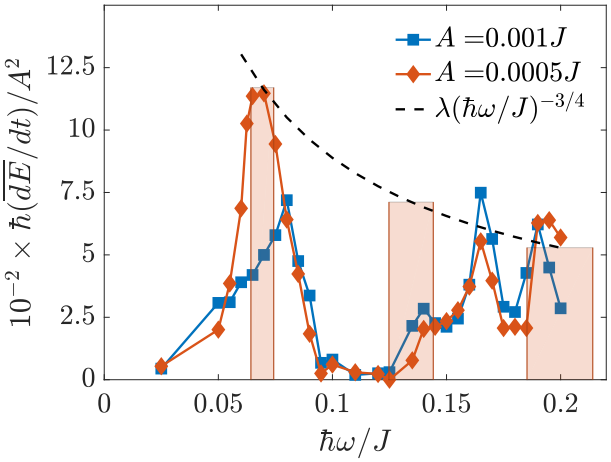

Figure 4.21: The energy absorption rate as a response to superlattice modulation at $\Delta = 50J$ for a system size $L = 192$ at Ising criticality $U_{c1} = 51.3J$ for amplitudes of the modulation $A = 0.001J$ (blue squares) and $A = 0.0005J$ (orange diamonds). Solid lines are guides to the eye and vertical bars indicate the predicted peak positions for different n. The dashed lines indicates the expected $\lambda(\hbar\omega/J)^{-3/4}$ behavior with λ fixed to agree with the $L = 192$, $A = 0.0005J$ peak.

4.4.2 Bond order wave phase

The Kosterlitz-Thouless (KT) transition is hard to pinpoint in a finite system since the bond order parameter decays slowly (cf. Fig. 2.6(d)). In the BOW to the left of the KT transition a gapped response followed by a sharp increase in the energy absorption rate is predicted within bosonization (see App. C),

$$\mathrm{Im}\chi(\omega) \sim \frac{1}{J}\sqrt{\left(\frac{\hbar\omega}{2M}\right)^2 - 1}\,, \tag{4.40}$$

where the onset of absorption is located at twice the mass M (minimum energy) of a soliton ($2M$ equals the spin gap), corresponding to the creation of a soliton-antisoliton pair. In the bond order wave phase the ground state is doubly degenerate. Singlets form on either odd or even bonds. The superlattice modulation spectroscopy, i.e. the application of the operator $\hat{B}$ (3.40), can only induce transitions from the singlet ground state to excited states within the same spin sector. The lowest available state is a pair

of solitons (domain walls) of opposite spins giving a threshold of twice the soliton mass.
Using t-DMRG we exploit the region to the left of the KT transition within the bond order wave. We time evolve systems of different sizes $L = 64,\ 128$ at $U = 52$ for a range of modulation frequencies and we extract the energy absorption rate from a fit of the slope (see App. B.1.2). In Fig. 4.22(b) the energy absorption rate is shown for the two system sizes. We observe distinct excitation peaks that are located at multiples of the spin gap as predicted by bosonization. The spin gap is obtained from static DMRG calculations in different $S_z = N_\uparrow - N_\downarrow$ sectors keeping up to 240 states and we define the spin gap as $\Delta_s = E_0(N = N_\uparrow + N_\downarrow = L, S_z = 2) - E_0(N = N_\uparrow + N_\downarrow = L, S_z = 0)$. For $U = 52J$ we find $\Delta_s \approx 0.049J$ for $L = 64$ and $\Delta_s \approx 0.024J$ for $L = 128$ converged in the matrix dimension to the given accuracy. For $L = 64$ we observe a sharp onset of energy absorption near once and twice the spin gap. For $L = 128$ we observe a sharp peak at twice the spin gap. The peak expected at once the spin gap is below the reach of our numerics for $L = 128$ due to the small frequencies at which the spin gap is located. The spin gap as a function of U is shown in Fig. 4.22(a). It decreases slowly across the region where the KT transition is expected. In an infinite system the spin gap closes at the KT transition which we cannot observe in our finite system. Approaching the KT transition from the bond order wave side, the soliton mass becomes smaller and smaller until the gap closes at the transition and a low energy feature arises on the Mott-insulating side, associated with spin excitations. These low energy excitations will be discussed in the following section 4.5. Consequently, the superlattice modulation succeeds in signaling the vicinity of the KT quantum critical point. Note, that the normal lattice modulation does not couple to the soliton-antisoliton excitation, see Fig. 4.22(b).

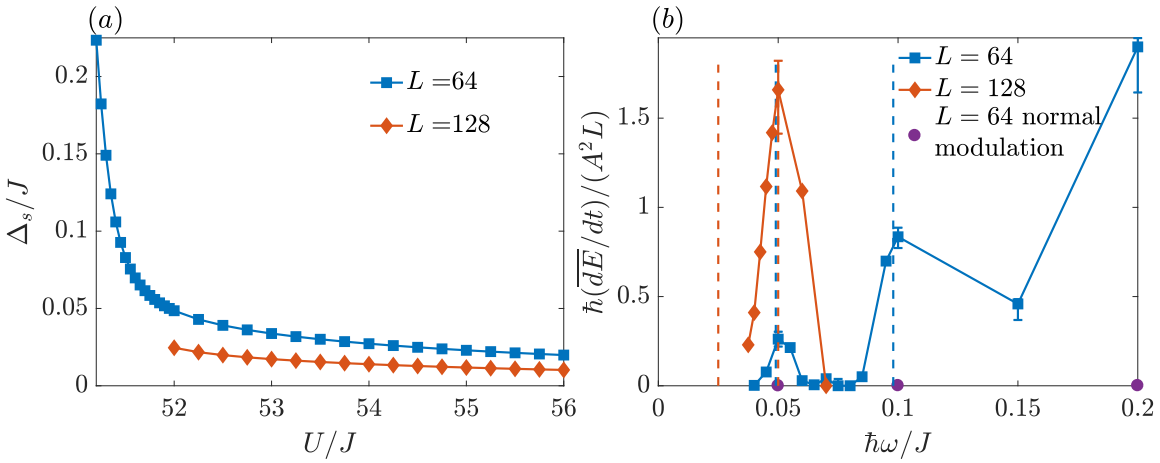

Figure 4.22: (a) The spin gap as a function of U at fixed $\Delta = 50J$ for system sizes $L = 64$ and $L = 128$. (b) The energy absorption rate at $\Delta = 50J$ within the bond order wave phase at $U = 52J$ as a response to superlattice modulation for different system sizes $L = 64$ with $A = 0.005J$ (blue squares) and $L = 128$ with $A = 0.001J$ (orange diamonds). Enhanced absorption occurs at once and twice the spin gap (vertical dashed lines) which corresponds to the creation of soliton-antisoliton pairs (see main text). Note that for $L = 128$, frequencies corresponding to once the spin gap are beyond the reach (too small) of our numerics. We compare to the normal lattice modulation for $L = 64$ with $A = 0.005J$ (purple circles) where no excitations are created. Solid lines are guides to the eye.

4.5 Mott insulating limit

In this section we study the energy absorption rate as a response to superlattice modulation spectroscopy on the Mott insulating side of the phase diagram at two values of $\Delta = 50J$ and $\Delta = 10J$ and for different interaction strengths U. We study both, low-energy spin excitations as well as gapped charge excitations

using t-DMRG in Secs. 4.5.1 and 4.5.2 respectively. We find a broad low-energy spectrum in accordance with the expectations for an isotropic Heisenberg chain and with bosonization predictions. At higher frequencies, we find distinct charge excitation peaks which can be partly interpreted in terms of the effective model (cf. Sec 4.2).
In t-DMRG we study systems of size $L = 64$. In order to obtain sufficient accuracy in the absorbed energy $E(t)$ we keep a matrix dimension of $D = 120$ at $\Delta = 50J$ and of $D = 160$ at $\Delta = 10J$. We conduct an error analysis by increasing the matrix dimension to 160 states (or 240 respectively) . In the Trotter-Suzuki time evolution we set $J\tau = 0.001\hbar$ and we use $J\tau = 0.0005\hbar$ to perform the error analysis. We determine the maximal uncertainties in the energy absorption rate due to the matrix dimension, the time step and the variation of the fit range (see App. A for details). The error bars are provided in the figures.

4.5.1 Spin excitations

At $\Delta = 50J$ we time evolve the system for different $U \gg \Delta$ and a range of modulation frequencies at small energies $\hbar\omega \lesssim 1J$. We extract the energy absorption rate from a fit of the slope of the time evolution of the energy (see App. B.1.3). The energy absorption rate is shown in Fig. 4.23(a) for two different interaction strengths. We find a broad excitation spectrum at low energies whose width and height decrease with increasing interaction strength.
In bosonization, see App. C, the low energy spectrum is predicted to be constant for infinite system sizes. For finite systems, peaks with equal weight are expected which blend into a constant spectrum for $L \to \infty$. This spectrum is bounded by a low-energy cutoff and its amplitude is predicted to decrease with increasing U. We do not resolve the peaks in our t-DMRG but our observations of decreasing width and height with increasing U corroborate the bosonization predictions.

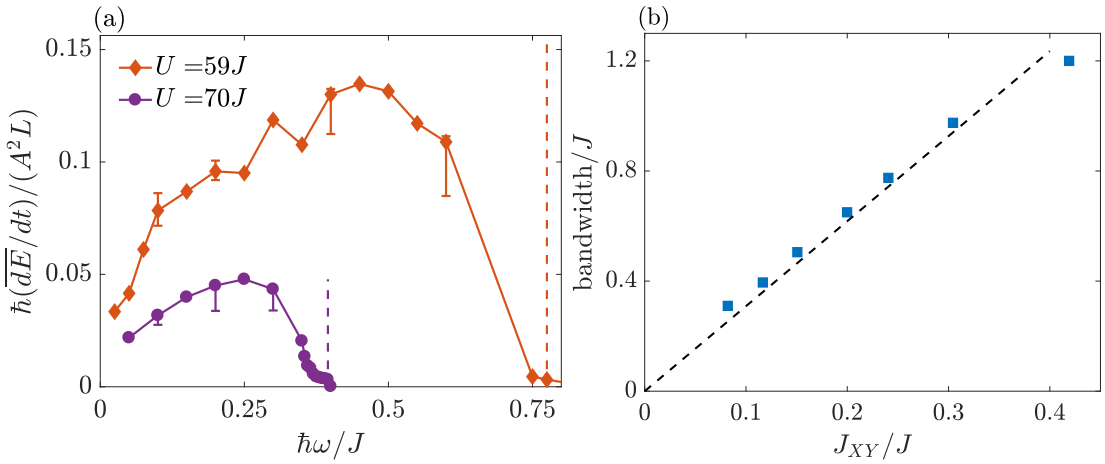

Figure 4.23: (a) The energy absorption rate in t-DMRG for a system size $L = 64$ at $\Delta = 50J$ for an an amplitude of the modulation $A = 0.005J$ on the Mott insulating side of the Kosterlitz-Thouless transition, $U = 59J$ and $U = 70J$. Dashed vertical lines indicate the bandwidth. (b) Width of the low-energy band of spin excitations in the Mott insulator, extracted from the width of the energy absorption rate, as a function of the effective spin coupling J_{XY} for $\Delta < U$ ($\Delta = 50J$, $L = 64$, $A = 0.005J$). The dashed line is a linear fit to the data. Figures adapted from Ref. [84].

For $J \ll (U - \Delta)$ the ionic Hubbard model can be mapped to an isotropic Heisenberg chain with exchange interaction $J_{XY} = J_Z = (4J^2)/[U(1 - (\Delta/U)^2)]$ [83] which exhibits low energy excitations within a band of width proportional to J_{XY}. We extract the width of the low-energy spectrum from the cutoff at the right boundary of the observed (broad) spectrum in t-DMRG, indicated by dashed vertical lines in Fig. 4.23(a). In Fig. 4.23(b) the extracted width for several U values is shown as a function of J_{XY}. We find that

the width of the absorption spectrum increases linearly with the strength of the Heisenberg exchange interaction J_{XY} which confirms the spin nature of the excitations.

4.5.2 Charge excitations

At higher frequencies gapped charge excitations are expected at $\hbar\omega \sim (U \pm \Delta)$ corresponding to the creation of a doublon-hole pair where the doublon (hole) is either located on a high energy site (low energy site) or vice versa. We time evolve the system at $\Delta = 10J$ and for different interaction strengths U and we extract the energy absorption rate from a fit of the slope (see App. B.1.3). The full spectrum for $U = 40J$ and $U = 50J$ is shown in Fig. 4.24(a) and (b) respectively. We observe three distinct excitation peaks at high energies near $\hbar\omega \sim (U - \Delta),\ U,\ (U + \Delta)$ with a narrow width. The $(U \pm \Delta)$ peaks are asymmetric while the U peak is approximately symmetric. The $(U - \Delta)$ peak shows a strong rise at the right boundary that decreases to very small values near the left boundary while the $(U + \Delta)$ peak exhibits a strong rise near the left boundary and decreases to very small values near the right boundary. The smaller peak at U possibly stems from two-site hopping processes which is in accordance with the reduced amplitude compared to the other two peaks. Note that we observe a similar low energy spectrum as for $\Delta = 50J$ in the previous section, see inset of Fig. 4.24(a).

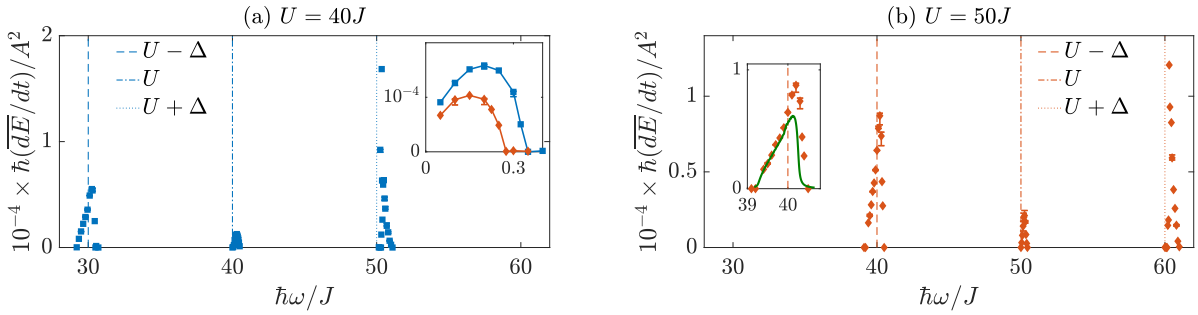

Figure 4.24: The energy absorption rate in t-DMRG for a system size $L = 64$ at $\Delta = 10J$ for an an amplitude of the modulation $A = 0.0005J$ on the Mott insulating site of the Kosterlitz-Thouless transition for $U = 40J$ (a) and $U = 50J$ (b). Vertical dashed lines indicate the energies $(U - \Delta),\ U,\ (U + \Delta)$ at which, naively, an excitation is expected. The inset of (a) shows the low energy spectrum for $A = 0.005J$. The inset of (b) shows a comparison to the averaged rate within the effective model for a broadening $\eta = 0.03J$.

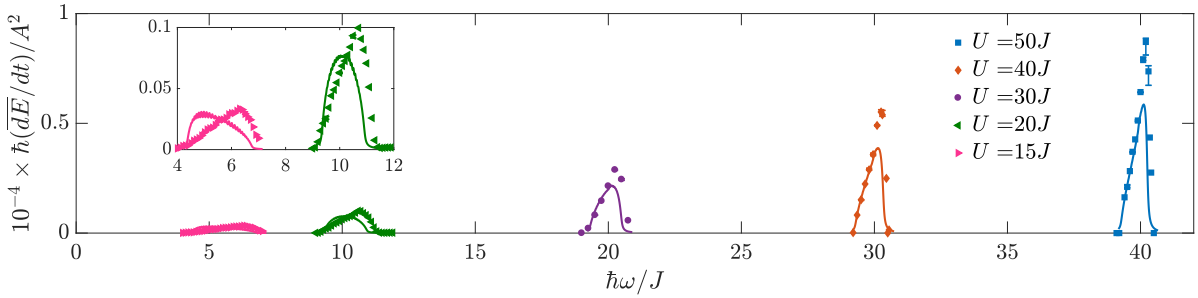

Figure 4.25: The energy absorption peak located near $(U - \Delta)$ in t-DMRG (filled symbols) compared to the averaged rate within the effective model (solid line) for a finite broadening $\eta = 0.04J$ ($L = 64$, $\Delta = 10J$, $A = 0.0005J$). The inset shows a close up of the peaks for $U = 15J$ and $U = 20J$.

We study in more detail the excitation peak located near $(U - \Delta)$. In Fig. 4.25 it is shown at $\Delta = 10J$ for interactions decreasing from $U = 50J$ deep in the Mott insulator to an interaction strength $U = 15J$ closer to the phase transition to the bond order wave. For decreasing interaction, the absorption peak

moves to smaller frequencies as the charge gap decreases. The peak height decreases while the width increases but the structure (strong enhancement at the right boundary) of the peak remains the same. We compare to the averaged energy absorption rate (3.31) obtained within the effective model (cf. Sec. 4.2.2) where we replace the δ-function in Eq. (3.31) by a Lorentz function with broadening η. The averaged rate is also shown in Fig. 4.25. It agrees well with our t-DMRG at $U \sim 30J - 50J$ ($U - \Delta > \Delta$) except for the peak height in the maximum which is underestimated by the effective model. However, the height of the peak within the effective model depends considerably on the choice of the finite broadening η of the Lorentz function. Here, the broadening is chosen such that we obtain a smooth curve. As a consequence the resonant feature at the right boundary of the peak is not resolved and the peak height is underestimated. For a decreased broadening the resonant feature can be better resolved but the curve is then no longer smooth. Separate narrow Lorentz peaks are then visible which makes it hard to compare to the overall behavior. For smaller U, the effective model captures well the width of the absorption peak but the structure of the peak changes while the structure of the t-DMRG peak remains the same. At $U = 20J$ ($U - \Delta = \Delta$) the averaged rate becomes symmetric and at $U = 15J$ ($U - \Delta < \Delta$) the symmetry is inversed and the maximum occurs near the left boundary.

Transition matrix elements In order to gain insights into the origin of the observed structure of the energy absorption rate within the effective model, we study the structure of the square of the transition matrix elements $|\langle AFM|\hat{O}_S|\alpha\rangle|^2$ from an antiferromagnetic ground state $|AFM\rangle$ to the lowest band of excitations $|\alpha\rangle$ within the effective model. In particular, we investigate the effect of the single processes contributing to the effective model, similar to our study in the band insulator (cf. Sec. 4.3.3).

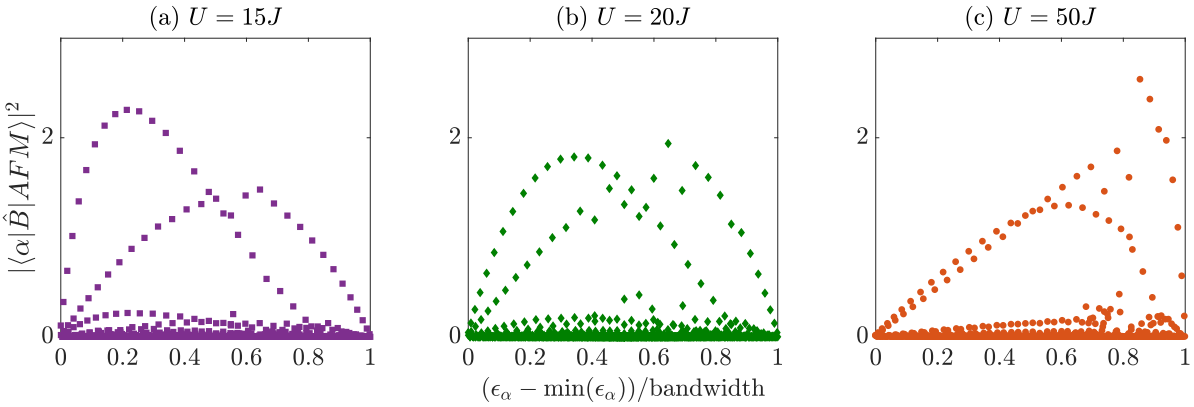

Figure 4.26: The transition matrix elements by superlattice modulation at $\Delta = 10J$ for a system size $L = 64$ at different interactions. At $U = 15J$ (a) for which $U - \Delta < \Delta$ the main weight is located in the left half of the resonant region. At $U = 20J$ (b) for which $U - \Delta = \Delta$ the weight is distributed across both halves of the resonant region and at $U = 50J$ (c) for which $U - \Delta > \Delta$ the main weight is located near the right boundary of the resonant region.

Let us first consider the full transition matrix element. It is shown in Fig. 4.26 at $\Delta = 10J$ for the three cases $U = 15J$, $(U - \Delta) < \Delta$ (a), $U = 20J$, $(U - \Delta) = \Delta$ (b) and $U = 50J$, $(U - \Delta) > \Delta$ (c). The main structure consists of a weak amplitude background on top of which two 'lobes' of larger amplitude occur. At $(U - \Delta) = \Delta$ (b) the structure is somewhat symmetric with one 'lobe' tilted to the left and the other to the right. This reflects the symmetric shape of the averaged energy absorption rate at $U = 20J$. In the two other cases, the structure becomes asymmetric. For $(U - \Delta) < \Delta$ (a), the left 'lobe' increases in amplitude and its maximum shifts further to the left half of the resonant region, corresponding to the increase in absorption at the left boundary of the averaged energy absorption rate at $U = 15J$. For $(U - \Delta) > \Delta$ (c) the maxima of both 'lobes' shift to the right half of the resonant region. One of the lobes increases further

in amplitude and its maximum shifts closer to the right boundary corresponding to the increase in the averaged energy absorption rate at the right boundary of the response within the effective model.
We now analyze the single processes contributing to the effective model. The different processes are explained in Sec. 4.2.2 and sketched in Fig. 4.4. Let us first consider only processes coupling from the first band of excitations to the ground state or to the second band of excitations at an energy difference $\mp(U-\Delta)$ respectively. The resulting transition matrix element squared is shown in Fig. 4.27(a). It displays an enhancement at the left boundary of the resonant region. This reflects the symmetry of the matrix element for $(U-\Delta) < \Delta$ which is in accordance with the processes of amplitude $1/|U-\Delta|$ dominating the Hamiltonian at $(U-\Delta) < \Delta < (U+\Delta)$. Let us now consider only processes coupling from the first band of excitations to the third band of excitations at an energy difference Δ. The resulting transition matrix element squared is shown in Fig. 4.27(b). It displays an enhancement at the right boundary of the resonant region. This reflects the symmetry of the matrix element for $(U-\Delta) > \Delta$ which is in accordance with the processes of amplitude $1/\Delta$ dominating the Hamiltonian at $(U+\Delta) > (U-\Delta) > \Delta$.

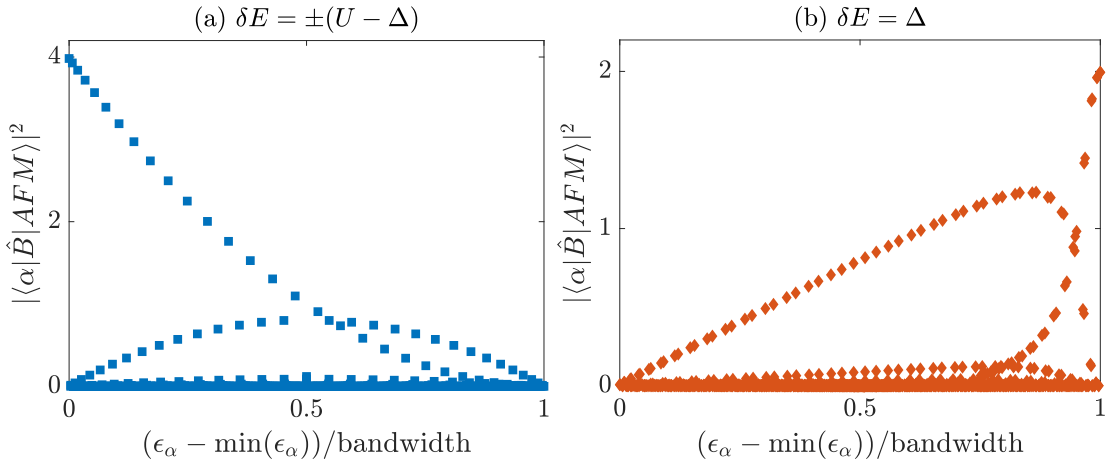

Figure 4.27: (a) The transition matrix element squared when only considering processes coupling via the ground state or the second band of excitations at an energy $\delta E = (\Delta - U), (U - \Delta)$ respectively. The matrix element is independent of the choice of U, Δ and enhanced values occur at the left boundary of the resonant region. (b) The transition matrix element squared when only considering processes coupling via the third band of excitations at an energy $\delta E = \Delta$. The matrix element is independent of the choice of U, Δ and enhanced values occur at the right boundary of the resonant region.

Let us finally comment on the validity of the effective model. Although the bandwidth is correctly captured, it fails to reproduce the symmetry of our t-DMRG results for $(U-\Delta) \leq \Delta$. We attribute this discrepancy to the presence of quantum fluctuations which lead to additional processes that we did not take into account. To gain a first insight into the validity of our approximation we check that the assumption of a Mott insulating ground state is justified for the considered parameters. We verify that the double occupancy is small and that antiferromagnetic correlations can be observed at all considered U, see App. D. However, the assumption of a classical antiferromagnetic ground state neglects quantum fluctuations which are particularly strong in one dimension such that the classical antiferromagnet is only a crude approximation of the real ground state. Including the correct ground state into our calculations for the effective model would bring additional complications. It is not pursued further here as we understand the main features of the observed response.

4.6 Connection to experiment and conclusion

In this chapter we studied the excitation spectrum of the one-dimensional ionic Hubbard model as a response to the superlattice modulation spectroscopy across the entire phase diagram, covering the band and Mott insulating limits as well as the intermediate bond order wave phase and its bordering phase transitions. We showed, using t-DMRG and an effective model, that this modulation provides detailed insights into the gapped excitation spectra in the band and Mott insulating phases as well as the low-energy spin excitation spectrum in the Mott insulator. Moreover, we demonstrate, using t-DMRG and bosonization techniques, that the superlattice modulation spectroscopy reveals features of both the Ising and Kosterlitz-Thouless transitions signaling the presence of the bond order wave phase. This approach could provide a first experimental glimpse into a phase that has so far evaded detection in the solid state context.
In order to reinforce the applicability of our superlattice modulation scheme as an experimental proposal to detect the bond order wave phase, in the following, we address experimentally relevant issues. We address the question of how an inhomogeneous potential usually present in experiments would influence the energy absorption in the different phases and we discuss the effects of finite temperatures at which experiments are performed. Furthermore, we comment on suitable experimental parameter ranges of the ionic Hubbard model.

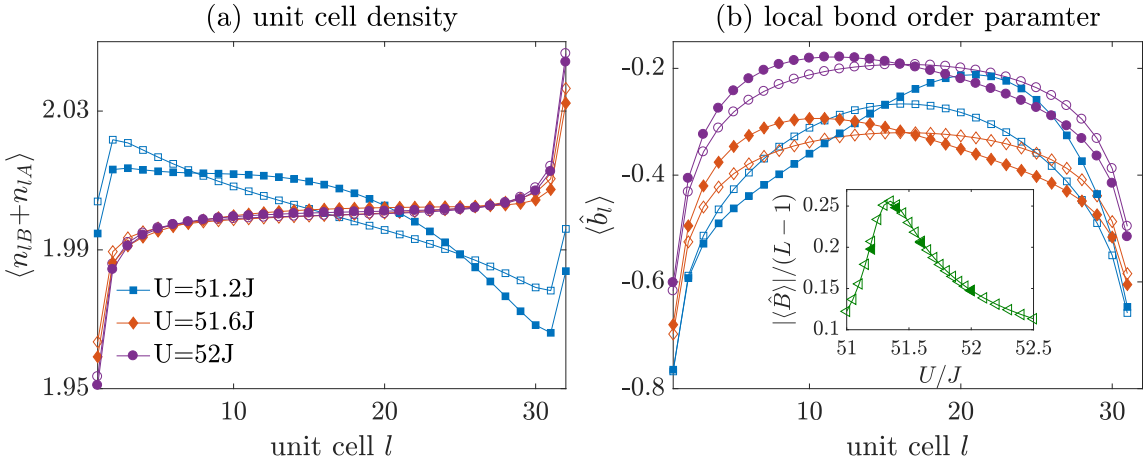

Figure 4.28: Influence of a weak harmonic trapping potential on the unit cell density $\langle n_{lB} + n_{lA} \rangle$ (a) and the local bond order parameter $\hat{b}_l = \langle -c^\dagger_{lA\sigma} c_{lB\sigma} + c^\dagger_{lA\sigma} c_{l+1B\sigma} + \text{H.c.} \rangle$ (b) with unit cell index $l = 1, ..., L/2 - 1$ in the bond order wave phase for a system size $L = 64$ at fixed $\Delta = 50J$ for different $U/J = 51.2,\ 51.6,\ 52$ at Ising criticality and across the bond order wave phase. We compare the homogeneous system (open symbols) to the trapped system (filled symbols) with weak site-symmetric trapping potential $V(j - L/2)^2$ of strength $V = 0.0002J$. (a) The unit cell density is robust to a weak trapping potential away from Ising criticality where the system is gapped. At the Ising critical point the charge gap closes and makes the system sensitive to small variations of the potential. (b) The local bond order parameter is slightly affected by a weak trap, also away from Ising criticality, however we find that the global bond order parameter $|\langle \hat{B} \rangle|/(L-1)$ (inset) is robust to a weak trap away from Ising criticality.

The band insulator and bond order wave phases, where both charge and spin degrees of freedom are gapped, are robust against temperature and small trapping effects. Both phases should be accessible in experiments if one takes care of adiabatically reaching the desired parameter space. In order to verify the robustness of these two phases to the presence of a trapping potential, we performed static DMRG calculations taking a weak harmonic (site-symmetric) trapping potential into account. We find that the band insulator is very robust to the presence of a trap as expected. Within the bond order wave (away from Ising criticality) we find that the unit cell density $\langle n_A + n_B \rangle$, shown in Fig. 4.28(a), is very robust to

the presence of the trap and the local bond order order parameter, shown in Fig. 4.28(b), survives in the presence of a trap, acquiring only a slight asymmetry. Furthermore, the global bond order parameter is practically unchanged away from Ising criticality, see inset of Fig. 4.28(b). At the Ising critical point the system is much more sensitive to external influences due to the closing of the charge gap. At Ising criticality, see Fig. 4.28(a), the unit cell density is modified considerably by the presence of the trap compared to the homogeneous system, in contrast to within the bond order wave. Note that the unit cell density in the homogeneous system at Ising criticality is already asymmetric due to boundary effects which was discussed in Sec. 2.5.2 (cf. Fig. 2.7(a)). The local bond order parameter at Ising criticality acquires a larger asymmetry in the presence of the trap than within the bond order wave phase. In fact, at Ising criticality a homogeneous trapping potential as realized in Refs. [69–71] would be advantageous to unambiguously detect the scaling behavior we identified in this chapter.

The effect of a finite temperature present in experiment needs to be discussed in the Mott insulating phase and at the Ising critical point where the gap closes. It would be desirable to conduct experiments at temperatures below the exchange interaction of the order $\sim J^2/(\Delta + U)$, the lowest temperature scale for spin and charge fluctuations. This is a similar scale as for the antiferromagnetic phase ($\sim J^2/U$) in the repulsive Fermi Hubbard model. Cold fermionic experiments are currently working on reaching these temperature scales and the experimental observation of relevant correlations was recently reported [17–19].

Let us now comment on suitable parameters ranges of the ionic Hubbard model for the detection of the bond order wave. The ionic Hubbard model was experimentally realized for a wide range of parameters [36], for example, Δ could be tuned between $0J$ and $40J$. In our case, it is important to choose parameters such that the bond order wave phase is robust and has a finite extension, preferably as large as possible, such that both phase transitions can be resolved in U. It has been shown that the extent of the bond order wave phase and the strength of the bond order parameter both increase with increasing Δ [98]. Therefore, using a large value for Δ would be beneficial. However, at the same time, the temperature should be below $\sim J^2/(\Delta + U)$ in order to obtain robust results at the Ising critical point as explained above. As this temperature bound decreases with increasing Δ and U, experimentally, one needs to find an acceptable compromise between these two requirements. Moreover, the strength of the applied superlattice modulation should be chosen a small fraction of the hopping amplitude ($\sim 0.05\% - 0.5\%$) in order to obtain results within the linear response regime (cf. App. B)

CHAPTER 5

Thermometry of ultracold fermions in optical lattices by modulation spectroscopy

In this chapter we present a scheme to directly measure the temperature of a fermionic gas confined to an optical lattice by means of modulation spectroscopy.
In fermionic lattice experiments one important macroscopic control parameter is the thermal energy which is intrinsically difficult to control due to the fact that the system is not coupled to a reservoir. A major challenge in the quantum simulation of the Fermi Hubbard model is a further reduction in temperature in order to realize interesting phases, for example long range antiferromagnetic order or unconventional superfluidity [37]. This is accompanied by the need of accurate temperature measurements, in particular when pursuing the goal to map out the equilibrium Fermi-Hubbard phase diagram as a function of temperature. However, experimentalists still lack reliable thermometry methods at low temperatures.
In the absence of an optical lattice potential, for the harmonically trapped gas in the weakly interacting regime, the temperature can be extracted from the integrated density profile imaged after a time-of-flight expansion which reflects the temperature-dependent momentum distribution of the particles trapped in the harmonic potential [53]. This is more difficult at strong interactions as the expansion is no longer ballistic but the temperature can be extracted from the 'tail' of the distribution in many cases. However, this becomes inaccurate at very low temperatures of a few percent of the recoil energy. Typically, the temperature is measured before and after ramping into the optical lattice. Assuming entropy conservation during the loading process, one can determine the temperature in the lattice from the initial entropy. This is markedly limited by non-adiabatic heating processes caused by the ramping of the lattice or by light scattering. Furthermore, it cannot be used for in-lattice cooling schemes. Thus, the development of in-lattice thermometry techniques is of relevance. Different possible schemes to directly measure the temperature of fermionic particles in the optical lattice have been proposed and tested in experiments. All these methods have their limitations and most cannot be extended into the low-energy regime of interest. Ref. [38] gives an overview on some of the thermometry schemes available for bosonic and fermionic particles. Here, we shortly summarize the most important thermometry setups for fermionic particles. For instance, the temperature can be extracted from the double occupancy [156, 157] which is sensitive to thermal fluctuations for temperatures on the order or above the on-site interaction strength. The authors of Ref. [158] suggest a temperature measurement based on the fluctuation-dissipation theorem and spatially resolved density-density correlations. This requires in-situ resolution in the measurement which has only recently been achieved [159–162]. It was suggested to use Raman spectroscopy, transferring the atoms to a third hyperfine state, such that the Raman signal depends on the temperature-dependent Fermi factor [163], or to use off-resonant light diffraction from atoms in the lattice as a thermometer since the

scattered intensity carries information on density-density fluctuations [164]. Later on, it was suggested to study the temperature-dependent fluctuations in the momentum distribution as a response to an artificial gauge field [165]. Moreover, the temperature of fermions in an anisotropic three-dimensional lattice has been extracted from a measurement of the nearest-neighbor spin correlator [166] and by spin-sensitive Bragg scattering of light [167].
Taking this background as a starting point we suggest lattice modulation spectroscopy as a possible thermometer for non-interacting fermionic particles confined to an optical lattice which is easy to implement in experiment and works particularly well for temperatures below the Néel temperature where antiferromagnetic ordering is expected to occur in contrast to the above methods which mostly fail in this temperature regime. Here, we present a thermometry setup based on the normal lattice modulation spectroscopy (cf. Sec. 2.6). In Sec. 5.1 we develop a multiple band tight-binding description for the considered setup, non-interacting fermionic particles in an optical lattice. This section is rather technical, no results will be given. The obtained tight-binding model will be used for all calculations in the subsequent sections. In Sec. 5.2 we explain in detail the detection scheme, a measurement of the number of excited atoms by means of the adiabatic band mapping technique and how this relates to the atom excitation rate within linear response theory. We then study the atom excitation rate as a response to a time-dependent modulation of the lattice amplitude for the one-dimensional homogeneous system in Sec. 5.3 and for the trapped system in one and two dimensions in Sec. 5.4. We show that the response reflects a clear signature of the Fermi distribution of the equilibrium system and we discuss the possibilities of thermometry considering realistic experimental parameters. In Sec. 5.5 we compare the results for the normal lattice modulation scheme to the superlattice modulation spectroscopy, another suitable setup for thermometry, which was investigated in the author's master thesis [168, 169]. Note that in the figures in Secs. 5.1 and 5.2 we will directly show the comparison to the superlattice modulation although the results will not be discussed before Sec. 5.5. In Sec. 5.6 we summarize and comment on the applicability of our scheme to systems of interest. The results of this chapter are published in Ref. [169].
More recently, by means of in-situ measurements, it has been demonstrated that the temperature can be determined from the equation of state which relates the temperature to the in-situ density profile [17, 54, 170, 171] or by a reconstruction of the local entropy from occupation probabilities [162]. At lower temperatures on the order of or below the hopping parameter, the temperature can be extracted from the spin structure factor [18, 19] or the nearest-neighbor spin correlations [17, 19]. However, away from half-filling numerical simulations are challenging such that adequate thermometry methods remain an important open question in some parameter ranges.

5.1 Two-band tight-binding model

In this section we introduce a multiple band tight-binding description which is a convenient description to study the response of the system to lattice amplitude modulation. We consider non-interacting fermionic atoms confined to the three-dimensional periodic potential $V_0(\vec{x})$ (2.2) in the absence of an additional external trapping potential. We assume the lattice to be sufficiently deep such that the lowest Bloch bands are well separated. We compute the eigenfunctions which are the Bloch functions along the different directions $x_i = x,\ y,\ z$ corresponding to $i = 1,\ 2,\ 3$. We denote the Bloch functions $\phi^{k_{x_i}}_{\alpha_{x_i}}(x_i)$ with corresponding eigenvalues $E_{\alpha_{x_i}}(k_{x_i})$ where α_{x_i} denotes the band index and the quasimomentum k_{x_i} lies within the first Brillouin zone $]-k_L, k_L]$. For details see Sec. 2.2.2 where we outline how to obtain the Bloch spectrum from the single-particle Schrödinger equation. The full spectrum in three dimensions is given by $E_\alpha(\vec{k}) = E_{\alpha_x}(k_x) + E_{\alpha_y}(k_y) + E_{\alpha_z}(k_z)$ as we consider non-interacting fermions for which the potential is separable. The index $\alpha \equiv \{\alpha_x, \alpha_y, \alpha_z\}$ labels the band. Note, that the Bloch functions

factorize $\phi^{\vec{k}}_{\alpha}(\vec{x}) = \phi^{k_x}_{\alpha_x}(x)\phi^{k_y}_{\alpha_y}(y)\phi^{k_z}_{\alpha_z}(z)$ in the tight-binding approximation, neglecting the coupling to other Bloch bands and the overlap of different sites. The unperturbed Hamiltonian (2.7) (for $V_{\text{trap}} = 0$ and $V(\vec{x} - \vec{x}') = 0$) in Bloch basis is then given by

$$H_0 \approx \sum_{\alpha,\vec{k},\sigma} \left(E_\alpha(\vec{k}) - \mu\right) c^\dagger_{\alpha\vec{k}\sigma} c_{\alpha\vec{k}\sigma}, \tag{5.1}$$

where $c^{(\dagger)}_{\alpha\vec{k}\sigma}$ are the fermionic annihilation (creation) operators and where we include a chemical potential μ which controls the particle number.
We apply normal lattice amplitude modulation along one direction x. We assume that initially only the lowest band $\alpha = 1 \equiv \{\alpha_x = 1, \alpha_y = 1, \alpha_z = 1\}$ is occupied and we consider excitations to a higher Bloch band $\alpha' = \{\alpha'_x > 1, \alpha'_y = 1, \alpha'_z = 1\}$. We count the bands starting from one, that means the lowest band $\alpha = 1$ is called the first band. Referring to the bands of excitations we also start counting from one. This means that the first band of excitations corresponds to the second band $\alpha' = 2$ and the second band of excitations corresponds to the third band $\alpha' = 3$. The basic idea is that the frequency-resolved atom excitation rate to higher Bloch bands will reflect the Fermi factor as it will depend on the temperature-dependent filling of the lowest band. The atom excitation rate will be investigated for the homogeneous and the trapped system in Secs. 5.3 and 5.4. From a measurement of the atom excitation rate to higher Bloch bands, the temperature can be extracted. A suitable detection scheme will be discussed in Sec. 5.2.

In the mean time, we construct the perturbing term (2.39) (added to the Hamiltonian by the lattice modulation) in Bloch Basis representation. In order to construct the perturbing operator $\hat{O}_N$ in Bloch basis representation, we need to determine the transition matrix elements from the initial state to the final state by the perturbing potential $\delta V(x) = \sin^2(k_L x)$ (cf. Sec. 2.6 where we derive the time-dependence of the modulated potential). Thus, the transition matrix elements of interest are given by

$$M_{(\alpha=1,\vec{k})\to(\alpha',\vec{k}')} = \frac{1}{\Omega_x} \int_{x_{\min}}^{x_{\max}} \mathrm{d}x\, \phi^{k'_x *}_{\alpha'_x}(x)\delta V(x)\phi^{k_x}_{\alpha_x=1}(x) \prod_{i\neq 1} \delta_{\alpha'_{x_i},\alpha_{x_i}=1}\, \delta_{k'_{x_i},k_{x_i}}, \tag{5.2}$$

where $\Omega_x = (L-1)a$ is the system size in x-direction with L the number of lattice sites and a the lattice spacing, $x_{\min} = -(L/2-1)a$ and $x_{\max} = La/2$. We used that the Bloch functions are orthonormal, i.e. $(1/\Omega_{x_i}) \int_{x_{i,\min}}^{x_{i,\max}} \mathrm{d}x_i\, \phi^{k'_{x_i}*}_{\alpha'_{x_i}}(x_i)\phi^{k_{x_i}}_{\alpha_{x_i}}(x_i) = \delta_{\alpha'_{x_i},\alpha_{x_i}}\delta_{k'_{x_i},k_{x_i}}$ such that the contributions along y and z direction reduce to δ-functions. We insert the perturbing potential $\delta V(x) = \sin^2(k_L x)$ and find that the perturbation, to a good approximation, only couples momenta $\vec{k}$ and $\vec{k}' \approx \vec{k}$. This is illustrated in Fig. 5.1(a) where the transition probability to the first band of excitations $\alpha'_x = 2$ as a function of k_x and k'_x is shown. All other matrix elements for $\Delta\vec{k} \neq 0$ are strongly suppressed. Quasimomentum is approximately conserved. This is in accordance with the common lowest band tight-binding approximation which conserves quasimomentum as may be seen from a Fourier transform of the operator $\hat{O}_N$ (2.40) in the lowest band tight-binding description, $\hat{O}_N = 2\sum_{k_x,\sigma} \cos(ak) c^\dagger_{k_x\sigma} c_{k_x\sigma}$. We approximate

$$M_{(\alpha=1,\vec{k})\to(\alpha',\vec{k}')} = M_{\alpha'_x}(k_x,k'_x) \prod_{i\neq 1} \delta_{k'_{x_i},k_{x_i}} \approx M_{\alpha'_x}(k_x)\delta_{\vec{k},\vec{k}'}, \tag{5.3}$$

such that in the multiple band tight-binding approximation the perturbing operator becomes

$$\hat{O}_N = \sum_{\vec{k},\sigma} M_{\alpha'_x}(k_x)\left(c^\dagger_{\alpha'\vec{k}\sigma} c_{\alpha=1\vec{k}\sigma} + \text{H.c.}\right). \tag{5.4}$$

The transition probability $|M_{\alpha'_x}(k_x)|^2$ for exciting atoms from the lowest band to the band $\alpha'_x = 2$ or $\alpha'_x = 3$ with zero momentum transfer $\Delta k_x = 0$ is shown in Fig. 5.1(b). Excitations to the first excited band $\alpha'_x = 2$ (blue solid line) are prohibited at the center $k_x = 0$ and the border $k_x = k_L$ of the Brillouin zone due to the symmetry of the Bloch functions. The maximum probability lies in between coinciding with the region of interest around the Fermi surface of a half-filled lowest band. This is advantageous as the temperature dependence of the Fermi surface will be captured by the response (atom excitation rate) of the system to lattice modulation spectroscopy. Additionally, the amplitude is sufficiently strong such that the atom excitation rate is strong enough to obtain a detectable signal at small perturbing amplitudes and reasonable perturbing times. We comment on the detectability in more detail, giving numbers for an experimental example (in the presence of an external trap) in Sec. 5.4.

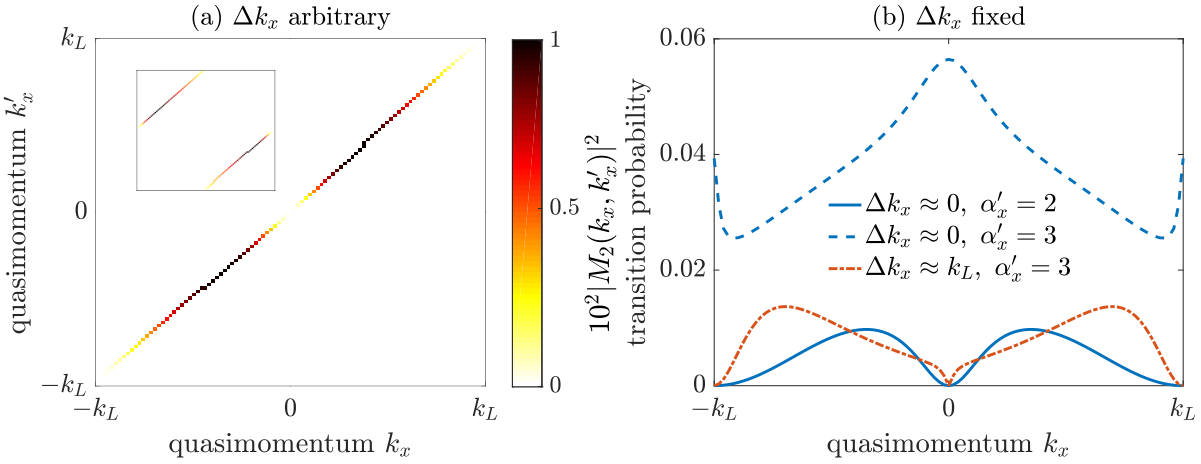

Figure 5.1: (a) The transition matrix elements squared $|M_{\alpha'_x=2}(k_x, k'_x)|^2$ for exciting atoms at quasimomentum k_x from the lowest band $\alpha = 1$ to the first excited band $\{\alpha'_x = 2, \alpha_y = 1, \alpha_z = 1\}$ for all k'_x by normal lattice amplitude modulation. The only non-zero elements correspond to $k'_x = k_x$. Inset: The transition matrix elements squared $|M_{\alpha'_x=3}(k_x, k'_x)|^2$ for exciting atoms at quasimomentum k_x from the lowest band $\alpha = 1$ to the second excited band $\{\alpha'_x = 3, \alpha_y = 1, \alpha_z = 1\}$ for all k'_x by superlattice modulation spectroscopy. In the case of the superlattice modulation, the only non-zero elements correspond to $\Delta k_x = k_L$. This case will be discussed in Sec. 5.5. (b) The transition probability $|M_{\alpha'_x}(k_x)|^2$ for exciting atoms to the first (blue solid line) $\alpha'_x = 2$ and the second excited (blue dashed line) $\alpha'_x = 3$ band at quasimomentum $k'_x = k_x$ by normal lattice modulation and for exciting atoms to the second excited band (orange dash-dotted line) $\alpha'_x = 3$ at quasimomentum $k'_x = k_x + k_L$ by superlattice modulation. In (a) and (b) we consider a lattice depth $V_0 = 7E_r$ in x-direction. Figures adapted from Ref. [169].

In contrast, excitations to the second excited band $\alpha' = 3$ (blue dashed line) are non-zero for all quasimomenta k_x and the amplitude is about three times larger, also see Fig. 5.1(b). The transition probability $|M_3(k_x)|^2$ is maximum at $k_x = 0$ and $k_x = k_L$ such that the response at the corresponding frequencies will be dominated by these contributions if considering the full range of excitations. Consequently, it is more favorable to use excitations to $\alpha' = 2$ for a temperature measurement at intermediate lattice heights.
Let us remark, that the increase of transition amplitude with increasing α' from 2 to 3 is in agreement with the harmonic oscillator approximation for deep lattices. In this case, the lattice wells almost decouple and each well can be approximated by a harmonic oscillator (cf. Sec. 2.2.2). The modulation spectroscopy then corresponds to a frequency modulation of the quantum harmonic oscillator, $\tilde{\omega}_{HO} = \omega_{HO}(1 + \rho)$, where ρ is a small parameter. This modulation couples to the second excited band, but transitions to the first excited band are prohibited by symmetry. We confirm that the transition probability to the first excited band $|M_2(k_x)|^2$ decreases for increasing lattice depths in accordance with the harmonic oscillator approximation.

5.2 Detection scheme

In this section we suggest a simple measurement scheme of the energy absorbed by the system as a response to the lattice amplitude modulation which enables one to measure the excitation rate quasimomentum-resolved and thus reflecting the temperature-dependence of the Fermi factor.
In bosonic systems, energy absorption imprints a characteristic signal in time-of-flight absorption images after sudden switch-off. The energy absorbed by the system is typically estimated from the broadening of the central peak of the momentum distribution. From this, precise information on the excitation spectrum can be obtained [21] (cf. Sec. 2.6). Moreover, it was demonstrated that a comparison of time-of-flight absorption images to Quantum Monte Carlo simulations for strongly interacting Bose gases on a lattice can be used as a direct thermometer [172] which enabled the experimental determination of the finite temperature phase diagram for bosonic superfluids in an optical lattice. Determining the energy absorbed by fermionic systems from the momentum distribution in time-of-flight images is much harder than for bosons. The momentum distribution is step-like due to fermionic statistics and not as sensitive to heating. It only depends on temperature by a smearing of the Fermi surface such that very high momentum resolution is necessary in order to extract the temperature. The concept considered here relies on the excitation to higher Bloch bands by means of modulation spectroscopy combined with the adiabatic band mapping technique.

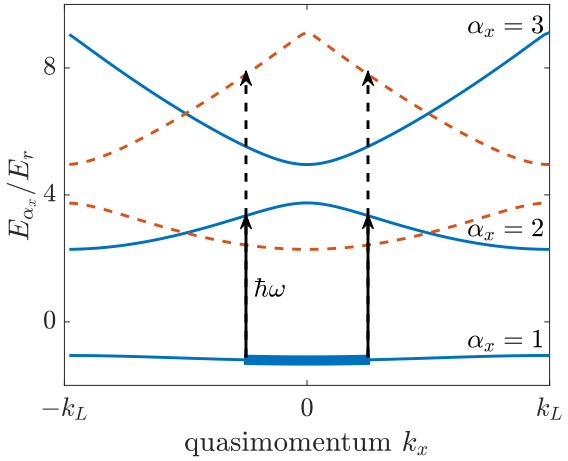

Figure 5.2: The three lowest Bloch bands of a homogeneous optical lattice along x-direction (blue solid lines). In the case of the normal lattice modulation the perturbing frequency (solid arrows) is chosen such that atoms are transferred from the lowest band $\alpha_x = 1$ to the first excited band $\alpha'_x = 2$ with conserved quasimomentum k_x. In the case of the superlattice modulation the perturbing frequency (dashed arrows) is chosen such that atoms are transferred from the lowest band $\alpha_x = 1$ at quasimomentum k_x to the second excited excited band $\alpha'_x = 3$ at quasimomentum $k_x + k_L$ which is equivalent to exciting to the shifted band $E_{\alpha_x=3}(k_x + k_L)$ (orange dashed line) at same quasimomentum k_x. The shifted band $E_{\alpha_x=2}(k_x + k_L)$ is also depicted by an orange dashed line. The minimal and maximal value of the possible excitation energies are related to the initial filling of the lowest band indicated by a thicker line, that corresponds to quarter-filling at zero temperature in this figure. The minimum possible excitation energy at zero temperature is indicated by the arrows. The band structure calculation was done for a lattice depth $V_0 = 7E_r$ along the x-direction.

We consider lattice modulation frequencies such that excitations from the lowest band $\alpha_x = 1$ to the first excited band $\alpha'_x = 2$ are created. Possible excitations are sketched in Fig. 5.2. The transition probability is non-zero for conserved quasimomentum $\Delta k_x \approx 0$ such that excitations occur vertically in quasimomentum space. As the second band is inverted and stretched (in energy) compared to the lowest band, exactly one quasimomentum pair $\pm k_x$ is on resonance for each excitation energy $\hbar\omega$. Thus,

a quasimomentum-resolved excitation is guaranteed and can be detected by a measurement of the transferred band occupation $\langle n_\omega^{\alpha'_x}(t)\rangle$ to the excited band α'_x without the necessity of quasimomentum resolution within the band

Possible excitations strongly depend on the initial filling of the lowest band. For example, in Fig. 5.2 the vertical arrows indicate the transition frequency corresponding to the largest occupied momentum pair (the initial occupation is indicated by the thick line which covers a fraction of the lowest band) which gives a lower bound for the possible excitation frequencies. At finite temperatures, the filling (occupation of single-particle states) of the lowest band is determined by the Fermi function which depends on temperature. Consequently, the response (atom excitation rate) is quasimomentum-resolved and reflects the temperature dependence of the occupation of the lowest band. We sometimes refer to this temperature dependence as Fermi dependence. Additionally, as the band of excitations is inverted and broader (in energy) compared to the lowest band, the Fermi dependence of the response will be magnified in energy space, i.e. the Fermi dependence is 'stretched' with respect to the initial Fermi distribution in the lowest band. Consequently, the required frequency resolution needed in experiment to resolve the Fermi tail is considerably reduced. Note that band inversion itself leads to a stretching of the Fermi distribution by a factor 2 which is strongly enhanced by the increased bandwidth of the excited band.

This is experimentally appealing because a measurement of the transferred band occupation amounts to merely counting the particles appearing in higher Brillouin zones in adiabatic band mapping [173]. The basic idea of this technique is to ramp down the lattice adiabatically such that quasimomentum is conserved in contrast to a sudden switch-off. Adiabatic means slow compared to the vibrational frequencies in the lattice but fast enough such that the population of the energy bands does not change during ramp down. Each state with quasimomentum k is finally mapped onto a free particle state with momentum k when the lattice is completely switched off. A particle in the n^{th} energy band is mapped onto the n^{th} momentum interval of the free particle. In a time-of-flight absorption image particles from the n^{th} energy band appear in the n^{th} Brillouin zone. Thus, applying adiabatic band mapping after a certain duration t of the perturbation gives access to the transferred band occupation $\langle n_\omega^{\alpha'_x}(t)\rangle$. Here, quasimomentum resolution in the measurement is not required as the excited quasimomenta are fixed by the perturbation frequency (cf. Fig. 5.2). A multiplication of the transferred band occupation with the perturbing frequency yields the absorbed energy $E(t) - E_0 = \hbar\omega\langle n_\omega^{\alpha'_x}(t)\rangle$. In the linear response regime (cf. Sec. 3.2) we expect a linear increase in time of the absorbed energy and similarly of the transferred band occupation. Within linear response theory, the slope of the transferred band occupation can be related to the atom excitation rate which can be obtained from the energy absorption rate $\overline{dE/dt}$ (3.30) and is given by

$$\frac{1}{|A|^2}\partial_t\langle n_\omega^{\alpha'}\rangle \;=\; \frac{1}{2\hbar}\frac{\pi}{Z_0}\left(1-e^{-\beta\hbar\omega}\right)\sum_{n,m}\left|\langle m|\hat{O}_N|n\rangle\right|^2 e^{-\beta E_n}\delta\left(\hbar\omega-(E_m-E_n)\right), \tag{5.5}$$

where $Z_0 = \sum_n \exp(-\beta E_n)$ is the partition function, $\beta = 1/(k_B T)$ is the inverse temperature, $|n\rangle$ and $|m\rangle$ are eigenstates of the unperturbed system H_0 (5.1) with corresponding eigenenergies E_n and E_m and the perturbing part of the Hamiltonian it given by $\hat{O}_N$ (5.4). The application of linear response to the considered situation of non-interacting fermions might seem counter-intuitive at a first sight because exact momentum resolution of the sinusoidal perturbation would lead to a resonant coupling of two discrete levels and induce clean Rabi-oscillations. However, in a typical experimental setup due to the presence of an additional trapping potential, weak interactions and a finite perturbation time, a group of states is excited by the perturbation which yields a linear rise in energy for sufficiently large times. One can verify the applicability of linear response theory using a time-dependent density-matrix renormalization group study. This was done considering an example case including a harmonic trapping potential or

nearest-neighbor interactions in Ref. [168].

5.3 Homogeneous system in one dimension

In this section, we consider the simplest case consisting of homogeneous one-dimensional tubes of atoms in an optical lattice oriented along the x direction. The perturbing operator (5.4) acting on the one-dimensional system becomes $\hat{O}_N = \sum_{k_x,\sigma} M_{\alpha'_x}(k_x)\left(c^\dagger_{\alpha'_x k_x \sigma} c_{\alpha_x=1 k_x \sigma} + \text{H.c.}\right)$ such that the atom excitation rate (5.5) becomes

$$\begin{aligned}\frac{1}{|A|^2}\partial_t \langle n^{\alpha'}_\omega\rangle &= \frac{1}{2\hbar}\frac{\pi}{Z_0}\left(1-e^{-\beta\hbar\omega}\right)\sum_{n,m}\left|\left\langle m\right|\sum_{k_x,\sigma} M_{\alpha'_x}(k_x)\left(c^\dagger_{\alpha'_x k_x\sigma}c_{\alpha_x=1k_x\sigma} + c^\dagger_{\alpha_x=1k_x\sigma}c_{\alpha'_x k_x\sigma}\right)\left|n\right\rangle\right|^2 \\ &\quad \times e^{-\beta E_n}\delta\left(\hbar\omega - (E_m - E_n)\right). \end{aligned} \tag{5.6}$$

The momentum-selectivity of the perturbation fixes the possible configurations of $|n\rangle$ and $|m\rangle$ which give non-zero expectation value at a certain k_x-value and a certain σ-value. We can thus drop the sum $\sum_{k_x,\sigma}$ keeping in mind that the sum over the states $\sum_{n,m}$ contains all possible configurations of k_x and σ at which an excitation can occur. We denote this sum as $\sum_{n(k_x,\sigma),m(k_x,\sigma)}$. Assuming that initially only the lowest band is occupied, the resonance condition becomes $E_m - E_n = E_{\alpha'_x}(k_x) - E_{\alpha_x=1}(k_x)$ and we can neglect the second term since $c^\dagger_{\alpha_x=1k_x\sigma}c_{\alpha'_x k_x\sigma}|n\rangle$ gives zero. We obtain

$$\begin{aligned}\frac{1}{|A|^2}\partial_t \langle n^{\alpha'}_\omega\rangle &= \frac{1}{2\hbar}\frac{\pi}{Z_0}\left(1-e^{-\beta\hbar\omega}\right)\sum_{n(k_x,\sigma),m(k_x,\sigma)}\left|M_{\alpha'_x}(k_x)\right|^2\left|\langle m|c^\dagger_{\alpha'_x k_x\sigma}c_{\alpha_x=1k_x\sigma}|n\rangle\right|^2 \\ &\quad \times e^{-\beta(E_n-\mu N)}\delta\left(\hbar\omega - (E_{\alpha'_x}(k_x) - E_{\alpha_x=1}(k_x))\right) \\ &= \frac{1}{2\hbar}\frac{\pi}{Z_0}\left(1-e^{-\beta\hbar\omega}\right)\sum_{n(k_x,\sigma),m(k_x,\sigma)}\left|M_{\alpha'_x}(k_x)\right|^2\langle n|c^\dagger_{\alpha_x=1k_x\sigma}c_{\alpha'_x k_x\sigma}|m\rangle\langle m|c^\dagger_{\alpha'_x k_x\sigma}c_{\alpha_x=1k_x\sigma}|n\rangle \\ &\quad \times e^{-\beta(E_n-\mu N)}\delta\left(\hbar\omega - (E_{\alpha'_x}(k_x) - E_{\alpha_x=1}(k_x))\right) \\ &= \frac{\pi}{2\hbar}\left(1-e^{-\beta\hbar\omega}\right)\sum_{n(k_x,\sigma)}\left|M_{\alpha'_x}(k_x)\right|^2\langle n|c^\dagger_{\alpha_x=1k_x\sigma}c_{\alpha'_x k_x\sigma}c^\dagger_{\alpha'_x k_x\sigma}c_{\alpha_x=1k_x\sigma}|n\rangle \\ &\quad \times\frac{e^{-\beta(E_n-\mu N)}}{Z_0}\delta\left(\hbar\omega - \left(E_{\alpha'_x}(k_x) - E_{\alpha_x=1}(k_x)\right)\right) \\ &= \frac{\pi}{2\hbar}\left(1-e^{-\beta\hbar\omega}\right)\sum_{k_x,\sigma}\left|M_{\alpha'_x}(k_x)\right|^2 f\left(E_{\alpha_x=1}(k_x)-\mu\right)\left(1-f\left(E_{\alpha'_x}(k_x)-\mu\right)\right) \\ &\quad \times\delta\left(\hbar\omega - \left(E_{\alpha'_x}(k_x) - E_{\alpha_x=1}(k_x)\right)\right), \end{aligned} \tag{5.7}$$

where the sum runs over all k_x in the first Brillouin zone and with the Fermi factor $f(E-\mu) = 1/(1+\exp((E-\mu)/k_BT))$. Using $\hbar\omega = E_{\alpha'_x}(k_x) - E_{\alpha_x=1}(k_x)$ we find

$$\left(1-e^{-\beta\hbar\omega}\right)f\left(E_{\alpha_x=1}(k_x)-\mu\right)\left(1-f\left(E_{\alpha'_x}(k_x)-\mu\right)\right) = f\left(E_{\alpha_x=1}(k_x)-\mu\right) - f\left(E_{\alpha'_x}(k_x)-\mu\right), \tag{5.8}$$

and Eq. (5.7) becomes

$$\begin{aligned}\frac{1}{|A|^2}\partial_t\langle n_\omega^{\alpha'}\rangle &= \frac{\pi}{2\hbar}\sum_{k_x,\sigma}\left|M_{\alpha_x'}(k_x)\right|^2\left[f\left(E_{\alpha_x=1}(k_x)-\mu\right)-f\left(E_{\alpha_x'}(k_x)-\mu\right)\right]\\ &\quad\times\delta\left(\hbar\omega-\left(E_{\alpha_x'}(k_x)-E_{\alpha_x=1}(k_x)\right)\right)\\ &= \frac{\pi}{\hbar}\sum_{k_x}\left|M_{\alpha_x'}(k_x)\right|^2\left[f\left(E_{\alpha_x=1}(k_x)-\mu\right)-f\left(E_{\alpha_x'}(k_x)-\mu\right)\right]\\ &\quad\times\delta\left(\hbar\omega-\left(E_{\alpha_x'}(k_x)-E_{\alpha_x=1}(k_x)\right)\right)\end{aligned} \tag{5.9}$$

The second term can be neglected as we assume that initially only single-particle states in the lowest band are occupied. Taking the continuum limit $\sum_{k_x}\to(L/2k_L)\int_{-k_L}^{k_L}\mathrm{d}k_x$ we obtain

$$\frac{1}{|A|^2}\partial_t\langle n_\omega^{\alpha_x'}\rangle^{1D}=\frac{\pi L}{\hbar k_L}\int_0^{k_L}\mathrm{d}k_x\,|M_{\alpha_x'}(k_x)|^2 f\left(E_{\alpha_x=1}(k_x)-\mu\right)\delta\left(\hbar\omega-\left(E_{\alpha_x'}(k_x)-E_{\alpha_x=1}(k_x)\right)\right). \tag{5.10}$$

This expression strongly depends on temperature through the Fermi function. As a realistic example we consider ^{40}K-atoms trapped in an optical lattice created from a laser wave of wave length $\lambda = 1064$nm for the band structure calculation and we conveniently express all energies in units of the atomic recoil energy $E_r = h^2/2m\lambda^2$. These parameters are used throughout the remainder of this chapter. Temperatures are expressed in units of the nearest-neighbor tunneling amplitude J of the atoms in the lowest band of the one-dimensional optical lattice $J = (E_{\alpha_x=1,\max} - E_{\alpha_x=1,\min})/4 \approx 0.04E_r$.

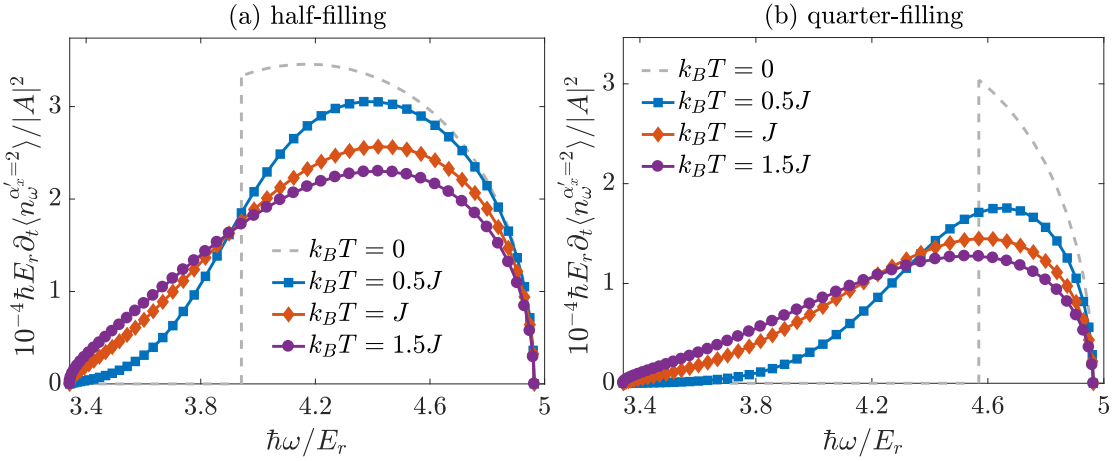

Figure 5.3: The atom excitation rate of the one-dimensional homogeneous system by normal lattice amplitude modulation to the first band of excitations $\alpha_x' = 2$ for a half-filled (a) and quarter-filled (b) lowest band at temperatures k_BT=0, 0.5J, 1J and 1.5J. Figures adapted from Ref. [169].

In Fig. 5.3 we show the atom excitation rate to the first excited band $\alpha_x' = 2$ for different temperatures at half- and quarter-filling of the lowest band in (a) and (b) respectively. At zero temperature, all states up to the Fermi energy are filled whereas all states above the Fermi energy are empty. Consequently, the minimal possible excitation energy corresponds to the excitation energy of an atom located at the Fermi surface (cf. Fig. 5.2). Smaller energies correspond to states located above the Fermi surface which are empty and the zero-temperature response vanishes. At higher excitation energies the response is finite as atoms below the Fermi surface can be addressed. The maximal excitation energy possible in this setup is always given by the energy needed to excite an atom with quasimomentum $k_x = 0$. At finite

temperatures the atoms get thermally excited around the Fermi surface such that the step-like nature of the response at zero temperature softens around the Fermi step according to the Fermi function. Now, the possible excitations depend on the Fermi distribution in the lowest band. There is no longer a sharp frequency cutoff in the response but the Fermi dependence of the occupation is reflected in the response as a function of excitation energy. We study temperatures k_BT=0.5J, 1J and 1.5J. For both fillings the temperature dependence of the response is clearly visible. The position of the Fermi tail depends on the filling due to the dependence of the the excitation energy $\hbar\omega$ on the quasimomentum k_x. The Fermi tail shifts to smaller energies for larger fillings as the center of the Fermi function is shifted to larger k_x. At higher temperatures the Fermi step smears out more which results in a broadening of the low frequency tail, in particular at low fillings. The possible broadening is limited by the upper band edge, limiting the resolution at high temperatures. Moreover, the Fermi tail is broadened in energy due to the increased bandwidth of the first excited band with respect to the lowest band. The different response functions can be clearly distinguished for the displayed temperatures in Fig. 5.3.

5.4 Trapped system

In this section we consider the response of the system in the presence of an external harmonic trapping potential as given by Eq. (2.3) which is present in typical experimental setups. In the presence of a trapping potential, the filling varies when moving through the trap. Consequently, we need to consider the effect of a trapping potential on the full response as the response strongly depends on the filling. We treat the trap within the local density approximation (LDA) which considers the external potential as a spatially varying chemical potential. We start by introducing the LDA in Sec. 5.4.1. We then apply it to obtain the atom excitation rate of the harmonically trapped system. We study the one-dimensional trapped system in Sec. 5.4.2 and we then extend our study to higher-dimensional trapped systems modulated along one direction in Sec. 5.4.3. In particular, we consider relevant experimental parameters in order to quantify the required frequency resolution in experiment.

5.4.1 Local density approximation

In the LDA [174], a d-dimensional trapping potential of the general form $V(\vec{x}) = V_{\text{trap}}(|\vec{x}|/a)^\gamma$ (with exponent γ), where $\vec{x}$ is the position vector in d dimensions, a is the lattice spacing and V_{trap} is the strength of the external confinement, is absorbed into the chemical potential. The chemical potential then depends on space as

$$\mu(x_j) = \mu_0 - V_{\text{trap}} \left(\frac{|x_j|}{a} \right)^\gamma , \tag{5.11}$$

where x_j denotes the d-dimensional position vector labeling each lattice site and μ_0 is the chemical potential in the center of the trap. Within the LDA any observable of the trapped system $A(x_j)$ can be related to the observable of the homogeneous system $A_h(\mu)$ as $A(x_j) = A_h(\mu(x_j))$. Consequently, different phases may coexist in the trap as the local density changes in space. The LDA can be used to a good degree of accuracy in many cases [175] but results are poor for narrow traps where the potential varies rapidly on the scale of the lattice spacing or near a phase transition due to proximity effects. Particles from one phase may leak into the neighboring phase such that there is no clean phase boundary between spatially separated different phases which is neglected in the LDA. This can be incorporated by numerical calculations.
In the LDA, the total particle number in the trap is obtained by summing the space-dependent local

occupancy n_j over the whole system. In the continuum limit one obtains

$$N = \sum_j n_j \approx \frac{\Omega_{d-1}}{a^d} \int \mathrm{d}x\, x^{d-1} n_h(x) = \left(\frac{D}{V_{\mathrm{trap}}}\right)^{d/\gamma} \frac{\Omega_{d-1}}{\gamma} \int_{-\infty}^{\bar{\mu}_0} \mathrm{d}\bar{\mu} (\bar{\mu}_0 - \bar{\mu})^{\frac{d}{\gamma}-1} n_h(\bar{\mu}), \tag{5.12}$$

where $n_h(x)$ is the density in the homogeneous system and Ω_{d-1} is the surface of a sphere in d dimensions, for example $\Omega_0 = 2$, $\Omega_1 = 2\pi$ and $\Omega_2 = 4\pi$, and the dimensionless chemical potential is given by $\bar{\mu} = \mu/D$ where D is the half-bandwidth. In the Fermi-Hubbard model, $D = zJ$ where z is the number of nearest neighbors. One defines the dimensionless characteristic density

$$\rho = N \left(\frac{V_{\mathrm{trap}}}{D}\right)^{d/\gamma} = \frac{\Omega_{d-1}}{\gamma} \int_{-\infty}^{\bar{\mu}_0} \mathrm{d}\bar{\mu} (\bar{\mu}_0 - \bar{\mu})^{\frac{d}{\gamma}-1} n_h(\bar{\mu}), \tag{5.13}$$

which does not depend on the strength of the confining potential as may be seen from the right hand side of the equation. Thus, the characteristic density can be used to describe experimental systems regardless of the particular realization of the trap. It can be experimentally controlled by either changing the total number of particles N or by reducing the half-bandwidth D through increasing the lattice depth. Finally, one obtains mean values $\bar{A}$ (in the trap) of local observables A_j as,

$$\bar{A} = \frac{1}{N} \sum_j A_j = \frac{\Omega_{d-1}}{\rho\gamma} \int_{-\infty}^{\bar{\mu}_0} \mathrm{d}\bar{\mu} (\bar{\mu}_0 - \bar{\mu})^{\frac{d}{\gamma}-1} A_h(\bar{\mu}), \tag{5.14}$$

which evidently only depend on the characteristic density ρ and on the chemical potential μ_0 in the center of the trap. All local quantities on the central site and all global quantities depend only on ρ as μ_0 itself only depends on ρ. Note that as an important consequence, the state diagram of the trapped system uniquely depends on the effective density ρ instead of on the particle number N and the trapping V_{trap} separately. For a fixed particle number, ρ changes upon variation of trapping strength V_{trap} or variation of lattice depth (corresponding to a variation of D). In contrast, the density of the homogeneous system is determined by the number of particles N present in the system and stays unchanged if the lattice depth is varied for a given particle number N.
We apply the LDA to obtain the atom excitation rate of the harmonically trapped system in one and two dimensions in the following sections. The harmonic confinement with $\gamma = 2$ is usually a good approximation of the trapping potential at the position of the atomic cloud. In Sec. 5.4.2 we also compare the LDA results to exact calculations, which supports the validity of the used approximation in this case.

5.4.2 Trapped system in one dimension

In this subsection we consider the one-dimensional system now subjected to an additional harmonic confinement. The mean atom excitation rate of the trapped system is obtained within LDA using Eq. (5.14) by summing the response of the homogeneous system per lattice site $\partial_t \langle n_\omega^{\alpha'_x} \rangle^{1D} / (|A|^2 L)$ over all chemical potential present in the trap. We normalize by the number of atoms and obtain

$$\overline{\frac{\partial_t \langle n_\omega^{\alpha'_x} \rangle^{1D}}{|A|^2}} = \frac{1}{NL|A|^2} \sqrt{\frac{2J}{V_{\mathrm{trap}}}} \int_{-\infty}^{\bar{\mu}_0} \mathrm{d}\bar{\mu} \frac{\partial_t \langle n_\omega^{\alpha'_x} \rangle^{1D}}{\sqrt{\bar{\mu}_0 - \bar{\mu}}} \tag{5.15}$$

with $\bar{\mu} = \mu/2J$ and $V_{\mathrm{trap}} = (m/2)\omega_{t,x}^2 a^2$ as $d = 1$ and $\gamma = 2$ and where the chemical potential in the trap center μ_0 is determined by the particle number N. The chemical potential μ_0 is obtained by an

interpolation of Eq. (5.12) since the total particle number N is known in experiments. In order to make connection to experiment we consider the example case introduced in Sec. 5.3 (^{40}K-atoms, lattice laser wave length $\lambda = 1064$nm) with an additional trapping potential given by the trapping frequency $\omega_{t,x} = 2\pi \times 24.5\text{Hz} = 5.6 \times 10^{-3} E_r$. We consider a typical initial atom number $N = 60$ at temperatures $k_BT = 0.5J$, $1J$ and $1.5J$. The resulting atom excitation rate (5.15) is shown in Fig. 5.4(a). Error bars correspond to 5% uncertainty on the initial atom number $N = 60 \pm 3$. The overall result resembles the homogeneous case (cf. Fig. 5.3) with a clear temperature dependence. However, the Fermi tail is less distinct as we sum over different fillings present in the trap.

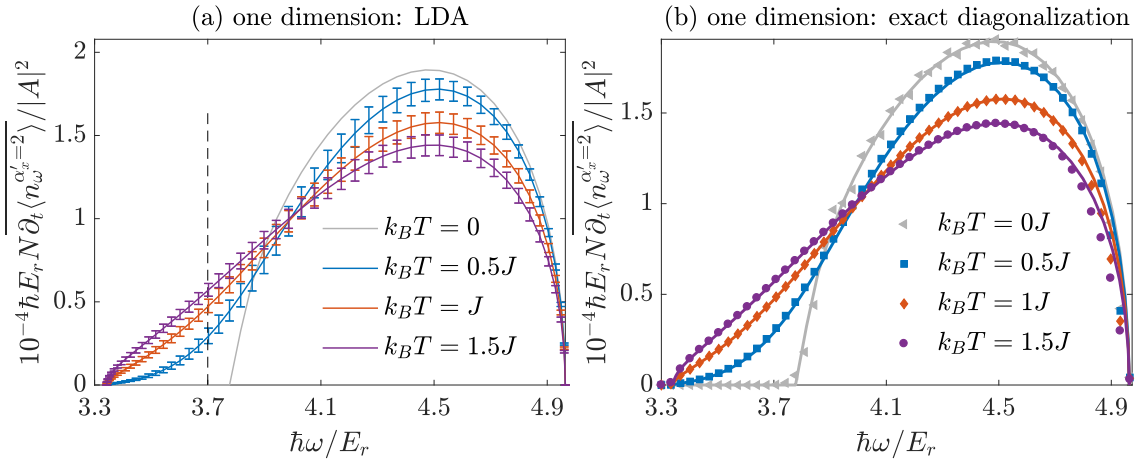

Figure 5.4: The atom excitation rate to the first excited band $\alpha_x' = 2$ of the one-dimensional system by normal lattice modulation, in the presence of a harmonic trapping potential and for temperatures $k_BT = 0J$, $0.5J$, $1J$ and $1.5J$. (a) The atom excitation rate obtained within LDA for an initial atom number $N = 60$ with error bars corresponding to 5% uncertainty on the initial atom number $N = 60 \pm 3$. The vertical dashed line indicates $\hbar\omega = 3.7E_r$ for which we determine the number of excited atoms (see main text). (b) The atom excitation rate obtained from exact diagonalization (markers) compared to the results obtained within LDA (solid lines). Figures adapted from Ref. [169].

In the region of the Fermi tail, we estimate from the horizontal distance of the curves that a frequency resolution $\Delta(\hbar\omega) \approx \pm 0.025 E_r$ is required to resolve the Fermi tail and distinguish the curves of different temperatures. In experiment, this corresponds to a perturbing time $t = 2\pi/\Delta\omega \approx 9$ms which is a typical duration. Within the Fermi tail, at $\hbar\omega = 3.7J$ (indicated by a vertical dashed line in Fig. 5.4(a)) as an example, we determine the mean number of atoms $\overline{\langle n_\omega^{\alpha_x'}(t)\rangle}$ excited during the time t which corresponds to the measured observable in experiment (cf. Sec. 5.2). From the Fig. 5.4(a) we extract the averaged rate at $\hbar\omega = 3.7J$ which is related to the mean number of excited atoms by

$$\overline{\langle n_\omega^{\alpha_x'}(t)\rangle} \quad = \quad N \times \overline{\partial_t \langle n_\omega^{\alpha_x'}\rangle^{dD}} \times t \tag{5.16}$$

in a d-dimensional system. For a sufficiently small amplitude of the modulation $A = 0.05 V_{0,x}$ where $V_{0,x} = 7E_r$, we obtain the mean number of excited atoms $\overline{\langle n_\omega^{\alpha_x'=2}(t)\rangle}$ at $\hbar\omega = 3.7E_r$ to lie between 3 and 7 for temperatures $k_BT = 0.5J - 1.5J$. Considering ~ 100 parallel one dimensional tubes of roughly equal filling in experiment, this gives a number of exited atoms $\sim 300 - 700$. The chosen temperatures have a temperature difference $\Delta k_BT = 0.5J$ (cf. Fig. 5.4(a)). Consequently, this temperature difference corresponds to a difference in number of excited atoms of ~ 150 which is measurable by current experimental means.

In order to verify that the LDA approximation is justified, we have treated the trapping potential exactly in

the one-dimensional case. The simulations are performed using exact diagonalization on the discretized version of the single particle Hamiltonian in the presence of the lattice and the harmonic trap, based on a code by Ameneh Sheikhan [169]. The space is discretized using $\Delta_x = a/50$ in x-direction considering 500 wells in the lattice. Using Eqs. (5.2) and (5.10) in the discrete form, the atom excitation rate from the lowest band to the excited bands is calculated

$$M_{(\alpha_x=1,i)\to(\alpha_x',i')} = \langle v_{\alpha_x',i'}|\delta V_x|v_{\alpha_x,i}\rangle, \tag{5.17}$$

$$N\frac{1}{|A|^2}\partial_t\langle n_\omega^{\alpha_x'}\rangle^{1D} = \frac{\pi}{\hbar}\sum_{i,i'}\left|M_{(\alpha_x=1,i)\to(\alpha_x',i')}\right|^2 f\left(E_{\alpha_x=1}(i)-\mu\right) \times \frac{1}{\sqrt{2\pi w^2}}e^{-\frac{1}{2\sigma^2}\left(\hbar\omega-\left(E_{\alpha_x'}(i')-E_{\alpha_x=1}(i)\right)\right)^2}. \tag{5.18}$$

The eigenenergy $E_{\alpha_x}(i)$ and the eigenstate $|v_{\alpha_x,i}\rangle$ for energy band α_x are calculated from the exact diagonalization and i labels different states in each band. The perturbing potential in the discrete form is denoted δV_x and the Dirac delta function is replaced by its Gaussian approximation with width $w \approx 0.007E_r$. We compare the LDA results to the exact diagonalization results for the atom excitation rate to the first excited band for temperatures $k_BT = 0J$, $0.5J$, $1J$ and $1.5J$ in Fig. 5.4(b). We find excellent agreement which justifies the use of LDA.

5.4.3 Trapped system in higher dimensions

Our thermometry scheme is not limited to the one-dimensional system. We now consider the response of the trapped system in higher dimensions, for example two-dimensional pancake-shaped lattice systems, modulated along one direction x in space. The atom excitation rate in the d-dimensional homogeneous lattice becomes

$$\frac{\partial_t\langle n_\omega^{\alpha'}\rangle^{dD}}{|A|^2} = \frac{\pi}{\hbar}\left(\frac{L}{2k_L}\right)^d\int_{BZ}\mathrm{d}^dk\,|M_{\alpha_x'}(k_x)|^2 f\left(E_1(\vec{k})-\mu\right)\delta\left(\hbar\omega-\left(E_{\alpha_x'}(k_x)-E_{\alpha_x=1}(k_x)\right)\right), \tag{5.19}$$

where the integral runs over the first Brillouin zone in d dimensions. The resonance condition is set by the change of the energy along x direction, $E_{\alpha_x'}(k_x) - E_{\alpha_x=1}(k_x)$, as we only modulate along this direction. Consequently, also the transition matrix elements depend only on k_x. The difference to the one-dimensional system occurs in the Fermi distribution of the equilibrium system which now depends on the energy of the d-dimensional system $E_{\alpha=1}(\vec{k})$. The signal in d dimensions remains k_x-resolved. However, at fixed k_x different quasimomenta in the other directions contribute to the response. These points have different locations in quasimomentum space with respect to the Fermi surface such that the detected response is a superposition of different points in the Fermi distribution. We illustrate this for the two-dimensional system at half-filling in the inset of Fig. 5.5. Consider an intermediate k_x value as indicated by the vertical line. All the k_y along this line within the shaded region will contribute to the response. However, a temperature dependence will only show up close to the Fermi surface whereas the bulk dominantly contributes with a constant value to the response. As a consequence, the temperature dependence in the atom excitation rate is less pronounced but thermometry is nonetheless possible in two-dimensional systems requiring a better experimental frequency resolution than in the one-dimensional case.

Within LDA the atom excitation rate in the two-dimensional system becomes

$$\frac{\overline{\partial_t \langle n_\omega^{\alpha'} \rangle^{2D}}}{|A|^2} = \frac{\pi}{NL^2|A|^2} \left(\frac{4J}{\overline{V_{\text{trap}}}} \right) \int_{-\infty}^{\bar{\mu}_0} \mathrm{d}\bar{\mu}\, \partial_t \langle n_\omega^{\alpha'} \rangle^{2D}(\bar{\mu}), \tag{5.20}$$

where $\bar{\mu} = \mu/4J$ and $\overline{V_{\text{trap}}} = (m/2)\sqrt{\omega_{t,x}^2 \omega_{t,y}^2}\, a^2$. In this case, in order to make connection to experiment, we consider the same example as in the previous section but we consider an initial atom number $N = 4000$ typical for two-dimensional systems and trapping frequencies $\omega_{t,x} = 2\pi \times 24.5\text{Hz} = 5.6 \times 10^{-3} E_r$ and $\omega_{t,y} = 2\pi \times 29.7\text{Hz} = 6.7 \times 10^{-3} E_r$. The corresponding atom excitation rate at temperatures $k_B T = 0.5J$, $1J$ and $1.5J$ is shown in Fig. 5.5. Again, error bars correspond to 5% uncertainty on the initial atom number $N = 4000 \pm 200$. In the region of the Fermi tail, we estimate from the horizontal distance of the curves that a frequency resolution $\Delta(\hbar\omega) \approx \pm 0.01 E_r$ is required to resolve the Fermi tail and distinguish the curves of different temperatures. In experiment, this corresponds to a perturbing time $t \approx 23$ms (which is a typical duration). Within the Fermi tail, at $\hbar\omega = 3.7J$ (indicated by a vertical dashed line in Fig. 5.5) as an example, we determine the mean number of excited atoms $\langle \overline{n_\omega^{\alpha_x'=2}(t)} \rangle$ using Eq. (5.16) for a small amplitude of the modulation $A = 0.02 V_{0,x}$. We find the number of excited atoms to lie between 150 and 180 for temperatures $k_B T = 0.5J - 1.5J$. This gives a difference in number of excited atoms of ~ 10 between the chosen temperatures with temperature difference $\Delta k_B T = 0.5J$. This may be demanding to measure but achievable with current experimental techniques.

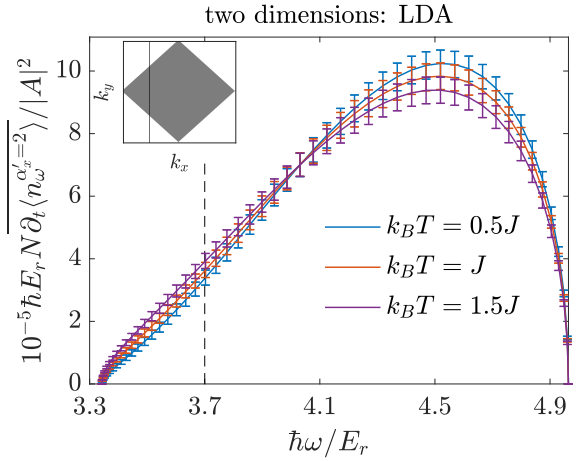

Figure 5.5: The atom excitation rate to the first excited band $\alpha_x' = 2$ of the two-dimensional system by normal lattice modulation along one direction, in the presence of a harmonic trapping potential. The rate was obtained within the LDA and is shown at temperatures $k_B T = 0.5J$, $1J$ and $1.5J$ with error bars corresponding to 5% uncertainty on the initial atom number $N = 4000 \pm 200$. The vertical dashed line indicate $\hbar\omega = 3.7 E_r$ for which we determine the number of excited atoms (see main text). Inset: Sketch of the occupation of the first Brillouin zone of the square lattice system. At zero temperature and half-filling all states below the Fermi surface are occupied (shaded region) and all states above the Fermi surface are empty. The vertical black line indicates the different k_y that contribute to the response at a fixed k_x. Figure adapted from Ref. [169].

Let us comment on the choice of the lattice modulation, that is the application along only one direction in space. This is reasonable as an application of the perturbation along several directions does not help to gain on resolution. The modulation decouples into the different directions such that it has the effect of one-dimensional perturbations along the different directions. For example, a lattice modulation along two directions decouples as $\delta V(\vec{x}) = \delta V(x) + \delta V(y)$. In consequence, the total number of excited atoms is

only enhanced by an overall factor 2 for an isotropic setup. There is no benefit from this factor as we are limited in minimum time by frequency resolution.

5.5 Thermometry by superlattice modulation spectroscopy

In this section we summarize the results obtained in the case of the superlattice modulation spectroscopy in an earlier work [168, 169] in order to compare to the results obtained in the previous sections for the normal lattice modulation spectroscopy.
In the case of a superlattice amplitude modulation, the perturbing potential is given by $\delta V(x) \approx \sin(k_L x)$. For details see Sec. 2.6 where we derive the perturbing potential for an example setup. For the equilibrium lattice considered here, $V_0(x) \sim \sin^2(k_L x)$ in one dimension, the superlattice modulation amounts to a perturbing potential $\delta V(x) \approx \sin(k_L x)$. As a consequence, the superlattice perturbation only couples quasimomenta $\vec{k}$ and $\vec{k}' \approx \vec{k} + (k_L, 0, 0)$ to a good approximation. This means that quasimomentum $\Delta k_x = k_L$ along the x-direction is transferred to the lattice. All other matrix elements are strongly suppressed (see inset of Fig. 5.1(a)). This is in accordance with the common lowest band tight-binding approximation. In this case, the perturbing operator (2.41) associated with the superlattice modulation adds quasimomentum π/a ($= k_L$) to the lattice as may be seen from a Fourier transform of Eq. (2.41), $\hat{O}_S = 2i \sum_{k_x,\sigma} \sin(ak) c^\dagger_{k_x+k_L\sigma} c_{k_x\sigma}$. This is in contrast to the normal lattice modulation which conserves quasimomentum (cf. Sec. 5.1). In the case of the superlattice modulation, excitations to the second excited band are most suitable for thermometry in many cases in contrast to the normal lattice modulation where we chose excitations to the first excited band. The reason is that the transition probability $|M_3(k_x)|^2$ in the case of superlattice modulation shows a similar behavior as $|M_2(k_x)|^2$ in the case of normal lattice modulation which is shown in Fig. 5.1(b). This is due to the similar structure of the excitation bands $\alpha'_x = 2$ for the normal modulation and $\alpha'_x = 3$ for the superlattice modulation due to a 'shift' by k_L in the latter case. We explain this in more detail in the following. In Fig. 5.2 possible excitations by the superlattice modulation (dashed arrows) are sketched in comparison to excitations by the normal lattice modulation (solid arrows). In the case of superlattice modulation, the transition probability is non-zero for a finite quasimomentum transfer of $\Delta k_x \approx k_L$ such that excitations occur 'vertically' in quasimomentum space only if one 'shifts' the excited bands in quasimomentum space by $\Delta k_x = k_L$. The situation for the 'shifted' third band in the case of the superlattice modulation is then similar to the normal lattice modulation considering excitations to the second band.
In the superlattice modulation case, the required experimental frequency resolution is further lowered compared to the normal lattice modulation due to the larger width of the second excited band compared to the first excited band. This is an advantage of the superlattice modulation spectroscopy, in particular in the presence of a trap, where small temperature differences can be distinguished more precisely (see below). For the superlattice modulation, the only changes in the averaged atom excitation rate given by Eq. (5.19) are the resonance condition, which is now $\hbar\omega = E_{\alpha'_x}(k_x + k_L) - E_{\alpha_x=1}(k_x)$ due to the finite momentum transfer, and the matrix elements $|M_{\alpha'_x}(k_x)|^2$ (see above) and we consider excitations to the second band of excitations $\alpha'_x = 3$. The response of the trapped system to the superlattice modulation in one and two dimensions for temperatures $k_B T = 0.5J$, $1J$ and $1.5J$ is shown in Fig. 5.6(a) and (b) respectively. We observe better frequency resolution compared to the case of normal lattice modulation (cf. Fig. 5.4) due to the enhanced width of the second excited band compared to the first excited band. In one dimension, a broad frequency resolution $\Delta(\hbar\omega) \approx \pm 0.15 E_r$ (as compared to $\Delta(\hbar\omega) \approx \pm 0.025 E_r$ in the case of the normal lattice modulation) is already sufficient in order to resolve the Fermi tail and distinguish the curves of different temperature with temperature difference $\Delta k_B T = 0.5J$. In experiment, this corresponds to a short perturbing time $t \approx 2.5$ms for the chosen parameters (same parameters as

for the normal lattice modulation). At an amplitude of the modulation $A = 0.05V_{0,x}$, considering a typical time of the modulation $t = 10$ms, and at $\hbar\omega = 7E_r$ as an example (indicated by a dashed line in Fig. 5.6(a)), we determine the mean number of excited atoms $\overline{\langle n_\omega^{\alpha'=3}(t)\rangle}$ using Eq. (5.16). We find the number of excited atoms to lie between 2 and 6 for temperatures $k_BT = 0.5J - 1.5J$. This means that we excite a couple of hundreds of atoms when considering ~ 100 parallel one-dimensional tubes of approximately equal filling with an atom number difference of ~ 150 between the different temperatures with temperature difference $\Delta k_BT = 0.5J$ which is detectable in experiments.
In two dimensions, the improved frequency resolution is a clear advantage compared to the normal lattice modulation. We find that a frequency resolution $\Delta(\hbar\omega) \approx \pm 0.025E_r$ (as compared to $\Delta(\hbar\omega) \approx \pm 0.01E_r$ in the case of the normal lattice modulation) is already sufficient in experiment which corresponds to a perturbing time $t \approx 9$ms. For an amplitude $A = 0.05V_{0,x}$ at $\hbar\omega = 7E_r$ we excite mean atom numbers $\overline{\langle n_\omega^{\alpha'=3}(t)\rangle}$ between 300 and 400 for temperatures $k_BT = 0.5J - 1.5J$ with an atom number difference of approximately 30 atoms between the curves with temperature difference $\Delta k_BT = 0.5J$ which is easier to detect in experiment than the smaller atom number difference in the case of the normal lattice modulation (~ 10 atoms).

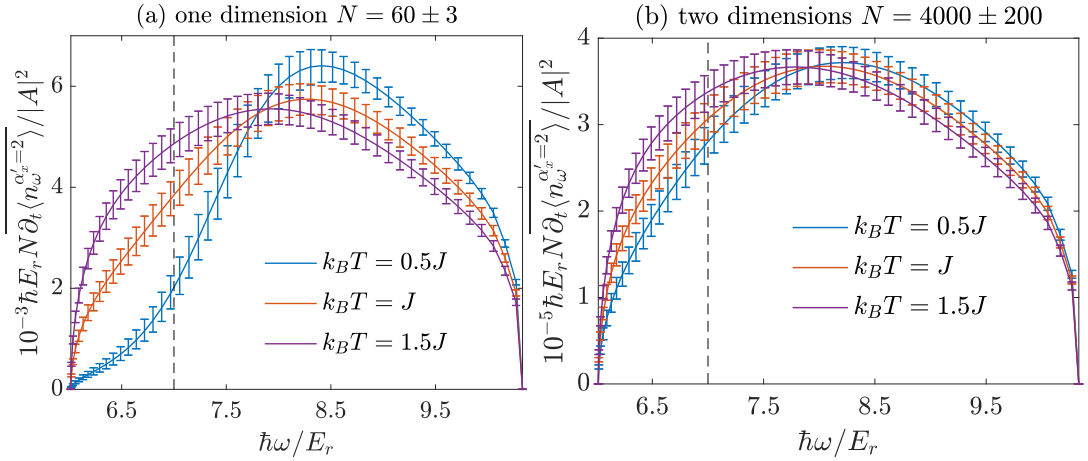

Figure 5.6: The atom excitation rate by superlattice modulation along one direction to the second excited band $\alpha'_x = 3$ in the presence of a harmonic trapping potential. The response is shown at temperatures $k_BT = 0.5J$, $1J$ and $1.5J$ with error bars corresponding to 5% uncertainty on the initial atom number N for the one-dimensional system (a) with initial atom number $N = 60$ and for the two-dimensional system (b) with initial atom number $N = 4000$. The vertical lines indicate $\hbar\omega = 7E_r$ for which we determine the number of excited atoms (see main text). Figures adapted from Ref. [169].

In this sense, the superlattice modulation is advantageous compared to the normal lattice modulation as less frequency resolution is required to extract the temperature in experiment. However, the superlattice modulation of the 'normal' equilibrium lattice is more challenging to implement experimentally compared to the standard amplitude modulation. For the superlattice modulation several laser beams have to be superimposed as explained in Sec. 2.6. Consequently, if the frequency resolution obtained by the normal lattice modulation is sufficient, the normal lattice modulation would be the preferred choice.

5.6 Conclusion

In this chapter we have investigated the temperature-dependent atom excitation rate to higher Bloch bands of non-interacting fermions in an optical lattice as a response to a time-dependent modulation of

the lattice amplitude. We demonstrated that it shows clear signatures of the Fermi distribution of the equilibrium system, also in the presence of an external trapping potential. We explored the possibilities of thermometry for different dimensionalities of the equilibrium system. We find that quasimomentum is conserved by the normal lattice amplitude modulation (cf Fig. 5.1) and excitations to the first excited band are most suitable for thermometry. In the case of a superlattice modulation, a finite quasimomentum k_L is transferred to the system and excitations to the second excited band are most suitable for thermometry. We considered temperatures of a few percent of the hopping amplitude J and find that the response shows a clear signature of the temperature-dependent Fermi factor in the lowest band for one- and two-dimensional equilibrium systems for both modulation schemes. The Fermi dependence in the atom excitation rate is strongly broadened in energy due to the much larger bandwidth of the higher bands compared to the lowest band. This is beneficial as it strongly reduces the required experimental frequency resolution such that the Fermi dependence can be resolved within typical durations of the perturbation. We estimate the number of excited atoms which we find to be sufficiently large to be measured in experiments.

We emphasize that the temperature dependence of the atom excitation rate becomes more pronounced for decreasing temperatures and the applicability of our scheme covers the regime of interest where antiferromagnetic ordering is expected to occur. In two dimensions, for which our thermometry scheme is well suited, spin ordering at half-filling in the homogeneous system is expected at entropies per particle below $s_N \sim 0.4k_B$ at intermediate interactions $(U/J) \sim 5 - 10$ [176] and at smaller entropies for weaker interactions. We relate temperature to entropy for the square homogeneous lattice at half-filling of a typical system size $L = 100$ in each direction within the grand-canonical ensemble. An entropy $s_N \sim 0.4k_B$ corresponds to a temperature $k_BT \sim 0.3J$ where our thermometry scheme is well suited. Our scheme also works at lower temperatures corresponding to lower required entropies for spin ordering at weaker interactions. Consequently, our thermometry scheme is applicable in the regime of interest where spin ordering is expected to occur in the homogeneous system. Note that homogeneous trapping potentials were recently realized [69–71]. The assumption of a homogeneous system also give a first rough estimate for the harmonically trapped system considering the Mott insulating regime at intermediate filling. In this case the entropy is small and approximately constant across the central Mott plateau [177]. Furthermore, the density is constant in the bulk, resembling a homogeneous system although some additional entropy will be added to the liquid wings. Note that in a recent experiment in two dimensions temperatures $k_BT \sim 0.25J$ were reached [19] and relevant correlations were observed [17–19].

Here, we investigated the applicability of our thermometry scheme for non-interacting particles but we believe it to be an important step in order to get also more complex systems under control by an adiabatic connection (entropy conserving) to the interacting system. Although for some strongly correlated atomic states, the assumption of an adiabatic process from the non-interacting atoms might not be suitable, there are several phases which could adiabatically be connected to the non-interacting atoms in the optical lattice that would be worth a thorough investigation. One example are weakly interacting Fermi liquids in the optical lattice where the influence of temperature and interactions on the properties of the quasiparticles, such as the effective mass or the life time of the quasiparticles, are not fully understood. This would be worth a detailed experimental measurement in order to test theoretical predictions from the microscopic model. In the solid state context, a direct measurement of the properties of quasiparticles is possible by angle-resolved photoemission spectroscopy which gives access to the single-particle spectral function [178]. However, a detailed comparison with theory remains difficult in solid states systems due to the complexity of the underlying system. In cold atom systems, a measurement of the single-particle spectral function is possible by momentum-resolved Raman or radio-frequency spectroscopy [31]. The influence of the interactions can be directly probed due to the high tunability of interactions in cold atom systems and due to the absence of other influences such as impurities or phonon-scattering. Some

properties of the Fermi liquid have been probed for the harmonically trapped gas, for example the quasiparticle dispersion and the effective mass have been studied in three- and two-dimensions [179, 180]. In the presence of an optical lattice potential, Raman spectroscopy has also been suggested to investigate the momentum-resolved quasiparticle peak [163]. However, further experimental investigation is required to connect better to the microscopic model and in particular to study the effect of temperature and interactions on the properties of the quasiparticle excitations.

CHAPTER 6

Superlattice modulation spectroscopy of ultracold bosons in optical lattices

In this chapter we study the excitations in the one-dimensional Bose-Hubbard model (2.25) by means of superlattice modulation spectroscopy at zero temperature using t-DMRG. We study both, the Mott insulating phase as well as the superfluid phase, and we compare to analytical results. A detailed discussion of the ground state phase diagram is given in Sec. 2.4 and a possible implementation of the superlattice modulation is discussed in Sec. 2.6.
We begin with the derivation of a description of the Mott insulating regime at integer filling within perturbation theory at strong interactions in Sec. 6.1. This enables us to obtain an analytical description of the energy absorption rate in this regime. Sec. 6.1 is rather technical and can be skipped if one is only interested in the results which are discussed in the subsequent section. In Sec. 6.2 we study the energy absorption in the Mott insulator using t-DMRG and we compare to the perturbation theory result. We discuss how, deep in the Mott insulator, a sharp spectral peak around $\hbar\omega \sim U$ enables a precise determination of the interaction parameter U in experimental setups. Moreover, we investigate the energy absorption rate close to the phase transition to the superfluid phase where the spectral response is broadened. In Sec. 6.3 we study the energy absorption rate using t-DMRG at weak interactions in the superfluid regime, both at commensurate and incommensurate fillings, where we observe excitations at low frequencies as well as a pronounced absorption peak at larger frequencies. Finally, we summarize and conclude in Sec. 6.4. The main results of this chapter are going to be published [181].

6.1 Perturbation theory at $U \gg J$

In this section we determine the eigenstates and eigenenergies of the Bose-Hubbard model (2.25) to lowest order in J/U within perturbation theory in the strong coupling regime. We consider the interaction term H_U as the unperturbed Hamiltonian and the kinetic term H_{kin} as a small perturbation. The obtained spectrum gives an intuitive notion of the nature of excitations at strong interactions and enables us to analytically obtain an approximate expression for the energy absorption rate in the Mott insulating regime within linear response which will be discussed in Sec. 6.2 in comparison to t-DMRG calculations.
The Bose-Hubbard model is given by Eq. (2.25). Here, we use a slightly different definition of the

interaction term such that the Bose-Hubbard model becomes,

$$H = H_{\text{kin}} + H_U = -J \sum_{j=1}^{L-1} (b_j^\dagger b_{j+1} + \text{H.c.}) + \frac{U}{2} \sum_{j=1}^{L} (n_j - \bar{n})^2, \tag{6.1}$$

where $b_j^{(\dagger)}$ are the bosonic annihilation (creation) operators at site j and n_j is the particle number operator, U is the on-site interaction strength and J is the tunneling matrix element. We replaced the usual notation $\sum_j n_j(n_j - 1) \rightarrow \sum_j (n_j - \bar{n})^2$ which amounts to a shift in energy. We work at fixed particle number $N = L\bar{n}$ where L is the number of lattice sites and we assume a Mott insulating ground state with $\bar{n}$ bosons per site (commensurate filling). Locally, an excess particle (occupation $\bar{n} + 1$ at site j) and a hole (occupation $\bar{n} - 1$ at site j') now both have an energy $U/2$ with respect to the initial occupation $\bar{n}$ in contrast to the usual notation (2.25) where the energy of an excess particle (hole) with respect to the initial occupation depends on the filling. However, in both cases a particle-hole pair has energy U with respect to the ground state.

Zero order The eigenstates of the unperturbed Hamiltonian H_U at commensurate filling and fixed particle number are given by Fock states with eigenenergies that are multiples of the on-site interaction strength U. The ground state is given by

$$|0\rangle = |\bar{n}, \bar{n}, ..., \bar{n}\rangle, \tag{6.2}$$

with eigenenergy $E_0 = \langle 0|H_U|0\rangle = 0$. The first excited state in the same particle number sector is created by removing one particle from a site denoted $m + d$ and putting it onto a different site m where d is the distance to the right from the site with occupation $\bar{n}+1$ to the site with occupation $\bar{n}-1$. This corresponds to the creation of a 'doublon-hole' pair on top of the commensurately filled background which is sketched in the inset of Fig. 6.1(b). The excited state is given by

$$|m, d\rangle = \frac{1}{\sqrt{\bar{n}(\bar{n}+1)}} a_{m+d} a_m^\dagger |0\rangle, \tag{6.3}$$

with $m = 1, \ldots, L$ and $d = 1, \ldots, L-1$ such that the state is a $L(L-1)$ degenerate eigenstate of H_U with eigenenergy $E_{m,d} = \langle m, d|H_U|m, d\rangle = U$. Note that we have periodic boundary conditions in m but open boundary conditions in d because $d = 1$ is not connected with $d = L - 1$. The second excited state corresponds to the creation of two 'doublon-hole' pairs with eigenenergy $2U$ and the third excited state with eigenenergy $3U$ is either given by three 'doublon-hole' pairs or one site with occupation $\bar{n} + 2$ and two sites with occupation $\bar{n} - 1$.

First order Switching on the kinetic part in the Hamiltonian, all states and eigenenergies get modified. The first order correction to the ground state energy vanishes as $\langle 0|H_{\text{kin}}|0\rangle = 0$. The first order correction to the ground state is given by

$$|\Psi_0^1\rangle = \sum_{m,d} \frac{\langle m, d|H_{\text{kin}}|0\rangle}{E_0 - E_{m,d}} |m, d\rangle = \frac{J}{U} \sqrt{\bar{n}(\bar{n}+1)} \sum_m \left(|m, 1\rangle + |m, L-1\rangle\right), \tag{6.4}$$

where we used $\langle m, d|H_{\text{kin}}|0\rangle = -J\sqrt{\bar{n}(\bar{n}+1)}\,(\delta_{d,1} + \delta_{d,L-1})$. Other excited states do not contribute to the sum as their overlap with $H_{\text{kin}}|0\rangle$ is zero. The modified ground state is then given by $|\Psi_0\rangle \approx |0\rangle + |\Psi_0^1\rangle$ to first order in J/U.

The corrections to the first excited state have to be determined within degenerate perturbation theory [182]. The lowest order correction is obtained by identifying the unperturbed degenerate eigenstates and to diagonalize the perturbation in this basis. This corresponds to determining the first-order energy shifts that lift the degeneracy while the lowest order states are not modified. To obtain higher order corrections one can use the formulas from non-degenerate perturbation theory but one has to exclude all contributions from the corresponding degenerate subspace. Here, we are only interested in the lowest order correction. Essentially, we need to diagonalize the matrix element

$$\langle m,d|H_{\rm kin}|m',d'\rangle = -J\left[(1+\bar{n})\left(\delta_{m',m+1}\delta_{d',d-1}+\delta_{m',m-1}\delta_{d',d+1}\right)+\bar{n}\left(\delta_{d',d-1}+\delta_{d',d+1}\right)\delta_{m',m}\right]. \quad (6.5)$$

Note that this expression is invariant for $m \to m+L$ due to periodic boundary conditions in m but in d we have open boundary conditions (see above). The diagonalization of the above expression can be achieved by a double Fourier transform in the m and d coordinates. The procedure is outlined in the following. The Fourier transform of the m coordinate is given by

$$|K,d\rangle = \frac{1}{\sqrt{L}}\sum_{m=1}^{L} e^{iKx_m}|m,d\rangle, \quad (6.6)$$

with $x_m = am$ where a is the lattice spacing and $K = 2\pi q/(La)$ with $q = 1,...,L$. One obtains

$$\begin{aligned}\langle K,d|H_{\rm kin}|K',d'\rangle &= \frac{1}{L}\sum_{m,m'=1}^{L} e^{-i(Kx_m-K'x_{m'})}\langle m,d|H_{\rm kin}|m',d'\rangle \\ &= -J\delta_{K,K'}r(K)\left(e^{i\theta(K)}\delta_{d',d-1}+e^{-i\theta(K)}\delta_{d',d+1}\right), \end{aligned} \quad (6.7)$$

where $r(K) = \sqrt{(\bar{n}+1)^2+\bar{n}^2+2\bar{n}(\bar{n}+1)\cos(Ka)}$ and $\theta(K) = (\bar{n}+1)\sin(Ka)/\left[\bar{n}+(\bar{n}+1)\cos(Ka)\right]$. The d-sector cannot be diagonalized by the 'standard' Fourier transform because of the open boundary conditions but a sine transform can be used,

$$|K,k\rangle = \sqrt{\frac{2}{L}}\sum_{d=1}^{L-1} e^{id\theta(K)}\sin(kx_d)|K,d\rangle = \frac{\sqrt{2}}{L}\sum_{d=1}^{L-1}\sum_{m=1}^{L} e^{id\theta(K)}\sin(kx_d)e^{iKx_m}|m,d\rangle, \quad (6.8)$$

where $x_d = da$ and $k = \pi p/(aL)$ with $p = 1,...,L-1$ and which is a good basis as $\langle K,k|K',k'\rangle = \delta_{K,K'}\delta_{k,k'}$. Finally, one can determine the matrix elements of $H_{\rm kin}$ in the new basis obtaining

$$\begin{aligned}\langle K,k|H_{\rm kin}|K',k'\rangle &= \frac{2}{L}\sum_{d,d'=1}^{L-1} e^{-id\theta(K)}e^{id'\theta(K')}\sin(kx_d)\sin(k'x_{d'})\langle K,d|H_{\rm kin}|K',d'\rangle \\ &= -2Jr(K)\cos(ka)\delta_{K,K'}\delta_{k,k'}, \end{aligned} \quad (6.9)$$

which is diagonal and gives the first order correction to the energy for $K = K'$ and $k = k'$. This correction completely lifts the degeneracy of the first band of excitations centered around U except for a translational invariance in K by $2\pi/a$. One can identify K with the center of mass momentum of the 'doublon-hole' pair created and k is related to its relative momentum. To first order, the lowest band of excitations is consequently given by

$$E_{K,k} = U - 2Jr(K)\cos(ka). \quad (6.10)$$

The lowest band of excitations for different center of mass momenta K is shown in Fig. 6.1(a). The maximum bandwidth $W = 12J$ is obtained for zero center of mass momentum $K = 0$ whereas the minimum bandwidth $W = 4J$ is obtained for $K = \pi$. Excitations in the first case can be created by a perturbation which conserves quasimomentum such that a 'doublon-hole' pair is created with zero center of mass momentum. This is the case for the normal lattice modulation which was considered in Ref. [39]. In order to create 'doublon-hole' pairs with $K = \pi$, a finite momentum transfer π of the perturbation is required. This is the case for the superlattice modulation such that excitations are created in a much narrower energy region compared to the normal lattice modulation.

Energy absorption Let us now consider the effect of the superlattice modulation spectroscopy. The energy absorption rate within linear response theory is given by Eq. (3.31). Our aim is to obtain a frequency-resolved excitation peak expected to occur at frequencies corresponding to the lowest band of excitations $E_{K,k}$ (6.10) such that we need to consider $E_m = E_{K,k}$ and $E_0 = 0$ for the resonance condition $\delta(\hbar\omega - (E_m - E_0))$ in Eq. (3.31). For the amplitude $\left|\left\langle 0\left|\hat{O}_S\right|m\right\rangle\right|^2$ it is sufficient to only consider the lowest order, that is $|0\rangle$ given by Eq. (6.2) and $|m\rangle = |K,k\rangle$ given by Eq. (6.8)[1].

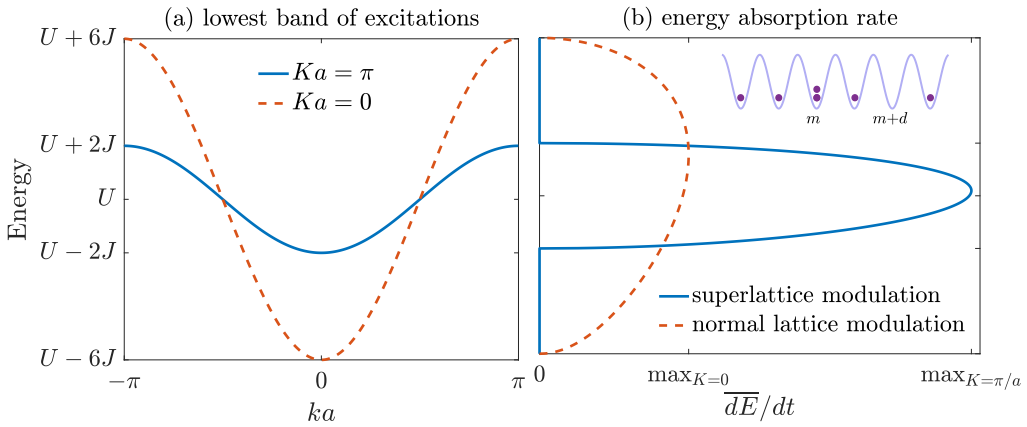

Figure 6.1: (a) The lowest band of excitations in the Bose-Hubbard model in lowest order in J/U for different center of mass momenta $K = 0,\ \pi/a$ of the 'doublon-hole' pair. In both cases, the energy band is centered around U but has different bandwidth $W = 12J,\ 4J$ respectively. (b) The energy absorption rate $\overline{dE}/dt$ as a response to the normal lattice modulation (orange dashed line) and to the superlattice modulation (blue solid line). The width of the excitation peak corresponds to the bandwidth of the lowest band of excitations for $K = 0,\ \pi/a$ respectively. Inset: Sketch of the excited state $|m,d\rangle$ in real space. One particle is added at position m while one particle is removed at position $m + d$, i.e. a 'doublon-hole' pair is created on top of a commensurately filled background.

For the superlattice modulation spectroscopy the perturbing operator $\hat{O}_S$ is given by Eq. (2.41) and the relevant matrix element becomes

$$\langle K,k|\hat{O}_S|0\rangle \quad = \quad \sqrt{2\bar{n}(\bar{n}+1)}\sin(ka)\eta_p\delta_{Ka,\pi}, \tag{6.11}$$

with $\eta_p = (1-(-1)^p)$. The finite momentum transfer π of the superlattice modulation is encoded in the Kronecker delta $\delta_{Ka,\pi}$. In the case of the momentum conserving normal lattice modulation the matrix

[1] In principle, the matrix element to the considered order is given by $|\langle\Psi_1|\hat{O}_S|\Psi_0\rangle|$ where $|\Psi_0\rangle = |0\rangle + |\Psi_0^1\rangle + O(J^2/U^2)$ and $|\Psi_1\rangle = |K,k\rangle - (J/U)\sqrt{2\bar{n}(\bar{n}+1)}\eta_p\sin(ka)|0\rangle + (J/U)\sum_\alpha|\alpha\rangle + O(J^2/U^2)$ where $|\alpha\rangle$ are states in addition to the Fock state $|0\rangle$ that are directly coupled via the kinetic term to the states $|K,k\rangle$. However, we find that the transition matrix element squared simplifies $|\langle\Psi_1|\hat{O}_s|\Psi_0\rangle|^2 = |\langle K,k|\hat{O}_S|0\rangle|^2 + O(J^2/U^2)$ such that it is sufficient to consider only the lowest order contribution.

element depends on $\delta_{K,0}$. The energy absorption rate normalized by the number of lattice sites becomes

$$\frac{1}{L}\overline{\frac{dE(t)}{dt}} = \frac{\pi}{L}\omega|A|^2\bar{n}(\bar{n}+1)\sum_{p=1}^{L-1}\eta_p^2\sin^2\left(\frac{p\pi}{L}\right)\delta\left(\hbar\omega - U + 2J\cos\left(\frac{p\pi}{L}\right)\right). \tag{6.12}$$

The sum $\sum_{p=1}^{L-1}$ can be replaced by $\sum_{p=0}^{L-1}$ since the contribution for $p = 0$ is zero. The continuum limit is obtained using $(1/L)\sum_{p=0}^{L-1}(1-(-1)^p)^2 f((p\pi/L)) \to (2/\pi)\int_0^\pi \mathrm{d}k f(k)$ and we find

$$\frac{1}{L}\overline{\frac{dE(t)}{dt}} = \frac{\omega|A|^2\bar{n}(\bar{n}+1)}{J}\sqrt{1-\left(\frac{U-\hbar\omega}{2J}\right)^2}. \tag{6.13}$$

Absorption occurs in the region $\hbar\omega \in [U-2J, U+2J]$ as expected since this corresponds to the bandwidth $4J$ of the lowest band of excitations for a finite center of mass momentum $K = \pi/a$ of the 'doublon-hole' pair. The absorption peak is shown in Fig. 6.1(b). Its maximum occurs at

$$\hbar\omega_0 = U\left(1+\left(\frac{2J}{U}\right)^2\right), \tag{6.14}$$

which is slightly larger than U. In Fig. 6.1(b) we also compare to the absorption peak as a response to the normal lattice modulation [39] which is broader in energy due to the enhanced bandwidth of the 'doublon-hole' pair created at $K = 0$ and more strongly asymmetric as the maximum occurs at $\hbar\omega_0 = U\left(1+((2J(2\bar{n}+1))/U)^2\right)$. Additionally, the signal is much weaker in the case of the normal lattice modulation.

6.2 Excitations in the Mott insulating phase

In this section we study the energy absorption on the Mott insulating side of the phase diagram at integer filling $\bar{n} = 1$, deep in the Mott insulator as well as close to the phase transition to the superfluid phase, using t-DMRG and comparing to the analytical results obtained in the previous section.
In t-DMRG we study systems of sizes up to $L = 96$. In order to obtain sufficient accuracy in the absorbed energy $E(t)$ we keep a matrix dimension of $D = 128$ and a local dimension $\sigma = 3$ ($\sigma = 7$) for $U \geq 20J$ ($U \leq 15J$) and we conduct an error analysis by increasing the matrix dimension to 196 states and the local dimension to 5 (9). In the Trotter-Suzuki time evolution we set $J\tau = 0.01\hbar$ and we use $J\tau = 0.005\hbar$ to perform the error analysis. We determine the maximal uncertainties in the energy absorption rate due to the matrix dimension, the local dimension, the time step and the variation of the fit range (see App. A for details). The error bars are provided in the figures.
We time evolve systems of size $L = 40$ for $U \geq 15J$ ($L = 64$ for $U \leq 10J$) for a range of modulation frequencies around $\hbar\omega \sim U$ where particle-hole excitations are expected to form and we extract the energy absorption rate from a fit of the slope (see App. B.2.1). We also consider different system sizes for some example cases. Additionally, higher order excitations are expected at multiples of U corresponding to multiply occupied sites or several particle-hole excitations. We do not study these here.
In Fig. 6.2(a) the energy absorption rate at strong interactions $U = 15J - 60J$ is shown in comparison to the analytical result (6.13). We observe strong energy absorption peaks approximately symmetric and centered slightly to the right of U and of width $\sim 4J$. By width we mean the full bandwidth at the

bottom of the peak [2]. The overall agreement with the analytical results is good and only small amounts of energy are absorbed on average outside of the analytically predicted region $\hbar\omega \in [U - 2J, U + 2J]$. Thus, the nature of excitations is well captured by the simple 'particle-hole' picture in lowest order perturbation theory. Slight deviations of the t-DMRG results compared to the analytical results occur in the peak maximum, which is slightly enhanced and shifted to the right (in the t-DMRG), in the width, which is slightly broader, and in the overall shape, which is 'flatter' in the wings and the left wing lies slightly below the predicted square-root-behavior. For decreasing interactions, the peak location shifts to smaller frequencies as it is located around $\hbar\omega \sim U$. At the same time, the location of the maximum of the t-DMRG peak shifts farther to the right with respect to U in accordance with the analytical prediction where the peak position (6.14) also shifts farther away from U for decreasing interactions. However, the shift in the t-DMRG is stronger which we attribute to higher-order corrections which would shift the center of the band of excitations away from U. For decreasing interactions, the deviations in the left wing also increase such that the peak becomes asymmetric at $U \sim 15J$. In the inset a close-up of the $U = 60J$ peak is shown for two different system sizes. The maximum of the peak decreases for increasing system sizes, approaching more the analytical prediction.

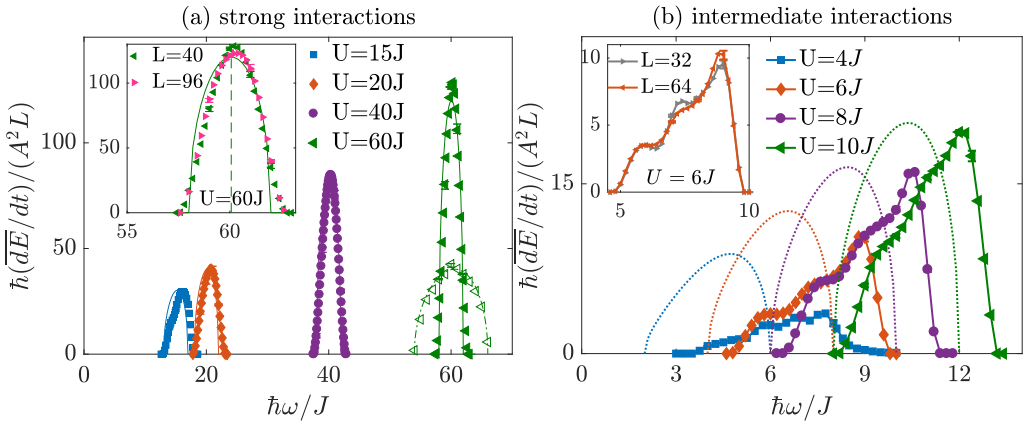

Figure 6.2: (a) The energy absorption rate for a system size $L = 40$ and for an amplitude of the modulation $A = 0.01J$ in the Mott insulator at strong interactions comparing t-DMRG (filled symbols) to the analytical result (solid lines). For $U = 60J$ the response to the normal lattice modulation is also shown (open symbols and dash-dotted line) which is weaker in amplitude and broader in width. The inset shows different system sizes $L = 40$ (green left-pointed triangles) and $L = 96$ (pink right-pointed triangles) at $U = 60$ compared to the perturbation theory result (solid line). The dashed vertical line indicates the position of the maximum within perturbation theory. (b) The energy absorption rate for a system size $L = 64$ and for an amplitude of the modulation $A = 0.01J$ in the Mott insulator at intermediate interactions comparing t-DMRG (filled symbols, lines are guides to the eye) to the analytical result (dotted lines). The inset shows different system sizes $L = 32$ (gray right-pointed triangles) and $L = 64$ (orange left-pointed triangles) at $U = 6$.

The agreement may be further improved by taking into account higher orders in the perturbation theory. Note that we found that a contribution from the first order correction in the states vanishes such that the deviations must stem from higher order corrections in J/U. We do not investigate this further as we understand well the main features and an improvement is not required for an experimental application: In lattice shaking experiments, the position of the spectral response is sometimes used to determine the on-site interaction strength U [183]. This is particularly useful, when the standard Bose-Hubbard approximation, which uses the lowest band Wannier functions and a δ-interaction potential to calculate

[2] The width is extracted from the t-DMRG data by defining the bounds as the mean between the frequency for which $\overline{dE/dt} < 10^{-3}J^2/\hbar$ and the neighboring frequency for which $\overline{dE/dt} > 10^{-3}J^2/\hbar$.

U, breaks down at, for instance, large interactions. We point out that our superlattice scheme provides experimentalists with a more precise measurement scheme due to the reduced width compared to the normal lattice modulation. A comparison to the normal lattice amplitude modulation is also shown in Fig. 6.2(a) for $U = 60J$.
Let us now discuss intermediate interactions $U = 4J - 10J$ approaching the phase transition to the superfluid state located at $U_c \approx 3.4J$ [75]. The energy absorption rate is shown in Fig. 6.2(b) compared to the perturbation theory result. For decreasing interactions, the spectral width increases while the peak maximum shifts farther to the right with respect to U and also the location of the onset starts deviating from the perturbation theory result. Moreover, the peak acquires an increased asymmetry for decreasing interactions which we also see in the perturbation theory. However, near the phase transition the deviations in t-DMRG from the perturbation theory are significantly strong which is in agreement with an expected breakdown of perturbation theory. The left wing of the absorption peak shows a 'step-like' profile which we attribute to finite-size effects as it smoothes out for increasing system sizes (see inset of Fig. 6.2(b)).
The frequency dependence of the energy absorption peak covering the entire Mott insulating region at strong and intermediate interactions is presented in Fig. 6.3 which displays the position of the peak maximum and the width extracted from the t-DMRG compared to the perturbation theory result. The position of the maximum near $\hbar\omega \sim U$ and the width is well captured by the perturbation theory for interactions $U \geq 15J$ presenting a reliable technique for the lattice depth calibration. For intermediate interactions, $6J \leq U < 15J$, the location of the peak maximum deviates. However, the width of the peak and the locations of the boundaries still reflect the width and the location of the analytical boundaries such that it may still be applicable for a lattice depth calibration, even at these interactions which are already close to the phase transition.

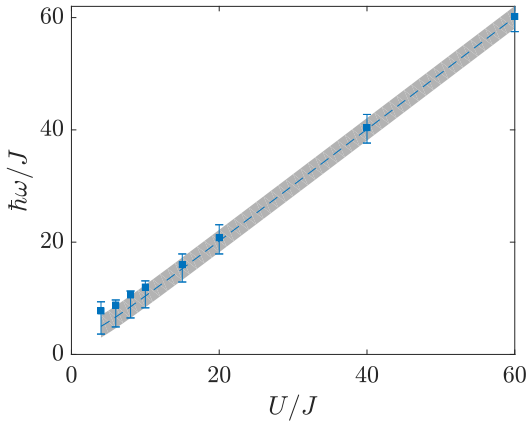

Figure 6.3: The position of the maximum and the width of the energy absorption rate as a function of interaction energy U. We compare the position and width extracted from t-DMRG (squared markers and vertical error bars) to the analytical result within perturbation theory (dashed line and gray shaded region). The width is extracted from the t-DMRG data by defining the bounds as the mean between the frequency for which $\overline{dE/dt} < 10^{-3}J^2/\hbar$ and the neighboring frequency for which $\overline{dE/dt} > 10^{-3}J^2/\hbar$.

6.3 Excitations in the superfluid phase

In this section we study the energy absorption as a response to superlattice amplitude modulation in the superfluid region of the one-dimensional Bose-Hubbard model. At commensurate filling the system is superfluid at weak interactions while it becomes Mott insulating at stronger interactions and the transition

takes place at $(U/J)_c \sim 3.4$ for $\bar{n} = 1$ [75]. The Mott insulating case was discussed in the previous section. At incommensurate filling, the system remains superfluid for all interaction strengths. Here we concentrate on systems at weak interactions $U \lesssim 3$ at integer filling $\bar{n} = 1$ and at incommensurate fillings $\bar{n} < 1$.

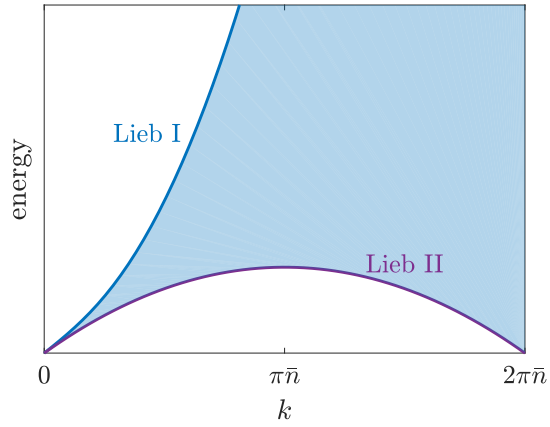

Figure 6.4: Sketch of the excitation spectrum of the Lieb-Liniger model. The Lieb I mode is sound-like at small quasimomenta and becomes particle-like at larger quasimomenta. The Lieb II mode exhibits the same sound-like behavior at small momenta but it is maximum at $k = \pi\bar{n}$ and vanishes again at $k = 2\pi\bar{n}$. The shaded area represents the continuum of excitations bounded between the two modes in the continuum model.

The low-lying excitations of the weakly interacting Bose gas are generally sound-like corresponding to fluctuations of the condensate phase [184]. One of the simplest models describing interacting bosons in one dimension is the Lieb-Liniger model [185, 186] which assumes a δ-interaction potential and describes particles in the continuum. The Lieb-Liniger model displays two distinct excitation modes, the Lieb I and the Lieb II mode which are sketched in Fig. 6.4. The Lieb I mode is sound-like at small quasimomenta and becomes particle-like at larger quasimomenta and corresponds to the single mode well known from Bogoliubov theory for the weakly interacting Bose gas [184]. The Lieb I mode is often simply called Bogoliubov mode. The additional Lieb II mode exhibits the same sound-like behavior at small momenta where the dispersion relations of both modes have the same slope. However, the Lieb II mode reaches a maximum at quasimomentum $k = \pi\bar{n}$ and vanishes again at $k = 2\pi\bar{n}$. The Lieb II mode is often simply called Lieb mode. In the context of cold gases, the Lieb-Liniger spectrum was investigated, for instance, by means of Bragg spectroscopy of ultracold bosons in the harmonic trap confined to one dimension in space [187, 188] where a broad feature in the extracted dynamical structure factor indicates contributions from both modes. The Bose-Hubbard model at weak interactions can also be described by the Lieb-Liniger model when taking the continuum limit [189]. The validity of this mapping is not completely general, however, the Lieb-Liniger model describes well some properties of the Bose-Hubbard model in the superfluid regime in a wide range of parameters. For example, the authors of Ref. [189] show that the sound velocity of an infinitesimally small density perturbation in the one-dimensional Bose-Hubbard model is well described by the sound velocity predicted by the Lieb-Liniger model for the parameter $\gamma = (U/J)/(2\bar{n}) \lesssim 10$.
Choosing the parameters accordingly, we assume our system to be well described by the Lieb-Liniger model and its excitation spectrum can be probed by the superlattice modulation. Notably, the superlattice modulation introduces a finite momentum transfer π where, at $\bar{n} = 1$, the Lieb dispersion is maximal. Within linear response, the resonance condition given by the δ-function in Eq. 3.31 would have a lower bound (below which no energy is absorbed) given by this maximum in the Lieb spectrum. Consequently, we expect to observe a gap in the excitation spectrum. At densities $\bar{n} < 1$, the maximum of the Lieb

branch at $\pi\bar{n}$ is located at a quasimomentum $< \pi$ such that a transferred momentum π corresponds to frequencies to the right of the maximum of the Lieb branch. Consequently, the gap value would reduce. This is in contrast to the normal lattice modulation which is quasimomentum conserving, i.e. the transferred momentum is zero, such that it would only couple to the low-frequency excitations in the linear part of the spectrum near $k = 0$ at any density.
In the t-DMRG we study systems of size up to $L = 128$ and with densities $n \sim 0.55 - 1$. In order to obtain sufficient accuracy in the absorbed energy $E(t)$ we keep a matrix dimension of $D = 128$ and a local dimension $\sigma = 7$ and we conduct an error analysis by increasing the matrix dimension to 196 states and the local dimension to 9. In the Trotter-Suzuki time evolution we set $J\tau = 0.01\hbar$ and we use $J\tau = 0.005\hbar$ to perform the error analysis. We determine the maximal uncertainties in the energy absorption rate due to the matrix dimension, the local dimension, the time step and the variation of the fit range (see App. A for details). The error bars are provided in the figures.

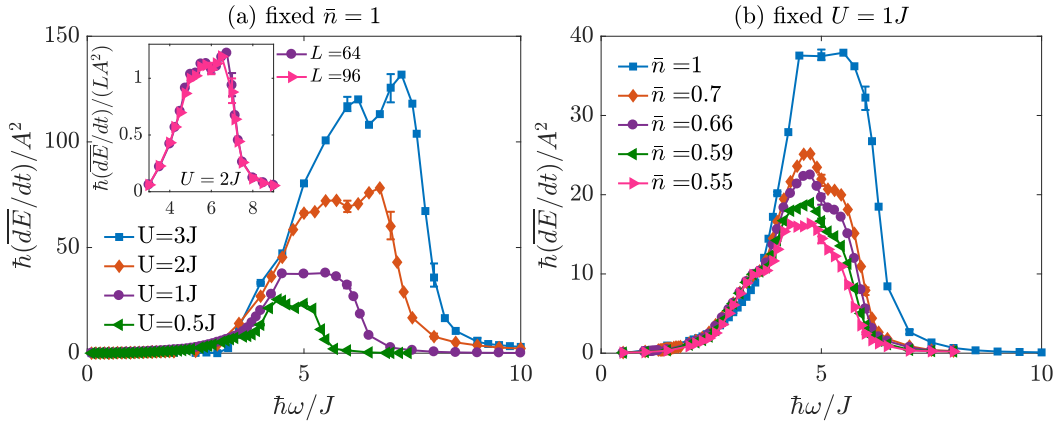

Figure 6.5: (a) The energy absorption rate for a system size $L = 64$ and for an amplitude of the modulation $A = 0.01J$ ($A = 0.05J$) for $\hbar\omega \geq 2J$ ($\hbar\omega < 2J$) at fixed density $\bar{n} = 1$ and different interaction strengths U (a) as well as at fixed interaction strength $U = 1J$ and different densities $\bar{n} \leq 1$ (b). The inset in (a) shows the energy absorption rate normalized by the system size L for different system sizes $L = 64$ (orange diamonds) and $L = 96$ (green left-pointed triangles) at $U = 2J$. Solid lines are guides to the eye.

In order to probe the gap in the Lieb mode by superlattice modulation, we time evolve the system for $L = 64$ at different interaction strengths U and at different fillings $\bar{n}$ for a range of modulation frequencies ranging from very small frequencies to $\hbar\omega \lesssim 10J$. For some parameters we also consider system sizes $L = 96,\ 128$. We extract the energy absorption rate from a fit of the slope (see App. B.2.2). The observed energy absorption spectrum at $\bar{n} = 1$ for different U is shown in Fig. 6.5(a) and the spectrum at $U = 1J$ for different $\bar{n}$ is shown in Fig. 6.5(b). We observe a continuous but weak onset at low frequencies while at larger frequencies a pronounced absorption peak develops. By continuous onset we mean that we observe an increase in energy already at very small frequencies $\hbar\omega \sim 0.5J$. The extracted slope is very small and only increases very slowly for increasing $\hbar\omega$ until the strong peak develops at $\hbar\omega \gtrsim 3J$. The location, height and width of the peak depend on both, interaction strength and density. For increasing interactions (at fixed density, see Fig. 6.5(a)), the height of the absorption peak increases and the maximum shifts to larger frequencies. Likewise, the width broadens with the right bound being shifted to larger frequencies while the onset of the peak (at the left side) shifts to slightly smaller frequencies. For increasing U the peak develops a substructure. However, this substructure gets less pronounced for increasing system sizes as may be seen from a comparison to $L = 96$ at $U = 2J$ in the inset of Fig. 6.5(a). For decreasing densities (at fixed interaction strength, see Fig. 6.5(b)), the height of the absorption peak decreases and the maximum remains approximately at the same location. The width decreases with the right bound

being shifted to smaller frequencies while the onset (at the left side) does not shift significantly.
For small ratios $\gamma = (U/J)/2n$, the onset of the absorption peak is related to the gap in the Lieb mode at finite momenta. However, in many cases this is hard to observe due to the smooth behaviour of the matrix elements [190]. In the Bose-Hubbard model, in contrast to the continuum model, the excitations above the Lieb branch are not continuous but we expect a band structure similar to the cases studied in the previous sections. The width of the observed peak is approximately given by the lowest band of excitations. We identify possible reasons for the 'soft' onset of the observed peak instead of a genuine gap predicted by Lieb-Liniger theory. The transition probability (of a two-level system) as a response to a sinusoidal perturbation depends on the strength and the finite duration of the perturbation [142]. A transition cannot be resolved sharply in frequency as the transition probability acquires a finite frequency broadening due to the finite excitation time such that the onset may appear 'soft'. Moreover, we may observe additional higher-order processes at low frequencies which are not captured within linear response. Due to the continuous onset, it is difficult to observe the reduction in the gap when $\bar{n}$ decreases from $\bar{n} = 1$ to smaller values.
In principle, the superlattice modulation could also couple to the Lieb spectrum where it is gapless and sound-like near $k = 2\pi\bar{n}$. This would be the case for densities $\bar{n} \sim 0.5$ such that the sound-like regime of the Lieb spectrum occurs near $k \sim \pi$ corresponding to the momentum provided by the superlattice modulation. Here, we do not investigate this case.
These results have only recently been obtained and a more detailed analysis, numerically and analytically, remains of interest in order to explain in more detail the rich structure of the excitation spectrum in the superfluid that we observe using t-DMRG.

6.4 Conclusion

In this chapter we have investigated the excitation spectrum of the one-dimensional Bose-Hubbard model at zero temperature as a response to the superlattice amplitude modulation in both, the Mott insulating and the superfluid regime.
In the Mott insulator we find a sharp excitation peak around $\hbar\omega \sim U$ corresponding to a particle-hole excitation on top of the commensurately filled background. The observed peak is significantly stronger and narrower compared to the normal lattice modulation which would enable a notably more precise calibration of the interaction parameter U in experiment for which the normal lattice modulation is sometimes used [183]. A comparison of theory and experiment would be particularly simple without the need of numerical input as we find very good agreement with the analytical results deep in the Mott insulator and even when approaching the phase transition to the superfluid state the observed peaks still overlap considerably with the analytical prediction.
In the superfluid regime, we observe a distinct excitation peak that can be explained within the Lieb-Liniger model. Its onset is related to the energy gap in the Lieb-Liniger spectrum at finite momenta to which the superlattice amplitude modulation couples (as it provides a finite momentum transfer π). A more detailed analysis of this spectrum, both numerically and analytically, remains of interest.

CHAPTER 7

Conclusion and Outlook

In this thesis we explored the possibilities of lattice amplitude modulation spectroscopy, a time-periodic modulation of the optical lattice amplitude, in order to more accurately characterize ultracold atoms confined to optical lattices. Energy is absorbed by the system whenever the modulation frequency ω corresponds to an available excitation in the system at energy $\hbar\omega$. Hence, valuable insights into the underlying many-body system can be obtained by monitoring the absorbed energy. Notably, we introduced a 'novel' lattice modulation scheme of dimerized geometry, which we named *superlattice* modulation, in the sense that the amplitude of one well is increased while the amplitude of the neighboring well is decreased. The superlattice modulation can be applied to optical (super)lattices by time-dependently tuning the dephasing between the laser waves constituting the optical lattice. The superlattice modulation transfers a finite momentum π to the optical lattice in contrast to the standard lattice amplitude modulation which is momentum-conserving. We studied the effect of both modulation schemes on different (mostly one-dimensional) systems of fermionic or bosonic atoms trapped in optical (super)lattices, theoretically described by (ionic) Fermi- and Bose-Hubbard models. We applied a modulation of small amplitude and studied the time evolution of the systems in the linear response regime by means of the time-dependent density matrix renormalization group method. From the time evolution of the energy we extracted the absorbed energy which we compared to different analytical approaches and made close connection to experimentally relevant situations.
We found the (super)lattice modulation spectroscopy to be a flexible tool which is a valuable probe in two different ways. On the one hand, we showed how the superlattice modulation can be used to experimentally detect unknown phases. In particular, it was used to detect signatures of bond order in the one-dimensional ionic Hubbard model which has so far evaded experimental detection. On the other hand, we found the (super)lattice modulation to be useful in determining unknown macroscopic and microscopic parameters in the experiment. Here we studied its applicability to extract the temperature of fermionic atoms and the interaction strength of bosonic atoms confined to optical lattices.

Detection of bond order In Ch. 4 we studied the excitation spectrum of the one-dimensional ionic Hubbard model as a response to the superlattice modulation. The ionic Hubbard model is given by the Fermi-Hubbard model with an additional staggered energy offset. The phase diagram was predicted to exhibit a so-called bond order wave phase [35], characterized by a spontaneous dimerization of the hopping, in between a band and a Mott insulating phase. Ultracold fermions in optical lattices provide an appealing novel avenue to detect this state. So far, a detection has been difficult, in particular, due to the lack of a suitable observable. In this thesis, we suggest to use superlattice modulation spectroscopy as a

probe since, due to its dimerized geometry, it would be a prominent candidate to directly couple to the bond order parameter in contrast to the available probes. We demonstrated, using time-dependent matrix renormalization group and bosonization techniques, that superlattice amplitude modulation spectroscopy reveals signatures of both phase transitions, signaling the onset of the bond order wave phase. The ionic Hubbard model was recently realized by fermionic atoms trapped in optical superlattices [36]. Thus, a detection of bond order in cold atomic experiments has come within reach in view of the recent realization of homogeneous trapping potentials [69–71] and temperatures below the exchange interaction [17–19]. This would permit the detection of the low-energy divergence in the excitations at the critical point between band insulator and bond order wave. Furthermore, we gained detailed insights into the excitation spectra in the band and Mott insulating phases. Deep in the band insulator we developed a thorough understanding of the charge excitations within an effective model using a Schrieffer-Wolff transformation for the excited states. Approaching the phase transition to the bond order wave phase, we could follow the closing of the charge excitation gap. On the Mott insulating site, we confirmed the spin nature of the low-energy excitations and also gained insights into the gapped charge excitation spectrum.

Thermometry An important control parameter in fermionic lattice experiments is the temperature which is hard to determine accurately. Motivated by the lack of reliable thermometry schemes, we studied in Ch. 5 the possibilities of thermometry for non-interacting fermionic atoms confined to optical lattices in different dimensions by means of standard lattice modulation spectroscopy. We also compared to the superlattice modulation spectroscopy investigated in an earlier work [168]. We showed how the atom excitation rate to higher Bloch bands as a response to the lattice modulation exhibits a clear signature of the temperature-dependent Fermi distribution of the particles in the lowest band. This temperature dependence is broadened in energy space due to the increased bandwidth of the excited bands with respect to the lowest band. Consequently, the required frequency resolution in experiment is reduced which facilitates a measurement. A measurement of the atom excitation rate would be particularly simple as it merely corresponds, due to the momentum-resolution of the excitation, to counting the particles transferred to higher Bloch bands. The number of transferred particles can be easily measured by means of the adiabatic band mapping technique without the necessity of momentum resolution in the measurement. We found that the temperature dependence survives in the presence of an additional harmonic trapping potential. We verified the measurability in experiment by estimating the number of excited particles and the required frequency resolution. Overall, we concluded that a temperature measurement would be possible in one- and two dimensional setups for both, the normal and the superlattice modulation. The superlattice modulation is advantageous as it requires less frequency resolution in the experiment. However, if the frequency resolution is sufficiently precise, the normal lattice modulation would be the preferred choice as it is easier to implement experimentally. Notably, this thermometer would work best in the low-temperature regime of interest where most other schemes fail [38].

Lattice calibration In Ch. 6 we studied the excitation spectrum of the one-dimensional Bose-Hubbard model as a response to the superlattice amplitude modulation. At commensurate filling and strong interactions, deep in the Mott insulating regime, we found that the superlattice modulation creates particle-hole pairs at an energy which is approximately equal to the on-site interaction strength as naively expected. We studied the spectrum using time-dependent density matrix renormalization group and a perturbative approach in the strong-coupling regime. We found that the width of the absorption peak, which is given by the bandwidth of the lowest band of excitations, is very narrow (and stronger in amplitude) compared to the absorption spectrum as a response to the normal lattice modulation [39]. This narrow resonance is a particularity of the superlattice modulation which transfers momentum π to the lattice. As a consequence,

particle-hole pairs are created with center of mass momentum π and reduced bandwidth compared to particle-hole pairs with zero center of mass momentum created by the normal lattice modulation. The absorption spectrum as a response to lattice amplitude modulation can be used to determine the on-site interaction strength in the experiment [183] such that our superlattice setup would enable a much more precise calibration compared to the normal lattice modulation. Moreover, we investigated the absorption spectrum in the superfluid regime at weak interactions and (in)commensurate fillings where we found a pronounced peak at intermediate interactions related to the Lieb-Liniger [185, 186] spectrum at finite momentum π.

In summary, we found the superlattice modulation spectroscopy to be a versatile tool in probing ultracold atoms in optical lattices. Its dimerized geometry enables the detection of exotic quantum phases such as the bond order wave phase in the one-dimensional ionic Hubbard model. Additionally, the finite momentum transfer π to the lattice provides a useful measurement scheme to extract unknown parameters in the experiment, giving more precise results than the normal lattice modulation in some cases. In the future, further applications of the superlattice modulation to different kinds of setups may shed light on open questions of quantum many-body physics. For example, it could be used to investigate the phase diagram of the extended repulsive Fermi-Hubbard model, given by the repulsive Fermi-Hubbard model with additional nearest-neighbor interactions. In this case, a bond order wave phase was predicted to exist at weak and intermediate interactions, between a charge density wave at dominating nearest-neighbor interactions and a spin density wave at dominating on-site interactions. This was theoretically studied, for example, in Refs. [191, 192] and references therein. Detecting the bond order wave phase in this model and characterizing the nature of its neighboring phase transitions remains to be done. At strong interactions, the bond order wave is predicted to vanish accompanied by the merging of the two phase transitions into one transition line. The vicinity of this so-called tricritical point is little understood and would be worth a thorough investigation. The extended Bose-Hubbard model was recently realized with a gas of strongly magnetic atoms in a three-dimensional optical lattice [193] where the long range character of the dipolar interactions leads to a nearest-neighbor term in the tight-binding description. In principle, the extended Fermi-Hubbard model should also be realizable by loading a dipolar Fermi gas, as for example prepared in Ref. [194], into an optical lattice. Moreover, also bosonic particles trapped in optical superlattices exhibit a rich phase diagram including Mott insulating states with fractional filling [75, 195] and further insights into the excitation spectrum may be obtained by the superlattice modulation.

The dimerization of the superlattice modulation $(-1)^j = \cos(\pi j)$ could be extended to introducing an arbitrary momentum transfer K, i.e. replacing the dimerization by $\cos(aKj)$. This is promising as a spectroscopic probe as it allows for the investigation of more complex lattice models and various intriguing quantum phases. One example would be the Bose glass phase, a localized phase, predicted to occur for bosonic particles trapped in disordered or quasi-periodic one-dimensional lattice potentials [60, 75]. The Bose glass phase occurs due to the interplay of disorder and interactions. Experimentally, this can be realized by superimposing two laser waves of arbitrary wavelength where the ratio of the wave numbers k_2/k_1 determines the periodicity. The phase diagram for the disordered and quasi-periodic one-dimensional systems is qualitatively similar, displaying Bose glass, superfluid and Mott insulating phases at commensurate filling. At incommensurate filling only the first two phases exist. The Bose glass is similar to the Mott insulating phase in the sense that it is localized and insulating. In contrast, the Bose glass is gapless and has a finite compressibility whereas the Mott insulator has a finite gap and zero compressibility. In a pioneering experiment [118], the authors detected indications for the onset of the Bose glass phase by means of modulation spectroscopy and time-of-flight coherence measurements. They detected a region where both, Mott insulating gap and superfluid long range phase coherence

vanish. However, an unambiguous characterization of the Bose glass phase was not possible, and remains difficult until today [196, 197]. Despite its qualitative similarities in the overall phase diagram, disordered and quasiperiodic setups were shown to respond notably different to a modulation of the lattice amplitude [119]. The excitation spectrum deserves more experimental and theoretical investigation. A lattice amplitude modulation of $\cos(aKj)$-geometry, corresponding to the geometry of the quasiperiodic lattice if $K = k_2/k_1$, may couple to a certain class of excitations. This possibly provides further insights into the properties of the Bose glass phase and the phase transitions to the superfluid and Mott insulating phases.

In this thesis, we considered small amplitude modulations probing the linear response regime and thus gaining information on the equilibrium system. However, the superlattice modulation or its extension to arbitrary momenta could also be used to engineer out-of-equilibrium *Floquet* states [198]. The basic idea is to coherently manipulate an isolated system by periodic driving. The periodic driving simulates the dynamics of an effective static Hamiltonian with potentially exciting and novel properties. It is readily realized in cold atoms setups by lattice shaking, moving lattices or time-dependent external fields [198] and leads to a modification of the tunneling matrix element. Prominent examples include the study of dynamic localization [199], i.e. the suppression of the inter-well expansion, of a Bose-Einstein condensate in an optical lattice, as well as the simulation of frustrated classical magnetism [200] or the creation of artificial gauge fields [201]. The effect of the superlattice modulation, or its extension to other momenta, at arbitrary frequency and strength are worth an investigation as this may potentially stabilize novel phases.

APPENDIX A

Numerical Convergence

In this appendix we give details on the error analysis of the energy absorption rate in t-DMRG. We extract the energy absorption rate from a fit of the time evolution of the energy (see for example App. B) for a given set of control parameters matrix dimension D, Suzuki-Trotter time step τ, and the local dimension σ in the case of bosons. The fit range is chosen to cover a sufficiently large region located within the linear regime. We use the *Matlab* environment [202] to obtain the fits.

Consider a given parameter set. We conduct an error analysis by increasing the matrix dimension D, by reducing the Suzuki-Trotter time step τ, or by increasing the local dimension σ in the case of bosons. We fit the time evolution of the energy with one of the control parameters changed and determine the change in the energy absorption rate with respect to the original set of control parameters. In each case, this defines an error as $\delta = x_{\text{param. varied}} - x$ where x is the fitted parameter for the initial control parameters and $x_{\text{param. varied}}$ is the fitted parameter with one of the control parameters changed.

Additionally, we vary the chosen fit region, either increasing the right fit bound or decreasing the left fit bound. We ensure that the chosen modified fit range is still suitable. We fit the time evolution of the energy with one of the fit bounds changed but original control parameters and determine the change in the energy absorption rate with respect to the original choice of fit range. In each case, this defines an error as $\delta = x_{\text{fit bound varied}} - x$ where x is the fitted parameter for the initial fit range and $x_{\text{fit bound varied}}$ is the fitted parameter with one of the fit bounds varied but original control parameters.

Furthermore, we consider the lower and upper confidence bounds on the fitted coefficients provided by *Matlab* [202] and determine the change in the energy absorption rate as an error. The width of the interval given by the lower and upper confidence bound indicates how uncertain one is about the fitted coefficients and it is typically large if not enough data points are considered. The bounds are defined with a level of certainty of 95%. Each bound defines an error as $\delta = x_{\text{conf. bound}} - x$ where x is the fitted parameter and $x_{\text{conf. bound}}$ is the lower or upper confidence bound.

The errors δ can be positive or negative. The maximum $\delta > 0$ of the above errors defines the upper error bar. The minimum $\delta < 0$ defines the lower error bar. If no δ is positive (negative), the upper (lower) error bar is set to zero. We do not observe a general pattern regarding which error dominates. This depends strongly on the physical situation and varies even for neighboring points on the same curve. Note, that we have verified for each situation at study that the ground state energy has converged to sufficient precision before carrying out the time evolution of the energy.

APPENDIX B

Time-dependence of the absorbed energy

In this appendix we comment on the time evolution of energy $E(t) - E_0$ obtained using t-DMRG in the different situations studied in this thesis.
In lattice shaking setups, the system absorbs energy whenever the modulation frequency ω corresponds to the energy of an available excitation in the system. Close to resonance, the time evolution of the energy typically shows an initial quadratic rise, then becomes linear in time at intermediate (and sufficiently large) times and eventually saturates at longer times. We consider the linear regime of the absorbed energy where the slope m, which we identify with the energy absorption, can be extracted from a fit of the absorbed energy. However, the chosen fitting functions and the considered time intervals depend on the situation at study. The extent of the linear region is related to the choice of the amplitude A of the perturbation. The amplitude needs to be chosen sufficiently large to obtain a measurable signal, but also small enough for the response to remain in the linear regime long enough (and not saturate at short times).
In this appendix, we comment on both, the choice of the perturbing amplitude A and on the fitting procedure in the different situations studied in this thesis. A detailed analysis of the time evolution of the energy is important in order to verify the validity of linear response and extract reliable values for the energy absorption rate.

B.1 Ionic Fermi-Hubbard model

In this section we discuss the time evolution of the energy as a response to superlattice amplitude modulation in different parts of the phase diagram of the ionic Fermi-Hubbard model studied in Ch. 4 of this thesis.

B.1.1 Ising criticality

As an example, in Fig. B.1 the time evolution of the energy $(E(t) - E_0)/A^2$ is shown at Ising criticality for two different system sizes $L = 96$ and $L = 192$ within the $n = 1$ peak and for two different amplitudes of the modulation. The typical linear increase is observed for times $\gtrsim 100\hbar/J$, modulated with the perturbation frequency. We extract the energy absorption rate from a fit of

$$E(t) - E_0 = mt + \text{offset} + h\cos(\omega t + \theta) \tag{B.1}$$

with fit parameters slope m, y-intercept offset, amplitude h ($h \approx A$ in many cases), and phase θ of the lattice modulation and with given frequency of the lattice modulation ω. The extracted energy absorption rate is discussed in Sec. 4.4.1 in the main part of this thesis. Due to the small frequencies of the modulation, only few periods of the modulation are accessible within numerical accuracy.

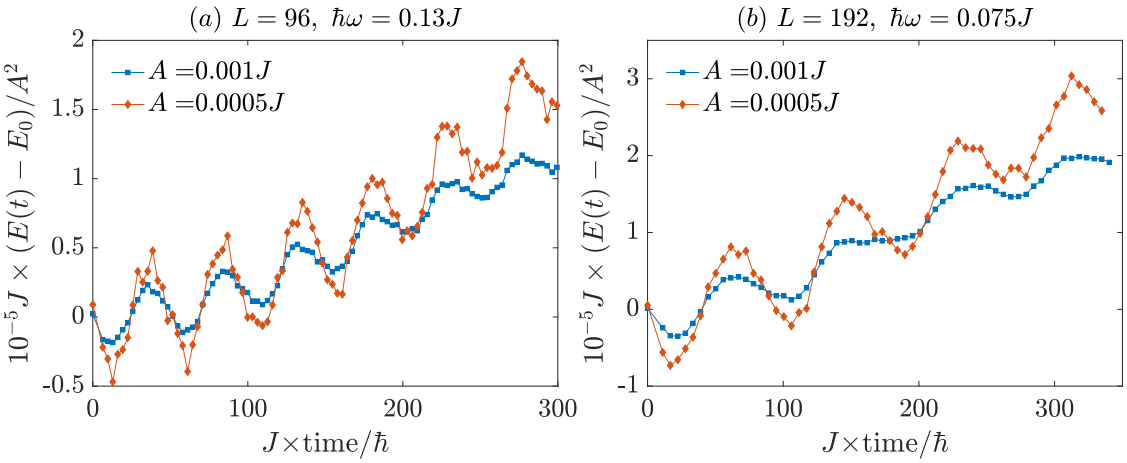

Figure B.1: The absorbed energy as a function of time in t-DMRG for $\Delta = 50J$ at Ising criticality for different amplitudes of the modulation $A = 0.001J$ (blue squares) and $A = 0.0005J$ (orange diamonds) for a system size $L = 96$ at $U_{c1} = 51.26J$ and at $\hbar\omega = 0.13J$ (a) as well as for $L = 192$ at $U_{c1} = 51.3J$ and at $\hbar\omega = 0.075J$ (b). Solid lines are guides to the eye. For $A = 0.001J$ saturation effects are strong, in particular for $L = 192$ where the energy saturates at times $< 200\hbar/J$.

For the smaller amplitude $A = 0.0005J$ we consider times up to $\gtrsim 300\hbar/J$. For the larger amplitude $A = 0.001J$ saturation sets in at earlier times as can be seen in Fig. B.1. For the linear response, we can only consider times below saturation which leads to an increased uncertainty in the fits and we clearly underestimate the energy absorption for $A = 0.001J$ as can be seen from a comparison of the energy absorption rate for the two amplitudes in Fig. 4.19(a). This justifies our choice of the $A = 0.0005J$ data for a quantitative determination of the critical velocity in the Sec. 4.4.1 (cf. table 4.1). The energy saturates particularly early for the system size $L = 192$ where absorption is strongest. For this system size the absorption occurs at the smallest considered modulation frequencies such that the number of observed oscillations is particularly small. For the amplitude $A = 0.001J$, the fits become unreliable, in particular around the maximum of the peak as the time evolution of the energy saturates early. This explains the asymmetry of the peak (cf. Fig. 4.19(a)). In addition, for $L = 192$ absorption is particularly strong in the center of the $A = 0.0005J$ peak which, even at this small amplitude, leads to saturation at early times at these frequencies. Consequently, we might slightly underestimate the peak height of the $L = 192$, $A = 0.0005J$ peak. This justifies our choice of the $L = 128$, $A = 0.0005J$ peak to determine the best estimate of the critical velocity u_c (and from this the expected peak positions of the $n = 1$ peak for the other system sizes) in Sec. 4.4.1.

B.1.2 Bond order wave phase

As an example, in Fig. B.2 the time evolution of the energy $(E(t) - E_0)/A^2$ is shown in the bond order wave at $U = 52J$ for the two system sizes at study $L = 64,\ 128$. We consider three different amplitudes of the modulation. We choose a frequency $\omega = 0.05J$. This frequency is located in the center of the peak at once and twice the spin gap, for the two considered system sizes, respectively. The typical linear increase is observed and only few periods of the oscillation are within the reach of numerical accuracy due to the

small frequencies of the modulation, similar to the observation at Ising criticality. We extract the energy absorption rate from a fit of Eq. (B.1). The extracted energy absorption rate is discussed in Sec. 4.4.2 in the main part of this thesis. Due to the large modulation period, time intervals up to $\sim 300\hbar/J$ are required to reliably extract the energy absorption rate.
Note, that the absorbed energy is very sensitive to the choice of A in this case. For $L = 64$ we compare amplitudes $A = 0.002J,\ 0.005J$ and $0.007J$ in Fig. B.2(a). For $A = 0.002J$, the absorption is very weak for the time interval considered. The linear regime only sets in at late times such that much longer times would be required to reliably extract the absorption rate. In contrast, for the larger values of A, the linear regime appears at earlier times. Since for $A = 0.007J$ saturation sets in early, we use the amplitude $A = 0.005J$ in order to extract the energy absorption rate. For $L = 128$ we compare amplitudes $A = 0.0008J,\ 0.001J,\ 0.002J$ in Fig. B.2(b). Here, the linear regime appears for all considered A. Saturation occurs at $A = 0.002J$ in contrast to the smaller system size $L = 64$ where the absorption is very weak at this amplitude for $L = 128$. We use the amplitude $A = 0.001J$ in order to extract the energy absorption rate.

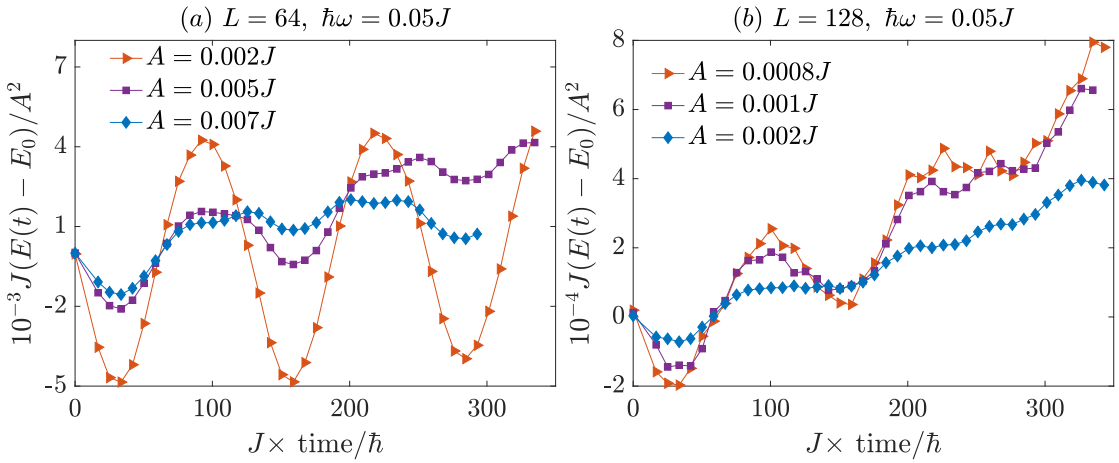

Figure B.2: The absorbed energy as a function of time at $\Delta = 50J$, $U = 52J$ and $\hbar\omega = 0.05J$ for different system sizes $L = 64$ (a) and $L = 128$ (b) and different amplitudes of the modulation. Solid lines are guides to the eye.

B.1.3 Mott insulator

Low-energy spectrum As an example, in Fig. B.3(a) the time evolution of the energy $(E(t) - E_0)/A^2$ is shown in the Mott insulator at $\Delta = 50J$ and $U = 59J$ for $\hbar\omega = 0.4J$. We observe a linear rise in energy modulated with the perturbation frequency over the entire considered time interval. Saturation is expected to set in at later times. Again, we can extract the energy absorption rate from a fit of Eq. (B.1). The extracted energy absorption rate is discussed in Sec. 4.5.1 in the main part of this thesis. We consider times up to $200\hbar/J$. In Fig. B.3(a) we compare three different amplitudes of the modulation $A = 0.003J,\ 0.005J,\ 0.007J$. No considerable difference is visible but at late times the $A = 0.007J$ data starts to slightly saturate and we conclude that $A = 0.005J$ is a good choice for our study. The authors of Ref. [124] reveal substructures in the spectrum of the homogeneous Hubbard model. First, a linear rise in energy is observed but at later times the absorbed energy either saturates or increases further with an increased slope. This leads to a comb-like structure in the absorption rate on top of a broad spectrum. Similar substructures may arise here but are not resolved within the considered time scales and would not affect our main results.

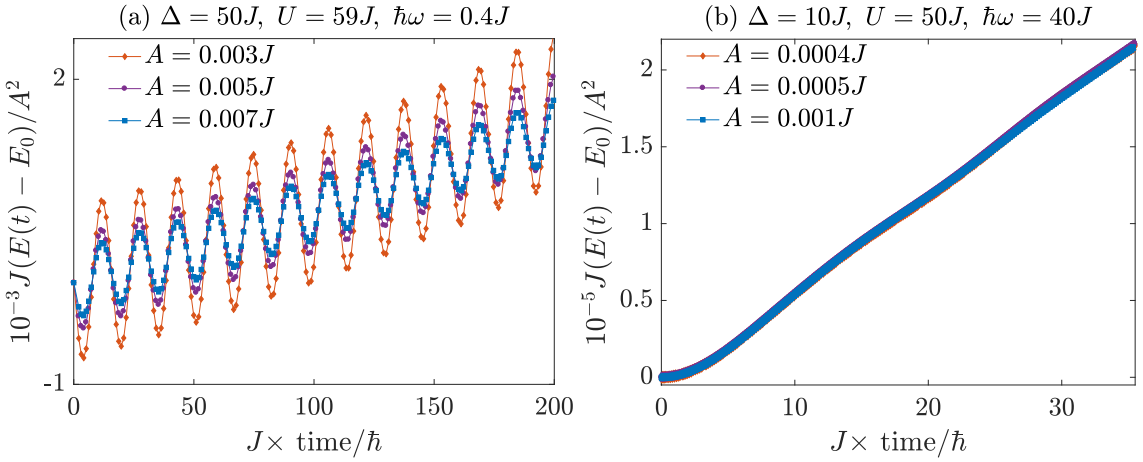

Figure B.3: The absorbed energy as a function of time for different amplitudes of the modulation at $\Delta = 50J$, $U = 59J$, $\hbar\omega = 0.4J$ (a) and at $\Delta = 10J$, $U = 50J$, $\hbar\omega = 40J$ (b). Solid lines are guides to the eye.

High energy spectrum As an example, the time evolution $(E(t) - E_0)/A^2$ in the U peak for $\Delta = 10J$, $U = 50J$ (cf. Fig. 4.24) at $\hbar\omega = 40J$ is shown in Fig. B.3(b) for different amplitudes of the modulation $A = 0.0004J,\ 0.0005J,\ 0.001J$. In all peaks an amplitude $A = 0.0005J$ is a good choice as we observe a sufficiently large linear regime. Similar to the band insulating case (cf. Sec. 4.3.2), we observe a superimposed oscillation of small frequency $\omega_{\text{obs}} \ll \omega$ on top of the typical linear rise in energy. In the $(U + \Delta)$ peak we extract the slope from a fit of Eq. (4.37) as the energy absorption is strong and the oscillation with modulation frequency is negligible, similar to the observation on the band insulating side of the phase diagram (cf. Sec. 4.3.2). In the U and $(U - \Delta)$ peaks the oscillation with modulation frequency is no longer negligible such that we extract the energy absorption rate from a fit of

$$E(t) - E_0 = mt + \text{offset} + \tilde{A}\cos(\omega_{\text{obs}}t + \varphi) + h\cos(\omega t + \theta) \tag{B.2}$$

with fit parameters slope m, y-intercept offset, amplitude $\tilde{A}$, frequency ω_{obs} and phase φ of the superimposed oscillation as well as amplitude h, and phase θ of the lattice modulation and with given frequency of the lattice modulation ω. The extracted energy absorption rate is discussed in Sec. 4.5.2 in the main part of this thesis.

B.2 Bose-Hubbard model

In this section we discuss the time evolution of the energy as a response to superlattice amplitude modulation in the Mott insulating and superfluid phases of the Bose-Hubbard model studied in Ch. 6 of this thesis.

B.2.1 Mott insulator

As an example, in Fig. B.4, the time evolution of the energy $(E(t) - E_0)/A^2$ at strong interactions $U = 60J$ (a) and at intermediate interactions $U = 6J$ (b) is shown for perturbing frequencies near the maximum of the absorption. We consider different amplitudes of the modulation $A = 0.05J,\ 0.01J,\ 0.005J$. The typical linear time-dependence, modulated by the perturbation frequency, is observed for times $\gtrsim 2\hbar/J$. Saturation does not occur within the considered time interval and the linear time interval is sufficiently large for all considered amplitudes. We consider an amplitude $A = 0.01J$ and extract the energy

absorption rate from a fit of Eq. (B.1). The extracted energy absorption rate is discussed in Sec. 6.2 in the main part of this thesis. We consider times up to $\sim 4\hbar/J$ at strong interactions and times up to $\sim 10\hbar/J$ at intermediate interactions. Examples of the fits are shown in the insets of Fig. B.4.

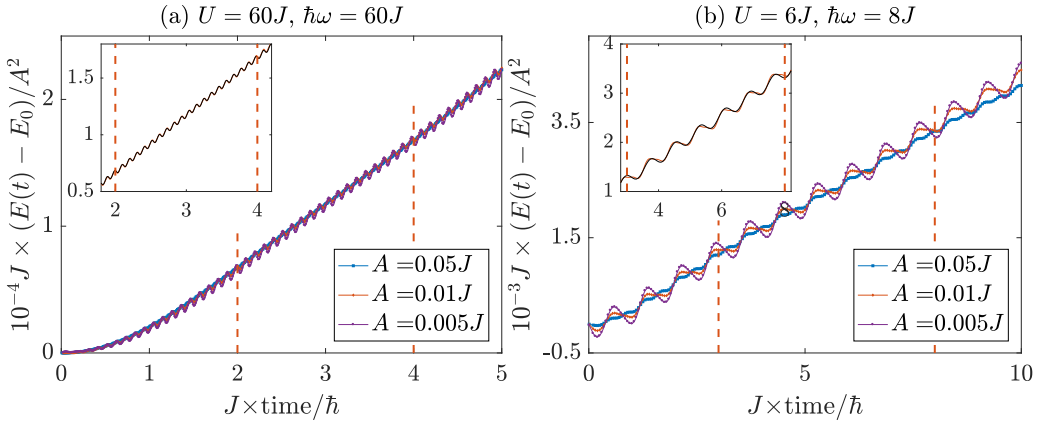

Figure B.4: The absorbed energy as a function of time at $U = 60J$, $\hbar\omega = 60J$ (a) and at $U = 6J$, $\hbar\omega = 8J$ (b) for different amplitudes of the modulation $A = 0.05J,\ 0.01J,\ 0.005J$. Solid lines are guides to the eye and vertical dashed lines indicate the chosen fit range. The inset shows the $A = 0.01J$ data (orange dots) compared to the obtained fit (black solid line).

B.2.2 Superfluid

As an example, in Fig. B.5, the time evolution of the energy $(E(t) - E_0)/A^2$ at an interaction strength $U = 1J$ is shown at low frequencies $\hbar\omega = 0.5J$ (a) and at larger frequencies $\hbar\omega = 4J$ (b). We consider different amplitudes of the modulation $A = 0.1J,\ 0.05J,\ 0.01J$ and $A = 0.05J,\ 0.01J,\ 0.005J$ respectively. For the smaller frequency we have chosen larger amplitudes as absorption is very weak. In both cases, the typical linear time-dependence, modulated by the perturbation frequency, is observed already at short times. Saturation does not occur within in the considered time interval and the linear time interval is sufficiently large for all considered amplitudes.

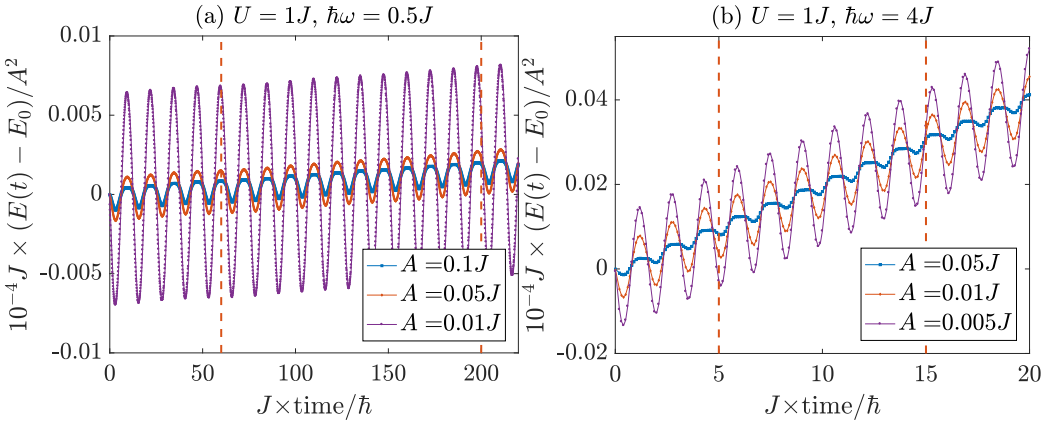

Figure B.5: The absorbed energy as a function of time at $U = 1J$ and at $\hbar\omega = 0.5J$ (a) and at $\hbar\omega = 4J$ (b) for different amplitudes of the modulation. Solid lines are guides to the eye and vertical dashed lines indicate the chosen fit range.

We consider an amplitude $A = 0.05J$ for $\hbar\omega < 2J$ and $A = 0.01J$ for $\hbar\omega \geq 2J$ and extract the energy absorption rate from a fit of Eq. (B.1). The extracted energy absorption rate is discussed in Sec. 6.3 in

the main part of this thesis. The considered times are chosen such that sufficiently many periods of the oscillation are covered. We chose to consider times up to $\sim 250\hbar/J$ at $\hbar\omega < 1J$, times up to $\sim 40\hbar/J$ at $1J \leq \hbar\omega \leq 2J$ and times up to $\sim 15\hbar/J$ at $\hbar\omega > 2J$.

APPENDIX C

Energy absorption within bosonization

In this appendix we sketch the derivation of the bosonization results for the energy absorption rate obtained in collaboration with Roberta Citro and Edmond Orignac [84]. We compare the bosonization results to our t-DMRG results in Ch. 4.

C.1 At the Ising transition

At the transition between the band insulator and the bond order wave phase, the ionic Hubbard at low energies is well described by an effective two-frequency sine-Gordon model (3.41). The transition falls into the Ising universality class (see Sec. 3.3.2 for details). In the vicinity of this transition, most operators of interest can be written in terms of the disorder parameter of the Ising model μ. Here, we want to express the order parameter of the transition given by Eq. (3.40), $\hat{B} \sim \int_0^{aL} dx \left[\sin\left(\sqrt{2}\phi_c\right)\cos\left(\sqrt{2}\phi_s\right)\right]$, in terms of μ. It was shown that $\sin\left(\sqrt{2}\phi_c\right)$ is expressible in terms of the disorder parameter μ [148], $\mu \sim \sin\left(\sqrt{2}\phi_c\right)$, while $\langle\cos\left(\sqrt{2}\phi_s\right)\rangle$ becomes a non-universal constant, C, which depends on the ratio of the spin gap to the full bandwidth. Consequently, the bond order parameter becomes

$$\hat{B} = \frac{\mathcal{A}C}{\alpha}\int_0^{aL} dx \sin\left(\sqrt{2}\phi_c\right) = \frac{\mathcal{A}C\gamma}{\alpha}\int_0^{aL} dx\mu, \tag{C.1}$$

with γ a dimensionless constant. The spectroscopic response function (in the case of superlattice modulation spectroscopy) is proportional to the imaginary part of the Fourier transform of the correlator

$$\chi(\tau) = \frac{1}{\hbar}\langle T_\tau \hat{B}(\tau)\hat{B}(0)\rangle, \tag{C.2}$$

where T_τ is the time-ordering operator and τ the imaginary time. At the Ising transition, the correlator becomes

$$\chi(\tau) = \frac{aL}{\hbar}\left(\frac{\mathcal{A}C\gamma}{\alpha}\right)^2 \int_0^{aL} dx\, \langle T_\tau \mu(x,\tau)\mu(0,0)\rangle. \tag{C.3}$$

For a finite system size L at criticality, the correlation function takes the form

$$\langle T_\tau \mu(x,\tau)\mu(0,0)\rangle = \left[\frac{\left(\frac{\pi\alpha}{aL}\right)^2}{\sin^2\left(\frac{\pi x}{aL}\right)+\sinh^2\left(\frac{\pi u_c \tau}{aL}\right)}\right]^{1/8}, \tag{C.4}$$

with scaling dimension $1/8$, where u_c is the sound velocity of charge excitations. This correlation function can be conveniently rewritten as

$$\chi(i\omega_n) = \frac{aL}{\hbar}\left(\frac{\mathcal{A}\mathcal{C}\gamma}{\alpha}\right)^2 \int_0^\infty d\lambda\, \lambda^{1/8-1}\, 2^{1/8}\left(\frac{\pi\alpha}{aL}\right)^{1/4} \int_0^{aL} dx \int_{-\infty}^{\infty} d\tau\, e^{i\omega_n\tau} e^{-\lambda\cosh\left(2\pi\frac{u_c\tau}{aL}\right)} e^{\lambda\cos\left(2\pi\frac{x}{aL}\right)}, \tag{C.5}$$

where λ is dimensionless. The integrals over x and τ are found in tables [203] and one obtains

$$\chi(i\omega_n) = \frac{(aL)^3}{\pi\hbar u_c}\left(\frac{\mathcal{A}\mathcal{C}\gamma}{\alpha}\right)^2\left(\frac{\pi\alpha}{aL}\right)^{1/4} 2^{1/8} \int_0^{+\infty} d\lambda\, \lambda^{1/8-1} I_0(\lambda) K_{\frac{iaL\omega}{2\pi u_c}}(\lambda), \tag{C.6}$$

which can be expressed in closed form [204] leading to

$$\chi(i\omega_n) \sim \frac{aL}{\hbar u_c}\left(\frac{aL}{\alpha}\right)^{7/4}\left|\frac{\Gamma\left(\frac{1}{16}+i\frac{aL\omega_n}{4\pi u_c}\right)}{\Gamma\left(\frac{15}{16}+i\frac{aL\omega_n}{4\pi u_c}\right)}\right|^2. \tag{C.7}$$

Under analytic continuation, one finds

$$\chi(\omega+i0) \sim \frac{aL}{\hbar\, u_c}\left(\frac{aL}{\alpha}\right)^{7/4} \frac{\Gamma\left(\frac{1}{16}+\frac{aL(\omega+i0)}{4\pi u_c}\right)\Gamma\left(\frac{1}{16}-\frac{aL(\omega+i0)}{4\pi u_c}\right)}{\Gamma\left(\frac{15}{16}+\frac{aL(\omega+i0)}{4\pi u_c}\right)\Gamma\left(\frac{15}{16}-\frac{aL(\omega+i0)}{4\pi u_c}\right)}. \tag{C.8}$$

Poles occur every time the argument of one of the Euler gamma functions in the numerator is a non-positive integer. Only considering positive energies, the poles are located at

$$\omega_m = 4\pi\frac{u_c}{aL}\left(m+\frac{1}{16}\right), \tag{C.9}$$

with $m \geq 0$ integer. One obtains the expression of $\chi(\omega)$ from calculating the residues at these poles. Taking the imaginary part, one finds Eq. (4.38),

$$\mathrm{Im}\chi(\omega+i0) \sim \left(\frac{aL}{\alpha}\right)^{7/4}\sum_{m=0}^{\infty}\left(\frac{\Gamma\left(m+\frac{1}{8}\right)}{\Gamma(m+1)}\right)^2 \delta\left(\hbar\omega - 4\pi\frac{\hbar u_c}{aL}\left(m+\frac{1}{16}\right)\right). \tag{C.10}$$

The energy absorption rate is proportional to $\omega\mathrm{Im}\chi(\omega)$ which we discuss in Sec. 4.4.1 in comparison to our t-DMRG results. In order to extract the infinite system behavior, one can take the limit $\omega \gg u_c/(aL)$ and finds the absorption rate to be proportional to $L\,\omega^{-3/4}$.

C.2 Near the Kosterlitz-Thouless transition

At the Kosterlitz-Thouless transition (see Sec. 3.3.2 for details) the charge sector remains gapped while the spin sector becomes critical. The bond order wave order parameter (3.40) can therefore be approximated

by

$$\hat{B} \simeq \frac{\mathcal{A}}{\alpha}\langle \sin\left(\sqrt{2}\phi_c\right)\rangle \int_0^{aL} dx \cos\left(\sqrt{2}\phi_s\right) = \frac{\mathcal{A}\mathcal{D}}{\alpha}\int_0^{aL} dx \cos\left(\sqrt{2}\phi_s\right), \tag{C.11}$$

where $\mathcal{D}$ is a non-universal constant.

In the bond order wave phase In the bond order wave phase, the spin modes are described by the massive sine Gordon model such that the response function can be obtained by applying the form factor expansion method [205–210]. In the proximity of the Kosterlitz-Thouless transition, $K_s \lesssim 1$, the only excitations of the massive sine Gordon model are solitons and antisolitons. Therefore, in the continuum limit, where the spin correlation length is much smaller than the system size ($\hbar u_s/\Delta_s \ll aL$), the response function takes the form

$$\begin{aligned}\mathrm{Im}\chi(\omega) \quad &= aL\left(\frac{\mathcal{A}\mathcal{D}}{\alpha}\right)^2 \sum_n \frac{(2\pi)^{2(1-n)}}{(n!)^2} \int \prod_{j=1}^{n} d\theta_{j+} d\theta_{j-} \, |\langle \theta_{1+}\theta_{1-}\ldots\theta_{n+}\theta_{n-}|\cos\left(\sqrt{2}\phi_s\right)|0\rangle|^2 \\ &\times \delta\left(\hbar\omega - \Delta_s \sum_{j,r=\pm}\cosh\theta_{jr}\right)\delta\left(\frac{\Delta_s}{\hbar u_s}\sum_{j,r=\pm}\sinh\theta_{jr}\right),\end{aligned} \tag{C.12}$$

where $\theta_{j+,-}$ are the rapidities for a soliton (+) or an antisoliton (−), Δ_s is the spin gap, and $|0\rangle$ is the excitation vacuum. This expression predicts thresholds at frequencies $2n\Delta_s$ where n is an integer. This means an excitation is created each time the modulation frequency is large enough to generate n soliton-antisoliton pairs. Near the lowest threshold, located at $\hbar\omega = 2\Delta_s$, the form factor is given by the following expression [208, 211] as only a single soliton-antisoliton pair can be created,

$$\langle\theta_+\theta_-|\cos\sqrt{2}\theta_s|0\rangle = \frac{i\sinh\left(\frac{\theta_+-\theta_-}{2}\right)}{\theta_+-\theta_-+i\pi}\exp\left[\int_0^{+\infty}\frac{d\psi}{\psi}\frac{e^{-\psi/2}}{\cosh(\psi/2)}\frac{1-\cosh\psi\left(1-\frac{\theta_+-\theta_-}{i\pi}\right)}{2\sinh\psi}\right]. \tag{C.13}$$

Then, inserting this into the previous expression (C.12), one finds, for $2\Delta_s < \hbar\omega < 4\Delta_s$,

$$\begin{aligned}\mathrm{Im}\chi(\omega) \quad &= \quad aL\left(\frac{\mathcal{A}\mathcal{D}}{\alpha}\right)^2 \frac{\hbar u_s}{\Delta_s^2}\frac{\sqrt{\left(\frac{\hbar\omega}{2\Delta_s}\right)^2-1}\,\theta(\hbar\omega-2\Delta_s)}{\frac{\hbar\omega}{2\Delta_s}\left[\pi^2+4\left(\mathrm{acosh}\frac{\hbar\omega}{2\Delta_s}\right)^2\right]} \\ &\times\exp\left[\int_0^{+\infty}\frac{d\psi}{\psi}\frac{e^{-\psi/2}}{\cosh(\psi/2)\sinh\psi}\left(1-\cosh\psi\cos\left(\frac{2\psi}{\pi}\mathrm{acosh}\frac{\hbar\omega}{2\Delta_s}\right)\right)\right].\end{aligned} \tag{C.14}$$

As $\hbar\omega \to 2\Delta_s$, one obtains $\mathrm{Im}\chi(\omega)$ to be proportional to $\sqrt{(\hbar\omega)^2-4\Delta_s^2}$ corresponding to Eq. (4.40) which we discuss in Sec. 4.4.2 in comparison to our t-DMRG results.

In the Mott insulator In the Mott insulator, the spin modes are gapless. Neglecting logarithmic corrections, the correlation function takes the form

$$\langle T_\tau \cos\sqrt{2}\phi_s(x,\tau)\cos\sqrt{2}\phi_s(0,0)\rangle = \left[\frac{\left(\frac{\pi\alpha}{aL}\right)^2}{\sin^2\left(\frac{\pi x}{aL}\right)+\sinh^2\left(\frac{\pi u_s\tau}{aL}\right)}\right]^{1/2}, \tag{C.15}$$

with scaling dimension $1/2$. In the infinite system, one finds $\mathrm{Im}\chi(\omega)$ to be proportional to the integral

$$I(\omega_n) = \frac{aL}{\hbar\alpha^2}\int_{-\infty}^{+\infty} dx \int_{-\infty}^{+\infty} d\tau\, e^{i\omega_n\tau}\left(\frac{\alpha^2}{x^2+(u_s|\tau|)^2}\right)^{\frac{1}{2}} = \frac{aL}{\hbar\alpha^2}\frac{2\pi\alpha}{|\omega_n|}.$$

Analytic continuation is obtained by the substitution $|\omega_n| \to -i(\omega + i0)$, leading to $\mathrm{Im}\chi(\omega) \sim (aL)/\alpha \times 1/(\hbar\omega)$. Consequently, the energy absorption rate $\overline{dE}/dt \sim \omega\mathrm{Im}\chi(\omega)$ is frequency-independent. In the finite system one recovers a discrete expression

$$\chi(i\omega_n) \sim \frac{1}{\hbar}\frac{\pi\alpha}{aL}\int_0^{aL} dx \int_{-\infty}^{\infty} d\tau e^{i\omega_n\tau}\int_0^{\infty} d\lambda\, \lambda^{-1/2} e^{-\lambda\cosh\left(2\pi\frac{u_s\tau}{aL}\right)} e^{\lambda\cos\left(2\pi\frac{x}{aL}\right)}, \tag{C.16}$$

similar to Eq. (C.5) such that it can be evaluated likewise and one obtains at positive frequencies

$$\mathrm{Im}\chi(\omega) \sim \sum_{m=0}^{\infty}\left(\frac{\Gamma\left(m+\frac{1}{2}\right)}{\Gamma(m+1)}\right)^2 \delta\left(\hbar\omega - 4\pi\frac{\hbar u_c}{aL}\left(m+\frac{1}{2}\right)\right). \tag{C.17}$$

The scaling dimension $1/2$ from Eq. (C.15) (instead of $1/8$ at the Ising critical point (C.4)) appears in this expression in both, the Γ-function and the δ-function. Eq. (C.17) displays a series of peaks n occurring at $\hbar\Omega(n) = 4\pi\hbar u_c/(aL)\,(n+1/2)$ with constant spectral weight in the absorption rate $\overline{dE}/dt \sim \omega\mathrm{Im}\chi(\omega)$.

APPENDIX D

Ground state of the ionic Fermi-Hubbard model in the Mott insulating limit

In this appendix we study the double occupancy and spin correlations in the ground state of the ionic Fermi-Hubbard model in the Mott insulating limit for all parameters considered in Sec. 4.5.2. We use static DMRG keeping up to 160 states .
In Fig. D.1(a) we show the global double occupancy normalized by the number of lattice sites $\sum_j \langle n_{j\uparrow} n_{j\downarrow}\rangle / L$ of the ground state as a function of $(U - \Delta)$. For all considered U, the double occupancy is small which is required for Mott insulating behavior.

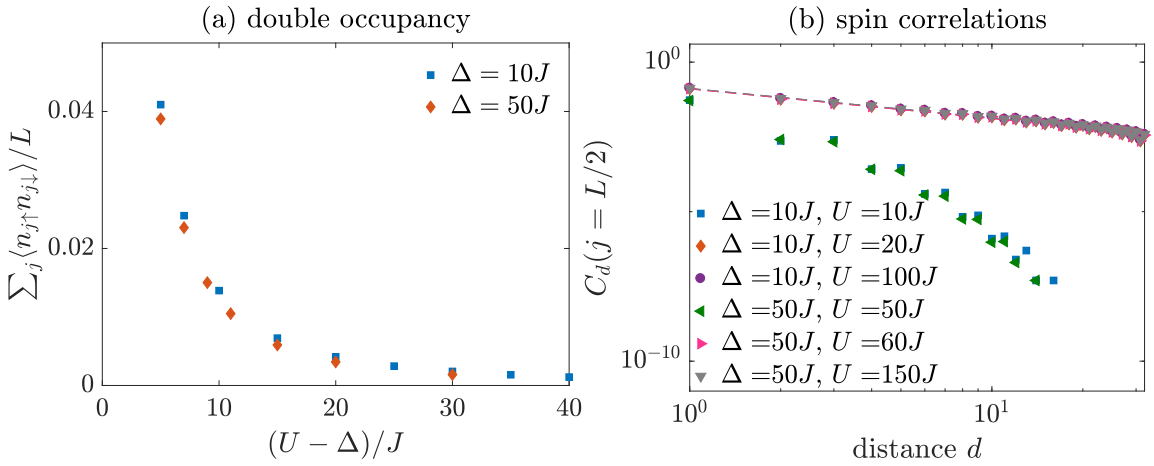

Figure D.1: (a) The global double occupancy normalized by the number of lattice sites $\sum_j \langle n_{j\uparrow} n_{j\downarrow}\rangle / L$ as a function of $(U - \Delta)$ for $U > \Delta$ for a system size $L = 64$. (b) The staggered spin correlator for a system size $L = 64$ at the bulk site $j = 32$. In the Mott insulator at $U > \Delta$, already at small $(U - \Delta) = 10J$, we observe algebraic decay of spin correlations. The dashed lines are fits $C_d \sim d^\alpha$ (there are several dashed lines on top of each other) which yield $\alpha = -1 \pm 0.02$ for all considered cases with $U > \Delta$ as expected for the one-dimensional isotropic Heisenberg model [27]. Additionally, logarithmic corrections to the staggered spin correlator would be expected $C_d \sim d^\alpha \sqrt{\ln(d)}$ but a detection requires finite size scaling or very large system sizes [212].

Furthermore, we determine the staggered spin correlator

$$\begin{aligned} C_d &= (-1)^d \langle S_{z,j} S_{z,j+d}\rangle \\ &= \frac{(-1)^d}{4} \times \left(\langle n_{\uparrow,j} n_{\uparrow,j+d}\rangle + \langle n_{\downarrow,j} n_{\downarrow,j+d}\rangle - \langle n_{\uparrow,j} n_{\downarrow,j+d}\rangle - \langle n_{\downarrow,j} n_{\uparrow,j+d}\rangle\right) \end{aligned} \tag{D.1}$$

with $d \in (1-j, L-j)$, where we used $S_z = (1/2)(n_\uparrow - n_\downarrow)$. The staggered spin correlator is shown in Fig. D.1(b). We observe algebraic decay of the spin correlator for $U - \Delta \gtrsim 10J$. This points to the existence of long ranged antiferromagnetic correlations in the ground state. In Sec. 4.2.2 we assume an antiferromagnetic ground state for the effective model.

Bibliography

[1] S. Chu, *Nobel Lecture: The manipulation of neutral particles*, Rev. Mod. Phys. **70**, 685 (3 1998).

[2] C. N. Cohen-Tannoudji, *Nobel Lecture: Manipulating atoms with photons*, Rev. Mod. Phys. **70**, 707 (3 1998).

[3] W. D. Phillips, *Nobel Lecture: Laser cooling and trapping of neutral atoms*, Rev. Mod. Phys. **70**, 721 (3 1998).

[4] M. H. Anderson, J. R. Ensher, M. R. Matthews, C. E. Wieman and E. A. Cornell, *Observation of Bose-Einstein Condensation in a Dilute Atomic Vapor*, Science **269**, 198 (1995).

[5] C. C. Bradley, C. A. Sackett, J. J. Tollett and R. G. Hulet, *Evidence of Bose-Einstein Condensation in an Atomic Gas with Attractive Interactions*, Phys. Rev. Lett. **75**, 1687 (9 1995).

[6] K. B. Davis, M.-O. Mewes, M. R. Andrews, N. J. van Druten, D. S. Durfee, D. M. Kurn and W. Ketterle, *Bose-Einstein Condensation in a Gas of Sodium Atoms*, Phys. Rev. Lett. **75**, 3969 (22 1995).

[7] E. A. Cornell and C. E. Wieman, *Nobel Lecture: Bose-Einstein condensation in a dilute gas, the first 70 years and some recent experiments*, Rev. Mod. Phys. **74**, 875 (3 2002).

[8] W. Ketterle, *Nobel lecture: When atoms behave as waves: Bose-Einstein condensation and the atom laser*, Rev. Mod. Phys. **74**, 1131 (4 2002).

[9] M. R. Andrews, C. G. Townsend, H.-J. Miesner, D. S. Durfee, D. M. Kurn and W. Ketterle, *Observation of Interference Between Two Bose Condensates*, Science **275**, 637 (1997).

[10] I. Bloch, T. W. Hänsch and T. Esslinger, *Measurement of the spatial coherence of a trapped Bose gas at the phase transition*, Nature **403**, 166 (2000).

[11] B. DeMarco and D. S. Jin, *Onset of Fermi Degeneracy in a Trapped Atomic Gas*, Science **285**, 1703 (1999).

[12] M. Greiner, O. Mandel, T. Esslinger, T. W. Hänsch and I. Bloch, *Quantum phase transition from a superfluid to a Mott insulator in a gas of ultracold atoms*, Nature **415**, 39 (2002).

[13] D. Jaksch, C. Bruder, J. I. Cirac, C. W. Gardiner and P. Zoller, *Cold Bosonic Atoms in Optical Lattices*, Phys. Rev. Lett. **81**, 3108 (15 1998).

[14] M. Köhl, H. Moritz, T. Stöferle, K. Günter and T. Esslinger, *Fermionic Atoms in a Three Dimensional Optical Lattice: Observing Fermi Surfaces, Dynamics, and Interactions*, Phys. Rev. Lett. **94**, 080403 (8 2005).

[15] R. Jördens, N. Strohmaier, K. Gunter, H. Moritz and T. Esslinger, *A Mott insulator of fermionic atoms in an optical lattice*, Nature **455**, 204 (2008).

[16] U. Schneider, L. Hackermüller, S. Will, T. Best, I. Bloch, T. A. Costi, R. W. Helmes, D. Rasch and A. Rosch, *Metallic and Insulating Phases of Repulsively Interacting Fermions in a 3D Optical Lattice*, Science **322**, 1520 (2008).

[17] L. W. Cheuk, M. A. Nichols, K. R. Lawrence, M. Okan, H. Zhang, E. Khatami, N. Trivedi, T. Paiva, M. Rigol and M. W. Zwierlein, *Observation of spatial charge and spin correlations in the 2D Fermi-Hubbard model*, Science **353**, 1260 (2016).

[18] J. H. Drewes, L. A. Miller, E. Cocchi, C. F. Chan, N. Wurz, M. Gall, D. Pertot, F. Brennecke and M. Köhl, *Antiferromagnetic Correlations in Two-Dimensional Fermionic Mott-Insulating and Metallic Phases*, Phys. Rev. Lett. **118**, 170401 (17 2017).

[19] A. Mazurenko, C. S. Chiu, G. Ji, M. F. Parsons, M. Kanász-Nagy, R. Schmidt, F. Grusdt, E. Demler, D. Greif and M. Greiner, *A cold-atom Fermi-Hubbard antiferromagnet*, Nature **545**, 462 (2017), Letter.

[20] R. P. Feynman, *Simulating Physics with Computers*, Int. J. Theor. Phys. **21**, 467 (1982).

[21] I. Bloch, J. Dalibard and W. Zwerger, *Many-body physics with ultracold gases*, Rev. Mod. Phys. **80**, 885 (3 2008).

[22] T. Stöferle, H. Moritz, C. Schori, M. Köhl and T. Esslinger, *Transition from a Strongly Interacting 1D Superfluid to a Mott Insulator*, Phys. Rev. Lett. **92**, 130403 (13 2004).

[23] J. Mun, P. Medley, G. K. Campbell, L. G. Marcassa, D. E. Pritchard and W. Ketterle, *Phase Diagram for a Bose-Einstein Condensate Moving in an Optical Lattice*, Phys. Rev. Lett. **99**, 150604 (15 2007).

[24] D. Clément, N. Fabbri, L. Fallani, C. Fort and M. Inguscio, *Bragg Spectroscopy of Strongly Correlated Bosons in Optical Lattices*, Journal of Low Temperature Physics **158**, 5 (1 2009).

[25] E. Haller, R. Hart, M. J. Mark, J. G. Danzl, L. Reichsöllner, M. Gustavsson, M. Dalmonte, G. Pupillo and H.-C. Nägerl, *Pinning quantum phase transition for a Luttinger liquid of strongly interacting bosons*, Nature **466**, pages (2010).

[26] H. Bethe, *Zur Theorie der Metalle*, Zeitschrift für Physik **71**, 205 (1931).

[27] T. Giamarchi, *Quantum Physics in One Dimension*, Oxford University Press (2004).

[28] S. R. White, *Density matrix formulation for quantum renormalization groups*, Phys. Rev. Lett. **69**, 2863 (19 1992).

[29] U. Schollwöck, *The density-matrix renormalization group in the age of matrix product states*, Annals of Physics **326**, 96 (2011), January 2011 Special Issue.

[30] A. Georges and T. Giamarchi, "Strongly correlated bosons and fermions in optical lattices", *Many-Body Physics with Ultracold Gases, Lecture Notes of the Les Houches Summer School: Volume 94, July 2010*, ed. by G. V. S. Christophe Salomon and L. F. Cugliandolo, Oxford University Press 2012, chap. 1.

[31] P. Törmä, *Physics of ultracold Fermi gases revealed by spectroscopies*, Physica Scripta **91**, 043006 (2016).

[32] H. M. McConnell, B. M. Hoffman and R. M. Metzger, *Charge transfer in molecular crystals*, Proc Natl Acad Sci U S A **53**, 46 (1965).

[33] J. B. Torrance, J. E. Vazquez, J. J. Mayerle and V. Y. Lee, *Discovery of a Neutral-to-Ionic Phase Transition in Organic Materials*, Phys. Rev. Lett. **46**, 253 (4 1981).

[34] J. B. Torrance, A. Girlando, J. J. Mayerle, J. I. Crowley, V. Y. Lee, P. Batail and S. J. LaPlaca, *Anomalous Nature of Neutral-to-Ionic Phase Transition in Tetrathiafulvalene-Chloranil*, Phys. Rev. Lett. **47**, 1747 (24 1981).

[35] M. Fabrizio, A. O. Gogolin and A. A. Nersesyan, *From Band Insulator to Mott Insulator in One Dimension*, Phys. Rev. Lett. **83**, 2014 (10 1999).

[36] M. Messer, R. Desbuquois, T. Uehlinger, G. Jotzu, S. Huber, D. Greif and T. Esslinger, *Exploring Competing Density Order in the Ionic Hubbard Model with Ultracold Fermions*, Phys. Rev. Lett. **115**, 115303 (11 2015).

[37] W. Hofstetter, J. I. Cirac, P. Zoller, E. Demler and M. D. Lukin, *High-Temperature Superfluidity of Fermionic Atoms in Optical Lattices*, Phys. Rev. Lett. **89**, 220407 (22 2002).

[38] D. C. McKay and B. DeMarco, *Cooling in strongly correlated optical lattices: prospects and challenges*, Rep. Prog. Phys. **74**, 054401 (2011).

[39] A. Iucci, M. A. Cazalilla, A. F. Ho and T. Giamarchi, *Energy absorption of a Bose gas in a periodically modulated optical lattice*, Phys. Rev. A **73**, 041608 (4 2006).

[40] A. Einstein, *Quantentheorie des einatomigen idealen Gases. Zweite Abhandlung.*, Sitzungsberichte der Preussischen Akademie der Wissenschaften zu Berlin, Sitzung der physikalisch-mathematischen Klasse, 3 (1925).

[41] S. N. Bose, *Plancks Gesetz und Lichtquantenhypothese*, Zeitschrift für Physik **26**, 178 (1924).

[42] H. J. Metcalf and P. van der Straten, *Laser Cooling and Trapping*, Springer Verlag (Heidelberg) (1999).

[43] W. Ketterle, D. S. Durfee and D. M. Stamper-Kurn, "Making, probing and understanding Bose-Einstein condensates", *Bose-Einstein condensation in atomic gases, Proceedings of the International School of Physics ""*, ed. by M. Inguscio, S. Stringari and C. Wieman, IOS Press, Amsterdam 1999, 67.

[44] P. Courteille, R. S. Freeland, D. J. Heinzen, F. A. van Abeelen and B. J. Verhaar, *Observation of a Feshbach Resonance in Cold Atom Scattering*, Phys. Rev. Lett. **81**, 69 (1 1998).

[45] S. Inouye, M. R. Andrews, J. Stenger, H.-J. Miesner, D. M. Stamper-Kurn and W. Ketterle, *Observation of Feshbach resonances in a Bose-Einstein condensate*, Nature **392**, 151 (1998).

[46] C. Orzel, A. K. Tuchman, M. L. Fenselau, M. Yasuda and M. A. Kasevich, *Squeezed States in a Bose-Einstein Condensate*, Science **291**, 2386 (2001).

[47] B. Paredes, A. Widera, V. Murg, O. Mandel, S. Fölling, I. Cirac, G. V. Shlyapnikov, T. W. Hänsch and I. Bloch, *Tonks-Girardeau gas of ultracold atoms in an optical lattice*, Nature **429**, pages (2004).

[48] T. Kinoshita, T. Wenger and D. S. Weiss, *Observation of a One-Dimensional Tonks-Girardeau Gas*, Science **305**, 1125 (2004).

[49] M. Ben Dahan, E. Peik, J. Reichel, Y. Castin and C. Salomon, *Bloch Oscillations of Atoms in an Optical Potential*, Phys. Rev. Lett. **76**, 4508 (24 1996).

[50] O. Morsch and M. Oberthaler, *Dynamics of Bose-Einstein condensates in optical lattices*, Rev. Mod. Phys. **78**, 179 (1 2006).

[51] T. Bourdel, J. Cubizolles, L. Khaykovich, K. M. F. Magalhães, S. J. J. M. F. Kokkelmans, G. V. Shlyapnikov and C. Salomon, *Measurement of the Interaction Energy near a Feshbach Resonance in a* ^{6}Li *Fermi Gas*, Phys. Rev. Lett. **91**, 020402 (2 2003).

[52] K. M. O'Hara, S. L. Hemmer, M. E. Gehm, S. R. Granade and J. E. Thomas, *Observation of a Strongly Interacting Degenerate Fermi Gas of Atoms*, Science **298**, 2179 (2002).

[53] W. Ketterle and M. W. Zwierlein, *Making, probing and understanding ultracold Fermi gases*, La Rivista del Nuovo Cimento, 247 (5-6 2008).

[54] E. Cocchi, L. A. Miller, J. H. Drewes, M. Koschorreck, D. Pertot, F. Brennecke and M. Köhl, *Equation of State of the Two-Dimensional Hubbard Model*, Phys. Rev. Lett. **116**, 175301 (17 2016).

[55] L. Tarruell, D. Greif, T. Uehlinger, G. Jotzu and T. Esslinger, *Creating, moving and merging Dirac points with a Fermi gas in a tunable honeycomb lattice*, Nature **483**, 302 (2012).

[56] T. Esslinger, *Fermi-Hubbard Physics with Atoms in an Optical Lattice*, Annual Review of Condensed Matter Physics **1**, 129 (2010).

[57] R. Grimm, M. Weidemüller and Y. B. Ovchinnikov, "Optical Dipole Traps for Neutral Atoms", ed. by B. Bederson and H. Walther, vol. 42, Advances In Atomic, Molecular, and Optical Physics Supplement C, Academic Press 2000, 95.

[58] C. Cohen-Tannoudji, J. Dupont-Roc and G. Grynberg, *Atom-Photon Interactions: Basic Processes and Applications*, Wiley-VCH, Weinheim, Germany (1998).

[59] P. Jessen and I. Deutsch, "Optical Lattices", ed. by B. Bederson and H. Walther, vol. 37, Advances In Atomic, Molecular, and Optical Physics Supplement C, Academic Press 1996, 95.

[60] G. Roux, T. Barthel, I. P. McCulloch, C. Kollath, U. Schollwöck and T. Giamarchi, *Quasiperiodic Bose-Hubbard model and localization in one-dimensional cold atomic gases*, Phys. Rev. A **78**, 023628 (2 2008).

[61] J. Sebby-Strabley, M. Anderlini, P. S. Jessen and J. V. Porto, *Lattice of double wells for manipulating pairs of cold atoms*, Phys. Rev. A **73**, 033605 (3 2006).

[62] S. Folling, S. Trotzky, P. Cheinet, M. Feld, R. Saers, A. Widera, T. Muller and I. Bloch, *Direct observation of second-order atom tunnelling*, Nature **448**, 1029 (2007).

[63] D. Pertot, A. Sheikhan, E. Cocchi, L. A. Miller, J. E. Bohn, M. Koschorreck, M. Köhl and C. Kollath, *Relaxation Dynamics of a Fermi Gas in an Optical Superlattice*, Phys. Rev. Lett. **113**, 170403 (17 2014).

[64] M. Modugno and G. Pettini, *Maximally localized Wannier functions for ultracold atoms in one-dimensional double-well periodic potentials*, New Journal of Physics **14**, 055004 (2012).

[65] N. W. Ashcroft and N. D. Mermin, *Solid State Physics*, Thomson Learning (1976).

[66] J. -L. Basdevant and J. Dalibard, *Quantum Mechanics*, Springer (2005).

[67] G. H. Wannier, *The Structure of Electronic Excitation Levels in Insulating Crystals*, Phys. Rev. **52**, 191 (3 1937).

[68] W. Kohn, *Analytic Properties of Bloch Waves and Wannier Functions*, Phys. Rev. **115**, 809 (4 1959).

[69] A. L. Gaunt, T. F. Schmidutz, I. Gotlibovych, R. P. Smith and Z. Hadzibabic, *Bose-Einstein Condensation of Atoms in a Uniform Potential*, Phys. Rev. Lett. **110**, 200406 (20 2013).

[70] B. Mukherjee, Z. Yan, P. B. Patel, Z. Hadzibabic, T. Yefsah, J. Struck and M. W. Zwierlein, *Homogeneous Atomic Fermi Gases*, Phys. Rev. Lett. **118**, 123401 (12 2017).

[71] K. Hueck, N. Luick, L. Sobirey, J. Siegl, T. Lompe and H. Moritz, *Two-Dimensional Homogeneous Fermi Gases*, arXiv:1704.06315 (2017).

[72] W. Zwerger, *Mott–Hubbard transition of cold atoms in optical lattices*, J. Opt. B: Quantum Semiclass. Opt. **5**, 9 (2003).

[73] N. Marzari and D. Vanderbilt, *Maximally localized generalized Wannier functions for composite energy bands*, Phys. Rev. B **56**, 12847 (20 1997).

[74] N. Marzari, A. A. Mostofi, J. R. Yates, I. Souza and D. Vanderbilt, *Maximally localized Wannier functions: Theory and applications*, Rev. Mod. Phys. **84**, 1419 (4 2012).

[75] M. A. Cazalilla, R. Citro, T. Giamarchi, E. Orignac and M. Rigol, *One dimensional bosons: From condensed matter systems to ultracold gases*, Rev. Mod. Phys. **83**, 1405 (4 2011).

[76] M. P. A. Fisher, P. B. Weichman, G. Grinstein and D. S. Fisher, *Boson localization and the superfluid-insulator transition*, Phys. Rev. B **40**, 546 (1 1989).

[77] T. D. Kühner and H. Monien, *Phases of the one-dimensional Bose-Hubbard model*, Phys. Rev. B **58**, R14741 (22 1998).

[78] T. D. Kühner, S. R. White and H. Monien, *One-dimensional Bose-Hubbard model with nearest-neighbor interaction*, Phys. Rev. B **61**, 12474 (18 2000).

[79] J. Hubbard, *Electron Correlations in Narrow Energy Bands*, Proc. R. Soc. Lond **276**, 238 (1365 1963).

[80] N. D. Mermin and H. Wagner, *Absence of Ferromagnetism or Antiferromagnetism in One- or Two-Dimensional Isotropic Heisenberg Models*, Phys. Rev. Lett. **17**, 1133 (22 1966).

[81] E. H. Lieb and F. Y. Wu, *Absence of Mott Transition in an Exact Solution of the Short-Range, One-Band Model in One Dimension*, Phys. Rev. Lett. **20**, 1445 (25 1968).

[82] C. Kollath, U. Schollwöck and W. Zwerger, *Spin-Charge Separation in Cold Fermi Gases: A Real Time Analysis*, Phys. Rev. Lett. **95**, 176401 (17 2005).

[83] N. Nagaosa and J.-i. Takimoto, *Theory of Neutral-Ionic Transition in Organic Crystals. I. Monte Carlo Simulation of Modified Hubbard Model*, Journal of the Physical Society of Japan **55**, 2735 (1986).

[84] K. Loida, J.-S. Bernier, R. Citro, E. Orignac and C. Kollath, *Probing the Bond Order Wave Phase Transitions of the Ionic Hubbard Model by Superlattice Modulation Spectroscopy*, Phys. Rev. Lett. **119**, 230403 (23 2017).

[85] P. J. Strebel and Z. G. Soos, *Theory of Charge Transfer in Aromatic Donor–Acceptor Crystals*, The Journal of Chemical Physics **53**, 4077 (1970).

[86] Z. G. Soos and S. Mazumdar, *Neutral-ionic interface in organic charge-transfer salts*, Phys. Rev. B **18**, 1991 (4 1978).

[87] J. Hubbard and J. B. Torrance, *Model of the Neutral-Ionic Phase Transformation*, Phys. Rev. Lett. **47**, 1750 (24 1981).

[88] T. Egami, S. Ishihara and M. Tachiki, *Lattice Effect of Strong Electron Correlation: Implication for Ferroelectricity and Superconductivity*, Science **261**, 1307 (1993).

[89] R. Resta and S. Sorella, *Many-Body Effects on Polarization and Dynamical Charges in a Partly Covalent Polar Insulator*, Phys. Rev. Lett. **74**, 4738 (23 1995).

[90] N. Gidopoulos, S. Sorella and E. Tosatti, *Born effective charge reversal and metallic threshold state at a band insulator-Mott insulator transition*, Eur. Phys. J. B **14**, 217 (2000).

[91] H. Otsuka and M. Nakamura, *Ground-state phase diagram of the one-dimensional Hubbard model with an alternating chemical potential*, Phys. Rev. B **71**, 155105 (15 2005).

[92] M. E. Torio, A. A. Aligia and H. A. Ceccatto, *Phase diagram of the Hubbard chain with two atoms per cell*, Phys. Rev. B **64**, 121105 (12 2001).

[93] T. Wilkens and R. M. Martin, *Quantum Monte Carlo study of the one-dimensional ionic Hubbard model*, Phys. Rev. B **63**, 235108 (23 2001).

[94] C. D. Batista and A. A. Aligia, *Exact Bond Ordered Ground State for the Transition between the Band and the Mott Insulator*, Phys. Rev. Lett. **92**, 246405 (24 2004).

[95] A. A. Aligia and C. D. Batista, *Dimerized phase of ionic Hubbard models*, Phys. Rev. B **71**, 125110 (12 2005).

[96] Y. Z. Zhang, C. Q. Wu and H. Q. Lin, *Inducement of bond-order wave due to electron correlation in one dimension*, Phys. Rev. B **67**, 205109 (20 2003).

[97] A. P. Kampf, M. Sekania, G. I. Japaridze and P. Brune, *Nature of the insulating phases in the half-filled ionic Hubbard model*, Journal of Physics: Condensed Matter **15**, 5895 (2003).

[98] S. R. Manmana, V. Meden, R. M. Noack and K. Schönhammer, *Quantum critical behavior of the one-dimensional ionic Hubbard model*, Phys. Rev. B **70**, 155115 (15 2004).

[99] Ö. Legeza, K. Buchta and J. Sólyom, *Unified phase diagram of models exhibiting a neutral-ionic transition*, Phys. Rev. B **73**, 165124 (16 2006).

[100] L. Tincani, R. M. Noack and D. Baeriswyl, *Critical properties of the band-insulator-to-Mott-insulator transition in the strong-coupling limit of the ionic Hubbard model*, Phys. Rev. B **79**, 165109 (16 2009).

[101] M. Hafez and S. A. Jafari, *Excitation spectrum of one-dimensional extended ionic Hubbard model*, The European Physical Journal B **78**, 323 (2010).

[102] M. Hafez Torbati, N. A. Drescher and G. S. Uhrig, *Dispersive excitations in one-dimensional ionic Hubbard model*, Phys. Rev. B **89**, 245126 (24 2014).

[103] Hafez-Torbati, Mohsen, Drescher, Nils A. and Uhrig, Götz S., *From gapped excitons to gapless triplons in one dimension*, Eur. Phys. J. B **88**, 36 (2015).

[104] A. Go and G. S. Jeon, *Phase transitions and spectral properties of the ionic Hubbard model in one dimension*, Phys. Rev. B **84**, 195102 (19 2011).

[105] L. Tarruell, "Spectroscopic Tools for Experiments with Ultracold Fermions in Optical Lattices", *Quantum Gas Experiments, Exploring Many-Body States*, ed. by P. Törmä and K. Sengstock, Imperial College Press, London 2015, chap. 11, 251.

[106] P. Törmä, "Spectroscopies - Theory", *Quantum Gas Experiments, Exploring Many-Body States*, ed. by P. Törmä and K. Sengstock, Imperial College Press, London 2015, chap. 10, 199.

[107] C. Kollath, A. Iucci, T. Giamarchi, W. Hofstetter and U. Schollwöck, *Spectroscopy of Ultracold Atoms by Periodic Lattice Modulations*, Phys. Rev. Lett. **97**, 050402 (5 2006).

[108] C. Schori, T. Stöferle, H. Moritz, M. Köhl and T. Esslinger, *Excitations of a Superfluid in a Three-Dimensional Optical Lattice*, Phys. Rev. Lett. **93**, 240402 (24 2004).

[109] C. Menotti, M. Krämer, L. Pitaevskii and S. Stringari, *Dynamic structure factor of a Bose-Einstein condensate in a one-dimensional optical lattice*, Phys. Rev. A **67**, 053609 (5 2003).

[110] G. G. Batrouni, F. F. Assaad, R. T. Scalettar and P. J. H. Denteneer, *Dynamic response of trapped ultracold bosons on optical lattices*, Phys. Rev. A **72**, 031601 (3 2005).

[111] A. Reischl, K. P. Schmidt and G. S. Uhrig, *Temperature in one-dimensional bosonic Mott insulators*, Phys. Rev. A **72**, 063609 (6 2005).

[112] G. Pupillo, A. M. Rey and G. G. Batrouni, *Bragg spectroscopy of trapped one-dimensional strongly interacting bosons in optical lattices: Probing the cake structure*, Phys. Rev. A **74**, 013601 (1 2006).

[113] M. Krämer, C. Tozzo and F. Dalfovo, *Parametric excitation of a Bose-Einstein condensate in a one-dimensional optical lattice*, Phys. Rev. A **71**, 061602 (6 2005).

[114] D. Podolsky, A. Auerbach and D. P. Arovas, *Visibility of the amplitude (Higgs) mode in condensed matter*, Phys. Rev. B **84**, 174522 (17 2011).

[115] L. Pollet and N. Prokof'ev, *Higgs Mode in a Two-Dimensional Superfluid*, Phys. Rev. Lett. **109**, 010401 (1 2012).

[116] M. Endres, T. Fukuhara, D. Pekker, M. Cheneau, P. Schau[bgr], C. Gross, E. Demler, S. Kuhr and I. Bloch, *The 'Higgs' amplitude mode at the two-dimensional superfluid/Mott insulator transition*, Nature **487**, 454 (2012).

[117] R. Sensarma, K. Sengupta and S. Das Sarma, *Momentum-resolved optical lattice modulation spectroscopy for bosons in optical lattices*, Phys. Rev. B **84**, 081101 (8 2011).

[118] L. Fallani, J. E. Lye, V. Guarrera, C. Fort and M. Inguscio, *Ultracold Atoms in a Disordered Crystal of Light: Towards a Bose Glass*, Phys. Rev. Lett. **98**, 130404 (13 2007).

[119] G. Orso, A. Iucci, M. A. Cazalilla and T. Giamarchi, *Lattice modulation spectroscopy of strongly interacting bosons in disordered and quasiperiodic optical lattices*, Phys. Rev. A **80**, 033625 (3 2009).

[120] S. De Sarkar, R. Sensarma and K. Sengupta, *Optical lattice modulation spectroscopy for spin-orbit coupled bosons*, Phys. Rev. B **92**, 174529 (17 2015).

[121] C. Kollath, A. Iucci, I. P. McCulloch and T. Giamarchi, *Modulation spectroscopy with ultracold fermions in an optical lattice*, Phys. Rev. A **74**, 041604 (4 2006).

[122] S. D. Huber and A. Rüegg, *Dynamically Generated Double Occupancy as a Probe of Cold Atom Systems*, Phys. Rev. Lett. **102**, 065301 (6 2009).

[123] R. Sensarma, D. Pekker, M. D. Lukin and E. Demler, *Modulation Spectroscopy and Dynamics of Double Occupancies in a Fermionic Mott Insulator*, Phys. Rev. Lett. **103**, 035303 (3 2009).

[124] F. Massel, M. J. Leskinen and P. Törmä, *Hopping Modulation in a One-Dimensional Fermi-Hubbard Hamiltonian*, Phys. Rev. Lett. **103**, 066404 (6 2009).

[125] A. Korolyuk, F. Massel and P. Törmä, *Probing the Fulde-Ferrell-Larkin-Ovchinnikov Phase by Double Occupancy Modulation Spectroscopy*, Phys. Rev. Lett. **104**, 236402 (23 2010).

[126] Z. Xu, S. Chiesa, S. Yang, S.-Q. Su, D. E. Sheehy, J. Moreno, R. T. Scalettar and M. Jarrell, *Response to dynamical modulation of the optical lattice for fermions in the Hubbard model*, Phys. Rev. A **84**, 021607 (2 2011).

[127] A. Tokuno, E. Demler and T. Giamarchi, *Doublon production rate in modulated optical lattices*, Phys. Rev. A **85**, 053601 (5 2012).

[128] A. Tokuno and T. Giamarchi, *Spin correlations and doublon production rate for fermionic atoms in modulated optical lattices*, Phys. Rev. A **85**, 061603 (6 2012).

[129] A. Dirks, K. Mikelsons, H. R. Krishnamurthy and J. K. Freericks, *Theoretical description of coherent doublon creation via lattice modulation spectroscopy*, Phys. Rev. A **89**, 021602 (2 2014).

[130] D. Greif, L. Tarruell, T. Uehlinger, R. Jördens and T. Esslinger, *Probing Nearest-Neighbor Correlations of Ultracold Fermions in an Optical Lattice*, Phys. Rev. Lett. **106**, 145302 (14 2011).

[131] N. Strohmaier, D. Greif, R. Jördens, L. Tarruell, H. Moritz, T. Esslinger, R. Sensarma, D. Pekker, E. Altman and E. Demler, *Observation of Elastic Doublon Decay in the Fermi-Hubbard Model*, Phys. Rev. Lett. **104**, 080401 (8 2010).

[132] J. Heinze, S. Götze, J. S. Krauser, B. Hundt, N. Fläschner, D.-S. Lühmann, C. Becker and K. Sengstock, *Multiband Spectroscopy of Ultracold Fermions: Observation of Reduced Tunneling in Attractive Bose-Fermi Mixtures*, Phys. Rev. Lett. **107**, 135303 (13 2011).

[133] J. Heinze, J. S. Krauser, N. Fläschner, B. Hundt, S. Götze, A. P. Itin, L. Mathey, K. Sengstock and C. Becker, *Intrinsic Photoconductivity of Ultracold Fermions in Optical Lattices*, Phys. Rev. Lett. **110**, 085302 (8 2013).

[134] S. R. White, *Density-matrix algorithms for quantum renormalization groups*, Phys. Rev. B **48**, 10345 (14 1993).

[135] G. Vidal, *Efficient Simulation of One-Dimensional Quantum Many-Body Systems*, Phys. Rev. Lett. **93**, 040502 (4 2004).

[136] S. R. White and A. E. Feiguin, *Real-Time Evolution Using the Density Matrix Renormalization Group*, Phys. Rev. Lett. **93**, 076401 (7 2004).

[137] A. J. Daley, C. Kollath, U. Schollwöck and G. Vidal, *Time-dependent density-matrix renormalization-group using adaptive effective Hilbert spaces*, Journal of Statistical Mechanics: Theory and Experiment **2004**, P04005 (2004).

[138] S. R. White, *Strongly correlated electron systems and the density matrix renormalization group*, Physics Reports **301**, 187 (1998).

[139] U. Schollwöck, *The density-matrix renormalization group*, Rev. Mod. Phys. **77**, 259 (1 2005).

[140] K. A. Hallberg, *New trends in density matrix renormalization*, Advances in Physics **55**, 477 (2006).

[141] T. Giamarchi, A. Iucci and C. Berthod, *lecture notes: Introduction to Many Body physics*, 2008-2013.

[142] C. Cohen-Tannoudji, B. Diu and F. Laloe, *Quantum Mechanics*, vol. 2, Hermann, John Wiley and Sons (1977).

[143] T. Giamarchi, "Clean and dirty one-dimensional systems", *Quantum Matter at Ultralow Temperatures, Proceedings of the International School of Physics "Enrico Fermi"*, ed. by M. Inguscio, W. Ketterle and S. Stringari, IOS Press, Amsterdam 2016, chap. 6, 413.

[144] F. D. M. Haldane, *'Luttinger liquid theory' of one-dimensional quantum fluids. I. Properties of the Luttinger model and their extension to the general 1D interacting spinless Fermi gas*, Journal of Physics C: Solid State Physics **14**, 2585 (1981).

[145] G. Delfino and G. Mussardo, *Non-integrable aspects of the multi-frequency sine-Gordon model*, Nuclear Physics B **516**, 675 (1998).

[146] Z. Bajnok, L. Palla, G. Takács and F. Wágner, *Nonperturbative study of the two-frequency sine-Gordon model*, Nuclear Physics B **601**, 503 (2001).

[147] G. Takács and F. Wágner, *Double sine-Gordon model revisited*, Nuclear Physics B **741**, 353 (2006).

[148] M. Fabrizio, A. Gogolin and A. Nersesyan, *Critical properties of the double-frequency sine-Gordon model with applications*, Nuclear Physics B **580**, 647 (2000).

[149] V. L. Berezinskii, *Destruction of Long-range Order in One-dimensional and Two-dimensional Systems having a Continuous Symmetry Group I. Classical Systems*, Sov. Phys. JETP **32**, 493 (3 1971).

[150] J. M. Kosterlitz and D. J. Thouless, *Ordering, metastability and phase transitions in two-dimensional systems*, Journal of Physics C: Solid State Physics **6**, 1181 (1973).

[151] V. J. Emery, "Theory of the one-dimensional electron gas", *Highly conducting one-dimensional solids*, ed. by J. T. Devreese, R. P. Evrard and V. E. van Doren, Plenum Press, New York and London 1979, 247.

[152] K. Loida, J.-S. Bernier, R. Citro, E. Orignac and C. Kollath, *Excitation spectrum of the one-dimensional ionic Hubbard model by superlattice modulation spectroscopy*, in preparation (2017).

[153] J. R. Schrieffer and P. A. Wolff, *Relation between the Anderson and Kondo Hamiltonians*, Phys. Rev. **149**, 491 (2 1966).

[154] C. L. Cleveland and R. M. A., *Obtaining a Heisenberg Hamiltonian from the Hubbard model*, American Journal of Physics **44**, 44 (1976).

[155] A. H. MacDonald, S. M. Girvin and D. Yoshioka, $\frac{t}{U}$ *expansion for the Hubbard model*, Phys. Rev. B **37**, 9753 (16 1988).

[156] M. Köhl, *Thermometry of fermionic atoms in an optical lattice*, Phys. Rev. A **73**, 031601 (3 2006).

[157] R. Jördens, L. Tarruell, D. Greif, T. Uehlinger, N. Strohmaier, H. Moritz, T. Esslinger, L. De Leo, C. Kollath, A. Georges, V. Scarola, L. Pollet, E. Burovski, E. Kozik and M. Troyer, *Quantitative Determination of Temperature in the Approach to Magnetic Order of Ultracold Fermions in an Optical Lattice*, Phys. Rev. Lett. **104**, 180401 (18 2010).

[158] Q. Zhou and T.-L. Ho, *Universal Thermometry for Quantum Simulation*, Phys. Rev. Lett. **106**, 225301 (22 2011).

[159] L. W. Cheuk, M. A. Nichols, M. Okan, T. Gersdorf, V. V. Ramasesh, W. S. Bakr, T. Lompe and M. W. Zwierlein, *Quantum-Gas Microscope for Fermionic Atoms*, Phys. Rev. Lett. **114**, 193001 (19 2015).

[160] E. Haller, J. Hudson, A. Kelly, D. A. Cotta, B. Peaudecerf, G. D. Bruce and S. Kuhr, *Single-atom imaging of fermions in a quantum-gas microscope*, Nat Phys **11**, 738 (2015), Letter.

[161] M. F. Parsons, F. Huber, A. Mazurenko, C. S. Chiu, W. Setiawan, K. Wooley-Brown, S. Blatt and M. Greiner, *Site-Resolved Imaging of Fermionic* ^{6}Li *in an Optical Lattice*, Phys. Rev. Lett. **114**, 213002 (21 2015).

[162] A. Omran, M. Boll, T. A. Hilker, K. Kleinlein, G. Salomon, I. Bloch and C. Gross, *Microscopic Observation of Pauli Blocking in Degenerate Fermionic Lattice Gases*, Phys. Rev. Lett. **115**, 263001 (26 2015).

[163] J.-S. Bernier, T.-L. Dao, C. Kollath, A. Georges and P. S. Cornaglia, *Thermometry and signatures of strong correlations from Raman spectroscopy of fermionic atoms in optical lattices*, Phys. Rev. A **81**, 063618 (6 2010).

[164] J. Ruostekoski, C. J. Foot and A. B. Deb, *Light Scattering for Thermometry of Fermionic Atoms in an Optical Lattice*, Phys. Rev. Lett. **103**, 170404 (17 2009).

[165] T. Roscilde, *Thermometry of Cold Atoms in Optical Lattices via Artificial Gauge Fields*, Phys. Rev. Lett. **112**, 110403 (11 2014).

[166] J. Imriška, M. Iazzi, L. Wang, E. Gull, D. Greif, T. Uehlinger, G. Jotzu, L. Tarruell, T. Esslinger and M. Troyer, *Thermodynamics and Magnetic Properties of the Anisotropic 3D Hubbard Model*, Phys. Rev. Lett. **112**, 115301 (11 2014).

[167] R. A. Hart, P. M. Duarte, T.-L. Yang, X. Liu, T. Paiva, E. Khatami, R. T. Scalettar, N. Trivedi, D. A. Huse and R. G. Hulet, *Observation of antiferromagnetic correlations in the Hubbard model with ultracold atoms*, Nature **519**, 211 (2015), Letter.

[168] K. Loida, *Superlattice Modulation Spectroscopy of Ultracold Atoms in Optical Lattices*, Master Thesis, University of Cologne (2014).

[169] K. Loida, A. Sheikhan and C. Kollath, *Thermometry of ultracold fermions by (super)lattice modulation spectroscopy*, Phys. Rev. A **92**, 043624 (4 2015).

[170] L. W. Cheuk, M. A. Nichols, K. R. Lawrence, M. Okan, H. Zhang and M. W. Zwierlein, *Observation of 2D Fermionic Mott Insulators of* ^{40}K *with Single-Site Resolution*, Phys. Rev. Lett. **116**, 235301 (23 2016).

[171] E. Khatami and M. Rigol, *Thermodynamics of strongly interacting fermions in two-dimensional optical lattices*, Phys. Rev. A **84**, 053611 (5 2011).

[172] S. Trotzky, L. Pollet, F. Gerbier, U. Schnorrberger, I. Bloch, N. V. Prokof'ev, B. Svistunov and M. Troyer, *Suppression of the critical temperature for superfluidity near the Mott transition*, Nat Phys **6**, 998 (2010).

[173] M. Greiner, *Ultracold quantum gases in three-dimensional optical lattice potentials*, PhD thesis, Ludwig-Maximilians-Universität München (2003).

[174] L. De Leo, J.-S. Bernier, C. Kollath, A. Georges and V. W. Scarola, *Thermodynamics of the three-dimensional Hubbard model: Implications for cooling cold atomic gases in optical lattices*, Phys. Rev. A **83**, 023606 (2 2011).

[175] S. Bergkvist, P. Henelius and A. Rosengren, *Local-density approximation for confined bosons in an optical lattice*, Phys. Rev. A **70**, 053601 (5 2004).

[176] T. Paiva, R. Scalettar, M. Randeria and N. Trivedi, *Fermions in 2D Optical Lattices: Temperature and Entropy Scales for Observing Antiferromagnetism and Superfluidity*, Phys. Rev. Lett. **104**, 066406 (6 2010).

[177] L. De Leo, C. Kollath, A. Georges, M. Ferrero and O. Parcollet, *Trapping and Cooling Fermionic Atoms into Mott and Néel States*, Phys. Rev. Lett. **101**, 210403 (21 2008).

[178] A. Damascelli, Z. Hussain and Z.-X. Shen, *Angle-resolved photoemission studies of the cuprate superconductors*, Rev. Mod. Phys. **75**, 473 (2 2003).

[179] J. T. Stewart, J. P. Gaebler and D. S. Jin, *Using photoemission spectroscopy to probe a strongly interacting Fermi gas*, Nature **454**, 744 (2008).

[180] B. Fröhlich, M. Feld, E. Vogt, M. Koschorreck, M. Köhl, C. Berthod and T. Giamarchi, *Two-Dimensional Fermi Liquid with Attractive Interactions*, Phys. Rev. Lett. **109**, 130403 (13 2012).

[181] K. Loida, J.-S. Bernier, R. Citro, E. Orignac and C. Kollath, *Accessing finite momentum excitations of the one-dimensional Bose-Hubbard model using superlattice modulation spectroscopy*, arXiv:1803.01951 (2018).

[182] J. J. Sakurai, *Modern Quantum Mechanics*, Addison-Wesley Publishing Company (1994).

[183] M. J. Mark, E. Haller, K. Lauber, J. G. Danzl, A. J. Daley and H.-C. Nägerl, *Precision Measurements on a Tunable Mott Insulator of Ultracold Atoms*, Phys. Rev. Lett. **107**, 175301 (17 2011).

[184] L. P. Pitaevskii and S. Stringari, *Bose-Einstein Condensation*, Oxford University Press (2003).

[185] E. H. Lieb and W. Liniger, *Exact Analysis of an Interacting Bose Gas. I. The General Solution and the Ground State*, Phys. Rev. **130**, 1605 (4 1963).

[186] E. H. Lieb, *Exact Analysis of an Interacting Bose Gas. II. The Excitation Spectrum*, Phys. Rev. **130**, 1616 (4 1963).

[187] N. Fabbri, M. Panfil, D. Clément, L. Fallani, M. Inguscio, C. Fort and J.-S. Caux, *Dynamical structure factor of one-dimensional Bose gases: Experimental signatures of beyond-Luttinger-liquid physics*, Phys. Rev. A **91**, 043617 (4 2015).

[188] F. Meinert, M. Panfil, M. J. Mark, K. Lauber, J.-S. Caux and H.-C. Nägerl, *Probing the Excitations of a Lieb-Liniger Gas from Weak to Strong Coupling*, Phys. Rev. Lett. **115**, 085301 (8 2015).

[189] C. Kollath, U. Schollwöck, J. von Delft and W. Zwerger, *One-dimensional density waves of ultracold bosons in an optical lattice*, Phys. Rev. A **71**, 053606 (5 2005).

[190] J.-S. Caux, P. Calabrese and N. A. Slavnov, *One-particle dynamical correlations in the one-dimensional Bose gas*, Journal of Statistical Mechanics: Theory and Experiment **2007**, P01008 (2007).

[191] M. Tsuchiizu and A. Furusaki, *Ground-state phase diagram of the one-dimensional half-filled extended Hubbard model*, Phys. Rev. B **69**, 035103 (3 2004).

[192] S. Glocke, A. Klümper and J. Sirker, *Half-filled one-dimensional extended Hubbard model: Phase diagram and thermodynamics*, Phys. Rev. B **76**, 155121 (15 2007).

[193] S. Baier, M. J. Mark, D. Petter, K. Aikawa, L. Chomaz, Z. Cai, M. Baranov, P. Zoller and F. Ferlaino, *Extended Bose-Hubbard models with ultracold magnetic atoms*, Science **352**, 201 (2016).

[194] B. Naylor, A. Reigue, E. Maréchal, O. Gorceix, B. Laburthe-Tolra and L. Vernac, *Chromium dipolar Fermi sea*, Phys. Rev. A **91**, 011603 (1 2015).

[195] V. G. Rousseau, D. P. Arovas, M. Rigol, F. Hébert, G. G. Batrouni and R. T. Scalettar, *Exact study of the one-dimensional boson Hubbard model with a superlattice potential*, Phys. Rev. B **73**, 174516 (17 2006).

[196] B. Gadway, D. Pertot, J. Reeves, M. Vogt and D. Schneble, *Glassy Behavior in a Binary Atomic Mixture*, Phys. Rev. Lett. **107**, 145306 (14 2011).

[197] D. Delande and J. Zakrzewski, *Compression as a Tool to Detect Bose Glass in a Cold Atomic Gas*, Phys. Rev. Lett. **102**, 085301 (8 2009).

[198] A. Eckardt, *Colloquium: Atomic quantum gases in periodically driven optical lattices*, Rev. Mod. Phys. **89**, 011004 (1 2017).

[199] H. Lignier, C. Sias, D. Ciampini, Y. Singh, A. Zenesini, O. Morsch and E. Arimondo, *Dynamical Control of Matter-Wave Tunneling in Periodic Potentials*, Phys. Rev. Lett. **99**, 220403 (22 2007).

[200] J. Struck, C. Ölschläger, R. Le Targat, P. Soltan-Panahi, A. Eckardt, M. Lewenstein, P. Windpassinger and K. Sengstock, *Quantum Simulation of Frustrated Classical Magnetism in Triangular Optical Lattices*, Science **333**, 996 (2011).

[201] J. Struck, C. Ölschläger, M. Weinberg, P. Hauke, J. Simonet, A. Eckardt, M. Lewenstein, K. Sengstock and P. Windpassinger, *Tunable Gauge Potential for Neutral and Spinless Particles in Driven Optical Lattices*, Phys. Rev. Lett. **108**, 225304 (22 2012).

[202] MATLAB, *version 9.1.0.441655 (R2016b), Curve Fitting Toolbox (version 3.5.4)*, The MathWorks Inc., Natick, Massachusetts, USA (2016).

[203] M. Abramowitz and I. Stegun, eds., *Handbook of mathematical functions*, Dover, New York (1972).

[204] H. Bateman, *Higher Transcendental Functions*, ed. by A. Erdelyi, vol. 1, McGraw-Hill, New York (1953).

[205] M. Karowski and P. Weisz, *Exact form factors in (1 + 1)-dimensional field theoretic models with soliton behaviour*, Nuclear Physics B **139**, 455 (1978).

[206] F. A. Smirnov, *Form Factors in Completely Integrable Models of Quantum Field Theory*, World Scientific, Singapore (1992).

[207] F. H. L. Essler and A. M. Tsvelik, *Dynamical magnetic susceptibilities in copper benzoate*, Phys. Rev. B **57**, 10592 (17 1998).

[208] H. Babujian, A. Fring, M. Karowski and A. Zapletal, *Exact form factors in integrable quantum field theories: the sine-Gordon model*, Nuclear Physics B **538**, 535 (1999).

[209] H. Babujian and M. Karowski, *Exact form factors in integrable quantum field theories: the sine-Gordon model (II)*, Nuclear Physics B **620**, 407 (2002).

[210] F. H. L. Essler and R. M. Konik, "Application of Massive Integrable Quantum Field Theories to Problems in Condensed Matter Physics", *From Fields to Strings: Circumnavigating Theoretical Physics*, ed. by M. Shifman, A. Vainshtein and J. Wheater, World Scientific, Singapore 2012, 684.

[211] S. Lukyanov, *Form Factors of Exponential Fields in the Sine–Gordon Model*, Modern Physics Letters A **12**, 2543 (1997).

[212] K. A. Hallberg, P. Horsch and G. Martínez, *Numerical renormalization-group study of the correlation functions of the antiferromagnetic spin-1/2 Heisenberg chain*, Phys. Rev. B **52**, R719 (2 1995).

Acknowledgements

Many thanks to all of those that have contributed to this thesis in one or the other way.

I would like to thank my supervisor Corinna Kollath for providing me with the opportunity to work on my PhD, for insightful discussions and for enabling me to take part in several summer schools and conferences. Similarly, I would like to thank all members of my group for good cooperation, (more or less) profound discussions and for reading parts of this thesis, in particular, Johannes Kombe for reading the entire thesis very carefully. Moreover, thanks to Harald van Pee for reliably taking care of our cluster and never getting mad at me for screwing up occasionally.

I would like to thank Roberta Citro and Edmond Orignac for the good collaboration on a project contributing to this thesis, for carrying out many calculations and providing a different perspective on various topics. In particular many thanks to Roberta for spending long hours explaining their results to me and for reading parts of this thesis.

Moreover, I would like to thank all people with whom I have discussed on many occasions during the past three years on topics directly related to this thesis or on more general grounds. I thank Hans Kroha, Martin Weitz and Thomas Bredow for being part of my thesis committee.

Zum Schluss aber dafür umso mehr, liebsten Dank an Ulla, Klaus, Paul und David.